

Factors controlling damage initiation in fatigue loaded unidirectional composites under the influence of different matrix properties

Vom Fachbereich Maschinenbau und Verfahrenstechnik

der Rheinland-Pfälzischen Technischen Universität Kaiserslautern-Landau

zur Erlangung des akademischen Grades

Doktor-Ingenieur (Dr.-Ing.)

genehmigte

Dissertation

von

Herrn

M. Sc. Andreas Baumann

aus Ludwigshafen am Rhein

Tag der mündlichen Prüfung: 28. Oktober 2024

Prüfungsvorsitzender: Prof. Dr.-Ing. Ulf Breuer

1. Berichterstatter: Prof. Dr.-Ing. Joachim Hausmann

2. Berichterstatter: Prof. Dr.-Ing. Holger Ruckdäschel

Vorwort

Diese Dissertation entstand während meiner Tätigkeit am Leibniz-Institut für Verbundwerkstoffe GmbH (IVW) und wurde im Rahmen des von der Deutschen Forschungsgemeinschaft (DFG) geförderten Projekts „Einfluss der Matrixeigenschaften auf das Ermüdungsverhalten von Faser-Kunststoff-Verbunden“ (Kennzeichen 468045930) durchgeführt. Ich danke der DFG herzlich für die finanzielle Unterstützung, die diese Forschung ermöglicht hat. Für die Materialbereitstellung danke ich der Covestro AG und Arxada AG, da insbesondere die Bereitstellung von unverstärkten Matrixpolymer im Bereich der thermoplastischen Tapes und die Kenntnis der chemischen Struktur der Duroplaste Grundvoraussetzung für den gewählten Untersuchungsansatz waren.

Mein tief empfundener Dank gilt zunächst meinem Betreuer, Herrn Prof. Dr.-Ing. Joachim Hausmann nicht nur für die fachliche Unterstützung und wertvollen Anregungen, sondern auch für die gewährte Freiheit und das Vertrauen, die es mir ermöglicht haben, mein Forschungsvorhaben eigenverantwortlich zu gestalten. Diese Unabhängigkeit hat wesentlich zu meinem persönlichen und wissenschaftlichen Wachstum beigetragen. Ebenso möchte ich mich bei Herrn Prof. Dr.-Ing. Holger Ruckdäschel für die Übernahme des Zweitgutachtens und bei Herrn Prof. Dr.-Ing. Ulf Breuer für den Prüfungsvorsitz bedanken.

Die kollegiale Zusammenarbeit und die Kultur der Eigeninitiative und Umsetzung ist es auch was ich während der zurückliegenden Zeit am IVW sehr geschätzt habe. Ein besonderer Dank gilt den Kollegen und Kolleginnen der Abteilung Bauteilentwicklung, die mich mit ihrem Wissen, ihrer Hilfsbereitschaft und ihrem Humor stets motiviert haben. Ohne die freundschaftliche Atmosphäre und die engagierte Zusammenarbeit, wäre diese Arbeit in dieser Form nicht möglich gewesen. Für den direkten Beitrag zum Erfolg dieser Arbeit möchte ich auch Petra Volk, Marc Hein, Werner Gölzer, Holger Franz, Jannis Hüppauff und Christian Becker danken. Auch möchte ich mich bei meiner Kollegin Janna Krummenacker für die stets gute Büroatmosphäre und das immer offene Ohr danken.

Meine Familie und meine Freunde verdienen meinen aufrichtigen Dank dafür, dass sie mir in stressigen Zeiten stets den Rücken gestärkt und an mich geglaubt haben.

Besonders möchte ich meiner Frau Katja und meinem Sohn Nico für ihre Geduld und Unterstützung danken, die mir in schwierigen Momenten neuen Mut und die nötigen Freiräume gegeben haben. Mein tief empfundener Dank gilt auch meinen Eltern, die mir durch ihre Unterstützung und ihren unermüdlichen Glauben an mich den Weg zu dieser Dissertation ermöglicht haben – auch wenn mir das nicht immer direkt bewusst war. Ihre Werte, Geduld und Liebe haben mich auf diesem Weg begleitet und geprägt. Abschließend danke ich allen, die zum Gelingen dieser Arbeit beigetragen haben. Diese Dissertation wäre ohne ihre Hilfe und Unterstützung nicht möglich gewesen.

Bad Dürkheim, November 2024

Andreas Baumann

Contents

Vorwort	i
Contents	iii
Abstract	vii
Kurzfassung	viii
Glossary	xi
Symbols	xiii
1 Introduction	1
1.1 Motivation	1
1.2 Research gap	1
2 Objectives and hypothesis	5
3 State of the art	6
3.1 Conceptual framework.....	6
3.2 Transverse tension-tension loading.....	10
3.2.1 Macro scale	10
3.2.2 Meso scale	12
3.2.3 Micro and sub-micro scale	16
3.3 Compression-compression loading	28
3.3.1 Macro scale	29
3.3.2 Meso scale	30
3.3.3 Micro scale	34
3.4 Approaches to fatigue	35
3.5 Homogenization of constituent properties	35
3.6 Fractography	36
3.7 Morphology property relation.....	38

3.8 Irradiation treatment	39
4 Materials and methods	43
4.1 Matrix polymers	43
4.2 Experimental approach and modification method.....	43
4.3 Neat polymer characterization	45
4.3.1 Specimen preparation and geometry	45
4.3.2 Quasi-static characterization	46
4.3.3 Influence of triaxiality	47
4.3.4 Fatigue characterization	48
4.3.5 Notch sensitivity in fatigue	49
4.3.6 TTS relaxation experiments and visco-elastic parameter fitting.....	50
4.3.7 Relaxation experiments	51
4.3.8 Irradiation induced relaxation.....	52
4.4 Laminate characterization	53
4.4.1 Specimen preparation and geometry.....	53
4.4.2 In-situ edge observation	54
4.4.3 Tension-tension loading.....	56
4.4.4 Compression-compression loading.....	61
5 Experimental results	64
5.1 Neat polymer characterization.....	64
5.1.1 Quasi-static characterization	64
5.1.2 Influence of triaxial loading	65
5.1.3 Rheological characterization.....	66
5.1.4 Fatigue.....	72
5.1.5 Fractography	76
5.2 Laminate fatigue characterization in tension-tension loading	80

5.2.1 Crack observation and in-situ evaluation	80
5.2.2 Scalar damage parameters on the macro scale	87
5.2.3 Conclusions from fatigue experiments on laminates.....	93
5.3 Laminate fatigue characterization in compression-compression loading.....	94
5.3.1 Quasi-static results	94
5.3.2 Load increase testing results	95
5.3.3 Influence of time under load	96
5.3.4 Damage formation	96
5.4 Fiber-Matrix adhesion.....	99
6 Multiscale modelling	102
6.1 Approach and aims	102
6.2 Homogenizing the material properties.....	103
6.3 Constituent properties	105
6.4 Transverse isotropic visco-elastic material.....	105
6.5 Fiber volume content dependent material	106
6.6 Meso model generation from images	107
6.6.1 Geometry and boundary conditions.....	107
6.6.2 Spatial fiber volume distribution.....	109
6.6.3 Pores and stitching fibers	110
6.7 RVE.....	111
6.8 Plasticity on the micro-scale.....	111
7 Numerical results.....	113
7.1 Influence of neighboring cracks.....	113
7.2 Identification of damage initiation sites.....	114
7.2.1 PC-CF.....	114
7.2.2 EP-CF	116

7.3 Elasticity	116
7.4 Triaxiality	118
7.5 Plasticity	119
7.5.1 PC-CF	119
7.5.2 EP-CF	120
7.6 Visco-elasticity.....	121
7.6.1 PC-CF.....	121
7.6.2 EP-CF	121
8 Discussion.....	123
8.1 Tension-tension loading	123
8.1.1 Macroscopic scale	123
8.1.2 Mesoscopic scale	124
8.1.3 Micro and sub-micro scale	125
8.1.4 Damage state	131
8.2 On-axis compression-compression loading.....	132
8.3 Conflicting requirements.....	135
9 Conclusion	138
10 Outlook	140
11 Appendix	142
12 Literature	146
13 Publications and symposia.....	162
14 Student theses	164
Curriculum Vitae	165

Abstract

A constituent-based analysis of the fatigue performance and damage initiation of unidirectional reinforced composites is an approach drastically limiting the number of variables to three, but simultaneously ignores other important aspects. Still, the constituent level is the basis for a better understanding of the main mechanisms driving early stages of fatigue damage. This is essential for a high flexibility in the choice of processing methods and the constituents themselves and allows for a targeted testing campaign including associated cost savings. This work investigates how variations in the matrix polymer's properties affect the fatigue performance under transverse tension-tension and on-axis compression-compression loading. Since it is acknowledged that the fiber-matrix level will only include part of the real composite, a multi-scale approach is pursued both experimentally and by Finite Element modelling. Carbon and glass fiber reinforced epoxy and carbon fiber reinforced polycarbonate are investigated. The results identify the relative stiffness and time-dependence as main polymer properties affecting fatigue damage, whereas plastic yielding has a limited influence. As essential additional factors in controlling damage initiation, residual stresses and interface failure could be identified. The concept of an in-situ S-N curve could be developed and showed that local variations in fiber-distribution need to be considered to get the intrinsic fatigue strength of any system. Similarly, polymer characterization needs to account for the local stress state within a composite, i.e., constrained conditions and loading sequence.

Kurzfassung

Faser-Kunststoff-Verbunde (FKV) in ermüdungsbelasteten Strukturen erfüllen in einzelnen Branchen eine Schlüsselfunktion, da beispielsweise die aktuell leistungsfähigsten Windkraftanlagen kaum wirtschaftlich mit anderen Werkstoffen realisierbar sind. Die Ermüdungscharakterisierung von endlosfaserverstärkten Kunststoffen ist hingegen häufig mit einem erheblichen Aufwand verbunden, da sowohl anisotropes, als auch zeit- und mittelspannungsabhängiges Werkstoffverhalten berücksichtigt werden müssen. Dieser Umstand schränkt in besonderem Maße die Flexibilität bei der Produktentwicklung ein, da der Wechsel eines etablierten Systems mit erheblichem Charakterisierungs- und Kostenaufwand verbunden ist. Erschwert wird dieser Umstand, da sich vielfach die tatsächlichen Werkstoffeigenschaften erst in der Produktrealisierung zeigen unter Berücksichtigung aller Einflussfaktoren. Im Wettbewerb der Werkstoffe und der Konkurrenz in vielen Branchen, stellt dieser Umstand eine Hürde in der Anwendung von FKV dar. Die Identifikation der wesentlichen Einflussfaktoren auf die Ermüdungseigenschaften stellt somit einen wesentlichen Schritt zu mehr Flexibilität in der Produktentwicklung und bei der Umsetzung von Multi-Sourcing Strategien dar.

Ausgehend von dieser Problemstellung ist das Ziel dieser Arbeit den Einfluss des Matrixpolymers unter Berücksichtigung der system- und prozessspezifischen Randbedingungen zu erfassen. Der dafür gewählte multi-skalen Ansatz wird sowohl experimentell, als auch in FE-Modellen (Finite Elemente) umgesetzt, da insbesondere die Rolle des Matrixsystems bei der Schädigungsinitiierung überwiegend auf Faser-Matrix Ebene zugänglich ist. Der Makro- und Mesoebene kommt dabei eine besondere Bedeutung bei der Berücksichtigung weiterer system- und prozessbedingter Einflüsse zu, wie beispielsweise dem Lagenaufbau oder auch Fertigungsfehler. Als Lastfälle mit besondere Relevanz des Matrixsystems liegt der Schwerpunkt der Untersuchung auf schwellender Querkzug- und Längsdruckbelastung. Eine Analyse des Standes der Technik zeigt, dass die gezielte Modifikation der Matrixeigenschaften eine besondere Herausforderung aufgrund der engen Kopplung der Prozessparameter und dem Verhalten der Basisbestandteile darstellt (z.B. Viskosität des Matrixpolymers während der Imprägnierung). Damit erschwert auch hier der Umstand, dass sich die tatsächlichen Systemeigenschaften erst in der Realisierung des Verbundwerkstoffes

darstellen, die Identifikation der Beiträge der Einzelkomponenten zu den Verbundeigenschaften. Als alternativen Modifizierungsansatz wird in dieser Arbeit die Bestrahlung mit γ -Strahlung gewählt. Das Verfahren bietet die Möglichkeit, bei geänderten Polymereigenschaften, sowohl Imprägnierung, als auch geometrische Anordnung über alle Skalen hinweg nicht zu beeinflussen. Damit können modifizierte Systeme erzeugt werden, bei denen sich lediglich bzw. überwiegend die Polymereigenschaften unterscheiden. Experimentell erfordert der Ansatz der energiereichen Strahlung ein mehrstufiges Vorgehen, bei dem zunächst in Vorarbeiten aussichtreiche Polymere identifiziert wurden, die dann sowohl als Reinpolymer und im FKV experimentell charakterisiert werden. Das zweistufige Vorgehen ist erforderlich, da das Ergebnis der Bestrahlung häufig stark vom untersuchten Polymer abhängt und schwer zu prognostizieren ist. Die experimentelle Erfassung der Polymereigenschaften berücksichtigt auch die Bedingungen eines Polymers als Bestandteil eines ermüdungsbelasteten Laminats wie bspw. Mittelspannung und Triaxialität. Im Rahmen der Arbeit werden verschiedene Konzepte zur Beschreibung des Polymerverhaltens unter dem übergeordneten Ansatz des Multi-Stage-Fatigue Modells vereint.

Die Schädigungsinitiierung in Laminaten unter schwellender Querkzug- und Längsdruckbelastung bildet die experimentelle Referenz, um die beobachteten Änderungen aufgrund der Matrixmodifikation zu diskutieren. Untersucht werden glasfaser- und kohlenstofffaserverstärktes Epoxidharz sowie ein kohlenstofffaserverstärktes Polycarbonat, jeweils in zwei Bestrahlungseinstellungen. Ein im Rahmen der Arbeit entwickeltes in-situ Mikroskop erlaubt eine Kantenbeobachtung unter zyklischer Belastung. Weiterhin gestattet die Systemauflösung auch die Dehnungsauswertung innerhalb einer querkzug-belasteten Lage. Ergänzt werden diese experimentellen Arbeiten durch mehrere korrelierte FE-Modelle. Ein eigens entwickelter Analyseprozess erlaubt es, die experimentelle Beobachtung in ein mesoskopisches FE-Modell zu übertragen. Dieses berücksichtigt neben Inhomogenität der Faserverteilung auch Fertigungsfehler. Die notwendigen Materialkennwerte sind durch ein Homogenisierungsverfahren aus den Basisbestandteilen berechnet. Dieses Vorgehen wird durch die Umsetzung einer im Stand der Technik identifizierten Berechnungsroutine, auf die Berücksichtigung eines transversalisotropen, visko-elastisches Werkstoffverhaltens erweitert.

Im Rahmen der Längsdruckbelastung liefern hingegen die Versagensniveaus von Laststeigerungsversuchen mit verschiedenen Signalformen die experimentelle Diskussionsgrundlage. Durch eine gekerbte Probe ist es hierbei möglich, ein Versagen durch Knickbänder (kink band) zu forcieren. Eine detaillierte Analyse der Ergebnisse zeigt allerdings auch, dass die gewählte Testmethode weiter optimiert werden muss.

Es zeigt sich über alle Ergebnisse hinweg, dass die Berücksichtigung der Vorschädigung ein wesentliches Entscheidungskriterium ist, ob und in welchem Maße einzelne Polymereigenschaften Einfluss auf die Schädigungsinitiierung nehmen können. Ist es bei der schwellenden Querkzugbelastung häufig der erste Lastwechsel, der Schädigung induziert, entwickelt sich diese graduell bei druckschwellender Belastung mit katastrophalem Endversagen. In beiden Fällen zeigt sich ein großer Einfluss der Faser-Matrix-Haftung, sodass das Matrixpolymer lediglich dazu beitragen kann, diese Schädigungsstelle frühzeitig zu entlasten bzw. deren Belastung zu begrenzen. Die inhomogene Faserverteilung in allen untersuchten Systemen konnte hierbei als limitierender Faktor identifiziert werden. Als weitere Einflussgröße bei der Schädigungsinitiierung zeigen sich auch im Rahmen dieser Untersuchung der Einfluss von Eigenspannungen. Auch wenn dieser Aspekt nicht den Schwerpunkt der Untersuchung bildet, zeigt deren Wirkung jedoch die Relevanz und unterstreicht die Bedeutung einer ganzheitlichen Betrachtung.

Die Ergebnisse zeigen jedoch auch, dass je nach Lastfall und Lagenaufbau unterschiedliche Anforderungen an das optimale Matrixsystem gestellt werden müssen. Gleichzeitig kann durch den Abgleich mit Eigenschaftskarten (Ashby Diagramm) auch gezeigt werden, dass bestimmte Eigenschaftskombinationen gegenwärtig nicht verfügbar sind. Polymerspezifische Besonderheiten wie Crazing können jedoch trotz ähnlicher Eigenschaften zu deutlich unterschiedlichen Ergebnissen führen und sind häufig in Eigenschaftskarten nicht ersichtlich.

Glossary

Abbreviations

BC	boundary condition
CC	compression-compression loading
CCD	charge-coupled device; Image sensor
CDS	characteristic damage state
CF	carbon fiber
CFRP	carbon fiber reinforced plastic
CI	confidence interval
CT	compact tension
ϵ -CTPZ	epsilon shaped crack tip plastic zone
2D/3D	two dimensional/ three dimensional
DCG	discontinuous crack growth
DIC	digital image correlation
DMTA	dynamic mechanical thermal analysis
EB	electron beam
EP	epoxy resin
EP-CF	epoxy resin carbon fiber reinforced
EP-GF	epoxy resin glass fiber reinforced
FE	finite element method
FFT	fast Fourier Transform
FOV	field of view
fps	frames per second
GF	glass fiber
GFRP	glass fiber reinforced plastic
Irr.	irradiated

LEFM	linear elastic fracture mechanics
NCF	non-crimp fabric
MSF	multi stage fatigue
PES	polyester
PA6	polyamide 6
PC	polycarbonate
PC-CF	polycarbonate carbon fiber reinforced
PEEK	polyetheretherketone
PTFE	polytetrafluoroethylene
RDV	representative damaged volume
Ref.	reference
RTM	resin transfer molding
RVE	representative volume element
SL	shear lag model
S-N	Wöhler curve
TT	tension-tension loading
TTS	time-temperature superposition
UCS	ultimate compression strength
UD	unidirectional
UMAT	constitutive material model implemented by the user
UTS	ultimate tensile strength
WD	working distance

Symbols

Greek symbols		Unit
β	geometry factor	1
γ	gamma radiation	
Δ	difference	
δ	phase offset	Rad
ε	strain	1
$\overline{\varepsilon}_{DIC}$	mean strain evaluated across all visible facets of the DIC strain map	1
$\varepsilon_e, \varepsilon_{e,p}$	elastic strain, elastic-plastic strain	1
ε_{true}	engineering strain measured by the calibrated extensometer	1
$\eta, l, k, G_{12}, G_{23}$	system of elastic constant proposed by Hashin	
θ	RVE orientation	Degree
ν	poisson's ratio	1
ν_m	poisson's ratio of the matrix polymer	1
ρ_w	density	kg/m ³
ρ	crack density	mm ⁻¹
σ	stress	MPa
σ_t	maximum stress, due to stress concentration	MPa
$\sigma_{n,smooth}$	nominal stress of the smooth specimen	MPa
$\sigma_{n,notch}$	nominal stress of the notched specimen	MPa
τ	time constant	s
Indices		
a	amplitude	

Eqv.	equivalent
i	running variable
ij	tensor component $i, j \in \{1, 2, 3\}$
I, II, III	principal stress or strain
Meso	mesoscopic stress
Mises	von Mises stress
n	nominal
max	maximum of a time series
min	minimum of a time series
ref	reference
rubbery	storage modulus above T_g
s	saturated
true	true with regard to a calibrated reference
x, y, xy	stress or strain component in global coordinates
0	initial
*	Laplace transformed equation

Coordinate systems

1, 2, 3	UD ply coordinate system
x, y, z	global coordinate system

Latin symbols		Unit
a, a_l, a_r	crack length (left, right)	mm
A	surface area analyzed	mm ²
$A_{fatigue}$	fracture surface showing striations	mm ²
C, C^{-1}	stiffness tensor and compliance tensor	
c	radius of the mirror and mist region	mm

\vec{d}	displacement vector	
D_{min}	minimum diameter of the cross-section D5R1 specimen	mm
ΔD	damage parameter	1
E	elastic modulus, Relaxation modulus	MPa; GPa
$E_{Charac.}$	elastic modulus from quasi-static characterization	MPa
E_{dyn}	dynamic modulus evaluated during cyclic loading (sinusoidal signal)	MPa
$E_{dyn,N}$	dynamic modulus in the N th loading cycle	MPa
E_{Model}	model prediction for the elastic modulus	MPa
E_{ramp}	modulus determined during the first loading ramp	MPa
$E_{rubbery}$	storage modulus above T_g	MPa
L	length	mm
I	indicator for dominant crack growth	1
K_ϵ	strain concentration	1
K_f	notch sensitivity	1
K_t	stress concentration factor	1
K_{IC}	fracture toughness	MPa×mm ^{0.5}
ΔK	stress intensity range	MPa×mm ^{0.5}
$K_{crit.}$	maximum stress intensity	MPa×mm ^{0.5}
ΔK	stress intensity range	MPa×mm ^{0.5}
ΔK_{th}	crack growth threshold	MPa×mm ^{0.5}
M_c	molecular weight between cross-links	
N	number of cycles	1
n	number of parallel Maxwell elements	1
p	polynom	

q	notch sensitivity	1
R_g	universal gas constant	J/mol
R	load ratio $\sigma_{\min}/\sigma_{\max}$	1
r	radius	mm
r_N	notch radius	mm
s	Laplace parameter	
T	absolute temperature	K
T_g	glass transition temperature	K
T_m	melting temperature	K
t	time	s
t_{90}	thickness of transverse ply	mm
u	displacement	
v_f	fiber volume fraction	1
W_{loss}	specific loss energy	mJ/mm ³
X	coordinate triplet in Cartesian coordinates	

Mathematical symbols

\mathcal{L}	Laplace operator
\mathcal{L}^{-1}	inverse Laplace transform
π	Pi ≈ 3.14159
Σ	summation
\int	integral
\ln	natural logarithm

1 Introduction

1.1 Motivation

Fiber-reinforced materials find their way in more and more applications in recent years. Some industries were historically faster to adapt this class of materials due to high potential operating cost savings, such as in the aircraft industry [1] or the mere feasibility of technical solutions such as megawatt wind turbines [2]. Upcoming industries to employ continuous fiber-reinforced composites might be found in pipelines for hydrogen transport or battery casings for electric-powered vehicles. All these industries make use of high specific stiffness and strength of continuous fiber-reinforced materials. If the latter can be sustained during cyclic loading depends greatly on the constituents (fiber, sizing and matrix), geometry, lay-up and processing parameters. A major challenge from an economic point of view is a much less standardized spectrum of materials and processing routes, which need to be integrated early into the product development process. This opens up a vast spectrum of potential candidate materials with most often a priori unknown fatigue performance. As a result, excessive testing campaigns are necessary at the outset and first build or if changes in the material supply are sought. A good example of an industry, acknowledging this, is the aircraft industry where a change in resin or fibers from a different supplier already necessitates significant testing campaigns [3, Para. 2.3.4]. As a result, a very limited number of materials and suppliers is favored. In addition, risks involving uncertainties in fatigue are kept low by rigorously strict strain limits, which ensures that in a flawed material no damage growth can occur or is slow enough to be detected [4], [5]. In contrast to this, other industries might need more flexibility in their material choice and design. Either in the pursuit of a multi-sourcing strategy to minimize supply chain risks or to utilize more of the composite's high performance in order to excel in competitive markets by breaking with low strain limits.

1.2 Research gap

This trade-off between flexibility and the necessary characterization effort can be addressed by a better understanding of causes for fatigue damage and the factors that induce system dependent properties. A system in this context not only comprises the constituents, but also the processing route leading up to the final set of properties. Numerous studies can be found on the type of damage introduced by fatigue loading

and damage propagation. A major challenge also faced in this work is the universality of these findings. Breaking up a composite system into its constituents fibers, matrix and fiber-matrix interface is a common approach to more universal results. In addition, one might add flaws like pores and auxiliary components like stitching fibers or binders as common features in many continuous fiber-reinforced composites. These additional features are not always present and frequently unwelcomed aspects of the production process. Still, it is necessary to acknowledge their role in fatigue loading as shown for stitching fibers and on-axis tension-tension loading. Here, stitching fibers contribute to the fatigue crack initiation [6], [7], [8], [9], [10]. This loading case has been found to be one of few thoroughly investigated with respect to the influence of the constituents. Instead of covering all three major constituents, this work focuses on the role of the matrix polymer, because of its prominence in damage initiation. Sticking with the example of on-axis loading, the special role of matrix and interface properties can be shown. In general, this type of loading leads to a shallow S-N curve, high specific fatigue strength and low stiffness degradation and is therefore the preferred loading case [11]. This is because most of the load is carried by fibers. Still, early damage propagation is controlled by the matrix material. Damage initiates from two distinct features. At first, weaker fibers break early in the fatigue life or during the first loading cycle [12], [13]. From this point onward, damage propagation is controlled by the matrix properties and fiber/matrix interface [12], [13], [14], [15]. The rate of damage propagation from these two constituents controls the lifetime of the laminate [16]. This is because, damage needs to be contained near the initially broken fibers to avoid further fiber breakage due to overstresses. Even though this is the preferred loading case, most applications will incorporate much more limiting loading scenarios like off-axis loading or on-axis compression. Deviations from on-axis tension loading might be necessary due to multiaxial loading or varying loading directions. Carraro and Quaresimin [17] proposed to further distinguish off-axis loading into two regimes, depending on the failure initiating stress component within the matrix material or at the fiber matrix interface. The extremes of these two cases are pure shear loading and transverse loading. Especially, transverse tensile loading is often critical, due to especially low failure strains compared to all other loading directions e.g. when debonding is initiated [18]. In all of these cases, the matrix polymer takes on an

important role in terms of early stages of fatigue damage as will be shown in the following.

Although many studies identify the area of damage initiation quite clearly it still remains mostly open what factors drive damage formation and what properties should be sought to prevent it. Only few investigations focus on the correlation between matrix properties and fatigue damage initiation. This is because alterations in the polymer property and related changes in fatigue damage are difficult to implement experimentally because additional laminate parameters are often affected simultaneously. Four modification approaches could be identified, each with a specific set of challenges [19]. The approaches can be categorized as follows:

- Altering the macromolecular structure
- Exchanging the matrix polymer (brittle thermoset→ductile thermoplast)
- Exploring different thermal sensitivity of the matrix and fiber properties
- Introducing another phase, which effectively forms a hierarchical composite

The two most prominent parameters studied in this respect are the polymers fracture toughness and the fiber-matrix interface. Shao et al. [20] focused their investigation particularly on these two aspects. Their investigation of a vinyl ester resin in tension-tension loading found that an increasing fracture toughness and improved fiber/matrix adhesion could improve the overall fatigue performance of the composite. A chemical modification of the resin was used as a modification method to introduce changes but keep the composite comparable. However, two factors have changed simultaneously, making it difficult to distinguish clearly the role of each component. Still many other parameters like geometry were kept constant and gradual changes of the polymer are possible.

An alternative approach would be to utilize a different polymer entirely, rather than modifying the existing base polymer. This enables a comparison of different polymer classes. As demonstrated by Hertzberg et al. [21], the fracture toughness and fatigue crack resistance of various polymers can vary considerably. Drastic differences might be expected between relatively brittle thermosetting resins and ductile thermoplastics. With this kind of comparison, it was also found that increasing matrix fracture toughness and variations in fiber matrix adhesion alter the resulting fatigue performance [22], [23], [24]. Despite great freedom in alterations of the matrix properties, this approach is limited by the secondary changes introduced. To name just

a few, the mesoscopic structure, fiber/matrix adhesion, residual stresses and pore content are often distinctly different when the polymer is changed. That these factors can additionally affect fatigue performance has been shown for mesoscopic structures [25], [26], fiber/matrix adhesion [23], residual stresses [27] and pore content [28], [29]. In the case of compressive loading, even small variations in fiber-waviness might lead to different results, which are determined due to geometry rather than differences in polymer properties [30].

The third modification option is based on the thermal sensitivity of most polymers, which is far greater compared to that of the fibers. Vieille et al. [31] used temperature induced changes in ductility of the polymers to further increase the difference between thermoplastic and thermosetting systems by testing above and below glass transition temperature, respectively. They found drastically different damage morphologies. Similarly, Majumdar and Newaz [32] also used different temperatures to study the influence on the fatigue of metal matrix composites. However, the residual stresses will also vary due to the differences in thermal expansion of fibers and matrix polymer.

Hierarchical composites offer another way of modifying the polymer properties. Hierarchical refers to the introduction of another constituent on a sub-fiber matrix level. It has been shown that these additional components can act as crack arresting inhomogeneity or as additional reinforcement depending on the type of particle introduced [33], [34], [35]. A major issue is self-filtration and a homogenous dispersion of the particles on a sub-fiber level with implications for initial flaws [33], [35].

It can be concluded that changes in the polymer system allow for the most significant differences but also introduce additional uncertainties in the interpretation of the resulting fatigue performance. A chemical modification appears in this regard most promising. Although not very common in the field of continuous fiber-reinforced composites, high-energy radiation treatment is another way to modify the polymer's chemical structure. Here modification can be the last step of the production process as frequently done for commodity plastics like Polyethylene [36]. However, Gohs et al. [37] also used high-energy radiation on continuous fiber-reinforced Polypropylene and showed that irradiation treatment lowers strength up to 54% and elastic modulus by 17%. Effects on the fiber-matrix adhesion depended largely on the fiber sizing [38].

2 Objectives and hypothesis

This brief overview shows that the matrix polymer could have a significant impact on damage formation and early stages of damage propagation. At the same time, modification methods to alter the polymer are frequently accompanied by additional changes obscuring the matrix effect. This poses not only a problem for a targeted investigation of the influence of the matrix polymer, but is also one of the reasons why generally each modification necessitates a new characterization campaign. Three basic hypotheses guide this work:

- H1. The matrix polymer's response to a load needs to be different depending on the loading case of the composite.
- H2. The conditions experienced by the matrix polymer within a composite will define the mechanical response to loading.
- H3. Laminates will only yield comparable results if the fiber-matrix arrangement is unchanged.

Derived from these hypotheses, the overall objective of this work is to identify aspects that contribute to a system-specific fatigue performance. This objective can be broken down into the following research questions:

- O1. What matrix properties are relevant?
- O2. How can matrix properties be categorized to enable easier identification?
- O3. Are property targets for the matrix polymer dependent on the laminate's loading case?
- O4. What is the role of the geometric arrangement on the scale of fiber bundles?

3 State of the art

3.1 Conceptual framework

Instead of analyzing the loading scenarios on a macro ($\sim 10^3$ - $10^5 \mu\text{m}$) or meso level ($\sim 10^1$ - $10^3 \mu\text{m}$) alone, it seems more general to take the perspective of the matrix material and analyze how global load and geometric arrangement affect the loads on a micro scale ($\sim 10^1 \mu\text{m}$). The overall conceptual framework found to categorize all properties follows the idea of different active mechanisms during the lifetime of a polymer as part of the composite. The underlying model is an extension of the multi-stage fatigue (MSF) model [39]. This model is well suited to describe the fatigue failure of isotropic materials like polymers and well established for the fatigue life of metals [5], [40], [41]. The stages of fatigue life are fatigue crack incubation, microstructural small crack growth and long crack growth [39]. All aforementioned stages of fatigue damage on the fiber-matrix level will initiate damage that then propagates through the meso and macro scales. Up to fatigue crack incubation, the polymer's response to loading will be homogeneous deformation, which could already affect the remaining life up to crack incubation. This deformation of the bulk of the polymer can be further described by the categories introduced by Haupt et al. [42] (see Figure 3-1). The response to loads is categorized by reversibility and time-dependence. For time independent deformation (top row in Figure 3-1) the categories are elastic and plastic deformation. In the elastic case, all strains can be fully recovered after unloading. In contrast to this, plastic deformation will result in some residual strain after unloading. The material's response to some applied stress will be independent of time. However, in the plastic case the material response is still path or history dependent, meaning that earlier loading cycles can affect the current response.

Most polymers not only show elastic and plastic deformation but also a time-dependent response (lower row in Figure 3-1). This effect can be understood in terms of applied strain rates. Each of the viscous responses contains one of the time independent responses as asymptotic response given enough time as indicated in the bottom row of Figure 3-1. As long as all strains can be recovered given enough recovery time, this behavior is classified as visco-elastic. The difference to purely elastic behavior is that in addition to elastic stresses viscous overstresses are present. The overstresses are rate-dependent and diminish for very slow loading rates. The material response is then

in an equilibrium and hence the elastic part of the visco-elastic material is elastic. Similarly, the plastic case can be extended to the visco-plastic response. Therefore, indefinitely slow loading yields also the equilibrium response, which might contain an irreversible component. A typical phenomenon associated with visco-plastic material behavior is a strain rate dependent yield point. This means that plastic deformation not only depends on the applied stress but also the loading rate.

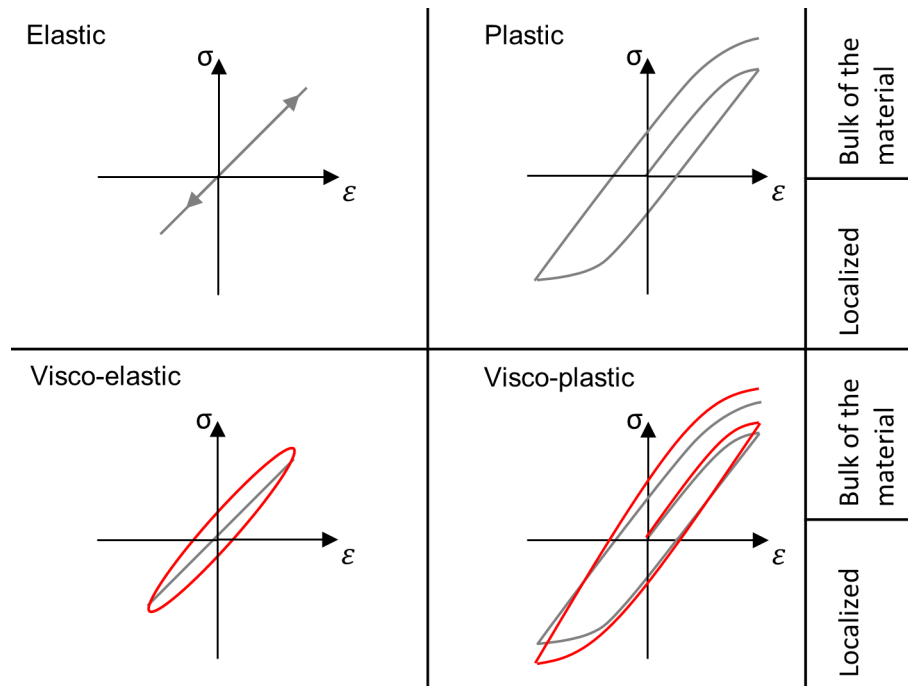


Figure 3-1 Homogeneous deformation categorized according to Haupt and extension by homogeneity. Equilibrium response (gray); Response with overstress (red); Adapted with permission from Haupt [42]

Each category is associated with a set of parameters defining the material response, mainly based on underlying material models used to describe it. Kinloch and Young [40] and others [43] introduce the concept of inhomogeneous deformation, which can be taken as an extension of both plastic and visco-plastic deformation [40]. This is because inhomogeneous deformation is usually introduced by plastic deformation taking place in a small region (size of macromolecules) of the polymer. Very localized plastic deformation can be found in some polymers in the form of crazes and shear bands. Bin Ahmad and Ashby [43] also place necking and cold drawing into this category. The observation of the aforementioned effects is highly dependent on the molecular morphology and a broad spectrum of loading parameters. Inhomogeneous deformation can often be treated as a precursor for crack initiation, as will be discussed

later in detail. Figure 3-2 (a) shows schematically how phases of crack growth can be preceded by a phase of inhomogeneous deformation in the MSF-model.

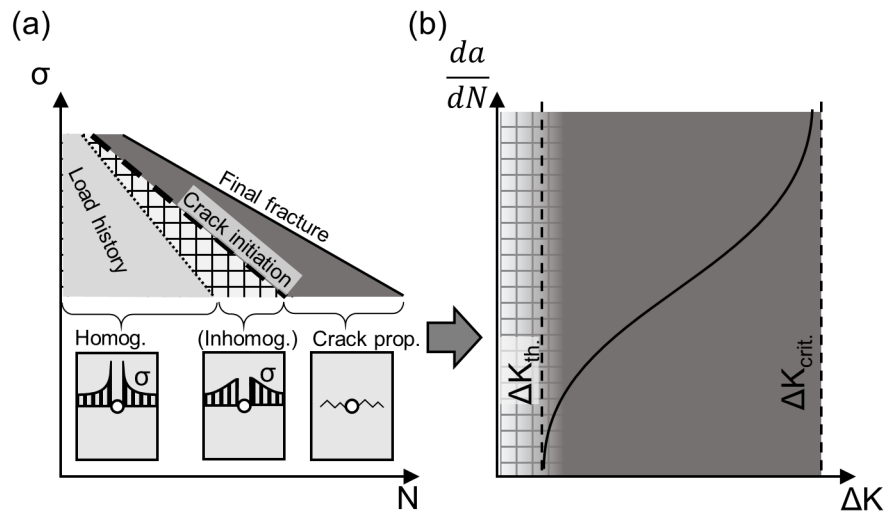


Figure 3-2 MSF-model in the context of polymer deformation; (a) MSF-model including the phase of inhomogeneous deformation; (b) phase of constant fatigue crack growth da/dN as a function of stress intensity range ΔK

After inhomogeneous deformation, small crack growth is initiated. In terms of the commonly used SN curve (shown on the left) the dashed line would be inevitably be crossed and final failure is preceded by small crack growth. Since not all materials show inhomogeneous deformation, this phase is optional and cracks usually initiated at stress concentrations such as holes or in case of the micro scale of a composite near fibers. Explicit investigations of the crack growth behavior of materials can usually be described during constant crack growth by the Paris Erdogan law schematically shown as linear segment in Figure 3-2 (b). At this stage of fatigue damage, the concept of stress concentration factors is left and stress intensities are used to describe the driving mechanism. The number of cycles between reaching the threshold ΔK_{th} enabling stable crack growth and rapid crack growth at the critical stress intensity $\Delta K_{crit.}$ can vary greatly. The phase of crack propagation can take up different portions of the lifetime [5].

As will be shown during the discussion of the literature all phases of the MSF-model are determined by the loading conditions experienced by the matrix polymer. These conditions can be analyzed in the synergistic or global to local approach [26], [44]. This approach selects the macro and meso scales to define the boundary conditions experienced on the microscale. At the same time, a feedback loop exists since the

micro-scale defines the global properties. This aspect is frequently used in homogenization of elastic properties. The latter concept is termed the hierarchical approach [45]. Figure 3-3 shows the two approaches along the multiple scales of a composite supplemented by a sub-micro scale to account for inhomogeneous deformation. However, during damage initiation both approaches appear equally valid. Only during later stages of damage accumulation problems might arise for the hierarchical approach. As Talreja [45] points out, transverse cracking starts at the fiber-matrix level but with increasing crack density a second length scale, namely crack spacing, becomes relevant, which is on the meso level. This is an inherent problem in the hierarchical approach where the micro level dictates the macro level.

To clarify the multi-scale approach global tension-tension (TT) loading on a strip of material with cross-ply lay-up in load control is analyzed, drawing heavily on the hypotheses described earlier. A stress controlled global load can easily result in strain-controlled loading of the transversely loaded plies, because the high stiffness of on-axis loaded unidirectional plies will draw most of the loading. If inhomogeneity within the transversely loaded plies is recognized it is obvious that stresses experienced by the polymer on the micro scale will be spatially dependent. For some polymers and loading conditions, a sub-micro scale can form as a result of inhomogeneous deformation discussed before. Exemplary for this could be a local disentanglement of macromolecules, namely a craze. If this effect occurs depends also on the stress state of the matrix polymer and is therefore connected to all conditions prescribed by larger scales.

The literature will be analyzed in the following going through each scale and identifying the relevant damage parameters, laminate and polymer responses to fatigue loading for both TT and compression-compression (CC) loading. With each refinement in scale, more details on the matrix polymer will become visible. Moving through the scales, can also be framed as moving backwards from macroscopic laminate failure to damage initiation.

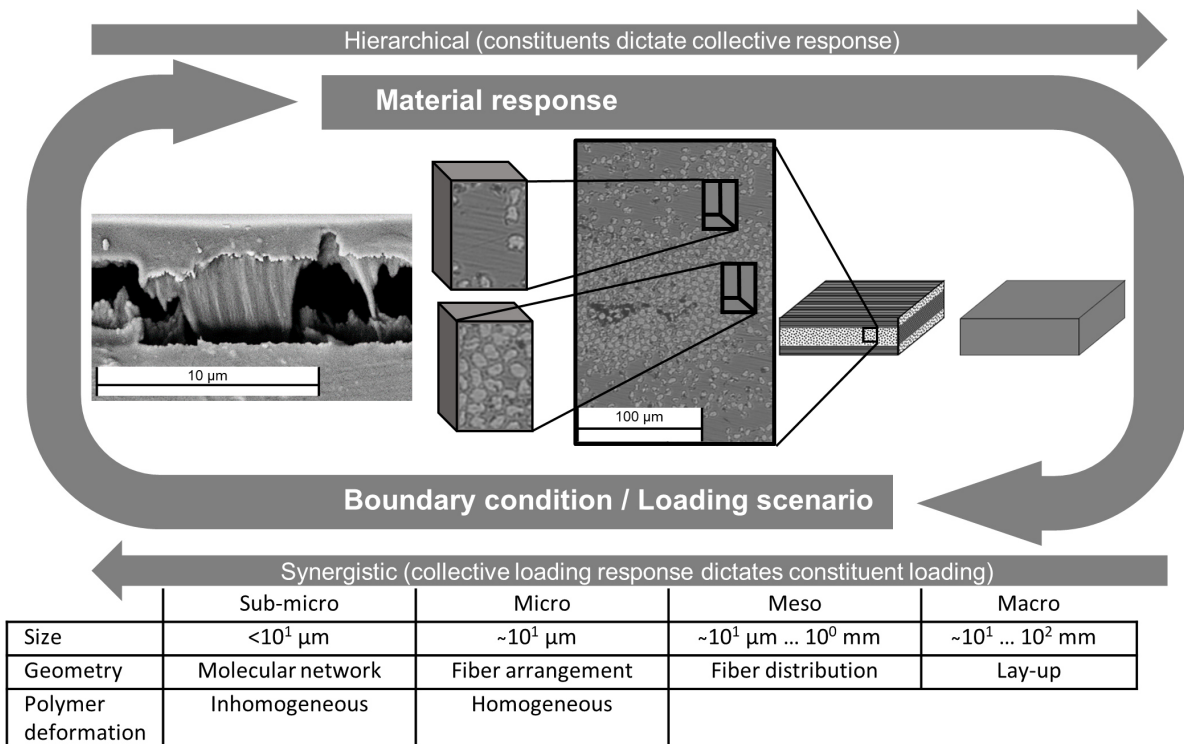


Figure 3-3 Approaches to the treatment of damage initiation and propagation within the framework of scales

3.2 Transverse tension-tension loading

3.2.1 Macro scale

3.2.1.1 Loading Parameters

On this scale, mainly external loading parameters and accessible damage parameters will be discussed. The applied load is typically a global stress applied cyclically (load controlled fatigue). Therefore, one load cycle is described by either pair of stress amplitude σ_a , mean stress σ_m and load ratio R . A real life component is usually loaded by a broad spectrum of loading amplitudes, mean stresses and loading frequencies. For simplicity, only one-stage fatigue loading with constant load ratio, amplitude, frequency and signal form are discussed in the following. For composites, a mean stress effect is well established [46], [47]. Another approach less often found is strain controlled loading, which can introduce differences in damage formation and propagation [48]. Li et al. [48] argue that for cases in which global stiffness is dominated by on-axis plies no big difference between the two loading modes exists.

3.2.1.2 Scalar damage indicators

The loading frequency can also affect the composites fatigue performance. Viscous deformation and internal friction at damage sites can lead to self-heating [49], [50], [51]. This global measure is sometimes used as an indicator for damage. In contrast, low testing frequencies can minimize this effect to the extent that it becomes immeasurable. Beside temperature changes, it is the laminate's stiffness indicating damage during fatigue loading, especially for laminates containing off-axis loaded plies [52]. For this kind of laminates a good correlation between the crack densities observed on a mesoscopic scale with the macroscopic stiffness changes has been found [52], [53], [54], [55]. However, for unidirectional laminates loaded transversely this is not the case because typically a single crack becomes critical before significant increases in crack density [52], [56]. Especially for cross-ply laminates, it is well established that damage follows three distinct phases, namely transverse cracking up to the crack saturation density, delamination growth and final failure [51], [53], [57]. Figure 3-4 shows schematically the phases in terms of stiffness degradation. Acknowledging the source of this stiffness drop leads inevitably to the mesoscopic scale because cracks and their stress perturbation can only be analyzed on the mesoscopic scale acknowledging the layered structure. Additional damage parameters on the global scale can be derived from the shape of the stress-strain response, which can be analyzed for the dissipated energy [52] or the existence of a knee point [55], [58]. The latter is typically analyzed for monotonic loading and has been related to the onset of cracking. Moving from one to two dimensions, Poisson's ratio has also been found to correlate closely with damage propagation [53], [58], [59], [60]. A problem on the macroscale is that the homogenization will obscure to some degree the onset of damage. This is because a single debond or partial crack will affect the global response only marginally.

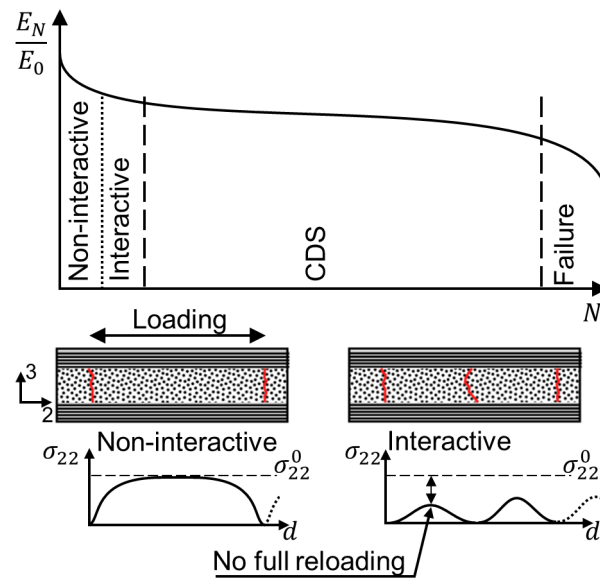


Figure 3-4 Typical stiffness degradation in tension-tension loading, with refined crack initiation phases up to the characteristic damage state (CDS)

3.2.2 Meso scale

3.2.2.1 3D damage indicators

Deeper insights into the damage onset within the transversely loaded plies can be gained on a mesoscopic scale because inhomogeneity on the ply level is acknowledged and can be investigated. Common techniques to study damage evolution are front- and backlight illumination for semi-transparent laminates [28], [51], [52], [54], x-ray radiographs [61], and edge observation [53], [62]. Especially in-situ observation has proven useful, because of the non-linear damage evolution, which is known, but in general unpredictable on a specimen-to-specimen basis. Therefore, intermittent techniques like x-ray imaging or ultrasonic scans need frequent stops to record the progression of damage. Observation of transparent materials has the benefit that it is even possible to distinguish between different damage types, by changing the illumination. Transverse cracks appear as dark lines in backlight illumination [55] whereas delaminations appear as more diffuse areas best visualized with illumination from the same side as the camera [28], [59].

3.2.2.2 Transverse crack morphology

However, all techniques described so far yield 2D-information of a 3D-transverse crack. For this reason, different definitions of transverse crack density exist. It is a matter of crack morphology, which measure might capture differences in transverse

cracking best. Naturally, the number of cracks per surface area or specimen length could serve as useful metric [53]. However, it is important to grasp transverse cracks as a planar flaw extending in both directions through thickness (3-direction in Figure 3-4) direction and across the width (1 direction in Figure 3-4) of the specimen [51], [61], [63]. This distinction is important because some researchers [51], [61], [64] found multiple short cracks (thickness direction) or partial cracks along the width. A controlling parameter regarding extension along the width could be the transverse ply thickness [51], [61]. Similarly, it is also a matter of transverse ply thickness if transverse cracks span the cracked ply completely in thickness direction. For both directions, thicker plies lead to cracks propagating faster and further [51], [61]. In both investigations cracks initiated predominantly from the edges of the specimen. Pakkam Gabriel et al. [54] argue that it is the relation between stresses to initiate a crack relative to those necessary for crack propagation, which controls the extent of cracking within the plies. Under this assumption, a small crack initiated in a thin ply poses a smaller defect and increases the necessary stress within the ply to propagate the crack along the width of the specimen. In contrast to this, in thick plies a crack will initiate at a similar stress, but an increased initial size lowers the ply stress necessary to propagate the crack across the width.

Also in terms of resulting crack density the empirical correlation in Eq. 3-1 gives the saturation crack density ρ_s as inverse to the ply (transversely loaded) thickness t_{90} [54].

$$\rho_s = \frac{1}{t_{90}} \quad \text{Eq. 3-1}$$

The concept of interactive and non-interactive transverse cracking is used with a slightly different notion depending on the authors. Some associate a multiplicity of active damage modes as interactive [53], e.g. simultaneous growth of delamination and transverse cracking vs. transverse cracking alone. Other definitions discriminate the two regimes based on the distance between cracks [54], [62], [63]. A common feature of both definitions is that the stress field around a crack is influenced by another damage nearby, which can be either a delamination or another transverse crack. The redistribution of loads near a crack or a delamination unloads some regions, which is termed a shielding effect. For transverse cracks, this unloaded distance can be calculated in terms of a distance normalized by the transverse ply thickness. From calculations with FE models this distance is specified with $4.5 \times t_{90}$ for carbon fiber-

reinforced epoxy [62] and $3 \times t_{90}$ for glass fiber reinforcement [54]. The stress redistribution back into the transverse plies follows a hyperbolic function [65] with unknown shape parameters. To fit the latter, FE models can be used [54]. Different analytical models have been suggested and can be found as shear lag model in the literature. One of the earlier models proposed by Hashin [66] is used in the following to compare different ply properties and their effect on the stress redistribution, depicted in Figure 3-5. The stress within the transverse ply is normalized by the nominal stress of the uncracked ply and plotted against a normalized coordinate. The material properties for the reinforced epoxy laminates are taken from Hashin's publication [66]. Here of course the major effect on the stress redistribution is caused by different fibers used. In order to include additional ply properties into the comparison, data for a carbon fiber-reinforced polyamide 6 (PA6) [67] and polycarbonate (PC) [68] is included (*). For the last two materials specimen fabrication and characterization is similar in addition to the fiber volume content, which is 48.5% and 44% respectively.

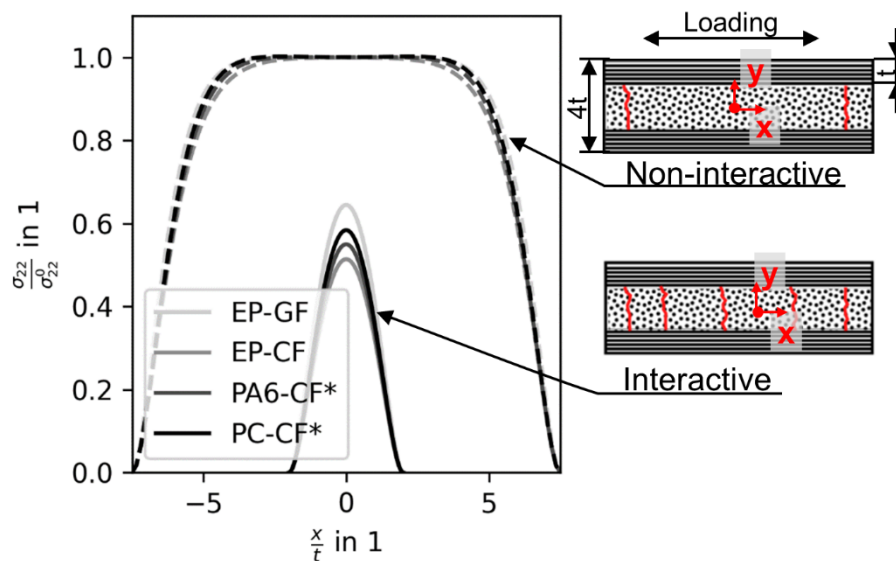


Figure 3-5 Stress redistribution according to Hashin's shear lag model for different ply properties under uniaxial tension load

Differences in reloading of the transverse ply can be found for equally chosen crack densities. For the non-interactive regime, the shielding distance is not drastically different for all four materials, even though the elastic constants are. In the interactive regime, variations in the peak stress between two cracks become visible. Still, the difference is limited as in the case of polycarbonate to polyamide to only 3%. Only extreme alterations would lead to significantly different stress states and affect the

resulting crack density. However, scattering in the evolution of transverse cracks is also a significant factor, which will affect experimental data significantly [62].

3.2.2.3 The role of defects and inhomogeneity

In addition to stress and strain perturbations introduced by transverse cracking manufacturing and inhomogeneity can also result in stress variations [26]. However, it can be very challenging to introduce typical flaws found in real life processes intentionally without altering other parameters like for example crystallinity [69]. A detailed study of glass fiber-reinforced epoxy laminate with and without pores was undertaken by Maragoni et al. [28]. They found that damage initiation is shifted to a lower number of cycles and in addition, cracks grow faster when pores are present. The resulting crack growth rates were enhanced by 75% for the investigated cross-ply laminate. After crack initiation and initial growth, further cracking was not different between the two configurations. In terms of crack morphology, some cracks formed but did not span the transverse layer fully. Maragoni et al. concluded that local stresses needed to be analyzed in order to understand the role of pore size and crack initiation. A multi-scale FE-model has been employed by Mehdikhani et al. [65] to include defects into the model. First two types of representative volume elements (RVE) are prepared, one of which includes damage (termed a representative damaged volume RDV). The resulting homogenized properties from these micro scale models (RVE and RDV) are then assigned randomly in a mesoscopic model, which also incorporates areas of very low stiffness representing voids. The authors found that a sufficiently high number of pores can affect steady crack propagation and lowers the necessary strains to onset transverse cracking. Experimental investigations employing in-situ observation techniques came to similar conclusions [56], [64], [70]. In-situ strain measurements from scanning electron microscope (SEM) images showed that pores lead to strain concentrations and cause localized plastic deformation. In-situ strain analysis has proven useful for the identification of cracking sites [64]. Pores within thermosetting laminates are typically elongated along the fiber direction [56], [65].

Even without flaws or cracks affecting the load distribution within the transverse plies local variations in fiber distribution can lead to strain concentrations [56]. These variations in fiber distribution lead to clusters of fibers, which can be investigated by FE-models either on a fiber-matrix level (micro) or by homogenizing fiber bundles to form regions of intrinsically homogeneous fiber volume content (meso). To the author's

knowledge, most investigations focus on the fiber-matrix level, although larger models or experimental validation might necessitate a homogenization approach. Sudhir and Talreja [26] used a fiber-matrix model to study the effect of fiber clustering. Under the assumption that cracks initiate near the fiber-matrix interface by dilatation, they found lowered strains to onset cavitation for clustered fibers. A similar investigation focusing on the role of resin rich areas within a RVE was presented by Huang et al. [71]. Here, interface properties were explicitly modelled and the tensile strength was estimated as a function of different resin rich areas. This investigation found a detrimental effect for an increased size of resin rich areas. In addition, orientation of elongated inhomogeneous areas matters. For resin zones oriented in loading direction, an increasing tensile strength was found because cracks are stopped by the resin rich areas, i.e. layers. This aspect leads to scattering in the relation between the size of the resin rich zone and the resulting tensile strength.

3.2.3 Micro and sub-micro scale

The microscopic scale now allows a detailed analysis of the polymer's loading condition and response. Before the literature is discussed in detail, three distinct features of the loading condition of the polymer within the laminate must be noted.

First, a polymer within a composite is typically in a highly constraint loading scenario, which leads to a three-dimensional stress state near the fiber-matrix interface in transverse loading [26]. Secondly, both tension-tension loading and compression loading comprise a mean stress. Third, it is very likely to encounter some flaw in the form of a debond at the fiber matrix interface, as perfect impregnation is unlikely. All three aspects are discussed with special attention to the responses of epoxy resin and polycarbonate under these conditions.

3.2.3.1 Homogeneous deformation

Up to the first stage of the MSF-model the polymer deforms homogeneous and at loads far below any yield stress an elastic or visco-elastic polymer deformation can be expected. Elastic deformation is usually associated with the linear stress-strain relation, namely Hook's law, and marked by a full recovery of all strains after load removal. However, authors like Boyce et al. [72] use a non-linear elastic model to describe the polymer's stress-strain relationship in the context of time-dependent material models. If non-linear elasticity is called for depends on the polymer in

question. In the case of epoxy resin (EP) and polycarbonate (PC), deformation is mainly linear up to the initiation of plastic effects for all technical purposes [73], [74]. The results presented by Krause [75] show that plastic deformation will arise gradually and explain the non-linear stress-strain response before excessive yielding in EP. The relation in elastic modulus between the polymer matrix and the reinforcing fibers affects the overstresses in the vicinity of neighboring fibers. The difference in lateral contraction of fibers and matrix leads to a highly constrained deformation. Due to the relatively high modulus of glass and carbon fibers in fiber direction, the stress state approaches a plane strain condition rather than a plane stress [26], [73], [76], [77]. Asp et al. [76], [77] and Fiedler et al. [73] therefore argue that it is important to investigate the polymer under such loading conditions. Similarly, Carraro and Quaresimin [17] also found good agreement across different off-axis angles (angle between fiber orientation and loading) with a failure criterion incorporating hydrostatic stress components. In addition, this argument is of particular relevance since both EP [73], [78] and PC [79], [80], [81] show a pressure sensitive yield limit. Therefore, the onset of plastic deformation depends on the hydrostatic pressure. For many polymers, it is known that the radius of the yield limit in the octahedral plane increases with increasing hydrostatic pressure (compressive is positive) and vice versa. For EP Kody and Lesser [78] found a linear relation between hydrostatic pressure and octahedral yield stress. Similar effects were found for PC by Raghava [81] using pipes under axial loading and inner pressure. Results gathered with a notched round bar indicate the opposite effect for PC, i.e., later yielding under lower hydrostatic pressure [74]. Christiansen et al. [80] also investigated the influence of hydrostatic pressure on the stress-strain response of PC and also found a decreasing yield stress. A possible explanation for the different results might be that different testing set-ups with different relations between the principal stresses were used (biaxial vs triaxial). A comparison between the stress states and calculated stress states on the fiber-matrix level is given in appendix A. After yielding strain softening is observed for PC [80]. However, hydrostatic pressure also affects the ductility of the polymer and limits the post yield strains [74], [80]. In comparison to PC, plastic flow is very limited for EP, due to the lower mobility of the macromolecules [82]. Still, depending on the EP system, some plastic flow is possible [73].

Besides hydrostatic stress, PC has reportedly lower yield strength under cyclic loading. It is noteworthy that this yield strength is half the monotonic value [83] but refers to the category of inhomogeneous very localized yielding and will be discussed together with the phenomenon of crazing. An earlier onset of yielding might, c.p., be beneficial for the stress state within the matrix polymer because the overstresses induced by the difference in stiffness between fibers and matrix could be mitigated. For notches, this effect can be captured by a plastic stress concentration factor [84].

The second material response without an equilibrium hysteresis is visco-elasticity. This time-dependence can affect local stresses/ strains by relaxation or creep and self-heating. Since tension-tension loading incorporates a mean stress, creep and relaxation phenomena can take place. If these aspects are relevant for a particular polymer depends on the internal time scale relative to the duration of the fatigue loading. Thus, relaxation of the matrix polymer will only alter the local stresses significantly, if relaxation occurs before final failure and cracking. For epoxy-based composites, crack initiation has been found very early during fatigue loading [59], [62]. This could be one example where coupling of internal time scales of the polymer's visco-elasticity and the applied loading rate differ too much in order to relax local stresses enough to make a difference in crack initiation. From this, it might be expected that a highly viscous response might be beneficial, due to rapid load transfer to the fibers and unloading of the matrix polymer. Yet, no investigations in this regard could be found. However, this could also incorporate significant lag in the stress-strain response of the polymer within one load cycle with detrimental implication to self-heating. Typically, this effect is evident by hysteresis opening in the stress-strain space. This can lead to thermal fatigue, which is less a cracking of the material but a temperature induced yielding [5]. Temperatures rise near T_g or T_m are highly detrimental for the fatigue performance of polymers [41]. In general, thermal fatigue failure can occur in both PC and EP if the strain rates are high enough and dissipated heat can accumulate over an extended number of cycles. Since heat accumulation depends on many factors outside the matrix polymer itself (e.g. geometry, conductive heat transmission) this aspect will be avoided within the experimental program of this work and is only incorporated as far as testing frequencies without significant self-heating are used.

Closely related to visco-elastic behavior is visco-plasticity. A common phenomenon falling into this category is rate dependent yielding of EP [78] and PC [85], [86], [87] even though both materials are relatively insensitive to strain rate. Kody and Lesser [78] found that the yield strength depended mainly on the octahedral shear strain rate for EP. A logarithmic relation was found, which approximately increases the yield stress by 2.2-2.6 MPa per decade of strain rate. From the data reported by Parvin and Williams [87] an increase of 2.7 MPa per decade was found for PC. The effect within a composite will be very complex because this leads to increases in yield stress for highly strained regions. A rate dependent yield stress could therefore prevent unloading of highly stressed polymer regions by suppressing plastic deformation. G'Sell and Gopez [85] argue for example, that an increasing yield stress extends the visco-elastic region of PC in terms of stress and strain.

If visco-plastic effects are present during fatigue loading, they can be estimated in part by the changes in hysteresis opening of the polymer. Here initial changes in hysteresis opening can point towards plastic effects when these changes persist even beyond a thermal equilibrium, because heat dissipation by visco-elastic effects would remain constant. Therefore, temperature changes can hint at visco-plastic effects, and vice-versa visco-plastic effects can delay the thermal equilibrium. For both PC and EP only minor heating and hysteresis opening is observed at load levels within the finite life region of the S-N curve. For PC several authors also reported a low sensitivity to testing frequency within this region of fatigue life [5], [39], [88]. Even within the low cycle fatigue regime, Mattioli and Quesnel [86] found no thermal run away for PC loaded with constant strain rates of $0.5\%s^{-1}$. This indicates low heat dissipation by plastic effects. Even though this strain rate corresponds to a relatively low loading frequency of 1/16 Hz a limited hysteresis would be expected due to the high loads, but this is not reported. Another extreme can be found by work done by Mackay et al. [89], who found no significant self-heating up to 20 Hz in PC for stress amplitudes below 6 MPa. Visco-plasticity may still be relevant for tension-tension fatigue loading because not only short-term cyclic loading is present but also mean stress or strains. Majumdar and Newaz [32] argued that visco-plastic deformation of the matrix changes the local load ratio from tension-tension to alternated loading within a metal matrix composite. That PC might be prone to visco-plastic effects was shown by Mattioli and Quesnel [86],

who found relaxation to be a function of applied strain for PC. This hints at visco-plastic effects or alternatively at nonlinear visco-elasticity.

3.2.3.2 Stress concentrations

That plasticity can help to reduce stress concentrations introduced by fibers or flaws has already been discussed but will be more concrete within realm of stress concentrations. Within the MSF-model, stress concentrators can identify locations of crack initiation. The associated polymer property is the notch sensitivity, which is a lowered crack onset stress/strain because of the presence of a notch. Different approaches can be taken to account for the influence of notches. Either the peak stress near the stress discontinuity is taken or the stress gradient is additionally accounted for [90], [91, p. 25]. Even though no stress gradient-based approach is chosen within this work, it is still an important aspect to keep in mind because ignoring the stress gradient introduces a size effect. The latter arises because a single scalar peak stress will not account for the volume, which is highly stressed. Numerous analytical and semi-empirical equations exist to estimate the stress concentration around a stress discontinuity [92]. A common way to express the stress concentration K_t is by normalizing the local stress peak to the nominal stress σ_n present in the remaining cross-section, assuming linear elastic material behavior (see Eq. 3-2). A notch sensitivity q can further be calculated for fatigue loaded specimens by normalizing the fatigue strength of unnotched specimens $\sigma_{n,smooth}$ with the fatigue strength of notched specimens $\sigma_{n,notch}$ for a given lifetime N and normalization [90]. By this normalization, the notch effect is represented by values between zero and one. Values near zero show a low notch sensitivity. The ratio K_f in Eq. 3-3 expresses the detrimental effect of the notch in terms of nominal stresses and relates this to the theoretical stress concentration present in the notch root (Eq. 3-2).

$$K_t = \frac{\max(\sigma)}{\sigma_n} \quad \text{Eq. 3-2}$$

$$K_f = \frac{\sigma_{n,notch}(N)}{\sigma_{n,smooth}(N)} \quad \text{Eq. 3-3}$$

$$q = \frac{K_f - 1}{K_t - 1} \quad \text{Eq. 3-4}$$

Differences in slope can of course lead to differences in notch sensitivity as a function of lifetime. That this could be expected for polycarbonate shows the work of Misaki and

Kishi [93], who found a higher notch sensitivity for fatigue-loaded specimens compared to quasi-static loading. Similarly, Mortazavian and Fatemi [90] also found converging S-N curves toward the single cycle strength for polypropylene and related this behavior to findings on ductile metals. The underlying explanation is that the low cycles regime is less affected by the presence of a stress concentrator [84, p. 209]. Yielding in the notch root can lower the stress peak in subsequent loading cycles by plasticity induced residual stresses. Neuber's approximation is a way to estimate the residual stresses introduced within the notch. Schijve [84] explained the principle as follows. Neuber's postulate assumes that the elastic prediction of the notch root stress with K_t gives an upper bound for the peak stress. If plastic yielding occurs, the actual stress will be lower and the strains higher. It is hypothesized that the two changes are mutually compensatory and therefore the product of stress and strain will remain constant. This leads to equation Eq. 3-5, where the left-hand side of the equation is the product of stress and strain in the vicinity of the notch with the actual constitutive relation $\sigma(\varepsilon)$. The right-hand side is the elastic prediction based on the elastic modulus E and the nominal stress σ_n adjusted by the stress concentration factor K_t . The constitutive relation can be based on quasi-static tensile tests or the cyclic response [90]. Under the assumption that yielding occurred in a limited volume, the stress-strain product gives an estimate of the actual stress and strain in the vicinity of the notch. Because unloading will follow the linear-elastic path, the difference between the elastic solution and the elastic-plastic solution gives residual stresses. This approximation has the benefit that it is in some cases possible to estimate plastic deformation from purely elastic FE models [94].

$$\max(\sigma)\max(\varepsilon) = \frac{(K_t\sigma_n)^2}{E} \quad \text{Eq. 3-5}$$

3.2.3.3 Inhomogeneous deformation

With the onset of any kind of plastic deformation, the transition to crack incubation becomes more likely especially if yielding occurs localized in the form of crazes and localized shear bands. Drawn from the comprehensive description of crazes by Takemori [95], a craze is an area of disentangled macromolecules, which can be distinguished from a crack by a capacity to transfer load. Kinloch and Young [40] conclude that only plastic deformation distributed homogeneous within the bulk of the polymer leads to ductile materials. PC is one example of a polymer, which shows a

ductile material response with cold drawing and necking under the right conditions but fails apparently brittle in other circumstances. In the latter case, crazes are frequently observed. Apparently, brittle refers to the very high strains within a craze, which quickly reach critical values, due to the high localization of yielding material. Strains of up to 40% are reported within a craze in PC [96]. This two-fold behavior is observed for many polymers and one form of ductile to brittle transition. However, PC is more likely to show these features because EP or cross-linked polymers are less prone to disentanglement due to a limited molecular mobility [40]. That crazing can still play a role in the fracture process of epoxy was shown by Mishara et al. [97]. In general, polymers with excessive softening after yielding are believed to be more sensitive to localized deformation mechanisms. This fact distinguishes PC and other amorphous polymers from semi-crystalline polymers like Polyamides. For the latter class softening is counteracted through hardening by reorientation [5].

The ductile to brittle transition is mainly studied for unreinforced polymers but could also be present if the polymer is used as matrix polymer in a composite [76], [77]. Especially polymers as part of a transversely loaded ply under tension-tension fatigue loading will meet many requirements for crazing and localized shear bands. In the following a non-conclusive compilation of factors favoring crazing in PC will be given. Where applicable craze favoring conditions in EP are included even though crazes are very limited in this material the existence is somewhat disputed. The conditions favoring crazing are:

- Plane-strain conditions with hydrostatic stress components [98], [99], [100]
 - EP [97], [101]
- Fatigue loading [93], [102]
- Increasing time [99], [103], [104]
- Interaction with preexisting shear bands [83], [105], [106]
- Thermal histories like annealing [107], [108]

Polymers as part of composites likely experience a highly constrained plane strain condition during loading. High fiber volume content and stiff fibers lead to this. Argon [98] reported that crazes in PC typically form at internal or external flaws like embedded dust particles or surface scratches. Avoiding surface flaws by polishing cannot completely suppress crazing but makes it unpredictable. For EP high triaxial stress states favor crazing especially preceding sharp cracks [97]. The likelihood for craze

formation seems high with respect to this finding in a composite. Under the assumption that cavitation initiates near the fiber-matrix interface but still within the matrix. Sudhir and Talreja [26] found from a RVE model that a higher longitudinal stiffness of carbon fibers compared to glass fibers lower the strain to onset cavitation. Even though it is experimentally challenging to identify precursors of extended cracks such as coalesced debonds, the conditions leading to cavitation and crazing are in good agreement with the role of the hydrostatic stress component. The latter is used in several failure criteria as invariant to predict damage initiation [17], [52], [63], [109]. The specific invariant of the stress tensor that best indicates failure depends on the off-axis angle [17]. Approximately 60° are suggested as limiting angle for glass fiber-reinforced epoxy. A second class of damage initiation criteria is similarly based on dilatational and deviatoric strain energy [26], [110].

Beside the stress state, it is also known that the duration and sequence of loading affects the craze initiation. Tension-tension fatigue loading leads to protocrazes and crazes in PC [93], [102]. Protocrazes are the earliest signs of crazing in the form of void like structures in the size of approximately 50 nm [102]. Unclear from these observations is, if crazes form because of cyclic stresses or due to the presence of a mean stress. Several authors reported craze initiation as time and load dependent [99], [103], [104]. Therefore, crazing takes on the nature of visco-plasticity. Interaction of shear bands could theoretically lead to the formation of crazes, too. As shown by Lai and Van Der Giessen [106] in a numerical study strain softening materials form two separate plastic zones at the tip of a notch, which makes crazing more likely. Both EP and PC fall into this category of polymers, given the right stress state [74], [77], [110]. This theoretical finding corresponds well with experimental investigations by James [83] and an extensive discussion by Takemori [95]. A close relationship and interaction between shear bands and crazes is suggested by many publications on this topic. However, an important aspect is the available space between fibers and the volume of polymer available for disentanglement. The ϵ -CTPZ (crack tip plastic zone) ahead of the crack tip or notch is large relative to the available space between the fibers of most polymers. These zones have dimensions of several tenths of a micrometer [83], [95]. Thermal history and annealing are relevant as far as this aspect might lead to different crazing behavior depending on the processing route. As explanation for more crazing after annealing it is suggested that this treatment increases the yield strength, which

suppresses shear bands and give crazes a more dominant role [107], [108]. It has to be expected that tape winding, autoclave consolidation or continuous hot pressing will all lead to different thermal histories, which differs from injection molding or extrusion often used to prepare neat polymer specimens. Within this work, however this aspect is constant between different polymer modifications. The discrepancy between laminate and neat PC persists, however.

Shear bands as a second inhomogeneous deformation mechanism appear to be less dominant in a transversely loaded ply because they are associated with plane stress conditions and action planes of high shear stresses. This would point towards resin rich areas. Shear bands do not strictly align with the plane of maximum shear stress, as shown by Kramer [111], who found a slightly deviating angle of 54° for tensile and 38° for compressive loading. With these aspects in mind and without deciding definitively on a failure criterion, it can be concluded that crazes or proto-crazes might precede cracking in fiber rich regions with highly constraint conditions. Principal stress-based failure criteria seem appropriate. On the other hand, if failure is to initiate in resin rich regions shear stresses and equivalent stresses like von Mises or Tresca seem good choices as a measure. The latter case appears to be unlikely because of the type of overstresses present between neighboring fibers [17], [109].

3.2.3.4 Crack propagation and final fracture

Similar to different deformation mechanisms, crack propagation is also very dependent on the material under study and initiates the final phase of the MSF-model. Especially for PC vastly varying crack propagation rates are reported. To account for this, crack propagation is further refined into a phase of discontinuous crack growth (DCG) and continuous crack growth [95], [112]. This distinction accounts for the fact that there is a phase during crack growth in glassy polymers when striations on the fracture surface do not match single load cycles but a sequence of several load cycles [112]. Takemori [95] attributes this phase to the formation of the ϵ -CTPZ. The observed mechanism is characterized by two shear bands forming at the crack tip and spreading from it epsilon shaped. This is assumed to shield the craze forming in front and collinear to the crack, which slows down degradation of the craze and crack propagation. The ϵ -CTPZ is similar to the localized shear banding numerically found for softening materials like PC [106]. As already mentioned earlier, for mechanisms promoting crazing it is questionable if enough material volume exists between the fibers to allow for the

ϵ -CTPZ. Therefore, it seems likely that DCG is potentially suppressed in fiber rich regions. In contrast to this, EP shows stable crack growth above a stress intensity threshold [113]. Besides this, stick-slip crack propagation in monotonic loading of EP also reveals crack blunting as a comparable factor able to stop and delay crack growth [114], [115]. Still, the plastic zone at the crack tip is vastly different for PC compared to EP [116], which can be traced back to the homogeneous and inhomogeneous deformation mechanisms described earlier, namely crazing ahead of the crack in PC. Mode I crack growth is sensitive to mean stress, stress triaxiality, strain rate and the molecular structure. The last aspect is explicitly included because irradiation treatment affects the molecular weight of PC and potentially the molecular weight between cross-links in EP. The overall effects of irradiation treatment on both polymers will be covered in detail in section 3.8. First, the role of mean stress on crack propagation will be discussed. A higher mean stress slows down fatigue crack growth rates in PC [117], [118], [119] but is detrimental in EP [113], [120]. Therefore, relaxation by viscous or plastic effects of the transverse ply can help to slow down crack growth in EP but could have exactly the opposite effect in PC. Another matter could arise if accumulated plasticity introduces compressive segments as this affects crack propagation speeds again as shown by Dumbleton and Bucknall [121]. HDPE shows a maximum in fatigue crack resistance at load ratios of $R=0$ [121].

Highly constraint crack tips in plane strain conditions promote faster crack growth and lower fatigue crack resistance in both EP [97] and PC [122], [123], [124]. The detrimental effect of plane strain on the fatigue crack resistance was shown by Pitman and Ward [123] by varying the thickness of compact tension specimens. The same effect can also be observed for the fracture toughness in monotonic loading of PC [87]. For EP the importance of the plane strain condition is underlined by the observation that machined notches will yield a higher fracture toughness compared to pre-cracked specimens [97], [125]. Mishra et al. [97] argue that this difference mainly stems from the stress state at the notch or crack tip. Recalculation of fracture mechanical experiments performed by Qiao et al. [125] agree with this. Furthermore, the results point towards a high influence of hydrostatic pressure on damage and generally the polymer's ductility. Qiao et al. could improve the prediction of fracture within the laminates by fitting the material properties to fracture mechanical testing results of the neat polymer instead of using macroscopically fitted properties (bulk material).

The same is also true for time dependency of fracture toughness. For both polymers it was found to decrease with increasing strain rates in EP [97] and PC [87]. However, for PC small crack growth is seemingly unaffected by strain rate. Hertzberg et al. [88] recorded fatigue crack propagation and used different signal forms (load-time signal) for loading. No significant change for crack propagation rates could be found between sinusoidal and rectangular waveforms. The authors pointed out that strain rates and time under load are affected simultaneously by this method. In this way, creep effects might be counteracted by strain rate effects. Similarly, a later investigation with different testing frequencies found no significant change in crack propagation up to 20 Hz [118].

The last stage of the MSF-model starts after passing the critical stress intensity, which asymptotically converges towards the fracture toughness of the material within crack propagation plots shown in Figure 3-2 (b) [34]. This last stage is marked by rapid and unstable crack growth. As a result, this phase contributes little, to the final failure of the specimen. However, it is this stage generally recorded as S-N curve in fatigue tests. Hence, all stages up to separation of the specimen are included in these curves and it remains mainly unclear how the specimen's lifetime is divided between different stages. Insightful in this indiscriminate view is that PC shows a lifetime inversion. Lifetime inversion means that at some lifetimes lowering the load will not extend the lifetime but shorten it. Takemori [95] argues that this inversion is caused by two different fatigue branches overlapping partially. One characterized by shear-dominated failure and a second by crazing. This would be supported by ductile failure reported for PC tested at relatively high strains [86]. Failure maps discriminating shear banding and the craze branch show in a normalized manner, how higher temperatures lower the yield stress and thereby promote shear bands [124]. Even though temperature is excluded in this work by assuming isothermal conditions, these maps remain relevant because other factors influencing the yield stress might also cause shifts between both branches. The phenomenon of lifetime inversion is explained by shear yielding and crazing both being active in the plastic zone at the crack tip and competing [124]. This distinction is based on the visual appearance of both mechanisms viewed from the side. Crazing is indicated by a clamshell appearance, whereas shear yielding produces a finger like appearance. Similarly earlier investigations also found crazes ahead of the

fatigue crack tip in PC [89], [126]. Lifetime inversion poses a problem for the prognosis of fatigue failure [95].

As before the conditions experienced by the matrix polymer within a composite, likely favor detrimental conditions in terms of fatigue crack resistance and fracture toughness. Especially in fiber rich regions, only a limited material volume is available, which restricts the potential for plastic deformation. For both materials under investigations, yielding and plastic flow is reported to slow down crack growth to the point of DCG, but the dimension of such zones in neat polymer specimens is in the range of approximately 20-100 μm [95], [97], [127]. From an idealized fiber arrangement, it is possible to estimate the free space available between the fibers and compare this to the size of plastic zones. Figure 3-6 shows the distance between two neighboring fibers as a function of fiber volume content normalized by the fiber diameter. The dimension is chosen under the premise of crossing a relatively large area. For carbon fibers of e.g. 10 μm , the plastic zone responsible for DCG is twice to ten times the fiber diameter. Therefore, depending on the fiber arrangement (cubic or hexagonal) only fiber volume contents of 17 or 30% would allow for planes large enough. This purely geometric estimation does not account for the stress distribution. Discontinuous crack growth or slow crack growth would therefore only be expected in resin rich zones. Protocrazes, however could still form, due to the small size of 50 nm.

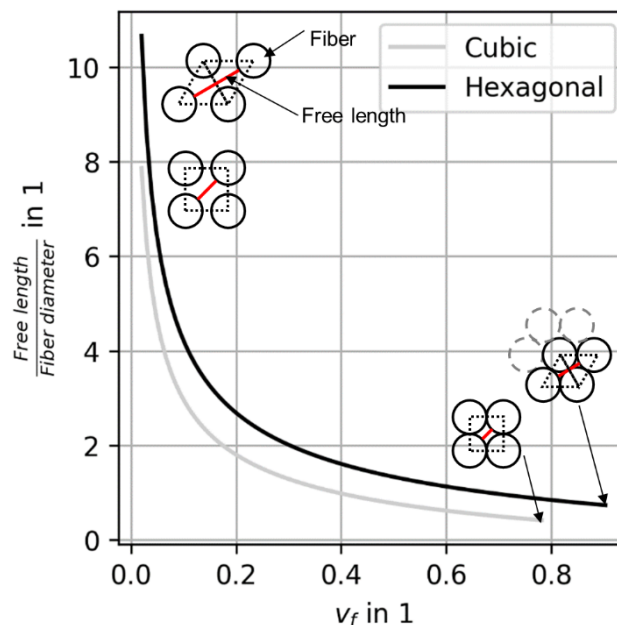


Figure 3-6 Free length as a function of fiber volume content v_f for two idealized fiber arrangements

3.3 Compression-compression loading

On-axis compression is another critical loading case for composites, as it significantly lowers the strength compared to tension. This is in contrast to an improved performance for compressive loading compared to tension transverse to the fibers [46], [128], hence on-axis loading will be discussed. Again, a synergistic view is well suited to separate the effects acting like boundary conditions and the locus of damage initiation. However, in contrast to transversely loaded plies in tension the conditions and interactions between different scales are much more complex. This is because two competing failure mechanisms are active. A strength-based failure mode and a stability problem. The latter can occur on different scales, ranging from fiber buckling to global buckling. By this, it is a gradual shift through the scales from a material intrinsic property to one determined by component geometry and stiffness. Still, instabilities on the micro or macro scale are better suited as compressive strength and a material property because these small-scale instabilities are material intrinsic and cannot be altered by design, e.g., a thicker laminate or stiffeners. Damage modes found in quasi-static compression tests are fiber-kinking, fiber crushing, longitudinal splitting, delamination and shear band formation [129].

Figure 3-7 shows schematically the different failure modes in both respects organized by different length scales. A major challenge is that final failure of a specimen or component will likely pass not only through the scales but can easily switch between scales. The gray arrows in Figure 3-7 show an example of how damage might progress through the scales and switch from strength-based failure to stability failure and ultimately final failure. This sequence of events is an example of a damage process involving kink bands. Here, the initial misalignment of a bundle of fibers might start from a single fiber failure, which evolves into a region of deformed fibers termed a kink band. From this mesoscopic damage, failure might occur directly on a macroscopic scale or a global instability could arise. The latter can also be treated as compression bending, due to slight asymmetries in the load path. For CC loading or compression dominated loading (mean stress is significantly compressive), the interaction between the scales can be expected to be even more complex and in addition different damage modes might be triggered as a function of load and time [49].

A major challenge is experimental verification of models and failure modes especially in fatigue [129], [130], [131]. In the following, different damage modes will be discussed organized by scale with special attention to the role of the matrix material.

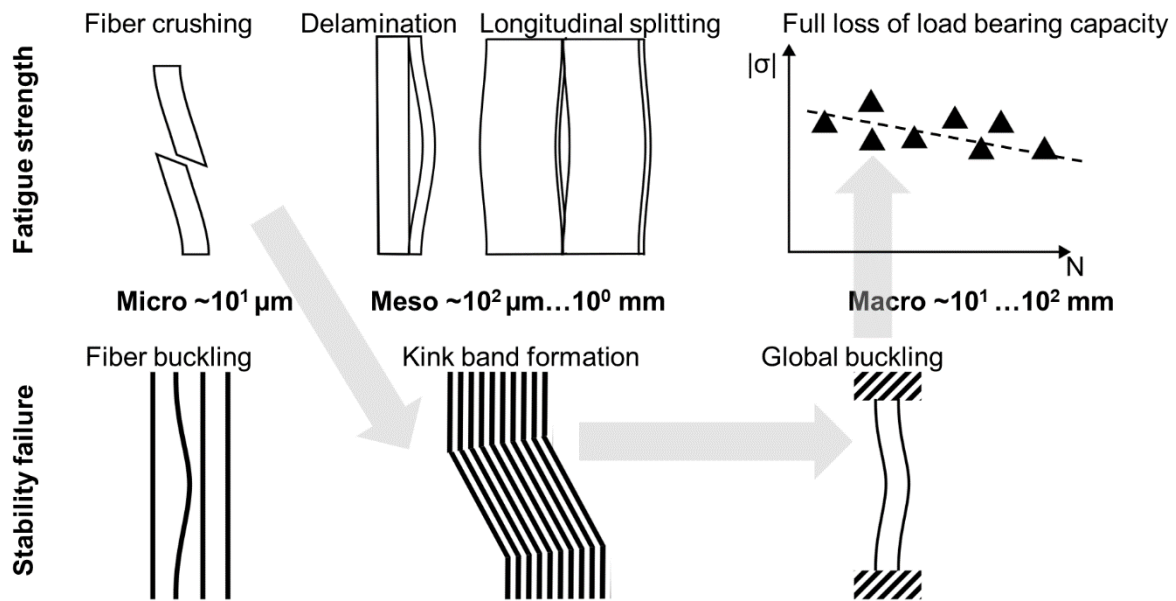


Figure 3-7 Competition between strength based and stability failure of on-axis loaded composites

3.3.1 Macro scale

On a macroscopic scale, the global laminate stress-time function will affect all other scales. Regarding this, a major question is the distinction between alternate loading and compression dominated loading. In a conventional Goodman diagram the separation line is $R=-1$. Kawai et al. [46] argue for the use of the critical loading ratio R_{crit} as a dividing line. This load ratio is defined as the ratio of quasi-static compression strength (UCS) divided by the ultimate tensile strength (UTS). Any load ratio left of this dividing line in a constant life diagram will then be taken to be compression dominated [$R \notin (R_{crit}, 1)$]. Treating both tension and compression dominated loading purely in terms of applied stresses could be an oversimplification for some materials, as time under load can easily play a significant role [49]. This introduces a frequency dependence into the prediction of fatigue failure under on-axis compressive loading. Due to the problems associated with experimental investigations of compression dominated fatigue loading driving damage mechanisms are seldom reported and mainly final failure is analyzed [132]. In addition, the experimental investigation of this loading case is often plagued by considerable scattering and clamping failures, which makes S-N curves especially challenging. Reasons for this can be found mainly from

quasi-static investigations. The results of Safdar et al. [133] show that it is the alignment of compressive loading and reinforcement direction, which leads to a flaw-driven failure in monotonic loading. This is because compared to different combined loading scenarios pure on-axis compressive loading shows especially high scattering [133]. Under the strength rank equal life assumption [134] an often shallow S-N curve will lead to extensive variations in lifetime when scattering in monotonic loading is already high.

3.3.2 Meso scale

3.3.2.1 Damage modes

Delamination and longitudinal splitting are two mesoscopic damage modes, which can easily grow to a global macroscopic failure. Especially near notches and in multiaxial laminates, both damage modes have been observed in CC fatigue loading [132], [135], [136]. Delaminations and longitudinal splitting mark the initiation of sub laminates (separated layer or ply), which are prone to buckling, due to a lowered flexural rigidity. Mixed mode cracking occurs, due to multiple stresses present at the crack tip [136]. To some degree, this also includes mode I crack opening, which makes some of the factors described for cracking under transverse tensile loading also valid. For both failure modes, crack propagation will be controlled by the polymer and fiber-matrix interface. In contrast to this, kink bands are a stability failure on the scale of several fiber diameters, which can comprise cracking, but the latter is no prerequisite. In the following, special attention will be given to kink band initiation, because it is a damage mode leading rapidly to failure without significant growth. This discriminates kink bands from most other compressive damage modes.

Choi et al. [132] found that damage depended on the amplitude of applied fatigue loads. For lower loads (40% of static maximum), longitudinal splitting was active, accompanied by delaminations at intermediate loads. For the highest loads, fiber buckling is reported as major damage mode, although the authors leave open how this damage mode was identified. Still, fiber buckling is often presumed to cause kink banding as well as initial alignment errors. Kink banding is frequently reported as a cause for failure in quasi-static loading and hence for relatively high loads [129], [137], [138], [138]. For this reason, similarities to the low cycle fatigue regime can be

expected. Subsequently, in monotonic loading, delamination and splitting might follow at larger scales for multi-axial lay-ups [138].

From investigations with different epoxy resins it was found that kink banding remains the dominant failure mode despite differences in toughness and stiffness of the polymer matrix and the reinforcement [129], [138]. A comparison of compressive failure modes at various temperatures shows that failure is a function of temperature and mechanical resin properties. Sun et al. [30] found splitting at ambient temperatures and fiber kinking at elevated temperatures (near T_g) in unidirectional (UD) glass fiber reinforced plastic (GFRP). Compressive strength and onset stress for kink bands increased as a function of the polymer tensile modulus [138]. The first model to demonstrate this phenomenon was proposed by Rosen, which directly correlates the compressive strength with the shear modulus of the matrix polymer [137]. The systematic categorization developed earlier will be used to discuss the role of elastic-plastic, visco-elastic and visco-plastic deformation. The relevance of these mechanisms has been acknowledged in numerous models and studies. A purely elastic approximation frequently overestimates the actual compressive strength by several factors [137], [139], [140]. Many models use plasticity to adjust the tangential stiffness at higher loads, which leads to more realistic predictions of the compressive strength [137], [141], [142], [143]. In addition, most models acknowledge the presence of initial misalignment as a parameter to lower kink band initiation stresses. A parametric study performed by Gutkin et al. [144] found a distinct effect of the constitutive plastic model chosen. Montiel and Venkataraman [142] showed in a FE-model how plastic deformation can accumulate through repeated loading and that this effect will lead to much easier kinking in subsequent loading cycles after a kink band is formed once.

Next, time-dependent effects will be discussed. These aspects appear especially relevant for fatigue loading, even though experimental studies are rare. Based on homogenized laminated properties, Slaughter and Fleck [145] studied the effect of visco-elasticity and creep. For visco-elastic properties of the laminate, their model shows a critical load below which no kink band formation will take place. Their parametric study also found that with an increasing viscous component the kink band deformation increases more rapidly. Schapery [146] came to similar results with his models. In an earlier work, Schapery [147] showed the influence of cyclic loading on

the shear strain within the kink band. For this, he assumed a power law for the relaxation modulus of the polymer and showed that with decreasing overstress from the viscous network shear strain increases more rapidly during cyclic loading.

Experimental indication of the importance of loading time in general can be found by a recent study of Leite et al. [148] for dynamic (high speed) loading. Experiments conducted on a double-edge notch specimen at high strain rates in the range of up to 770 s^{-1} revealed that high strain rates could suppress kink band formation and shift the failure mode to fiber buckling. In addition, the fracture toughness of the material was found to increase with increasing strain rates. Quite the opposite might be expected for extended periods under mean stress in fatigue loading. As shown for creep failure of multiaxial quasi-isotropic laminates by Vinet and Gamby [149] kink band formation can be a function of both time and applied load. In addition to the experimental results, an analytical visco-plastic model for the matrix material showed that the rotation of the fibers within the kink band steadily increases with time until failure. Vogler and Kyriakides [150] also found a rate dependence in kink band propagation stress with different applied strain rates and correlated this to the composites overall rate dependence in shear loading.

3.3.2.2 The role of defects

Beside the composites constitutive relation, many models already acknowledge a flawed material. In addition, damage after the first initiation of a kink band can have a similar effect. The most common flaws are misalignment and voids. Kyriakides et al. [131] could show experimentally significantly lower stresses for propagation compared to initiation. Furthermore, an accompanying parametric FE-model shows that the amplitude and wavelength of a wavy misalignment directly affects the difference between initiation and propagation stress. From this and other investigations it can be concluded that initial misalignment and other defects lower initiation stresses significantly compared to theoretical values [30], [131], [133], [139], [140], [144]. In contrast to this Kosmann et al. [151] didn't find a correlation between compressive strength and void content in a GFRP multiaxial laminate. Similarly, in-situ observation of kink band propagation revealed a complex influence of voids, which at times impeded kink band propagation or altered their morphology [151]. However, it seems plausible that defects will contribute to an earlier onset and easier propagation of kink bands, but given the numerous failure modes, it is likely that particular effects can be

obscured. Residual plastic stresses and accumulated damage during cyclic loading can have a comparable impact on subsequent kink band initiation, as shown by Diaz Montiel and Venkataraman [142] with a FE-model cyclically loaded. Once a kink band is initiated, it will propagate more easily during fatigue because plasticity and damage at the fiber-matrix interface accumulate. These findings point towards a separation into initiation and propagation or re-initiation of kink bands. Re-initiation refers to the phenomenon whereby a previously formed kink band is straightened again by subsequent tensile loads. It is therefore important to understand at which stress kink bands propagate and what limits kink band rotation. If this limit is reached, even a straightening of the fibers will not lead to a significant increase in load bearing capacity. This is likely to be due to any sudden loss in load bearing capacity, such as excessive failure in the fiber-matrix interface [152].

3.3.2.3 Combined loading and targeted kink band initiation

Beside voids and misalignment, combined loading with in-plane shear and on-axis compression also contribute to an earlier initiation of kink bands [152], [153], [154]. Safdar et al. [133] developed a strain-based failure envelope for this load case and found a concave relation between on-axis compression and in-plane shear strains. The convex shape of the failure envelope is explained by different active failure mechanisms. The authors associate micro buckling with pure compressive loading, kink band formation with combined loading and shear failure for pure shear loading. Scattering decreases with increasing influence of shear loading. Although the failure envelope predicted by [139], [144] do not share the convex shape a significant influence of the combination of shear loading and on-axis loading could also be found. Several authors also used shear loads and specific specimen geometries to target kink band initiation specifically. One very controlled approach to this problem is combined compression-torsion loading of tubes because different combinations of shear stress and on-axis compressive stress are possible. Jelf and Fleck [153] used this set-up and found a linear relationship between decreasing compressive strength under increasing shear stress. Alternatively, Pinho et al. [155] used a compact compression specimen with a cross-ply lay-up and could initiate and grow kink bands through the laminate in a displacement controlled monotonic loading ramp. Based on this investigation, He et al. [156] modified the lay-up to introduce in-plane shear stress in addition to on-axis compressive loads. The plies under investigation were oriented slightly off-axis, from

3° to 15°. Kink bands initiated more easily with increasing in-plane shear stress. In addition, slight off-axis angles are reported to control whether in-plane or out of plane kinking will be favored or if a combination of both will form [150], [157], [158]. Bažant et al. [159] used differently oriented notches to prevent longitudinal splitting. They found that by orienting the notch in the same angle as the out-of plane kink band observed in preliminary tests, longitudinal shear splits could be avoided. An alternative to a notched specimen is an indentation at the edge. Vogler and Kyriakides [150] used this method to lower kink band initiation stresses. Wilhelmsson et al. [157] on the other hand used specimens similar to standardized quasi-static compression specimens with short measuring length. From the results, it was found that this leads to a combination of in-plane and out-of-plane kink band formation. The authors argue that this combination is caused by competing in-plane shear stresses and out-of-plane shear stresses induced by the fiber waviness of the non-crimp fabric (NCF) used.

3.3.3 Micro scale

A comprehensive understanding of the underlying mechanisms that lead to on-axis compression failure is lacking at the micro-scale. Instead, these mechanisms have been treated as part of homogenized laminate properties. For instance, the elastic modulus of the matrix polymer will affect the shear modulus of the fiber bundles and subsequently kink band initiation. No details further than these are available. This is likely caused by difficulties in the observation of damage formation experimentally or the necessary model size to capture instabilities. Still some implications on the loading state and deformation experienced on the fiber-matrix level can be found such as the presence of transverse tensile stresses, due to differences in Poisson's ratio of fibers and matrix polymer [129]. These tensile stresses could of course play a role in debonding as precursor for kink banding. That debonding might be relevant has been shown numerically and experimentally by several authors [30], [139], [160], [161]. The role of plastic deformation and an accompanying decrease in connecting shear stiffness of the fibers is thoroughly discussed by Kyriakides et al. [131]. Their FE model shows for a PEEK-CF laminate that the tangential shear modulus of the PEEK matrix is decreased by approximately 90% at the initiation of kink banding.

3.4 Approaches to fatigue

For both loading scenarios, the literature showed that pre-damage and flaws can have a significant impact on early stages of fatigue damage. Which aspects of the polymer's properties actively contribute to damage propagation depends on the stage within the MFS-model. Two approaches to fatigue can be taken, either assuming a flawless material or a flawed material [5]. Often a flawless material is assumed and hence a considerable percentage of the material's lifetime should be spent initiating cracks and open up the phase of small crack growth in the MSF-model. However, for composites this approach appears non-conservative because even if impregnation is good and porosity is low, a great number of interfaces need to bond sufficiently to the polymer matrix and flaws are likely. Most neat matrix polymers follow roughly the MSF-model it appears important to consider that early damage formation could be offset by manufacturing flaws. Indeed, at the micro or sub-micro scale crack propagation could begin right from the start of fatigue loading, rather than undergoing a period of crack incubation. As shown by Zhuang et al. [44] numerically, neighboring fibers tend to kink out the debond from the interface towards the next fiber. This leads to coalescing and the formation of a crack. In addition to flaw like debonds sub-micro defects can be present. In addition, the matrix polymer itself can also be flawed. For neat PC specimens, Hughes et al.[39] found unmolten pellets in the fracture surface. Fractography of EP specimens also reveals flaws at the crack initiation zones in EP [127].

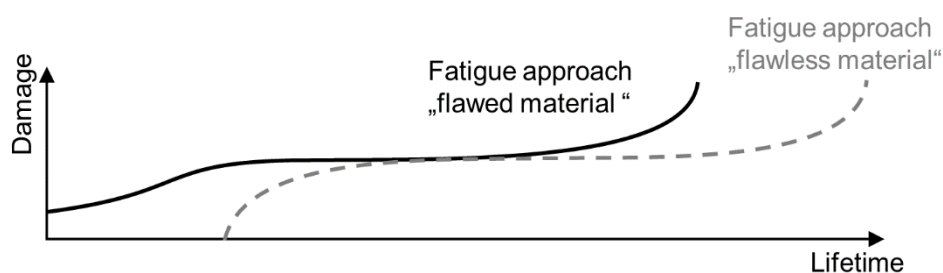


Figure 3-8 Approaches to fatigue

3.5 Homogenization of constituent properties

On the mesoscopic scale, variations of fiber volume content and fiber orientation could be accounted for. However, investigating these local variations is tedious because it requires preparing and characterizing unidirectional laminates with different fiber volume contents to determine their elastic constants. An alternative approach is to

calculate the elastic constants from the constituent properties. A comprehensive compilation of different models is presented by Schürmann [162] including many models with semi-empirical corrections to improve the prediction. A closed framework of similar kind is proposed with the method of cells by Aboudi [163]. This framework can be extended to account for linear visco-elastic material behavior. By a Laplace transformation of the constituent material model, it is possible to do the algebraic calculations within Aboudi's framework. Subsequently, using an inverse Laplace transformation is used to recover the time-dependent visco-elastic properties of the laminate, which are a function of the constituents and can easily be varied in fiber volume content. Since a unidirectional ply is transversally isotropic, it is possible to use evaluated properties as input parameters to a differential modelling approach for isotropic visco-elastic materials proposed by Zobeiry et al. [164].

3.6 Fractography

Fracture surfaces of PC after fatigue loading often show striations or marks similar to these. The latter is frequently the case for DCG and therefore most likely after crack initiation [39]. Because no clear indication could be found on how to distinguish between both phenomena, a counting of striation marks is not possible to estimate the lifetime spent in crack propagation or the small crack growth stage in the MSF-model. One notable feature is that the markings are more widely spaced at the beginning and then abruptly become more refined before spacing out again as shown schematically in Figure 3-9 for PC. The DCG topology is a result of the three-dimensional formation of shear bands, which shield the craze [95]. In the last stage of long crack growth of the MSF-model, a relatively featureless fracture zone is present [39]. Macroscopically shear lips can give an indication if plastic yielding took place (Figure 3-9 c). From compact tension specimens it was found that so-called shear lips can indicate the regions of plane strain and plane stress [87], [165]. It is believed that shear lips form in less constrained areas of the specimen, whereas highly constrained zones fracture with smooth appearance and mainly normal to the loading direction. These observations are in part the basis for the concept that crazing is favored by highly constrained triaxial stress states. Shear lips are also related to the molecular weight of the PC under investigation and are suppressed for low molecular weights [123]. Some authors argued that shear lip size can be related to the fracture toughness and as an extension to fatigue crack resistance [5], [108], [123]. A specific feature for amorphous

thermoplastics is the distinction between shear-induced failure and crazing caused by the main principal stress within the fracture surface (see Figure 3-10). In the first case a ridge like appearance of larger sheets of materials becomes visible [85]. In contrast to this closely spaced sheets stacked on top of each other hint toward a broken down craze [166]. Both phenomena are likely found in areas of unstable crack growth and therefore near final fracture.

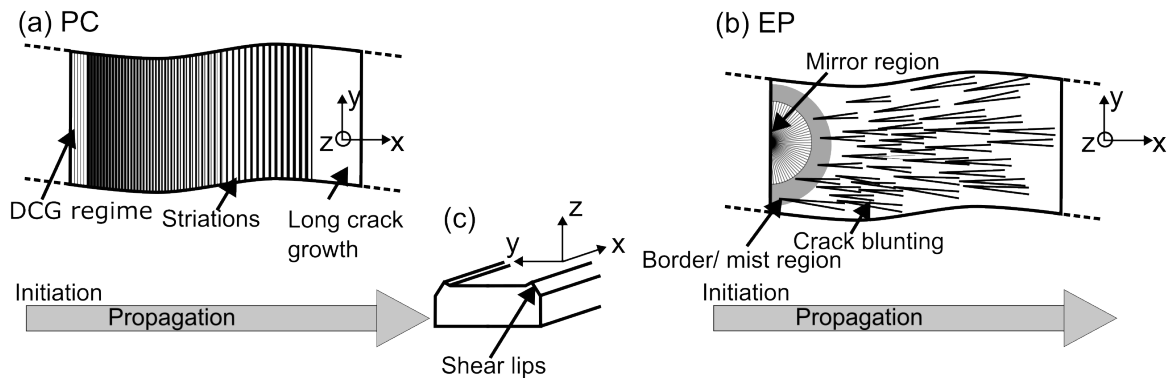


Figure 3-9 Compilation of features observed in fracture surfaces of polycarbonate (a,c) and epoxy resin (b) after fatigue loading; Loading in z-direction; Adapted with permission from EP [127], [167], PC [95], [165]

The phenomenon of shear lips is not limited to fracture surfaces of PC but is also found in EP specimens with similar implications for the fracture toughness and ductility. Crawford and Lesser [114] argue that shear lips can be taken as indicator of ductile failure in EP with low cross-linking density. The authors conclude that shear lips and the ability of an epoxy resin for plastic deformation are factors favoring crack tip blunting. Besides this similarity to PC, epoxy resins fracture mostly different. Within the available literature, no reports on striations or similar markings in EP were found. Furthermore, no influence of fracture toughness [97], creep [113] and fatigue failure [120] is evident for EP's fracture surfaces. Roughness however is reportedly increasing for lower strain rates or creep loading [97], [113]. The authors argue that slower loading enables plastic deformation and disentanglement, which in turn yields crack tip blunting. Two zones are typically reported for fracture surfaces of epoxy resin. A relatively smooth mirror region surrounding the crack initiation site and a region with increasing roughness extending from a border (mist region) separating the two zones (see Figure 3-9). Cantwell et al. [167] argue that the mirror region marks the area of sub-critical crack growth in fatigue loading. Plangsangmas et al. [168] on the other hand developed a relation between the size of the mirror and mist region and the fracture toughness K_{Ic} of the epoxy resin. The equation is based on the LEFM

assumption. Input parameters are the fracture stress σ and the radius of a semicircular crack c .

$$K_{IC} = 1.24\sigma c^{0.5} \quad \text{Eq. 3-6}$$

Outside the mirror zone, all reports agree upon a generally rougher zone. The roughness is affected by molecular weight [82], strain rate [97] and crack propagation rate [168].

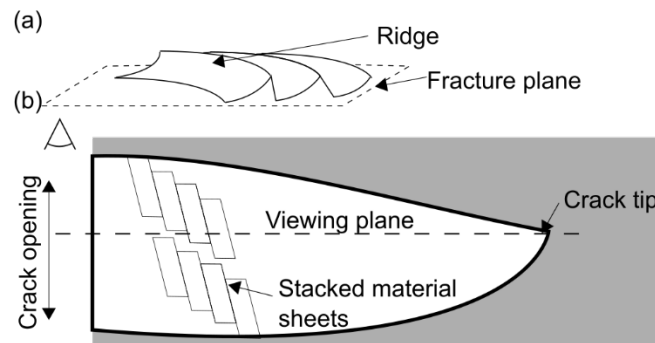


Figure 3-10 Features identifying broken down shear bands (a) and crazes (b); Adapted with permission from [85], [166]

3.7 Morphology property relation

The aim of irradiation treatment within this research is to introduce changes in the polymers morphology and hence the mechanical properties. Earlier work by Pitman and Ward [108], [123] already employed electron beam irradiation to alter the molecular weight of PC. As will be discussed in more detail in section 3.8 irradiation treatment lowers the molecular weight of PC. Crack propagation rates increase and fracture toughness decreases for lower molecular weights in PC. Beside the length of the macromolecules, their orientation is also reported to affect the crack initiation in PC. This was concluded by Donald et al. [105] because crazes appear to be less stable if initiated in formerly yielded zones. Higher stretch of the fibrils within pre-yielded zones makes a craze breakdown more likely. A similar effect could also explain a reduced crack resistance for smaller macromolecules because this length also limits the maximum disentanglement possible before crazes break down.

Cross-linking in EP on the other hand limits disentanglement and plasticity quite naturally. The cross-linking density or inversely the molecular weight between cross-links is a common parameter studied for EP. However, in terms of fatigue crack resistance, the role of this parameter remains somewhat unclear. Kishi et al. [82] and Skibo et al. [112] reported increasing fatigue crack resistance for lower cross-linking densities. In contrast to this, Trappe et al. [169] found ten times lower crack

propagation rates for increased cross-linking densities. The main difference between both studies is that in one case the thermal curing cycle is altered, whereas in the other case the chemical composition is different. Similarly, the effect of cross-linking density on fracture toughness is also inconclusive mainly for the same reasons [168]. Intuitively, it seems likely that lower cross-linking improves fracture toughness and fatigue crack resistance because the ability for plastic deformation improves. This could then translate into easier crack tip blunting and other crack arresting mechanisms. A limited plasticity for high cross-linking densities also shows in the failure maps produced by Kody and Lesser [78]. Not only increases the yield stress with increasing cross-linking but for very high cross-linking densities the failure mode shifts from ductile to brittle failure. Hydrostatic pressure dependence, on the other hand, is not affected by the molecular structure. The cross-linking density of thermosetting resins can be calculated from a temperature sweep in a dynamic mechanical thermal analysis (DMTA) [168], [170]. The molecular weight between cross-links M_c can then be calculated from the universal gas constant R_g , the absolute temperature T , the polymer density ρ_w and the storage modulus above glass transition temperature $E_{rubbery}$. The factor three accounts for the fact that equation Eq. 3-7 relates to the elastic modulus instead of the shear modulus under the assumption of incompressible flow. The latter gives a Poisson's ratio of 0.5 and therefore a three times greater elastic modulus with respect to the shear modulus.

$$M_c = \frac{3R_g T \rho_w}{E_{rubbery}} \quad \text{Eq. 3-7}$$

3.8 Irradiation treatment

Two competing processes are responsible for changes in polymers by high-energy radiation. First, chain scissioning occurs, which can lead to a growth of the macromolecules by crosslinking or to a decrease in molecular weight if no crosslinking occurs. If the majority of the cut macromolecule ends are left unlinked, the polymer degrades [36]. If crosslinking or chain scissioning is dominant depends mainly on the chemical structure of the macromolecules and is difficult to predict. However, a vast variety of experimental investigations can be found, intended either to change the polymer on purpose or to understand the resistance of a specific polymer against high-energy radiation. Especially polymers used for composites are primarily investigated with regard to their radiation resistance due to their exposure to radiation in particle

accelerators [171], nuclear fusion [172] or fission plants [173] or related fields like nuclear waste storage [174], [175]. High-energy radiation or particles in these applications are γ -rays and fast neutrons. In order to modify a polymer or to apply high dose rates electron beams (EB) are another source of radiation. Comparable are only γ -rays and EB, whereas fast neutrons are typically more drastic in their effect on polymers, due to secondary γ -rays, which are emitted during the slowdown of the fast neutrons. In terms of commodity polymers or for some specifically modified compounds of short fiber-reinforced composites irradiation treatment can also be part of the manufacturing process mainly by an electron beam [36]. The literature review in the following focuses on investigations, which either used electron beams or γ -rays. A major parameter to control the molecular changes can be found in the applied dose, expressed in Gray (Gy) or kGy. In this respect, the review is limited to studies focusing on low dose ranges, which can be applied within days to weeks instead of years of exposure. For EB dose rates can be adjusted whereas γ -rays are the result of the natural decay of for example Cobalt 60. This leads to different treatment sequences sometimes with implications for the resulting polymer changes. EB typically apply higher dose rates for several shorter exposure times, whereas γ -irradiation is applied in lower rates continuously. Table 3-1 gives an overview of studies focusing on changes induced by irradiation into PC. It is widely reported across a broad range of dose settings that PC mainly degrades, with yield stress, fracture strain and fracture toughness decreasing as the dose increases. However, for the highest reported doses degradation progresses up to a partial dissolution of the polymer.

Table 3-1 Effect of irradiation on Polycarbonate

Dose in kGy	Irr. by	Effect of increasing dosage	Ref.
20-200	γ	<ul style="list-style-type: none"> Decreasing molecular weight Decreasing storage modulus in DMTA test 	[176]
10-200	γ	<ul style="list-style-type: none"> Relatively stable up to 100 kGy and beyond decreasing elongation at break, tensile strength and izod impact strength 	[177]
25-200	EB	<ul style="list-style-type: none"> Decreasing tensile strength and elongation at break above 100 kGy Decreasing molecular weight Low dose rates degrade the mechanical properties more 	[178]
340	γ	<ul style="list-style-type: none"> No significant difference for high strain rate loading Increasing β-transition temperature which suggests a more ductile material response 	[179]
100-225	EB	<ul style="list-style-type: none"> Molecular weight decreased by 36% for 225 kGy Blisters visible in the fracture surface of PC exposed to 100 kGy and above 	[180]
684-4341	γ	<ul style="list-style-type: none"> Decrease in elongation at break (78.75% to 1.2% at 684 kGy) Decrease in elongation at break (59.7MPa to 28.1 MPa at 684 kGy) Granular appearance of fracture surface above 684 kGy 	[174]
340	γ	<ul style="list-style-type: none"> Decreasing molecular weight Elongation at break and tensile strength decrease Decreasing total fracture work in notched bending specimens SEM images show brittle fracture in notched and irradiated bending specimens 	[181]
10-75	γ	<ul style="list-style-type: none"> First increasing (10 kGy) and then decreasing strain at break and tensile strength Slightly decreasing glass transition temperature 	[182]

Much less, literature on the effect of irradiation on EP can be found and most studies focus higher doses (above 1 MGy). Another aspect limiting the transfer of literature data to a given system at hand is the dependence on the chemical structure of the epoxy resin. Two common types are Bisphenol-A and Bisphenol-F based. Bisphenol-A type epoxies are reported to deteriorate under irradiation with decreasing mechanical properties (strength and elastic modulus) [183], [184], [185]. The results of Zheng et al. [185] show that despite deterioration of quasi-static properties, the relative fatigue performance can nevertheless be improved by irradiation. For this observation, the

relative fatigue strength has to be compared for the different dose levels. The reported SEM images show embrittlement of the matrix material due to the irradiation. Similarly Beura et al. [186] and Hoffman and Skidmore [187] also found changes in the fracture surface of irradiated samples of Bisphenol-A based continuous fiber-reinforced epoxy. Bisphenol-F type epoxy composites are reported to show an improved inter laminar shear strength for moderate doses in the range of 1MGy [188]. For irradiation cured epoxy materials, the comparison shows a faster cure for Bisphenol-F compared to Bisphenol-A type epoxy [189], [190]. It can be concluded for EP that moderate doses up to approximately 1 MGy can improve the mechanical properties, whereas higher doses typically lead to degradation. If degradation is present, it is mainly in the form of embrittlement. Except for tendencies like decreasing strength or molecular weight, it appears hard to predict how a polymer will change due to irradiation treatment.

4 Materials and methods

4.1 Matrix polymers

The influence of matrix properties on the fatigue performance of carbon and glass fiber reinforced laminates is investigated for Epikote RIMR 135 cured with Epikure RIMH137 produced by Hexion Inc. [191]. As thermoplastic matrix polymer, a non-commercial bisphenol-A based polycarbonate supplied by Covestro AG is used. The latter is a low-viscosity type. However, at the outset four additional polymers have been identified, which could be modifiable by γ -rays and are viable candidates as matrix polymer in a composite. Therefore, a non-commercial thermoplastic polyurethane (ether type) supplied by Covestro AG is also included. To extend the group of thermosetting materials Arxada AG supplied one commercial cyanate ester resin Primaset BA-200 and two modified versions. Details on irradiation treatment, neat polymer fabrication and produced laminates will be given in the following chapters and in an earlier publication [19].

4.2 Experimental approach and modification method

The experimental approach tries to avoid changes apart from those intended for the properties of the matrix polymer by irradiation treatment. A major benefit of this method is that it can be the final step of specimen fabrication. Therefore, many if not all parameters like geometric arrangement, fiber properties, fiber sizing, and thermal history remain constant. A major drawback is the unpredictability of changes for different polymer systems. Because it is not known a priori, which dose affects the polymer sufficiently a two-stage approach is used at the outset of this work. In the first stage, promising polymers and dose settings are identified and later these settings are used. The results and methods presented within this work focus on the second stage. Still a brief description on material selection and parameter identification process will be given in the following. From the available literature and the requirements of composite manufacturing, a group of six polymers was studied in broad range of applied doses. Since tensile tests on neat polymer specimens can be considered, a rapid characterization method with potential relevance for the fatigue performance, screening is centered on this test. The doses were selected based on literature reports, ranging from 30 to 500 kGy. Thermoplastic polyurethane specimens showed significant warping as a result of irradiation treatment and only minor property changes

up to an applied dose of 200 kGy. Of the cyanate ester resins especially Primaset BA-200 showed noteworthy changes in terms of fracture toughness. However, this conclusion is primarily based on the type of fracture observed in tensile tests because no dedicated fracture mechanical tests were performed. A detailed discussion on the screening experiments and the results for cyanate ester resins and thermoplastic polyurethane can be found in an earlier publication [19]. Ultimately, the induced changes and processing requirements led to the selection of polycarbonate and epoxy resin. Here, 200 kGy and 500 kGy for PC and EP respectively were found to be the most promising material-dose combinations for the objectives. The remainder of this work will focus on the aforementioned doses and non-irradiated state. For easier reference, irradiation states are referred to as configurations. All specimens were sealed in vacuum bags to prevent the presence of atmospheric oxygen during irradiation. As irradiation source, a Cobalt-60 source is employed and specimens are exposed to 3-5 kGy/h. Based on the polymer/ dose selection from the screening a more in-depth study of the polymer properties in an irradiated and non-irradiated state is done. The characterization focuses on the potentially relevant property areas identified in the conceptual framework. Figure 4-1 shows the experiments in the context of this framework and assigns each material response a test to capture it.

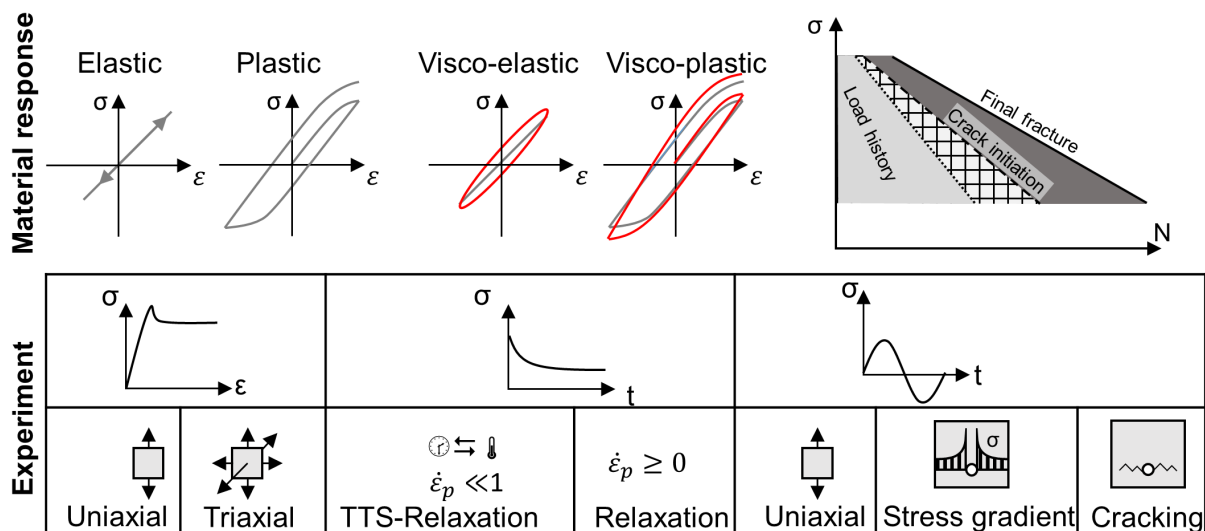


Figure 4-1 Experimental program used to capture the polymer's response to fatigue loading as comprehensively as possible

With a thorough understanding of the properties of both materials in both configurations, continuous fiber-reinforced specimens are prepared for the two identified loading cases (TT and CC) and tested in fatigue loading. The findings generated there are then related to the polymer characterization results.

4.3 Neat polymer characterization

4.3.1 Specimen preparation and geometry

PC specimens were injection molded according to the manufacturer's specification. Because available tooling is limited, two basic geometries can be manufactured. A small tensile specimen in accordance with DIN EN ISO 527-2 type 1BA and custom specimen with a round cross-section $\varnothing=5$ mm and similar dimensions. Figure 4-2 shows the specimens. From the 1BA tensile specimen, a notched specimen can be manufactured (1BA notch) and is used to characterize the notch sensitivity. The effect of triaxiality is investigated with a round cross-section and a circumferential notch (D5R1). The cross-sectional change at the notch leads to a constraint of the lateral contraction of the material within the notch [74]. This approach was originally employed in the context of necking of metals and also polymers [74], [192].

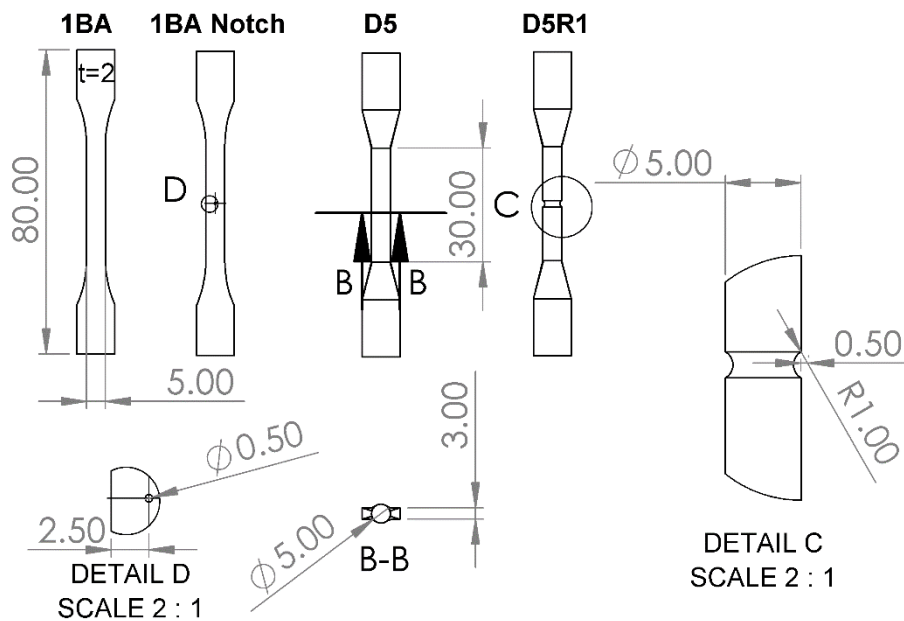


Figure 4-2 Neat polymer specimens

EP specimens are manufactured from RIM135/RIMH137 in a resin-transfer molding (RTM) tooling in plates of size $500 \times 400 \times 2$ mm³. This approach aims to keep the parameters for laminate and neat polymer processing as similar as possible. The curing cycle consists of 4 h at 80°C. After unmolding the plate, 1BA specimens are manufactured by milling. No specimens with circular cross-sections were manufactured for EP for several reasons. First, there are additional obstacles during manufacturing and second, the relatively brittle EP system is expected to show less

influence of triaxiality compared to the PC. A good indicator and alternative approach to this problem has been taken by works of Asp et al. [77], [110]. Here, two restricting metal discs introduce a triaxial stress state within the polymer. However, shielding by the metal discs was deemed problematic for the modification method.

Although water uptake may influence both EP and PC, the specimens were not conditioned before testing, as different irradiation doses are expected to modify the molecular structure regardless of the initial material state, provided it is identical across all specimens, including water content. Thus, significant effects would likely arise only if there were notable differences in water content between the neat polymer specimens and laminates. This was assumed unlikely. Any combined effect of irradiation and water content would be considered part of the irradiation dose effect. While oxygen presence during irradiation is noted as relevant, no literature indicates an impact of water content on irradiated EP and PC.

4.3.2 Quasi-static characterization

The quasi-static tensile tests were done according to DIN EN ISO 527-2 with slight deviations concerning the cross-head speed and changes thereof, which are described later. The tests were done on a Zwick RetroLine 10 kN testing machine equipped with a KAP-Z force sensor of class 0.05. Strains are recorded with an OPTRONIS CP20-25-M-72 camera and optics with 120 mm focal length and a frame rate of 1 fps for 600 frames. For synchronization purposes, both the video signal and the force recording start at a preload of 5 N. The specimens are loaded with a strain rate of 1 %/min, which corresponds to 0.6 mm/min with regard to the free clamping length of 58 mm. To limit the total testing time, the normative standard allows switching the testing speed after recording the elastic modulus. However, for this characterization campaign, the testing speed was increased only after necking occurred. Preliminary tests show that neck formation is completed after approximately 8% strain. After that, the testing speed is increased to 15 mm/min only. For notched round bars (D5R1 geometry in Figure 4-2), the procedure differs slightly. Instead of just assuming a free measuring length of 58 mm, a reduced measuring length of 3 mm is chosen spanning the notch. Through preliminary tests, a testing speed of 0.25 mm/min is appropriate to reach a strain rate of approximately 1 %/min as mean rate over the notch. The latter is verified by evaluating the DIC measurements.

The strain signal is evaluated by GOM Correlate (vers. 2016). Two virtual extensometers are used to evaluate the longitudinal and transversal strains, with a base length of 25 and 3 mm respectively. In order to place the extensometers identical for all specimens, an automatic identification algorithm is used. The latter is based on the spatial frequency content of the speckle pattern relative to the plain background of the image.

4.3.3 Influence of triaxiality

The triaxiality ratio is defined as the ratio of hydrostatic pressure σ_m to deviatoric stress represented by the von Mises stress σ_{Mises} [192]. This ratio can be approximated for a notched round bar according to equation Eq. 4-1, where D_{min} is the minimum diameter of the cross-section and r_N is the notch radius. This leads to a maximum triaxiality of the specimens under investigation of nominally 1.0. However, this value can only be taken as an estimate, because the equation is derived under the assumption of uniform plastic strain across the minimum cross-section [193]. Furthermore, the discussion by Earl and Brown also shows that notch geometry not only depends on the radius but other parameters, too.

$$\frac{\sigma_m}{\sigma_{Mises}} = \frac{1}{3} + \ln\left(1 + \frac{D_{min}}{4r_N}\right) \quad \text{Eq. 4-1}$$

Eq. 4-1 is therefore supplemented by numerical results shown in Figure 4-3. Here a linear elastic material is assumed. The fully plastic deformation is approximated by setting the Poisson's ratio near incompressibility. From the results, it is evident that equation Eq. 4-1 overestimates the triaxiality, which can be introduced by the circumferential notch. A minimum notch radius of 1 mm and minimum diameter of 4 mm were mainly chosen for testing and manufacturing purposes. The comparison of the incompressible and the actual material behavior shows that the triaxiality will remain nearly unaffected and increases slightly. With the given specimen geometry a maximum triaxiality of 0.6 can realistically be reached. From the RVE models, it was found that near the fiber-matrix interface even higher levels of triaxiality might be present which cannot be reached with realistic specimen geometries of the type notched round bar.

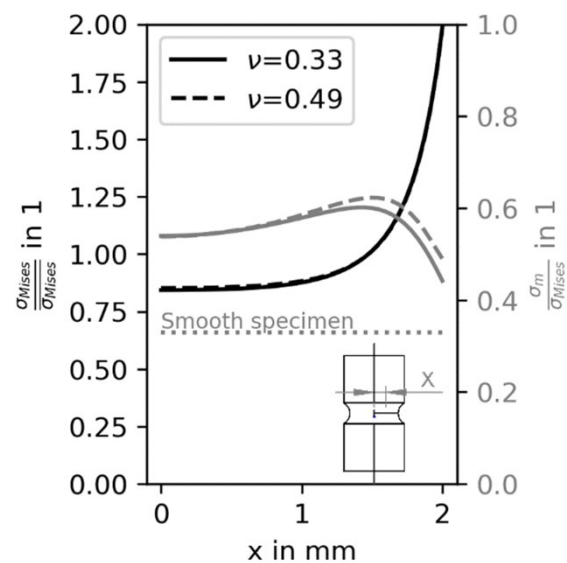


Figure 4-3 FE results of normalized von Mises stress and triaxiality ratio as a function of radial position for two types of lateral contraction

4.3.4 Fatigue characterization

The neat polymers are also characterized under cyclic loading conditions. A low testing frequency of 2 Hz is chosen across all fatigue tests including neat polymer characterization, even though literature reports suggest low self-heating up to 20 Hz. The limiting case is seen in fatigue loading of laminates under shear, which is not the focus of this work, but should rely on a common data foundation. Load controlled loading is employed with a sinusoidal waveform and a loading ratio of $R=-1$. In this way, fatigue-creep interaction should be kept to a minimum.

Fatigue characterization is done with the same specimen geometry employed for quasi-static characterization. This slender geometry is prone to buckling, which can be avoided by a novel anti-buckling device shown in Figure 4-4. The main benefit is that the measuring length remains mainly accessible, which allows the use of an extensometer during the fatigue experiments. The buckling guide subdivides the measuring length into shorter segments. The position of the supports along the specimen's measuring length are calculated from combined Euler buckling cases. Intermittently supported beams can be subdivided into one of the four basic Euler buckling cases, as described in reference [194]. The resulting cases are hinged-hinged and fix-hinged, as shown in Figure 4-5. The remaining free length for each of the segments is chosen based on an equal critical buckling load. Compared to the fix-fix case with $L_0=58$ mm, the buckling load can be increased by a factor of 3.7. For

polymers of exceptionally high strength, this may not be sufficient. However, for EP and PC specimens the stress amplitude for fatigue failure is below the buckling load and hence uncritical. Subdivision of the measuring length is only necessary in the direction of low flexural rigidity and therefore the specimen's thickness direction. The actual design consists of two bracing arms, which form the support. To avoid a second load path, movement should only be constrained in the direction indicated in Figure 4-4 (top-left detail). Especially in the direction of loading, the supporting points offer low resistance to longitudinal displacement by allowing a rotation around a solid hinge. The latter is a 0.1 mm spring steel sheet.

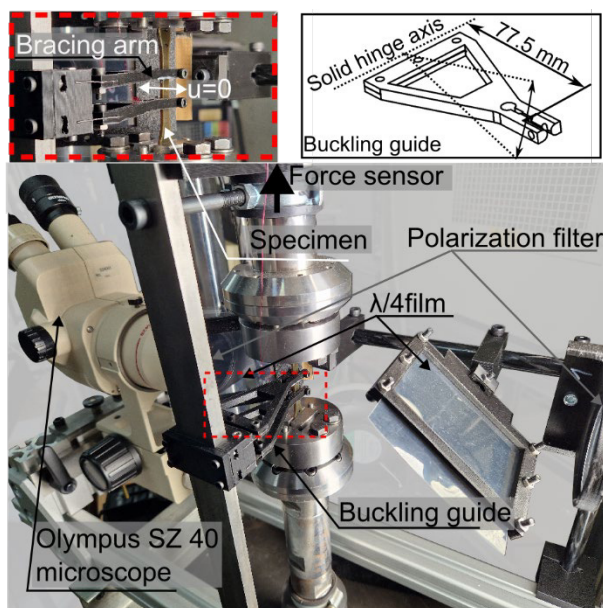


Figure 4-4 Anti-buckling device incorporated into a circular polarisator for photoelastic imaging

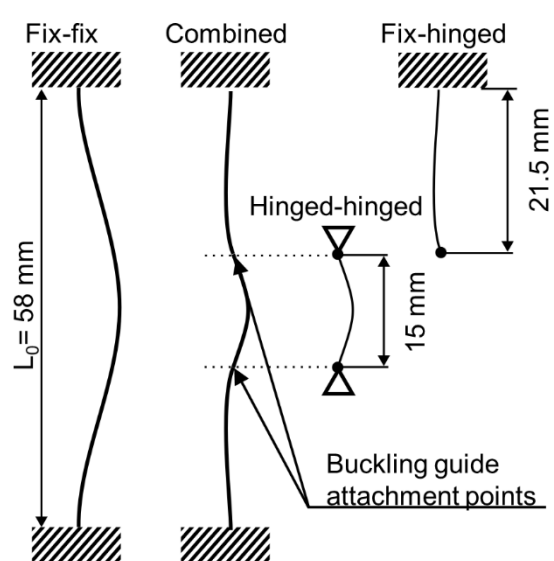


Figure 4-5 Working principle of the anti-buckling guide

4.3.5 Notch sensitivity in fatigue

In the MSF-model the onset of cracking can be affected by stress concentrators like notches but also internal material flaws. This effect is well known for metals and polymers [90], [91]. Extensive investigations in metal fatigue indicated that not only stress concentration (i.e., stress peak) matters but also the stress gradient [91]. Ignoring this can introduce a size effect. A hole was drilled in the center of the specimens to act as notch. The hole diameter was chosen to be small enough that the stress decay could develop asymptotically, but is still large enough to be manufactured in 1BA tensile specimens. A centered hole of $\varnothing=0.5$ mm suits both. From the equations given by Peterson [92] a stress concentration factor of 2.73 will be active for the given geometry.

The crack length was assessed by continuous video recordings during fatigue loading by an Olympus SZ 40 shown in Figure 4-4. Because both materials show a photoelastic effect in both configurations (irradiated and non-irradiated), a stress optical set-up is used. Here a circular polarizer (Figure 4-4) shows the stress distribution around the hole and in the second stage of the MSF-model around the crack. Although the actual stress distribution is of minor interest changes in the fringe pattern allowed for an easier identification of the crack tip.

4.3.6 TTS relaxation experiments and visco-elastic parameter fitting

The application of the time-temperature superposition (TTS) enables the implementation of a timesaving methodology for the evaluation of both long- and short-term relaxation. The rectangular cross-section of 1BA tensile specimens was used in a dual cantilever set-up. Three specimens are evaluated per material and irradiation configuration. The temperature range was selected from -15°C to 100°C in order to cover both short-term relaxation in the time scales of a single loading cycle at 2 Hz and long-term relaxation. Temperatures were set in steps of 5°C with 5 minutes of loading and 30 minutes of strain recovery. As reference temperature, 20°C is used. All experiments were performed on a DMA Q800 machine from TA Instruments. Shifting of the resulting stress-relaxation curves to a master curve was done within the software of TA Instruments (vers. 4.5A). Afterward, it is visually verified that the resulting master curve is smooth, that overlaps are correct and that no data points are used with significant amounts of plastic deformation, i.e. lowered strain recovery. The temperature range covered a very broad time spectrum well beyond the time scales needed for visco-elastic modelling in section 6. The acquired master curves are then fitted to a Wichert model as shown in Figure 4-6. Similar to Krause [75] the time constants are predefined and the elastic coefficients are adjusted for a good representation of the measured master curve in the time range from 10^{-6} to 10^5 s. In total, five parallel Maxwell elements and one spring for the infinite response are used. This choice is based on additional comparisons done for PC beforehand because the number of elements as well as the definition of time constants significantly affects the representation of the master curve by the model [195]. For the time constants, a different spread in the time range and different center values were compared and lead to the final choice given along with Figure 4-6.

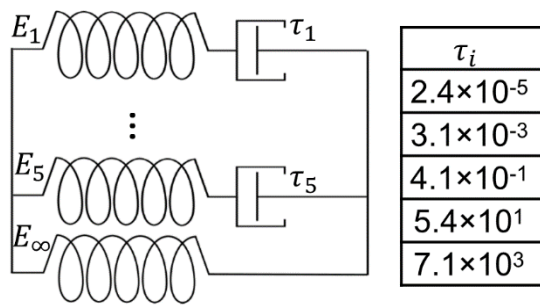


Figure 4-6 Wiechert model and fixed time constants

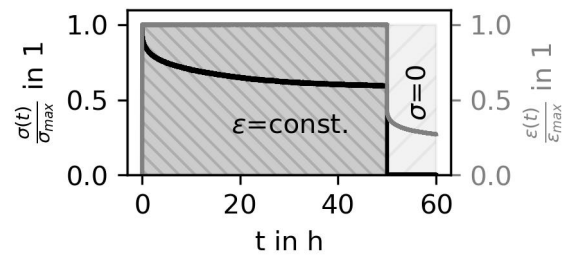


Figure 4-7 Loading sequence of relaxation experiments

4.3.7 Relaxation experiments

TTS relaxation experiments are performed at low strains of 0.1% to avoid any plastic effects. Therefore, this data provides a basis for the description of the visco-elastic behavior. Strains encountered within the polymer as part of a laminate are typically higher and therefore additional relaxation experiments at strains up to 2% are performed. It has been shown that the concept of Haupt [42] can be used for the identification of the polymer's equilibrium response by intermittent relaxation tests [75], [196]. The underlying assumption is that the equilibrium response of the material consists of elastic and plastic parts, and that intermittent relaxation allows finding the stress-strain points by identifying the asymptotic decrease of viscous overstresses towards these values. Within this work, an alternative approach is chosen to validate and compare the fitted Wiechert parameters to conventional relaxation experiments and still get an indication on the equilibrium response. Although intermittent relaxation might provide a comprehensive estimate of the equilibrium response, it was deemed necessary to rely on conventional relaxation experiment with the specimens loaded with a single strain level. This is because first experiments suggested that PC shows localized visco-plastic behavior indicated by crazing, which makes an informed choice on the intermittent relaxation times challenging. Furthermore, relaxation is relatively slow which prolongs the testing times for the materials under investigation.

Relaxation is therefore studied by applying a constant strain for 52 h, followed by a strain recovery step to estimate the residual strain. This additional step allows viscous effects to recover, with strains recorded for an additional 10 h after unloading. Figure 4-7 shows the loading sequence and the two different control modes. The final residual stress is taken as estimate of visco-plastic and plastic deformation. Strains are recorded by a clip-on extensometer, which is also the control channel used. With the

available hydraulic testing machine, it was not possible to produce strain jumps directly in strain control. To circumvent this problem the initial strain jump is produced by specifying a displacement of the hydraulic cylinder based on an initial guess. The resulting strain is then used as target value and the control is switched to the extensometer to correct for temperature drifts and relaxation within the clamps. Three specimens per strain level, material and irradiation configuration are tested in this way. Crazeing, observed in-situ, is being studied as a potential visual indicator of time-dependent plastic deformation in PC. To record the formation and growth of crazes in PC, a modified Olympus SZ40 microscope in combination with an indirect illumination was used to make crazes visible. The illumination direction relative to the craze affects the visibility of crazes greatly. The optimal set-up was chosen with an already crazed sample. Crazes are most visible if the observation axis is parallel to the plane formed by the craze and illumination is applied under an angle of approximately 30° to this plane from the opposite side.

4.3.8 Irradiation induced relaxation

The influence of irradiation is mainly described in terms of the effects on chemical and mechanical properties. From the initial material screening and selection [19] it was found that some materials undergo either volumetric changes or residual stresses are freed. Against this backdrop, it was deemed necessary to investigate the effect of irradiation treatment on residual stresses in more detail. A challenge in this regard is the existence of residual stresses on different scales, which are especially challenging to investigate on the fiber-matrix level. As an alternative approach to this question, it was decided to replace naturally occurring residual stresses from processing (e.g., solidification and cool down) with artificial strain loads and estimate the potential change in residual stresses based on the relaxation behavior. Two relaxation processes can then be compared, one with and one without irradiation treatment. To overcome the problem of measuring the relaxation during irradiation treatment stress optics and unreinforced polymer specimens (1BA tensile specimen) are used. Even though stress optics are well suited as a method for investigating residual stresses in both polymers across all configurations changes in photoelastic sensitivity need to be considered. A detailed discussion on the set-up and procedure can be found in [197]. In the following, only a brief description will be given. To compare both relaxation routes, tensile specimens are clamped into an aluminum fixture to apply a fixed strain

during irradiation treatment. Aluminum is chosen for its relatively low absorption of γ -rays and durability under irradiation exposure. The specimens are also sealed in vacuum bags during irradiation treatment. An identical set of specimens is meanwhile stored without irradiation exposure. Changes in fringe spacing indicate relaxation. An important feature investigated separately is the photoelastic sensitivity in terms of fringes per principal stress difference. The fringe sensitivity is evaluated by determining the fringe pattern in a three point bending set-up and comparing it with the principal stress difference calculated from a FE model. For this, also tensile specimens are used in irradiated and non-irradiated configuration. With a calibrated fringe sensitivity, it is then possible to calculate the stress state before and after the relaxation and compare the routes with and without irradiation exposure.

4.4 Laminate characterization

4.4.1 Specimen preparation and geometry

Carbon and glass fiber-reinforced plates are manufactured by vacuum assisted resin transfer molding. Curing of the resin is identical to the neat resin plates. The reinforcing fibers are unidirectional non-crimp fabrics with an aerial weight of 200 g/m² for the HT-carbon fibers and 402 g/m² for the E-glass fibers. The stitching fibers are in both non-crimp fabrics (NCF) E-glass and polyester fibers. All RTM manufactured plates have a nominal thickness of 2 mm. A cross-ply lay-up is used for both TT and CC testing. For TT loading, the on-axis plies allow for a continuous observation of transverse cracking instead of just one crack leading to final failure [52]. Furthermore, a thick transversely loaded ply increases the chances that a transverse crack visible on the edge of the specimen spans the whole specimen width, making edge observation representative as discussed in section 3.2.2. For CC, on-axis loading is of main interest. Additional transverse plies should counteract tendencies for longitudinal splitting. A common lay-up fulfilling both requirements is a cross-ply arrangement with the majority of middle plies oriented as required for TT or CC loading. With the aim of using a similar fiber volume content across all plates, this leads to a [0/90₂]_s lay-up for the glass fiber-reinforced epoxy (EP-GF) and [0/90₃]_s for carbon fiber-reinforced (EP-CF) plates. The nominal fiber volume content of 48 and 45% is reached, respectively. The carbon fiber-reinforced polycarbonate plates (PC-CF) are supplied externally and have also a lay-up of [0/90₃]_s with a nominal plate thickness of 1.4 mm and fiber volume content of

48%. The plates are prepared from tapes by continuous compression molding. The matrix polymer for plate manufacturing and neat polymer characterization is identical. However, the thermal history for reinforced specimens and neat polymer specimens differs. All specimens are prepared without tabs to avoid alignment errors, which are detrimental for the in-situ observation. Rectangular tensile specimens $250 \times 20 \text{ mm}^2$ are cut from the plates by a water-cooled diamond saw. Slightly smaller specimens of $200 \times 20 \text{ mm}^2$ with a middle notch are prepared by milling for the compression tests. Details on the notch geometry are given in section 4.4.4 together with the set-up.

4.4.2 In-situ edge observation

Detailed recording of the sequence of damage formation in fatigue experiments is typically challenging because most damage parameters, such as stiffness degradation, are a cumulative response from both damaged and undamaged regions. In-situ observation techniques are a common method to overcome this limitation. Because of the hypothesized importance of the local stress state on the micro level and because transverse cracking initiates on this level, it is deemed necessary to observe this scale. It is common to document fatigued specimens intermittently on the edges. However, drawbacks of this method are the necessity to dismount the specimen and the time spent for this process. Alternatively, the test is stopped to refocus and capture the same specimen region with a microscope fixed to the testing rig. Overall, these factors make edge microscopy very tedious. In addition, cracks can only be observed in the unloaded state, which can easily make small cracks difficult to identify. Within this work, it was aimed to overcome the problem by using a microscope in-situ. To achieve this, it is necessary to find an optical system with high magnification, large field of view (FOV), large depth of view and big working distance. These requirements are somewhat contradicting because working distance, numerical aperture and focal length are related and conflicting [198]. A high magnification system will have a low depth of view and limited working distance. Still, these drawbacks can be circumvented to some degree. As part of this work, a novel set-up is developed to allow for in-situ crack observation, which will be described in the following.

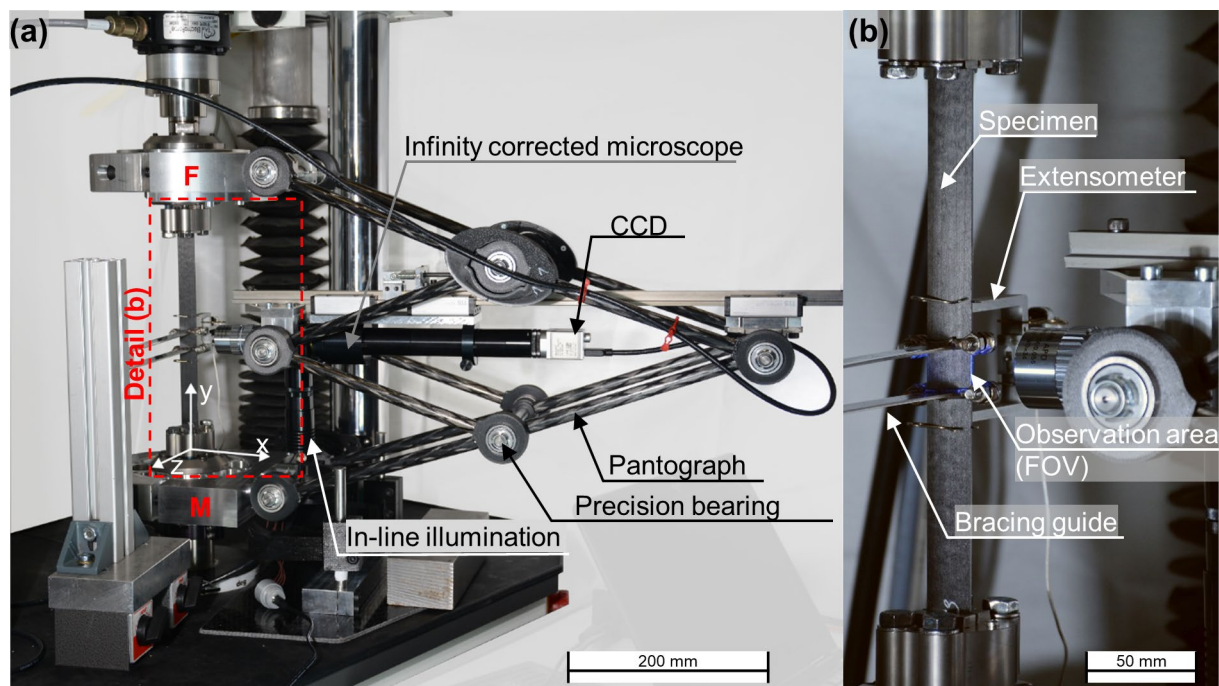


Figure 4-8 (a) In-situ microscopy for imaging during fatigue testing; (b) Detail of a clamped specimen. Adapted from [199]

Commercially available long working distance objectives can be used to distance the sensitive lenses from the specimen's edge. A second geometric necessity is the field of view, which needs to be big in order to compensate for the specimen's deformation and subsequent movement. This movement is inherent for the one-actuator system shown in Figure 4-8 and schematically in Figure 4-9 (a). In a system like this, one specimen end is constraint (fix [F] Figure 4-8 and 4-9 c), whereas the second end is displaced by a single actuator (movable [M] Figure 4-8 and 4-9 c). A two-actuator system could overcome this problem because both specimen ends could be moved in a way that the observation area will remain static relative to the microscope (Figure 4-9 b). The second approach to solve the problem is by moving the microscope alongside the specimen synchronized to the specimen deformation. Within a morphological study, it was found that the pre-cnc technique of a so-called "copy-milling machine" could solve the problem by relying on pantograph. This arrangement of guiding rods can magnify or reduce the movement of one point relative to a second point (displacement vectors \vec{d}_1 and \vec{d}_2 in Figure 4-9 (c)). Under the assumption that a specimen under tensile loading will elongate symmetrically a point in the middle will be displaced exactly half the total elongation. In addition, a movement in a plane normal to the specimen axis (x in Figure 4-8 and 4-9 c) will also be translated exactly half. Under this assumption, a pantograph was designed guiding an infinity corrected

microscope exactly half the displacement of the specimen end connected to the actuator. Expressed in terms of displacement vectors, \vec{d}_1 is exactly half of \vec{d}_2 if all hinge points are connected with equidistant connecting rods of length L_{Rod} , shown in Figure 4-9. Unfortunately, some specimens showed asymmetries in thickness direction (z in Figure 4-8), which made it necessary to use a guidance system to prevent movement in the direction of the asymmetry. The infinity-corrected microscope is suspended from a linear guidance rail to adjust the focus onto the specimen's edge. A more elegant piezoelectric adjustment in the infinity space between objective and tube lens of the microscope could not be realized due to time and cost restrictions but could also be used to adjust the focus rapidly. However, the infinity space is still an important feature of the set-up because pre-trials showed that only with in-line illumination fibers and matrix can be distinguished clearly. The objective, beam splitter, and lenses were sourced from Edmund Optics Ltd.

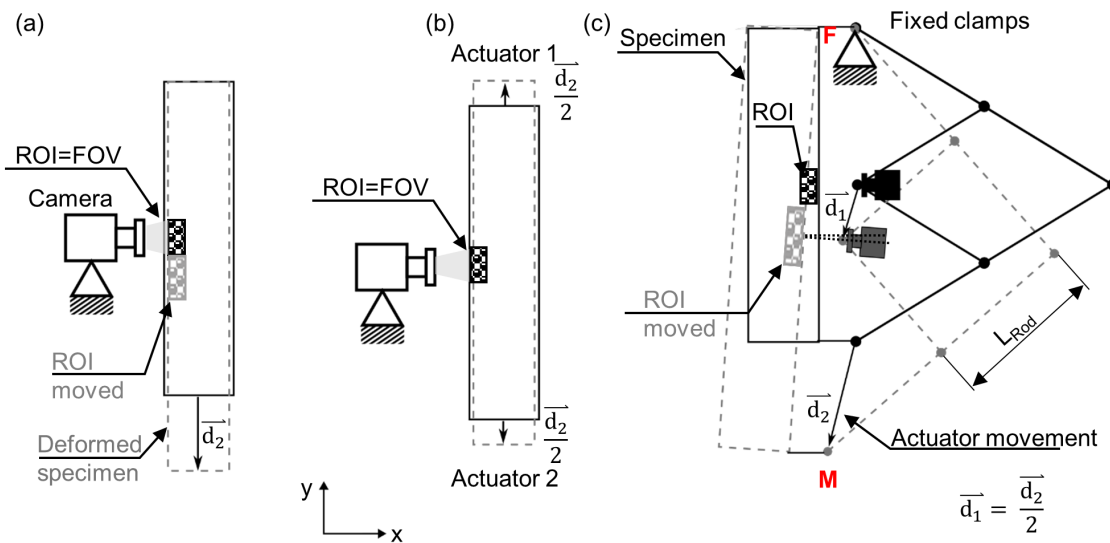


Figure 4-9 (a) Schematic of the specimen deformation and relative movement of the FOV to a fixed camera; (b) Two actuator system with a fixed camera; (c) Following mechanism in the novel set-up. Adapted from [199]

4.4.3 Tension-tension loading

Tension-tension fatigue tests are performed with a loading frequency of 2 Hz and a loading ratio of $R=0.1$. The fatigue tests consist of a sequence of loading ramps and cyclic blocks, as shown in Figure 4-10. This approach serves mainly in-situ edge observation. The fatigue block consists of 500 sinusoidal cycles, which are followed by a ramp to maximum force for imaging purposes. In this way, the specimen state can be documented after each fatigue block. Even though it is in principle possible to record the specimen edges continuously, it was decided to limit the amount of data to one

photo every 500 cycles. At the beginning and end of each fatigue experiment, a ramp is added with continuous video recording of 1 fps. The specimens are loaded with 200 N/s to the maximum load applied during cyclic loading. The video recorded during the ramps before and after serves two purposes. First, for PC-CF a significant amount of cracking can be observed during the first loading cycle or ramp. Second, especially for glass fiber-reinforced epoxy, cracks are sometimes challenging to identify on microscopic images of the specimen's edge. To overcome this problem, it is possible to use digital image correlation (DIC) on the recorded videos. Strain perturbations are then an indicator and verification for the existence of cracks. EP-GF can additionally be observed by backlight illumination due to the transparency of the material. For this, a second camera system is aligned orthogonally to the edge-observation imaging system (i.e., looking through the specimen's thickness direction) and triggered synchronously. During the complete loading sequence, an extensometer with a measuring length of 50 mm is used overlapping the observation area. The recorded stress-strain signal allows for the evaluation of stiffness degradation, strain amplitude and specific loss energy per cycle.

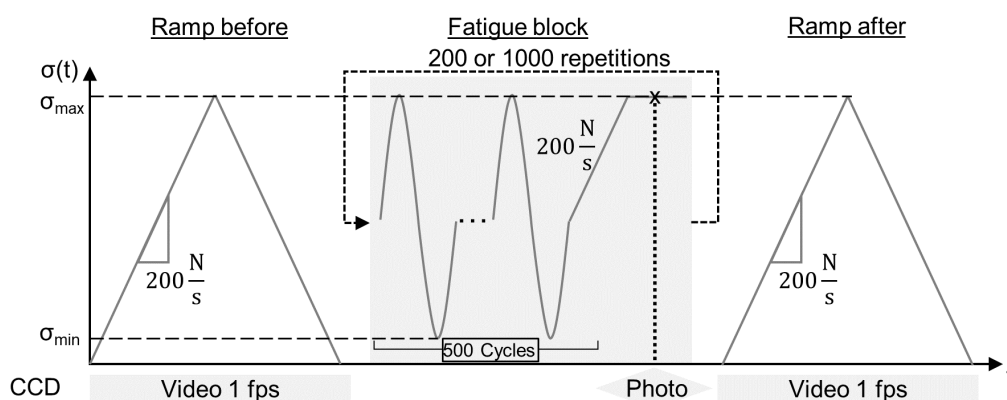


Figure 4-10 Fatigue loading sequence applied to laminate specimens and corresponding CCD-camera documentation. Adapted from [199].

The in-situ images show mainly where cracks start within the transverse plies and the speed of propagation during the fatigue block. Furthermore, it is possible to use the fibers as pattern for DIC, which in turn can give indications on the strain perturbations introduced by cracks or dry spots. However, the strains evaluated in this way need to account for possible variations in working distance (WD). This is because despite a limit for the depth of view of only 91 μm the still relatively low working distance of the microscope (34 mm) can introduce a systematic error of 0.27% according to the

formulas (Eq. 4-2) derived by Sutton et al. [200]. Under the assumption that the strains measured by the extensometer represent global strains identical to the mean strain within the in-situ observation area, it is possible to calculate a correction factor $\frac{\Delta WD}{WD_0}$, despite unknown changes in working distance. This assumption agrees with the premise of the classical laminate theory that all plies share a common strain load. By using the mean of the DIC strain field it is acknowledged that strain inhomogeneity can exist within a ply. The correction factor is the ratio between the DIC mean strain $\overline{\varepsilon_{DIC}}$ and the strain measured by the extensometer. The latter is taken as true strain ε_{true} in this case. Where needed this correction is used to get the true local strain without errors introduced by different working distances.

$$\overline{\varepsilon_{DIC}} = \frac{\Delta WD}{WD_0} \varepsilon_{true} \quad \text{Eq. 4-2}$$

To ensure accurate DIC analysis, it is crucial to differentiate between images captured during ramp loading and those taken intermittently during the fatigue block. For the latter, the reference frame must be the initial image captured before any loading. The problem here is that the number of disturbances increases drastically with increasing time between reference frame and currently analyzed frame. This is because in addition to changes in the working distance it is likely that slight variation in the temperature affect the lens system. Furthermore, the ramps to peak load are not recorded and therefore no extensometer data is available for the specific peak. Recognizing these uncertainties, strains evaluated from the images taken during the fatigue block are only considered as relative measures for identifying strain hot spots. For the ramp before and after the fatigue block the first image of the recorded video can be taken as reference and absolute strain values are therefore accessible and can be used for comparison. Local peak strains can be evaluated by taking the ratio of the local maximum strain $\max(\varepsilon(X, t))$ and normalizing it to the mean overall strain of the transverse ply $\bar{\varepsilon}(t)$, the result is a concentration factor K_ε . To reduce signal noise, the mean value over an extended period can be used. A prerequisite for this is that the strains both increase linear with time.

$$K_\varepsilon = \frac{\varepsilon(X, t)}{\bar{\varepsilon}(t)} \quad \text{Eq. 4-3}$$

The crack density, however, is not accessible from microscopic in-situ imaging, due to the limited observation area, which spans only 2.8 mm along the specimen axis. With

Eq. 3-1 the saturation crack spacing is expected to be 1.1, 1.5 and 1.3 mm for PC-CF, EP-CF and EP-GF. This shows that 2.8 mm of observed edge length is not sufficient to determine a crack density. Still, crack density is an important evaluation parameter and is expected to differ as a result of altered matrix properties. A larger portion of the specimen's edge is documented by stitched microscopic images of comparable magnification with a Leica DM6000M to evaluate the crack density. The region for documentation by stitched images extends symmetrically to neighboring areas of the in-situ frame. In this way, the crack density can be evaluated on a total length per specimen of 22.4 mm. Stitched imaging is intentionally centered around the in-situ observation area, because this is also where strains are documented by extensometer measurements. Since most materials within this work are not transparent, edge observation is the primary source for damage evaluation. The crack density ρ is defined as the sum of all individual crack lengths L_i (through thickness) normalized by the observation area A .

$$\rho = \frac{\sum L_i}{A} \quad \text{Eq. 4-4}$$

Stress-strain data recorded during the tension-tension fatigue loading sequence described in section 4.4.3 can give some indications on the damage formation and propagation as well. Scalar descriptors for the laminate's damage state analyzed in the following are the stiffness degradation and loss energy W_{loss} . A major challenge is noise present in both the load and strain signal. To overcome this problem fitting functions are used instead of the actual signal. Because both signals can be reasonably represented by sinusoids due to the linear stress-strain relation, it is possible to fit all points of both signals in one cycle to a sine function using routines available in Python's SciPy (vers. 1.7.3). The timely lag (phase difference δ) between stress and resulting strain can then be drawn from the fitting functions along with the stress σ_a and strain ε_a amplitudes. Eq. 4-5 gives the resulting specific loss energy W_{loss} . In addition, this fit has also proven useful for calculating the dynamic modulus E_{dyn} . Especially for the latter case, slight variations in the strain reading lead to noisy results when evaluated from extreme points per cycle. Figure 4-11 shows an example of an overestimated strain amplitude, due to noise in the strain signal.

$$W_{loss} = \pi \sigma_a \varepsilon_a \sin \delta \quad \text{Eq. 4-5}$$

The ramp before and after the fatigue block allows for direct integration because a higher sampling frequency gives sufficient points for the application of a Savitzky-Golay-Filter implemented in the Python module SciPy (vers. 1.7.3). This loss energy gives an indication of ongoing damage formation processes and viscous or frictional energy dissipation during the ramps. Under the assumption that frictional effects are limited and viscous energy dissipation is constant, the difference in energy dissipation ΔW_{loss} of the ramps before and after could indicate ongoing fracture processes. In addition, all three dissipative features are lower if more load is shifted to the on-axis plies.

Stiffness degradation is another damage parameter available during both ramps and the fatigue block. For quasi-static loading ramps, it is known that a knee-point can form and hint at the onset of transverse cracking [55]. A knee-point might be detectable by subsequent loading ramps or by analyzing the stiffness continuously. Here again noise in the input signals needs to be considered. Instead of a derivative of the stress-strain curve, several linear regressions are used on subsets of the ascending stress-strain path as shown schematically in Figure 4-12. As a result, a semi-continuous modulus can be evaluated.

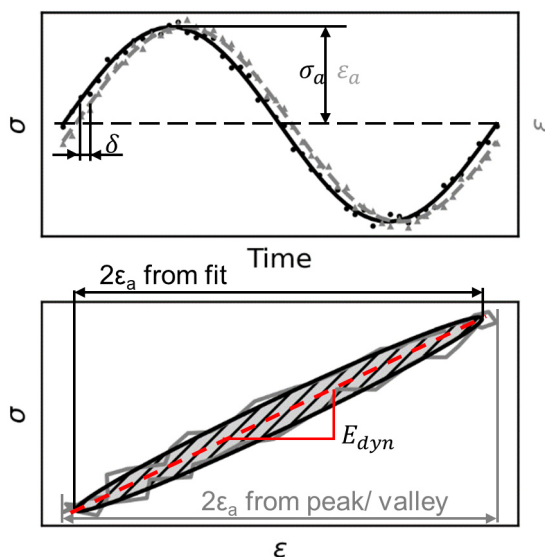


Figure 4-11 Hysteresis evaluation

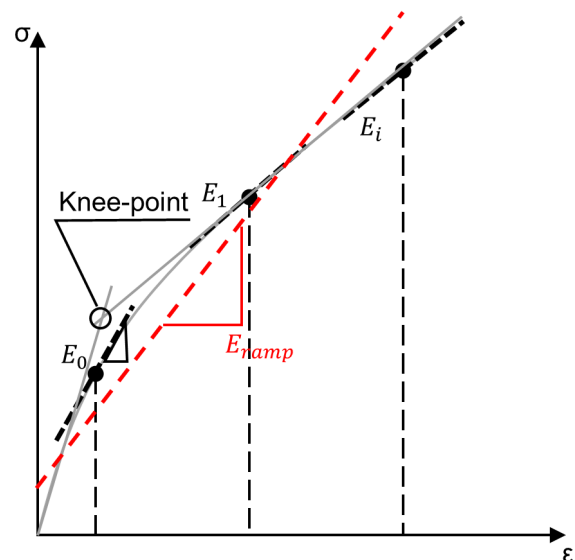


Figure 4-12 Determination of a continuous modulus by linear regressions along the quasi-static ramps before and after fatigue loading

Stiffness degradation during cyclic loading is an already known damage parameter used in many investigations. However, because damage forms for many specimens already in the first loading cycle it was decided to use the linear regression of the first

ascending part of the loading ramp before E_{ramp} as reference stiffness (Figure 4-12). A problem in this approach is however that the stiffness might also vary due to different loading signals (ramp with 200 N/s vs. sinusoidal with $F=2$ Hz). It is intended to capture as many aspects of damage formation as possible and remove the influence of different loading signals. Assuming that damage is indicated equally during ramp and sinusoidal loading in terms of stiffness and that strain rate effects remain constant, any additional decrease in stiffness is related to increasing damage. Capturing this is the damage parameter ΔD defined according to eq. Eq. 4-6. By this definition, the relative change in stiffness during the fatigue block is calculated and represents additional damage introduced in the cycle N . Ideally, the modulus of the first segment (E_0 in Figure 4-12) at low stresses would be taken as reference to benchmark any additional change against this presumably undamaged state. This theoretical benefit of capturing the damage continuously is contradicted by the also present alignment effect in all specimens described later in this section in detail.

$$\Delta D = \frac{E_{dyn,1}}{E_{ramp}} - \frac{E_{dyn,N}}{E_{ramp}} \quad \text{Eq. 4-6}$$

4.4.4 Compression-compression loading

CC fatigue loading employs a loading ratio of $R=10$. However, it must be recognized that this ratio is often problematic because of scattering and buckling. The latter can only be avoided by lateral support of the specimen or by a short free measuring length. From the literature, two major drivers for scattering can be identified. First, a shift between different damage modes as a function of load and possibly time under load. Second, a flaw-driven failure typically known from brittle materials like glass [201]. Two major deviations from typical fatigue tests are used to mitigate these challenges. For one, notched specimens are used to introduce in-plane shear stresses, which make kink band formation more likely. In this way, experiments focus on a particular failure mode. In addition, a load increase test is used, as it has already been proven a reliable method to generate time-dependent compressive failure without excessively long experimental time [49]. It is expected that an ascending loading sequence will not alter the kink band initiation stress because the models predict kink band initiation and propagation to be active only after reaching a critical load. This is different from, e.g. plastic yielding at notches, where initial loading might lower local stress peaks. To define adequate loading steps, quasi-static loading is used to determine a compressive

strength of the notched specimens. Specimens are loaded with 0.2 mm/min until failure. Based on the average failure load per material and configuration, CC loading starts with a maximum compressive load of 40% of this quasi-static failure stress. After 2×10^4 cycles, the load is increased by 5% until specimen failure. It is assumed that load levels below 40% of the monotonic failure stress will not significantly contribute to fatigue damage or failure. Due to the catastrophic failure present in most specimens, no additional sensors are used except a high-speed camera with 5×10^4 fps during monotonic loading and the light transmission technique for EP-GF specimens in the load increase test. Due to the specimen's lay-up, the observation angle and pre-trials, it was deemed unlikely that kink band formation can be studied directly by high-speed imaging. Instead, a DIC pattern was applied and a reference frame in the unloaded state was taken. In this way, strains can be evaluated by DIC. A propagating kink band is expected to be visible as inhomogeneity in the strain field. The main investigation was done with sinusoidal load-controlled loading and testing frequency of 2 Hz. To include the influence of creep-fatigue interaction, additional experiments were performed with the trapezoidal loading signal shown in Figure 4-13. The load is held constant for 0.8 s and two Hamming shaped ramps load/unload the specimens within 0.1 s at the beginning and end of each cycle.

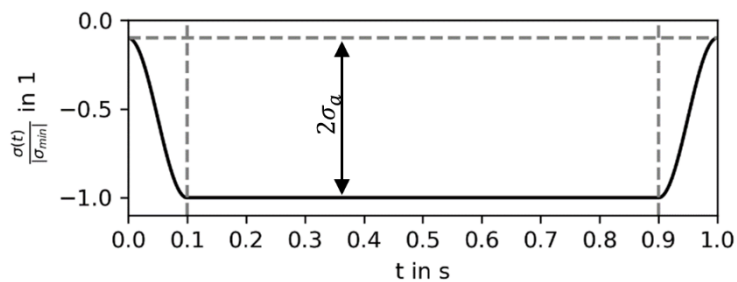


Figure 4-13 Trapezoidal loading signal used to increase the time under load

As shown by several authors, kink bands can evolve in-plane or out-of plane depending on the shear stress, type of notch and constraints [150], [158]. For this investigation, it was decided to keep constraints near the targeted initiation location to a minimum, which leads to the buckling guide shown in Figure 4-14. The size of the unsupported area is chosen small enough to avoid premature buckling and still keeps lateral support limited to allow for out of plane kinking. The contact area between anti-buckling guide and specimen uses a PTFE tape to reduce friction. It was tested manually before each test, that the anti-buckling guide can be moved easily after mounting it to the machine grips. This ensures a limited load transfer over the second load path compared to the

testing loads. Additional stops for lateral movement are in place by adjustable screws with a polyamide cap nut. This measure is necessary to avoid buckling in the remaining free section between the clamps and the anti-buckling guide.

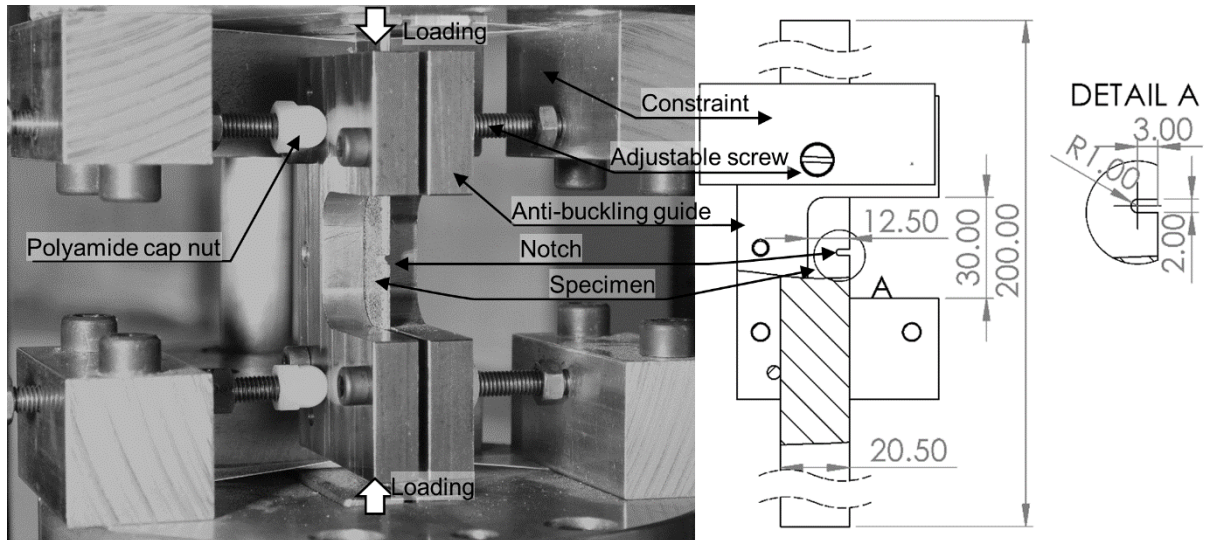


Figure 4-14 Compression-compression set-up with notched specimen

In pre-trials on specimens of the PC-CF, it was also tested if off-axis loading might initiate a more stable kink band growth at lower loads. For these configurations, it was found that off-axis specimens tend to buckle prematurely. By triggering a high-speed camera at the moment of specimen failure during the load increase test, it was found the macroscopic failure remains sudden and catastrophic despite slight off-axis loading. Also slanted notches might prove useful to avoid longitudinal shear splits as suggested by Bažant et al. [159]. However, this modification of the specimens was not pursued because determining the notch angle necessitates pre-trials. This was not feasible, as the necessary notch angle may need to be redefined due to the altered polymer properties after irradiation treatment.

5 Experimental results

5.1 Neat polymer characterization

5.1.1 Quasi-static characterization

The effect of irradiation treatment is visible in the stress-strain response of both materials, as shown in Figure 5-1. Strain is measured by DIC up to the yield point and from there on the crosshead displacement is used as strain source because necking peels off the paint used for DIC. For irradiated PC, yielding starts earlier and the maximum yield stress decreased by 9% compared to the non-irradiated configuration. Strain at break is for both configurations high, with slightly higher values for non-irradiated PC. The elastic modulus is not significantly affected by irradiation exposure. In contrast to this EP shows an increasing tensile modulus after irradiation treatment as well as increasing yield stress. Overall stiffening and a less ductile material response can be observed with decreasing strain at break from 7 to 5% after irradiation treatment for EP, as shown in Figure 5-1. Elastic constants and yield stress are summarized in Table 5-1. It is noteworthy, that despite literature predicting deteriorating properties of bisphenol-A-based EP, yield strength and tensile modulus both increased.

Table 5-1 Tensile properties of neat polymers in both configurations; Bracketed values give the bounds of the 95% confidence interval

	Tensile modulus in MPa	Poisson ratio in 1	Max stress in MPa	Strain at break in %
PC 0 kGy	2672 [2398;2947]	0.42 [0.25;0.58]	56 [56;57]	36 [16;57]
PC 200 kGy	2715 [2371;3059]	0.48 [0.37;0.60]	51 [50;52]	19 [13;25]
EP 0 kGy	2699 [2573;2826]	0.40 [0.27;0.52]	60 [59;61]	7 [6;8]
EP 500 kGy	3169 [2998;3340]	0.40 [0.35;0.45]	63 [63;63]	5 [5;6]

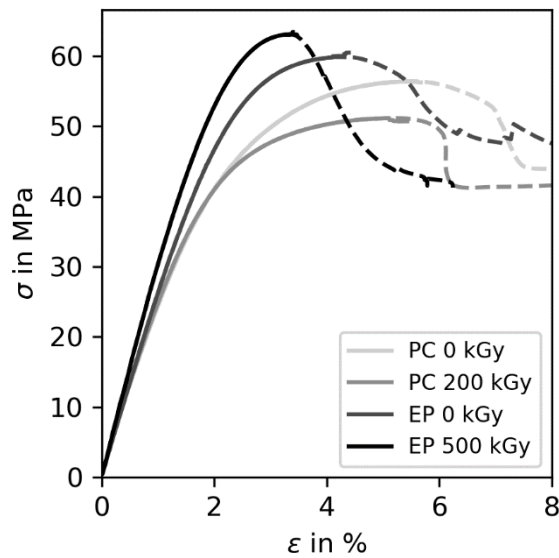


Figure 5-1 Mean stress-strain response of both materials in both irradiated and non-irradiated configuration; Dashed extension is the strain evaluated via cross-head displacement

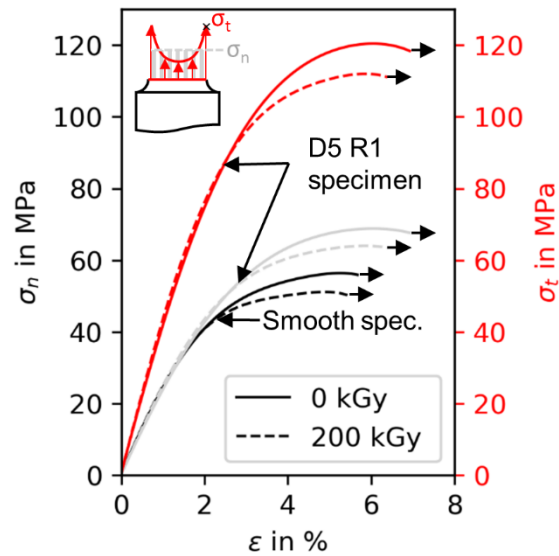


Figure 5-2 Stress-strain curves for notched (nominal stress σ_n , stress peak σ_t) and smooth PC specimens

5.1.2 Influence of triaxial loading

Figure 5-2 compares the response of a notched specimen with higher triaxiality to that of smooth specimens. Notched specimens show a generally stiffer stress strain response. This might in part be caused by the fact that the strain within the notch is not measurable optically and had to be approximated by a virtual extensometer of a measuring length of 3 mm reaching across the notch. Consequently, strains at the root of the notch may in fact be slightly higher for a given stress. In addition to the nominal stress, the theoretical stress peak is shown in Figure 5-2 with a stress concentration factor of 1.75 given by Peterson [92]. From the experiments, it is not possible to identify the location of yielding clearly. This poses a problem because the FE-results presented in Figure 4-3 during specimen design suggest not only varying stresses throughout the specimen's cross-section but also in terms of triaxiality. Therefore, the light gray curves could be taken as conservative stress-strain responses with an average triaxiality of 0.56 corresponding to the averaged nominal stress σ_n . The true response could be higher between the red and light gray curves depending on the location of yielding at a triaxiality between 0.44 and 0.60. The stiffer response is in agreement with the findings of Asp et al. [77] for epoxy resins. The relationship between the irradiated and non-irradiated PC remains similar for both specimen types. However, in the case of irradiated PC 40% of the specimens failed before any yielding took place.

Embrittlement and an increasing yield strength for higher triaxiality ratios is in agreement with the findings of Tiejun et al. [74].

5.1.3 Rheological characterization

5.1.3.1 DMTA

In order to compare morphological changes after irradiation treatment to literature reports, a temperature sweep seems appropriate to detect irradiation-induced changes in the glass transition temperature and in the case of EP the molecular weight between cross-links. A single cantilever beam set-up is used for this purpose. The temperature range investigated is -130-250°C for EP. Excessive softening limits the temperature range for PC to 180°C. A loading frequency of 1 Hz is chosen for the sweep. In terms of glass transition temperature T_g only a minor drop from 142 to 140°C can be observed for irradiated PC. For EP, however, T_g drops from 73°C to 63°C after exposing the material to 500 kGy. This already hints at molecular changes. Further calculation of the molecular weight between cross-links for the epoxy resin reinforces this because it increases from 858 to 1690 g/mol after irradiation treatment (Eq. 3-7). Therefore, the cross-linking density decreases as a result of irradiation exposure. These weights are comparable to the ones reported by [114], [168].

5.1.3.2 TTS relaxation experiments

For both EP configurations, the time range covered by the master relaxation curve slightly smaller compared to the one of PC. In total, three specimens per configuration were tested. To form a shared master curve, all data points were combined into one set after individually shifting the relaxation curves to form a specimen-specific master curve. Figure 5-3 gives the relaxation modulus of the fitted Wichert elements in relation to the measured data points of the master curve. It can be seen that the overall response is reasonably covered, even though some unsteadiness is visible with increasing time. These dents could be avoided by using more Maxwell elements, at the cost of increasing the number of fitting and modelling parameters.

Irradiation leads for both materials to slightly shifted master curves, which run mainly in parallel. Comparing both materials, the results suggest faster relaxation for the EP specimens in the time range investigated. Given that EP is a highly cross-linked material, this finding was unexpected, as higher relaxation was anticipated in PC. It

was verified that the temperatures used to generate the master curve for EP up to 10^5 s do not contain data from measuring temperatures near T_g .

The fitted model parameters are verified against the elastic modulus determined by the quasi-static tensile tests, due to the fundamental role of the Wichert model and its material response for section 6. Beforehand it was verified that the strain rates of the quasi-static tensile test are in accordance with the testing standard and are approximately 1%/min. With this, the elastic modulus of the Wichert model is calculated under constant strain rate. Table 5-2 presents a direct comparison of the elastic moduli from the Wichert model compared to the quasi-static results. Except for irradiated PC, the observed agreement is deemed satisfactory. High scattering observed for irradiated PC might explain some of the difference between the Wichert model prediction and the quasi-static result. More importantly, the relationship between irradiated and non-irradiated EP remains consistent. This is considered to be of greater importance because for EP, the quasi-static characterization revealed variations in elastic modulus, whereas for PC, it is mostly unchanged with significant uncertainties, due to high scattering.

Table 5-2 Comparison of tensile moduli calculated with the Wichert model compared to the quasi-static tensile tests

	Tensile modulus tensile test	Tensile modulus Wichert model	Relative modulus $\frac{E_{Model}}{E_{Charc.}}$
	in MPa	in MPa	in %
PC 0 kGy	2672	2453	92
PC 200 kGy	2715	2248	83
EP 0 kGy	2699	2933	109
EP 500 kGy	3169	3229	102

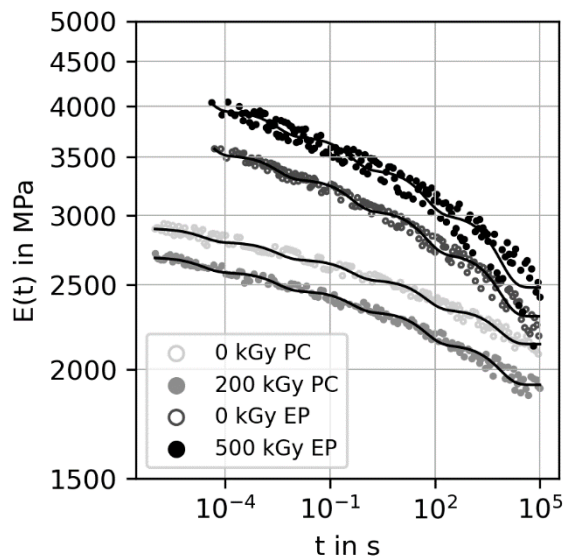


Figure 5-3 Relaxation modulus as a function of time with the fitted Wichert model response for both materials and both configurations; Only every 10th data point is shown for better visualization

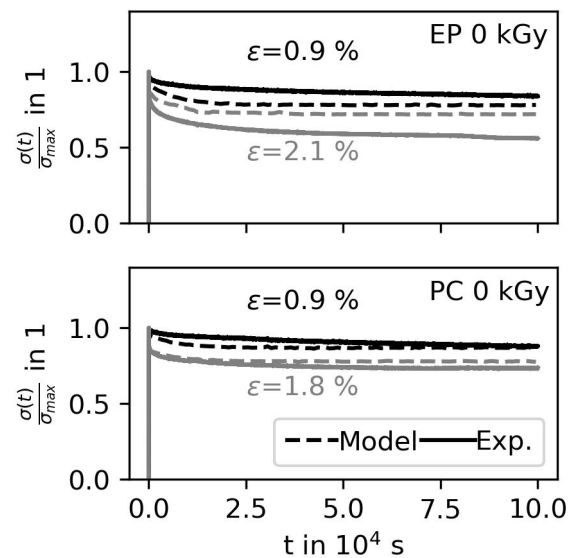


Figure 5-4 Comparison of the relaxation behavior at low strains in a TTS relaxation experiment and an actual relaxation experiment at higher strains

5.1.3.3 Relaxation experiments

TTS relaxation experiments focus on the visco-elastic response, as they target small strains and strain recovery is used as quality control prohibiting plastic deformation. Conventional relaxation experiments at higher strains, on the other hand, provide a combined response of visco-elastic and visco-plastic material behavior. This needs to be considered when comparing the relaxation behavior from both types of test. Still, a comparison seems worthwhile because plastic effects might show up by a deviation between both experimental datasets. A major challenge in this regard is the load application for relaxation experiments at high strains. Even though strain loads are applied rapidly in under 10 s and often even faster, it typically takes an additional 10 to 30 s seconds until a stable strain level is reached. Therefore, a direct comparison between the Wichert model calibrated from the TTS relaxation data and the actual relaxation data for each specimen needs to account for this and no idealized step response can be used as reference. Figure 5-4 shows a comparison between stress relaxations observed experimentally and the theoretical response calculated with the calibrated Wichert model. For the latter, the actual strain signal of the experimental data is used as strain input. Because the signals of individual specimens are

normalized to the first stress peak, the Wichert model response should be identical within one material. The fact that they are not is caused by differences in experimental strain application between the specimens. This means that for each specimen, deviations in the strain rate can occur, emphasizing the necessity to use the actual experimental strains as model input. The Wichert model overpredicts the experimental stress relaxation at low strains, as shown in Figure 5-4. For longer loading and high strains, however, it can be seen that the experiment will produce consistently higher stress relaxation or tends towards this trend. This reversal could either be a visco-plastic or non-linear visco-elastic material response not captured in the linear Wichert model. Additional indication for this is found across all materials and configurations by the generally higher relaxation speed with increasing applied strain shown in Figure 5-5. Overall, the conventional relaxation experiments confirm that epoxy resin in both configuration relaxes more within 10^5 s and in addition show that relaxation is a function of applied strain.

A specific feature was observed for PC. For this material, high strain levels could not be tested after irradiation treatment because the specimens fractured prematurely. This aspect shows that for the special case of inhomogeneous polymer deformation, not all strain-time points exist, just like for creep loading, high stress levels will lead to rapidly failing specimens, i.e., some stress-time points do not exist. This is somewhat contrary to the expectations based on the arguments of Haupt [42], [196]. In-situ microscopic observation of polished PC specimens with indirect lighting, however, showed that crazes form and grow as a function of time. Therefore, preliminary failure of the irradiated PC specimens might point toward less stable crazing, which transitions earlier into a crack. This is in agreement with the works of Pitman and coworkers, who found irradiation treatment leads to lower molecular weights and thereby increased crack propagation rates [108], [123]. Crazing shows that at least part of the faster relaxation with increasing strain level can be attributed to visco-plasticity instead of non-linear visco-elastic effects.

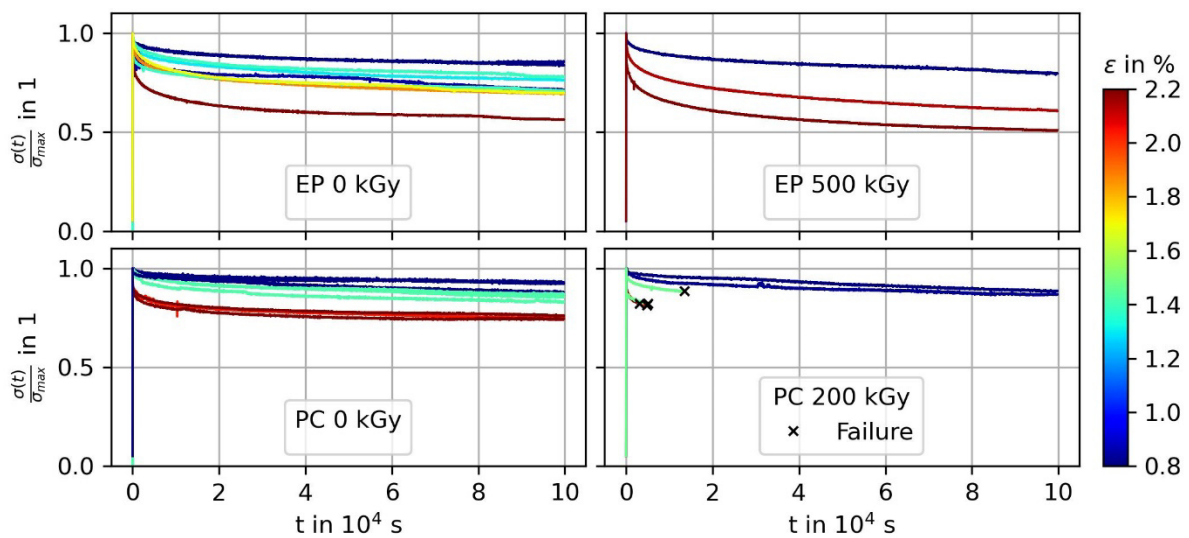


Figure 5-5 Relaxation behavior for different strain levels up to 10^5 s (27.8 h)

An evaluation of the strain recovery after the relaxation experiment also indicates a more significant influence of visco-plastic relaxation because non-recoverable strain is a function of the applied load. Figure 5-6 depicts the residual strain as a function of applied strain for a 52 h relaxation experiment (fixed strain) and 10 h period without loading (zero stress). This subsequent unloading phase yields an asymptotic material response converging towards the shown residual strains. Although the number of data points for different strains is limited especially in the irradiated configuration, a linear relation captures the residual strain well. If the linear regression is extrapolated to zero, residual strain and plastic effects might arise as early as 0.6 and 0.8% for PC and EP respectively for the non-irradiated configuration. Irradiated PC could not be evaluated in this way, due to preemptive failure. Except for crazing in PC, no obvious visual references to the onset of visco-plastic deformation is visible.

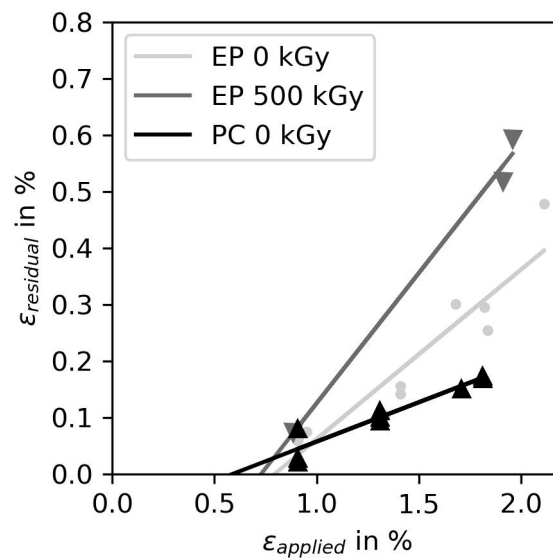


Figure 5-6 Residual strains after 10 h of unloading after 52 h of relaxation as a function of applied strain during relaxation

5.1.3.4 Irradiation induced relaxation

A detailed account of the effect of irradiation induced relaxation of residual stresses can be found in [197]. In the following, only the main findings will be summarized because residual stresses are known to affect local loading significantly. The stress optical set-up revealed a fringe pattern initially present across all configurations, even in the unloaded state. By saw cuts, it was found that this fringe pattern represents indeed residual stresses within PC, in contrast to EP, for which no clear source of the pattern could be identified. Only a correlation between the fringe pattern and surface dents was apparent. The dented surface is likely caused by uneven shrinkage of the plate in thickness direction. However, thickness variations as the reason for the fringe pattern could be discarded.

For both materials, these initial artifacts prevent a definite starting point with known stress. Therefore, it was decided to evaluate predominantly the gradient in principal stress difference instead of absolute stresses at any point. At the outset, the stress optical sensitivity was determined and found to decrease slightly for both materials (increase in fringe coefficient). All specimens kept under constant strain load were evaluated before and after 72 days of relaxation. This relaxation period was mainly dictated by organizational reasons¹. After the relaxation without irradiation exposure,

¹ Irradiation exposure is done externally and therefore specimens had to be packaged, transported and the allotted processing slot had to be met.

no relaxation could be detected by the stress optical set-up. A different result was found for specimens exposed to the same doses used throughout the work. Here, PC relaxed by 27% 95% CI [12; 41]² and EP by 36% 95% CI [27; 44]. At the same time, scattering in terms for relaxation increased for both materials by irradiation exposure. An increased scatter can be attributed to the irradiation treatment, since scattering is drastically lower for the non-irradiated specimens across both materials. Although the relaxation experiments are relatively susceptible to random changes, introduced by a greater number of handling steps (vacuum sealing, packaging and shipping), irradiation treatment is still most likely the source of scattering. This is because scattering is increased across most other mechanical properties as well. Without the latter observation, it would also be possible, though unlikely, that the strain loading of the specimen changed by slippage resulting from the handling steps.

5.1.4 Fatigue

Figure 5-7 and 5-8 show the S-N curves of smooth specimens and specimens notched with a hole of $\varnothing=0.5$ mm. For PC, a power law regression shows a lower absolute stress level but additionally also a decreased slope for unnotched specimens. In contrast to this, the EP specimens without a notch lead to nearly identical S-N curves for both dose settings. However, for both materials and both configurations (irradiated/non-irradiated) scattering is considerable. All data points shown failed inside the measuring length. For the case of PC, scattering might additionally be increased by the lifetime inversion reported within the literature [95]. A feature found across both polymers is that neither of the two materials show degradation in terms of stiffness degradation or hysteresis opening. Because this finding was somewhat unexpected, some additional tests for non-irradiated polymer showed that a very small hysteresis opening could be achieved by changing the load ratio ($R=0.1$) to include a mean stress. In that case, the hysteresis closed rapidly at the beginning of the test, which implies time-dependent effects or plasticity as cause and verified that a missing hysteresis is indeed a material property for $R=-1$. Comparing the smooth specimen results to the

² Confidence intervals are given following APA style recommendations [202]. The format is X 95% CI [LL,UL] with X being the mean value of the sample followed by the indication of the confidence level and the lower limit LL and upper limit UL; All confidence intervals are calculated under the assumption of random sample from a normal distribution with unknown variance [203]

notched specimens, a notch effect is visible for both materials in terms of nominal stress.

Table 5-3 gives the regression results for all configurations tested. With the formulae given by Peterson for a hole in a finite width thin element the stress concentration factor is calculated to $K_t=2.73$ for the given specimens. With the nominal stresses for smooth and notched specimens, it is possible to quantify the notch sensitivity for both materials. For all investigated materials, the notch sensitivity q in Eq. 3-4 is low on a scale from zero to one. Irradiation treatment of PC increases the notch sensitivity from near zero to 0.18 and thereby in the same range as EP.

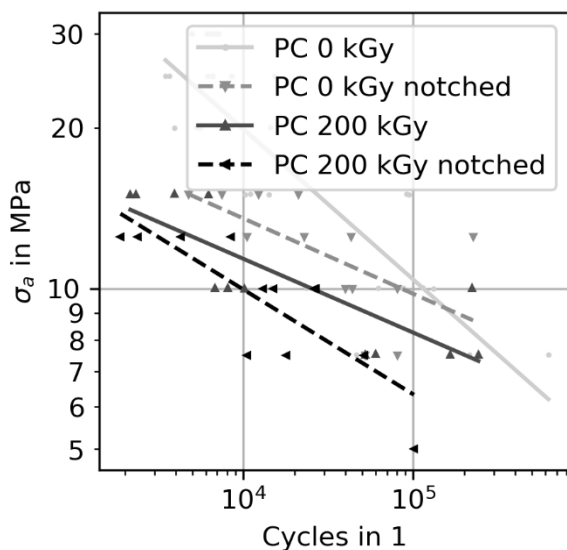


Figure 5-7 S-N curves of polycarbonate with and without a notch; The nominal stress amplitude is reported

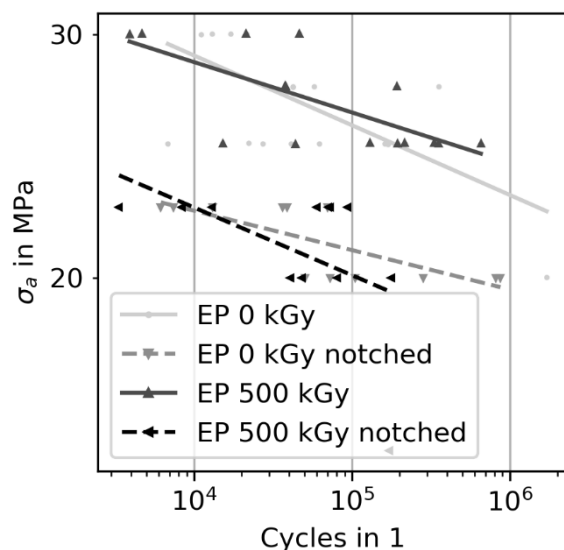


Figure 5-8 S-N curves of epoxy resin in different configurations with and without a notch; The nominal stress amplitude is reported

Table 5-3 Regression results for smooth and notched neat polymer samples

	Dose in kGy	Slope		Fatigue strength for 10 ⁵ cycles				
		Smooth	Notched	σ_{Smooth}	σ_{Notch}	$K_t \times \sigma_{Notch}$	$\frac{\sigma_{Notch}}{\sigma_{Smooth}}$	q in Eq. 3-4
EP	0	-0.050	-0.029	25.8	20.9	57.2	0.81	0.13
EP	500	-0.036	-0.049	26.3	20.1	54.8	0.76	0.18
PC	0	-0.282	-0.141	10.4	9.8	26.7	0.94	0.04
PC	200	-0.138	-0.196	8.3	6.3	17.3	0.77	0.18

However, all results shown above represent only the final specimen failure and therefore the last stage of the MSF-model. Fracture toughness and resistance to fatigue crack propagation is reportedly another important aspect and was documented for the notched specimens by the polarization set-up and continuous video recording.

The latter also limits the notched fatigue test to below 5×10^5 cycles. The crack tip is tracked from final failure backwards until no clearly identifiable crack tip is visible in the video. This information can be used to estimate the fatigue crack resistance during the small crack growth stage. To determine the stress intensities, tabulated β values reported by Waldman [204] are used. The β -factors are tabulated from numerical models for two collinear cracks propagating from a hole within a finite strip of material of a diameter to width ratio of 0.1. This is the case for the produced 1BA specimens. The data includes also differences in crack length if two cracks propagate simultaneously from the hole but with different speeds. The evaluation procedure starts by manually selecting the endpoints of one or two propagating cracks. Moving backwards manually (from final failure), a selection is done every 40 cycles or more if crack growth is very slow. By normalizing the crack length a to the hole radius r values for β can now be interpolated within the tables provided by Waldman [204]. However, since tabulated values for β are only available for $0.01 \leq \frac{a}{r} \leq 2$ the crack length used for evaluation is limited to this range. In addition, most specimens show one crack as dominantly propagating whereas the second crack progresses very slow or only near final fracture. Since the β -factors will depend on both lengths, it was decided to select a primary crack for evaluation based on Eq. 5-1. In other words, a slowly growing nearly stationary crack will also show increasing stress intensities if the opposite crack grows. These types of cracks are excluded from the evaluation. Here a_l and a_r denote the crack length left and right. By this criterion, a value near one will symbolize crack growth primarily for the right crack and vice versa for a value of -1. It was found that the mean value of l should be in the range of ± 0.8 to indicate simultaneous crack growth. If l exceeds the range the corresponding dominant crack was selected for the evaluation.

$$l = \frac{a_r(N) - a_l(N)}{a_r(N) + a_l(N)} \quad \text{Eq. 5-1}$$

Crack growth over the number of cycles is further fitted with a second order spline to represent the data reasonably well but avoids discontinuities. The resulting crack growth for PC and EP in both configurations is shown in Figure 5-9 and 5-10. From the results, it can be seen that scattering is significant, especially for PC. A slight tendency to a lower fatigue crack resistance for the irradiated configuration can be identified. A regression to the Paris power law description did not yield meaningful results, due to

scattering. A likely cause for large scattering might be found in the experimental set-up in combination with the discontinuous crack growth reported for PC. Indeed, for many specimens the crack appeared stationary at early stages of fatigue crack growth. In contrast to PC, crack growth was often limited to one dominant crack in epoxy resin specimens in both configurations. In terms of fatigue crack resistance, no difference between both configurations can be identified in Figure 5-10. However, during the manual crack labeling it became evident that especially irradiated epoxy shows markedly shorter periods of fatigue crack growth in terms of cracks length. From the common understanding that at the critical stress intensity, small crack growth will transition to rapid crack growth marked by the critical stress intensity, which in turn is related to the fracture toughness. Hence, the latter can be approximated from crack growth experiments. A critical stress intensity at the transition, could not be evaluated since the crack length is outside the tabulated values in Waldman [204]. It is assumed that under similar loads and geometry the crack length leading to unstable crack growth can also hint at the fracture toughness of the material. At least in terms of a relative comparison attempted here. Figure 5-11 shows the critical crack length leading to failure within one load cycle. EP shows a marked difference after irradiation treatment, whereas PC remains nearly unchanged. It is noteworthy that, for PC the crack sometimes grows nearly through the whole cross-section to one side of the hole before failure occurs. From the video recordings, it can be seen that plasticity plays a role during the late stages of fatigue growth. For some specimens, an initially unique crack plane appears as black line, which can later be accompanied by two additional lines above and below. That the initial black line is indeed a crack is verified by the stress optical set-up because it is surrounded by the kidney shaped fringe pattern. The additional lines forming at high crack length could be shear lips. Details in this regard are discussed further in the next section 5.1.5.

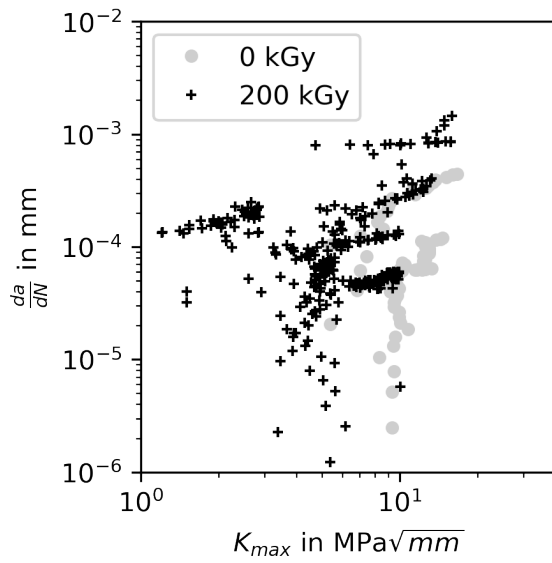


Figure 5-9 Crack growth rates for both PC configurations

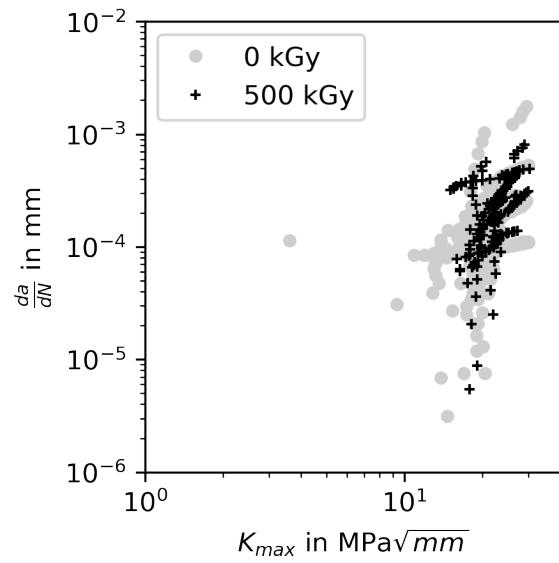


Figure 5-10 Crack growth rates for both EP configurations

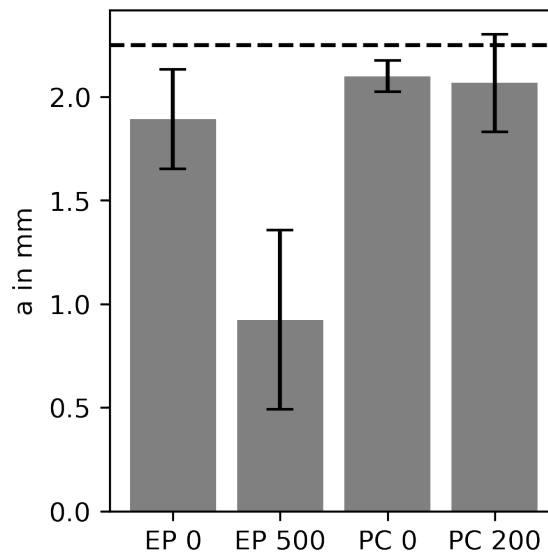


Figure 5-11 Critical crack length leading to failure within one load cycle; Error bars represent the 95% confidence interval; Dashed line represents maximum crack length limited by the specimen's width.

5.1.5 Fractography

Fracture surfaces are an established indicator for the active mechanisms during crack propagation. Therefore, all materials and configurations are analyzed in this respect. The studied specimens are fatigued smooth 1BA specimens, i.e. without a notch. The observed mechanisms are similar in both notched and plain specimens. Figure 5-12 shows representative examples for the fracture surfaces of the irradiated and non-

irradiated configuration for both materials. Both specimens were tested with an identical stress amplitude of 10 MPa.

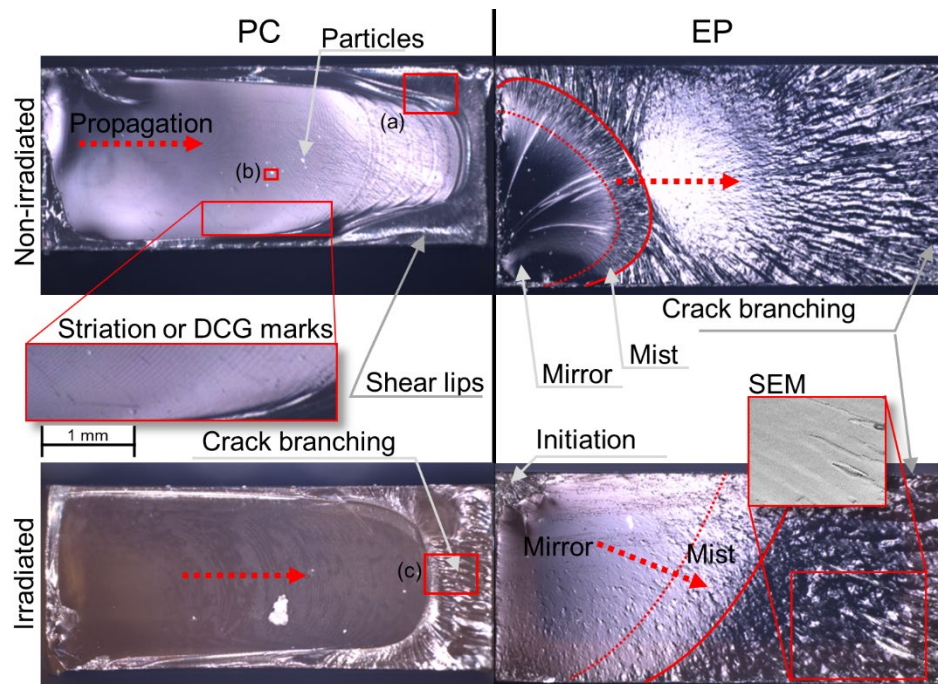


Figure 5-12 Fracture surfaces of the irradiated (PC 200 kGy/ EP 500 kGy) and non-irradiated samples after fatigue loading; Red lines for EP mark an area with identifiable crack arresting lines; Adapted from [19]

It becomes evident that especially near the end of crack propagation shear lips are present in PC. For non-irradiated PC the shear lips are larger and surround the whole area of fatigue crack propagation. Striation marks or DCG propagation marks are present in both PC configurations. Especially, the surface of final fracture and unstable crack propagation is vastly different (right side of specimens in Figure 5-12). For non-irradiated PC this surface is mainly smooth and looks like the rest of the shear lips surrounding the crack propagation zone. These features could be found across all non-irradiated specimens. In contrast, this region in irradiated PC exhibits a lamellar structure with larger ridges. This hints at a limited ability to shear flow and generally unstable shear bands during final fracture. G'Sell and Gopez [85] found similar features in shear loaded PC. Figure 5-14 (a) and (c) highlight this difference in final fracture by SEM imaging. From Figure 5-14 (c), it can further be seen that the ridges transform to a stack of sheets from left to right, which corresponds to the crack propagation direction. A close-up detail shown in Figure 5-14 (Detail c) reveals a striation like surface on top of the material sheets. Instead of fatigue striations, these marks are likely a result of additional disentanglement repeatedly breaking down. Both effects point towards less stable yielding and disentanglement of irradiated PC. In addition,

unmolten particles can be found within the fracture surfaces (b) in Figure 5-12 and Figure 5-14. This is similar to the finding of Hughes et al. [39]. No correlation between the number of particles within the fracture surfaces and fatigue life rank could be found. However, a clear correlation between the applied stress amplitude and the resulting size of the fatigue fracture surface could be identified (Figure 5-13). No difference between both irradiation configurations was found, which aligns with the findings on the fatigue crack propagation.

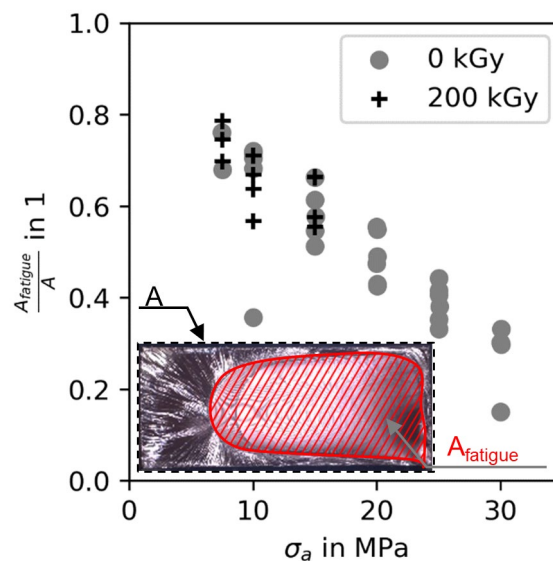


Figure 5-13 Ratio of fatigue fracture surface to total fracture surface as a function of applied stress amplitude of fatigue tested PC

Because several fatigue specimens also show craze like features some distance away from the final fracture zone, this factor is investigated separately. To verify that these are indeed crazes and not small cracks, in-situ observation under constant strain load is deemed appropriate. This seems necessary because after unloading, it is likely that crack fronts or crazes close, due to the elastic material surrounding the craze or crack. However, only non-irradiated specimens could be investigated in this way because irradiated specimens fracture before showing multiple crazed regions. With the aim of documenting crazes in a loaded state, bending specimens ($80 \times 10 \times 2$ mm³) are placed in a 3D-printed fixture that secures them in a bent shape with a defined radius, as illustrated in Figure 5-15 (top left). The radius is directly related to the strain in the extreme fiber. It can be seen in the left column of Figure 5-15 (a, d and e) that under 1.5% strain a fibrillar structure extends from the crack fronts. Detail (d) shows the craze morphology just before breakdown. In contrast to multiple small crazes and cracks in the 1.5% specimen, a load of approximately 4% leads to larger cracks and only very

sparsely distributed fibrillar structures. Instead, the highly strained region shows some cracks with relatively featureless crack surfaces. The only exceptions found are shown in the right-hand column of Figure 5-15 (b, c and f). Detail (b) shows a lamellar surface similar to the one observed from the top in the final fracture surface of irradiated PC. Detail (f) is a higher magnified image of the fracture surface visible in (c). Viewed with lower magnification, a mainly brittle failure is suggested. However, the close-up shows that the surface also bares signs of disentanglement. From these observations, it can be concluded that at higher strain levels localized softening leads to higher strain rates, which prevents extended disentanglement and therefore crazes transition directly to cracks.

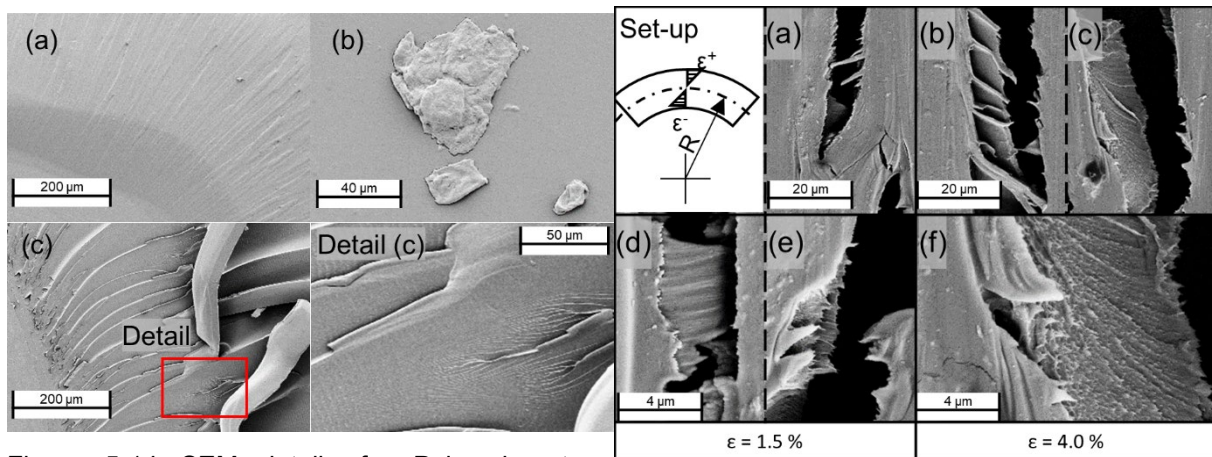


Figure 5-14 SEM details for Polycarbonate; Positions according to macroscopic images of Figure 5-12

Figure 5-15 Crazing in Polycarbonate for different strain levels; Scanned in-situ under load

As already suggested by the literature, no striation marks can be found in both EP configurations. However, the mirror zone is significantly smaller for irradiated epoxy specimens. According to Plangsangmas et al. [168] a smaller mirror and mist region translates to a lower fracture toughness of the material. To quantify this observation, the mirror region is measured by fitting a circle through the transition zone. Because the mist region is not always uniquely identifiable, only the mirror region size is evaluated. The mirror zone radius for irradiated specimens is 0.62 mm 95% CI [0.52; 0.72] and for non-irradiated EP 1.60 mm 95% CI [1.54; 1.66]. With Eq. 3-6 it is possible to calculate the critical stress intensity K_{IC} taking the stress amplitude for each specimen as input parameter for the fracture stress. The resulting fracture toughness is 0.8 MPa \times m^{0.5} 95% CI [0.75; 0.85] for irradiated epoxy resin and 1.4 MPa \times m^{0.5} 95% CI [1.32; 1.42] for the non-irradiated configuration. This calculation is an extension of the one performed by [168] and assumes that long crack growth starts after

transitioning from the mirror surface and that the end of small crack growth converges towards the material's fracture toughness.

In light-microscopic images, the region of unstable crack growth appears very rough. However, SEM images show that this is not true. The main difference between both imaging techniques is that the transparency of the specimens allows for the identification of sub surface cleavages and cracks. Therefore, it is likely that the crack front leads to numerous blunts during propagation mainly visible by reflections in light-microscopic fractography. This appears to be especially relevant for cracks in quasi-statically loaded specimens in Figure 5-16. In this case, the apparent roughness and three-dimensionality of cracked and blunted zones persists only in the irradiated specimens, but is not present in the pristine configuration. Cantwell et al. [167] found the same effect by increased testing temperatures, where higher temperatures lead to a smoother appearance of the fracture surface. With this observation, it could be stated that plasticity after irradiation treatment is also limited to small regions, which leads to repeated reorientation and blunting of the crack.

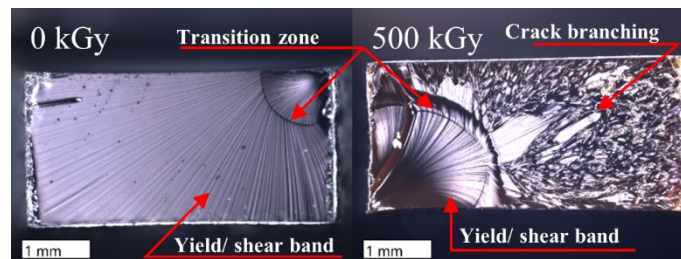


Figure 5-16 Quasi-static fracture surfaces of epoxy samples for 0 and 500 kGy; Adapted from [19]

5.2 Laminate fatigue characterization in tension-tension loading

5.2.1 Crack observation and in-situ evaluation

5.2.1.1 PC-CF

An unintended common feature across all PC-CF plates in this work is the presence of some transverse cracks before any mechanical testing. The source of these cracks could not be fully clarified. However, specimen preparation could be excluded as the source. DIC applied to in-situ images shows that most additional cracking occurs in the interactive regime, although DIC strain evaluation is hindered by the relatively low applied strains. Another feature, which became evident, is that within single rovings areas with bad fiber impregnation or dry spots exist. Polishing of the edges was the only method that clearly revealed of this feature, as non-impregnated fibers broke out.

In high-resolution x-ray microscopy (Zeiss Xradia 520 Versa, scans; 1 μm voxel size) dry spots are barely discernible presumably, due to the locally increased fiber volume content. The in-situ images show that in both configurations (irradiated and non-irradiated) significant cracking is present during the first loading ramp. A more detailed discussion of the ply and sub-ply stresses will be given in section 7 from the FE-analysis. A common feature across all specimens is that numerous small cracks formed mainly from and around dry spots as shown in Figure 5-17. Although no obvious influence of irradiation treatment on the crack growth could be observed, a difference in crack density as a function of maximum applied laminate stress becomes evident. In Figure 5-18 it can be seen that for the irradiated configuration the crack density is slightly higher for all stress levels tested. Another interesting feature is that the difference in crack density seems to vanish with increasing load and is more prominent at low stress levels. An additional feature, which revealed itself only from the acquired data during fatigue testing, is a possible difference in crack density before any mechanical loading. Therefore, irradiation treatment remains as singular difference between both groups of specimens. The dashed lines in Figure 5-18 show the basic crack density of PC-CF in both configurations before mechanical loading. This basic damage state is determined from additional microsections of plate material in both irradiation conditions, before any mechanical loading. In terms of the predicted crack saturation density (Eq. 3-1) of 0.95 mm^{-1} this is a significant pre-damage. Still, it is important to note that most specimens reach crack densities well above the prediction.

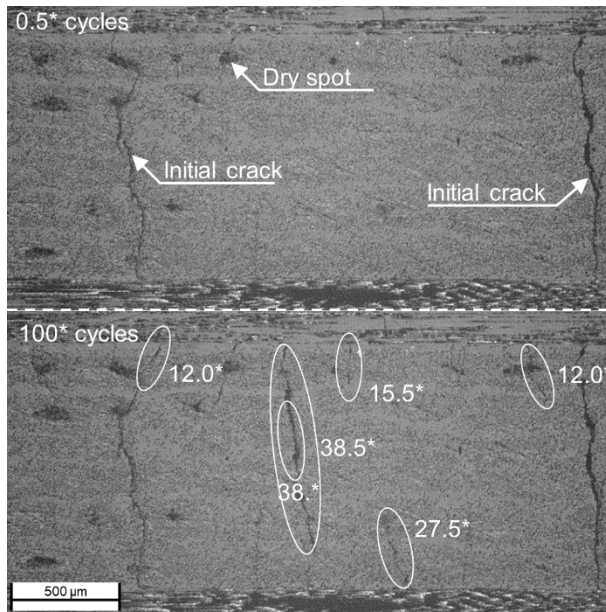


Figure 5-17 Example of crack initiation sites and crack growth in PC-CF irradiated configuration loaded with $\sigma_{max}=60$ MPa; * in thousand cycles

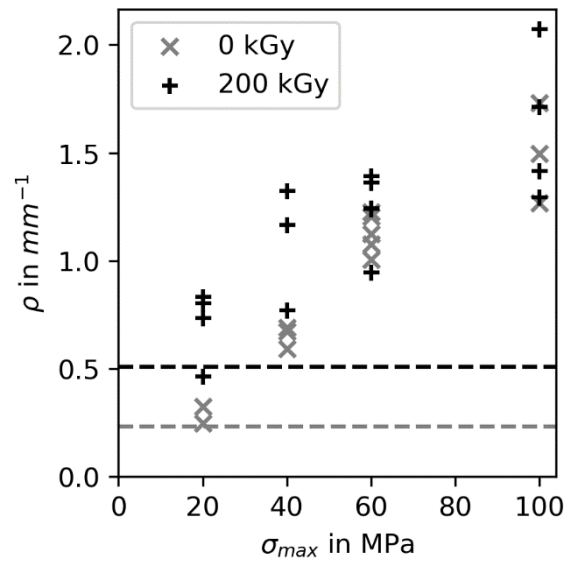


Figure 5-18 Crack density after fatigue loading; Dashed lines show different base levels of transverse cracking before mechanical loading

5.2.1.2 EP-CF

EP-CF plates show a good impregnation and no pre-cracking. In contrast to PC-CF, no apparent cracking can be observed during the first loading ramp. During cyclic loading, crack growth can be observed directly within the in-situ image and indirectly by changes in the strain field. For both configurations, crack growth emanates frequently from stitching fibers and the crack spans the whole ply thickness within approximately 500-1000 cycles. Higher magnified images taken on separate microsections after the fatigue test reveal the crack to be a set of interconnected debonds propagating along the interfaces of the stitching fibers and the epoxy matrix, as shown in Figure 5-19. Polyester fibers are used for stitching in the NCF. The strain analyzed in the video recorded during the first loading ramp indicates regions with stitching fibers as highly strained areas. A more detailed investigation of this phenomenon reveals that first debonds within the stitching fibers develop during the initial loading cycle. A distinction between strain concentrations from spatially varying elastic moduli and debonding is possible based on local strain-time signals because crack onset leads to jumps in the signal. The strain level to introduce these strain jumps is approximately 0.5 to 0.6% across both configurations. More details on the method can be found in [199]. The available strain-time points before local crack onset are further used to calculate K_{ϵ} for areas containing stitching fibers in both configurations.

The number of points, which can be evaluated in this way varies from specimen to specimen. K_ε is slightly higher for the irradiated configuration with 1.31 95% CI [1.22; 1.41] compared to 1.16 95% CI [1.06; 1.26]. It is interesting to note that for both materials K_ε can reach values of up to 1.6. Especially high strain peaks can be found for extended areas containing stitching fibers. Figure 5-19 shows a top view of the dry carbon NCF, with larger areas of connected stitching in the load path, primarily found at the intersections where top and bottom stitching fibers interlace. The orientation of the stitching fibers with respect to the plane of the microsection can be estimated by the shape. Within the blue colored area the stitching fibers appear elongated, whereas in the red area a more circular shape can be seen. These two orientations can only be found within a single ply at the intersections of the tricot stitching. From these observations, it can be summarized that damage is initiated often during the first loading by debonding between the polyester fibers and the epoxy matrix. Foremost in areas where stitching is directly part of the load path. From the in-situ strain map, these regions show higher strain localization.

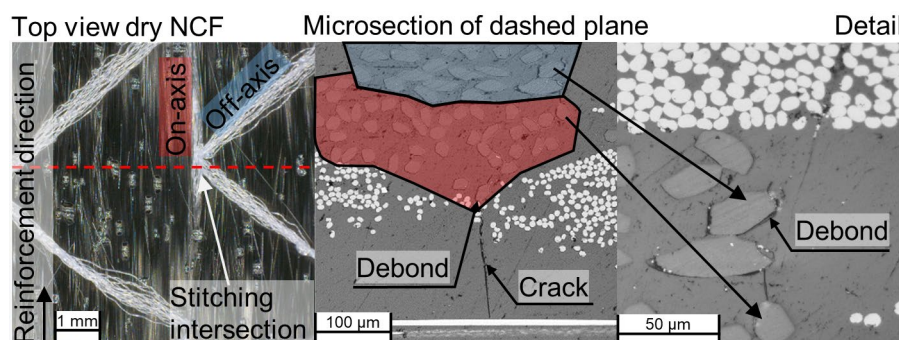


Figure 5-19 Debonding and crack initiation within stitching fibers (Dashed red line in left image marks exemplary a possible plane of the microsections seen in images to the right)

If cracks form in an interactive or non-interactive regime can also be verified on a crack-by-crack basis with the available strain data. As shown in Figure 5-20, a low strain region exists to the right of the crack (named 2nd crack) after loading the specimen for 10^5 cycles. The low strain region extends along the specimen axis. To verify the position of the next crack the stitched microscopic images can be used. As shown in Figure 5-20, the next crack is approximately 3.1 mm to the right of the 2nd crack. To determine when the 1st crack formed, strains in ε_{22} are evaluated along the vertical lines marked in Figure 5-20 for each image taken between the fatigue blocks. Up to the 14,500 cycles the strains are homogenous and do not vary over the ply thickness (vertical axis in Figure 5-20). Figure 5-21 compares ε_{22} for different cycles after inhomogeneity

becomes evident. As can be seen from the strain profiles after 15,000 cycles the 2nd crack forms still in the non-interactive regime because the strain perturbations do not reach the crack initiation site. Instead, the transverse ply is fully loaded again after approximately 1.9 mm. After 38,500 cycles when both cracks coexist stresses cannot be reintroduced fully into the material. This kind of evaluation shows the relevance of neighboring cracks for the local stress state within the observation area and needs to be considered within the FE model in section 6.

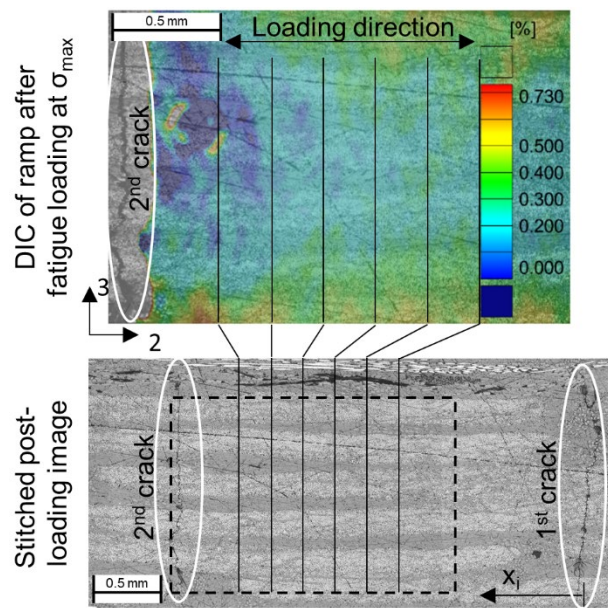


Figure 5-20 Strains evaluated by DIC based on in-situ microscopic images

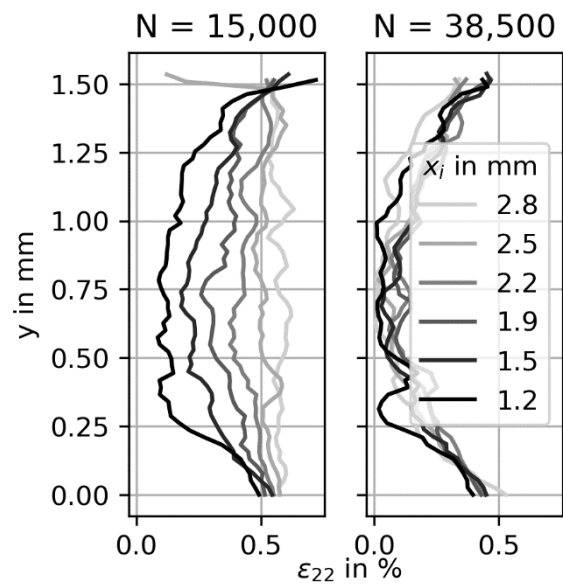


Figure 5-21 Evaluation lines at different positions relative to the 1st crack in Figure 5-20

A problem encountered during testing is that the maximum stress corridor (choice for σ_{max}) necessary to introduce transverse cracks within 10^5 cycles is relatively narrow because high stress levels sometimes lead to failure within the clamps and for lower stresses no cracks develop. As common load level for a comparison between the irradiated and non-irradiated EP-CF laminates $\sigma_{max}=180$ MPa maximum stress is used. Figure 5-22 shows the crack density for both configurations. From these results, it becomes evident that some specimens in the irradiated configuration show very low crack densities or no cracks. Similar to the neat polymer characterization scattering also increases due to the irradiation treatment. It could be argued that for low crack densities, the analyzed length (22 mm) might be prone to error. To test this argument the crack density was correlated to the stiffness degradation and the results agreed well as will be shown in section 5.2.2. The experimental crack densities are slightly below or at the prediction for the saturated crack density of 0.67 mm^{-1} for this laminate (Eq. 3-1).

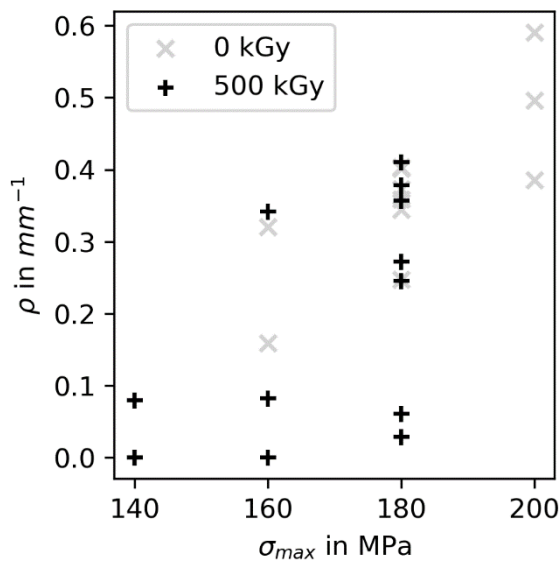


Figure 5-22 Crack density of EP-CF after fatigue loading

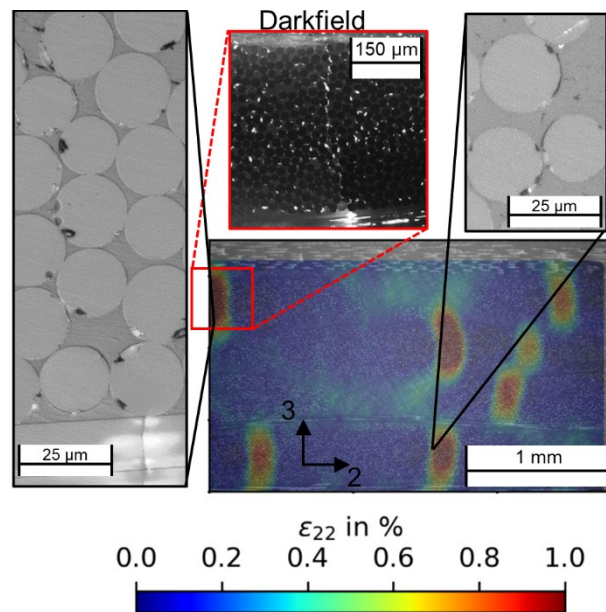


Figure 5-23 Strain map and corresponding cracks with higher magnification specifically prepared microsections (plane difference 0.7 mm in width direction of the specimen)

5.2.1.3 EP-GF

In addition to edge observation, the light transmission technique is used for EP-GF specimens. As this has been proven a successful method for identifying transverse cracks and also delaminations [28], [51], [59]. As a result, not only crack propagation through the thickness of the specimen becomes visible but also across the width. Due to the limited number of specimens available for this type of reinforcement, only three to four specimens were tested with a maximum stress of $\sigma_{max}=50$ MPa. Unlike EP-CF specimens, cracking is visible during the first loading ramp, mainly for non-irradiated specimens. For the irradiated specimens however, no cracking can be observed in the first loading cycle. Another difference to EP-CF is the types of cracks forming. Instead of a single crack, spanning the transverse plies completely, multiple cracks form within fiber bundles as shown in Figure 5-23 by the strain map at maximum load. In contrast to the cracks present in both carbon fiber-reinforced plastics (CFRP), cracks are only visible by the strain concentration but not by the crack opening. This is caused in part by low strains to onset transverse cracking, in the range of 0.2-0.3%. In addition, unintended preparation artifacts exist and obscure the cracks further. To verify that preparation quality is not the main cause for hardly visible cracks, additional microsections are cut from the specimen and prepared separately. Although cracks are still hardly visible, connected debonds could be identified at locations of high strain,

as shown in Figure 5-23. It must be noted that the viewing plane and the former specimen edge are offset by 0.7 mm, due to preparation of the microsection by grinding and polishing. Additional strain hot spots can be identified from the strain maps not related to cracking or debonding but correlated to resin pockets. This aspect can be attributed to the size of the resin pockets and the stiffer fiber bundles, which results from the higher transverse fiber stiffness of E-glass compared to that of HT carbon fibers. Although crack densities could not safely be evaluated due to low visibility of existing cracks, the strain hot spots suggest a crack spacing much below 1.3 mm predicted for the saturated crack density by Eq. 3-1.

The existence of multiple cracks within the in-situ observation area and because crack initiation takes place within the fiber bundles instead of the stitching fibers makes an evaluation of the local crack onset strain and number of cycles a valuable objective for the comparison of both EP-GF irradiation configurations. In contrast to the carbon fiber-reinforced epoxy laminates, the structure is also coarser and the facet size in DIC is small enough not to overlap fiber bundles and resin pockets.

Two cases are considered for this analysis: cracking during the first ramp and cracking during fatigue loading. For cracking during the first loading ramp the corrected strain at the cracking site just before crack initiation can be used and gives a measure for the static strength of the transverse ply. The local strain-time signal is used to identify crack onset clearly. As shown in Figure 5-24 crack onset shows up as jumps in the strain-time signal. For the case of crack formation during fatigue loading, it is possible to record the crack onset with a resolution of 500 cycles, as indicated by the error bars in Figure 5-25. Again, the video before fatigue loading is used to evaluate the onset strain, because of the limitations present for the images taken during fatigue loading. This time however, the strain at peak load is used. This evaluation procedure is therefore a slight compromise, because local strains at the cracking site could be affected by already existing neighboring cracks. The last step to generate the S-N curve is the determination of the fiber volume content within the fiber bundles. For the glass-fiber reinforcement, the resulting fiber volume content within the rovings is relatively homogeneous and therefore taken as constant with 60%. The resulting transverse modulus for both configurations is then calculated from the constituent properties. Figure 5-25 shows the calculated stresses and the number of cycles for both configurations to onset cracking. Delayed cracking is clearly visible for the irradiated

configuration. Although these first coalesced debonds appear at relatively low stress and strain levels, it is important to note that crack growth is stopped in most cases and doesn't leave the transverse ply. Additional confirmation for crack onset at these low strains can be found by the light transmission images. The dotted line in Figure 5-24 marks crack onset in the light transmission images. The delayed transverse cracking in the irradiated configuration is also confirmed.

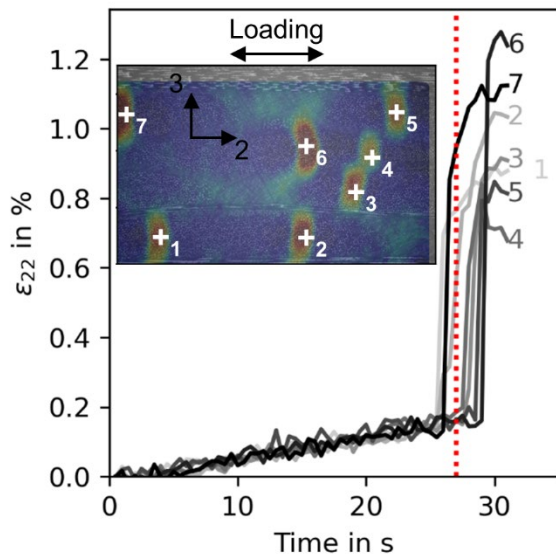


Figure 5-24 Local strains at cracking sites during the first loading ramp (only the ascending part of the ramp is shown); Dotted line marks visual crack onset from light transmission images

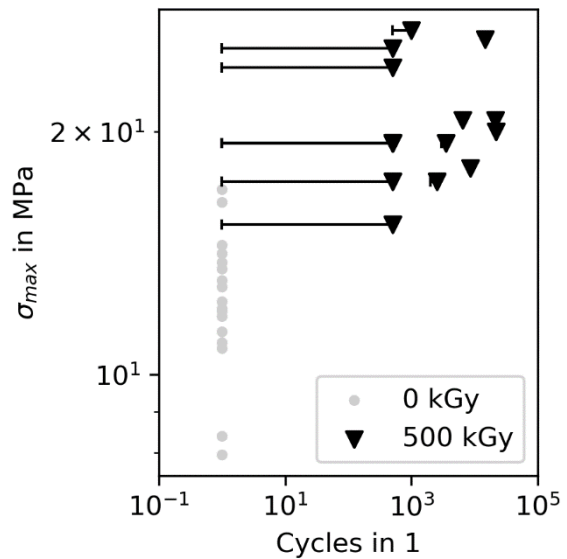


Figure 5-25 In-situ S-N curve estimated from strains recorded during first loading ramp

5.2.2 Scalar damage parameters on the macro scale

5.2.2.1 PC-CF

In many specimens of PC-CF, edge observation showed that a significant amount of damage forms within the first loading cycle. Fatigue loading then contributes mainly to the growth of existing cracks or introduce secondary cracks. Therefore, it would be expected that the semi-continuous modulus reduces with increasing applied load during the first loading ramp. To test this, the modulus is analyzed for both configurations. Figure 5-26 shows the modulus before and after fatigue loading in terms of mean curves for easier interpretation. In order to use all available data points, the continuous modulus is determined for the individual specimens. Data points are then normalized to the initial modulus value E_0 . All strain-stiffness points are then fitted by a single polynomial regression. Due to scattering in the individual stress-strain

curves, the overall coefficient of determination is relatively low, especially for fitting the ramp before the fatigue block. Figure 5-27 shows the individual polynomial fits to the data points per specimen and demonstrates that a second order polynomial is generally able to capture the response. The mean stiffness-strain response described by a second order polynomial was deemed best to represent all specimens by a single regression despite differences in applied maximum load.

In terms of these mean curves, it becomes evident that for both configurations stiffness in the loading ramp before the fatigue block initially declines. For non-irradiated specimens this decline seems to reverse with increasing strain, whereas for the irradiated configuration it appears to level out near the maximum applied strain. These changes in stiffness as a function of applied strain are likely caused by two contradicting effects, namely alignment of the specimen or fibers and formation of damage. That alignment might play a role becomes evident from the fact that for many specimens a lateral movement can be seen in the in-situ microscope's video recordings. Here, the specimen moves in the thickness direction perpendicular to the specimen's axis. If the specimen's lateral movement is restricted, however, the movement observed in the video recording also reduces. This proves that the lateral movement is not caused by some asymmetries in the pantograph guiding the microscope but are instead related to the specimen or the load introduction by wedged clamps. The alignment effect persists over all ramps recorded for both configurations. At this point, it must also be noted that the alignment effect is only visible through the semi-continuous modulus and is not noticeable in stress-strain plots. More importantly, the initial drop in modulus is not present in the ramps after the fatigue block, which suggests that this effect is indeed related to the damage forming during the first loading ramp as seen in the in-situ recordings. To avoid confusion, it must be noted that the reference E_0 corresponds to the individual loading ramps before and after. An increasing crack density correlated to a lower stiffness is in agreement with the literature [48], [54], [55], [59]. If alignment effects are assumed identical for both configurations, this suggests that the initial damage in the first loading ramp is more pronounced for the irradiated configuration.

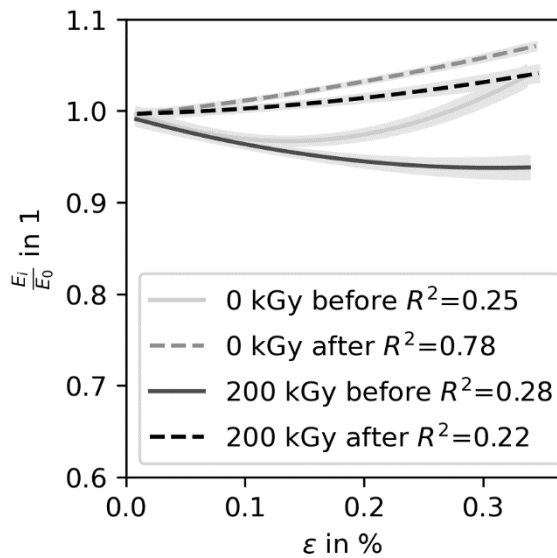


Figure 5-26 Mean curves calculated by a second order polynomial fit with shaded area marking the 95% confidence interval for the regression PC-CF laminates

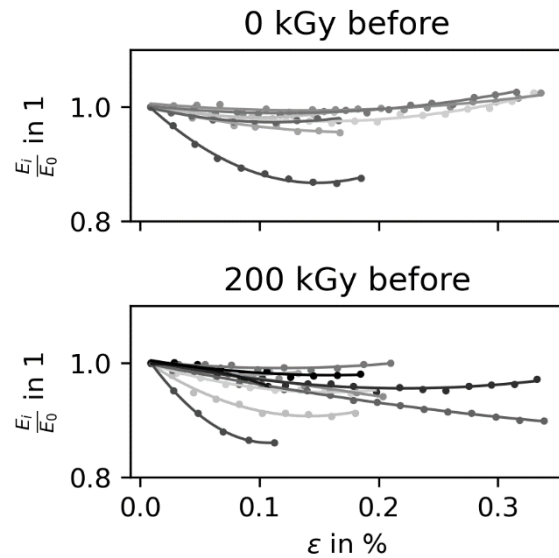


Figure 5-27 Determination of a continuous modulus by linear regressions along the quasi-static ramps before and after fatigue loading; Each line represents an individual specimen; different shades of gray are used solely for better visualization.

A closer examination of the ramps before and after fatigue loading shows also that the hysteretic opening decreases. To quantify this effect, the loss energy is calculated for each of the two ramps. Figure 5-28 shows this change in loss energy ΔW_{loss} as a function of maximum applied stress during the fatigue. The loss energy evaluated from the hysteresis curves during fatigue loading shows the same dependency on σ_{max} in absolute terms. However, these curves do not show a significant difference between the two configurations. Only the ramps before and after fatigue loading hint at a slightly higher closing of the hysteresis for the irradiated configuration. This could indicate that especially the first loading cycle introduces most of the damage and load transfer.

Figure 5-29 shows the evolution of damage for both PC-CF configurations as a function of applied number of cycles and maximum applied stress σ_{max} . As before, the curves are mean curves calculated across different specimens on the same load level. Damage evolves similar for both materials. In both configurations, the maximum applied stress also controls damage formation in both cases. However, the additional damage introduced during fatigue loading is higher for the non-irradiated configuration. At first glance, this finding disagrees with the higher crack density. In absolute terms, the initial stiffness E_{ramp} of both configurations is already different with 27.4 GPa 95% CI [26.5; 28.4] and 24.2 GPa 95% CI [22.9; 25.4]. It was deemed necessary to analyze

the initial crack density before the loading sequence but after irradiation treatment. From these additional microsections, it was found that the crack density is generally higher for irradiated material and approximately twice the value of the non-irradiated specimens as already indicated in Figure 5-18. This explains the difference in initial stiffness, which is accordingly lower for irradiated specimens. Despite this, loading can still introduces more damage in this configuration even though damage formation typically shows a digressive behavior with decreasing cracking rates as shown in Figure 3-4. Hence, degradation is higher for the irradiated laminate. This is also implied by the higher change in loss energy of the hysteresis before and after fatigue loading, in Figure 5-28.

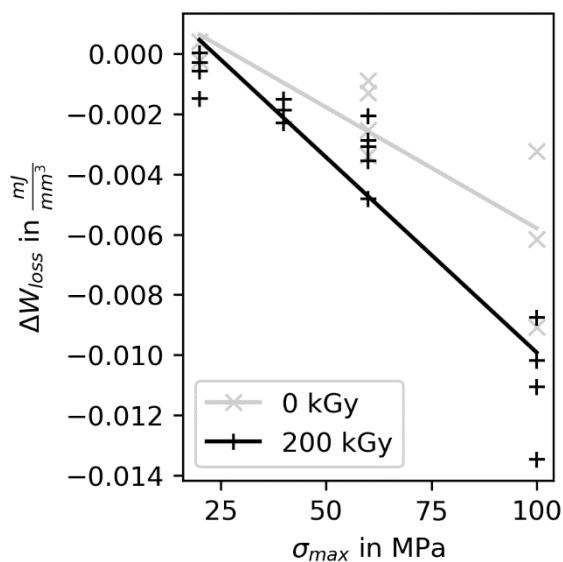


Figure 5-28 Change in loss energy during the ramps as a result of fatigue loading in PC-CF

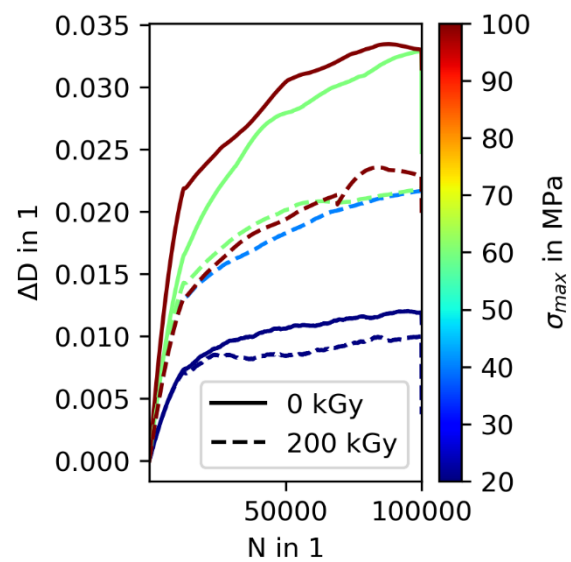


Figure 5-29 Damage increase ΔD (Eq. 4-6) over applied cycles for both PC-CF configurations

5.2.2.2 EP-CF

Carbon fiber-reinforced epoxy laminates also show slight differences in the semi-continuous modulus of both configurations shown in Figure 5-30, although alignment effects are a dominant factor. For the non-irradiated configuration, a slight decrease in modulus is visible above approximately 0.4% strain. The latter strain level is near the strain to onset debonding within the interlocks of stitching fibers observed through in-situ imaging during the static ramps (see section 5.2.1.2). Across all specimens, an increase in stiffness related to alignment effects is visible after fatigue, but no further demise in stiffness. A comparison of the loss energy from the first and last cycle only shows minor changes. Loss energy evaluated from the hysteresis during fatigue

loading indicates a slightly increasing loss energy. The dissipated energy is similar to the one determined by Drvoderic et al. [52] for loading directions other than $\pm 45^\circ$. A challenge in this respect is the very limited hysteresis opening and multiple dissipative sources, which could account for energy loss like internal friction, cracking and viscous effects. Nevertheless, the energy losses increase with increasing transverse cracking. In-situ observation verifies the latter aspect. Damage calculated from the stiffness degradation is shown in Figure 5-31. As already discussed, the main load level for a comparison is $\sigma_{max}=180$ MPa. From the damage variable ΔD , it can be seen that more damage forms in the non-irradiated configuration. In addition, it was verified that irradiated specimens with unusually low crack density also relate to the lowest stiffness degradation. The discontinuity in Figure 5-31 is a result of a single specimen stopped preliminary but still used for the evaluation of ΔD and the mean curve calculation.

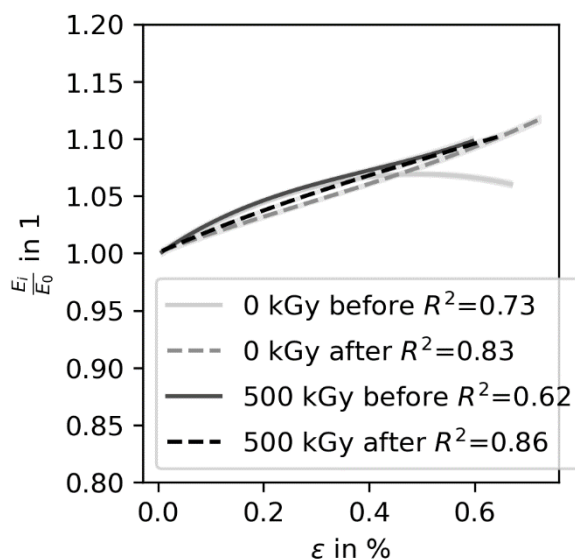


Figure 5-30 Mean curves calculated by a second order polynomial fit with shaded area marking the 95% confidence interval (imperceptibly small) for the regression EP-CF laminates

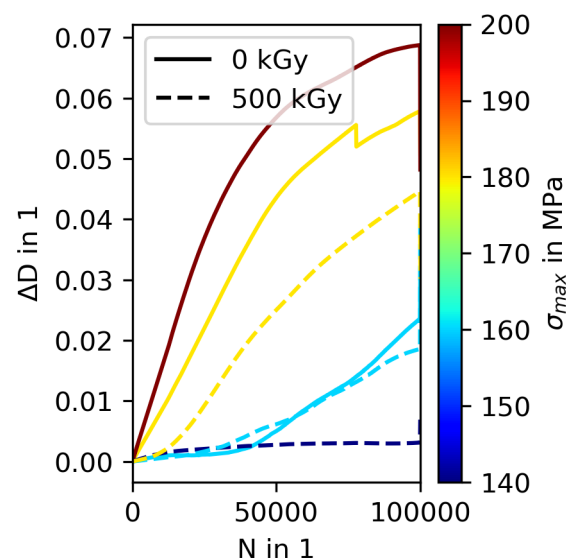


Figure 5-31 Damage increase ΔD (Eq. 4-6) over applied cycles for both EP-CF configurations

5.2.2.3 EP-GF

The agreement between observed damage formation and scalar damage parameters is good for EP-GF. A first significant difference between the irradiated and the non-irradiated configuration is a much more pronounced hysteresis opening for the pristine configuration in the first loading ramp. Similarly, the semi-continuous modulus decreases by almost 30% despite counteracting alignment effects. In contrast to this, neither of both effects is present in the initial loading ramp of the irradiated

configuration. Figure 5-32 shows representative examples of the initial loading ramp for both configurations. For the non-irradiated configuration, a knee point is present similar to the literature [55], [58]. The knee-point could also be roughly correlated to the onset of cracking in the in-situ images, discussed in [199]. Furthermore, the comparison of the ascending and descending parts of the loading curve suggest cracking as cause for the energy losses instead of viscous effects, because only the ascending portion shows non-linearity. An ideally viscous cycle should comprise non-linearity on both parts of the loading curve, caused by the timely offset between stress and strain. For reference, the dotted line indicates a linear regression of the descending portion of the stress-strain curve. Friction or plastic deformation could account for the remaining opening after unloading. The latter is also supported by the fact that crack or coalesced debonds close smoothly, which might introduce remaining plastic deformation on a macroscopic scale.

After fatigue loading both configurations are in a similar damage state as indicated by a comparable stress-strain response in the ramp after fatigue loading. During this loading ramp, no significant additional damage seems to be introduced, which is visible by both the semi-continuous modulus and very little hysteresis opening. These implications also align with the in-situ observation, that both irradiation configurations reach comparable damage states during fatigue loading. Therefore, damage formation is delayed but not fully suppressed for the irradiated configuration within 10^5 cycles. Figure 5-33 shows how damage accumulated during the first loading ramp directly translates to less additional damage during fatigue loading of the non-irradiated EP-GF. This effect is similar to the one observed in PC-CF only that in terms of irradiation the roles are reversed. Meaning that damage onset in fatigue is shifted to later stages of loading by the irradiation treatment.

Because in glass fiber-reinforced epoxy numerous damage sites form within the in-situ observation area the damage state visible there could be more representative of the overall specimen. This allows for a more detailed discussion of the role of dissipated energy during fatigue loading. In contrast to both CFRP materials were cracking is more distributed and in-situ observations are less representative of the overall damage state. As shown in Figure 5-33, energy dissipation for the non-irradiated configuration starts on a high level, whereas irradiated material starts lower. Both configurations converge towards a similar level of energy dissipation with a slight gap of 0.2 mJ/cm^3

remaining. The major difference on a laminate level between both materials is the amount of transverse cracking at the beginning of cyclic loading and differences in the polymer properties. Similar effects deduced from other damage parameters like initial crack density are believed to be present also in EP-CF and PC-CF. Low initial damage leads to increasing energy dissipation, whereas high pre-damage leads to a decreasing energy dissipation.

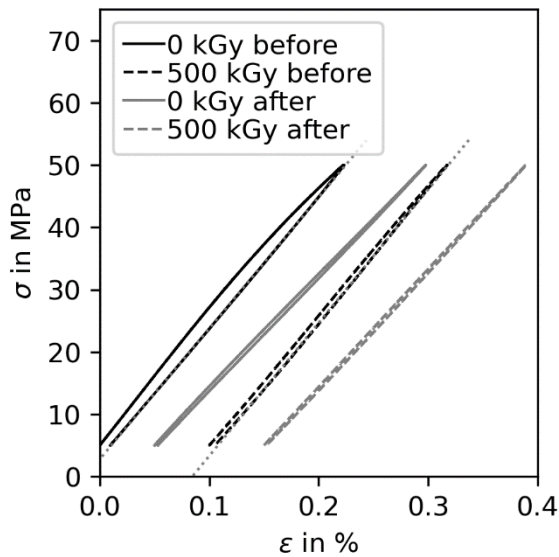


Figure 5-32 Representative stress-strain response for both EP-GF configurations; The offset (0.05%) between curves is only for better visualization

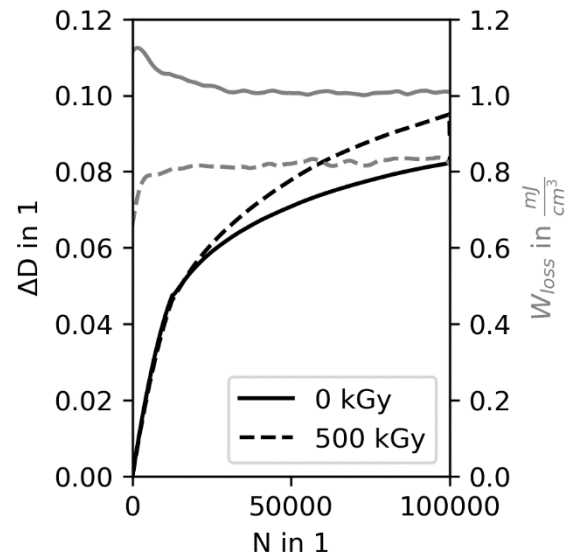


Figure 5-33 Damage increase ΔD (Eq. 4-6) and W_{loss} over applied cycles for both EP-GF configurations

5.2.3 Conclusions from the fatigue experiments on laminates

From this section, the following points can be concluded, for easier reference in the discussion:

- PC-CF plates are already in a pre-damaged state before testing and by irradiation treatment more damage is present even before external mechanical loading
- PC-CF specimens accumulate more damage after irradiation treatment
- PC-CF specimens show cracking mainly emanating from dry spots
- EP-CF specimens show strain concentrations and cracking mainly in regions where stitching fibers are interlaced
- EP-CF specimens after irradiation treatment sometimes show very little cracking

- EP-GF specimens after irradiation treatment show delayed cracking even though the cracks develop fully within 10^5 cycles
- EP-GF specimens show multiple densely spaced transverse cracks within the rovings
- EP-GF specimens show strain concentrations in resin rich areas

5.3 Laminate fatigue characterization in compression-compression loading

5.3.1 Quasi-static results

In quasi-static loading, all specimens failed in a sudden collapsing manner, as shown exemplary for irradiated EP-CF in Figure 5-34. From the fractured specimens, it is evident that failure is initiated by out-of-plane kinking. DIC performed on the high-speed images also shows that a local failure propagates rapidly along the width of specimen and appears as collapse. Figure 5-35 gives the mean ultimate compression strength (UCS) per configuration together with the 95% confidence interval. The failure stress is the nominal stress without accounting for stress localization near the notch root. From the evaluation, it can be seen that PC-CF does not show any significant difference between both configurations. Irradiation treatment increases the failure load for both epoxy-based laminates. This effect agrees with literature models, which suggest an increasing kink band initiation stress with increasing shear modulus of the composite.

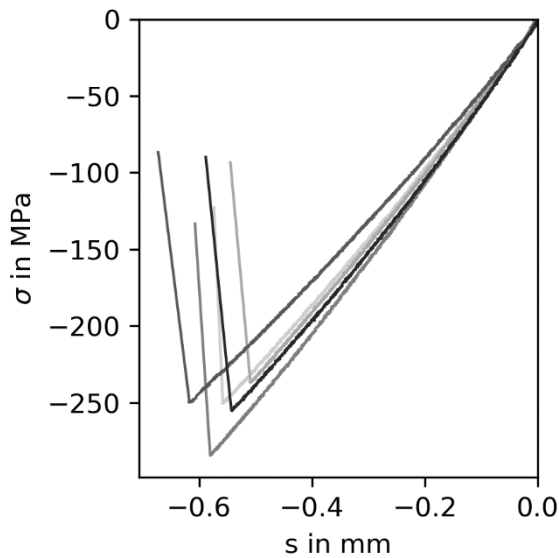


Figure 5-34 Example for the sudden failure of EP-CF in the irradiated configuration

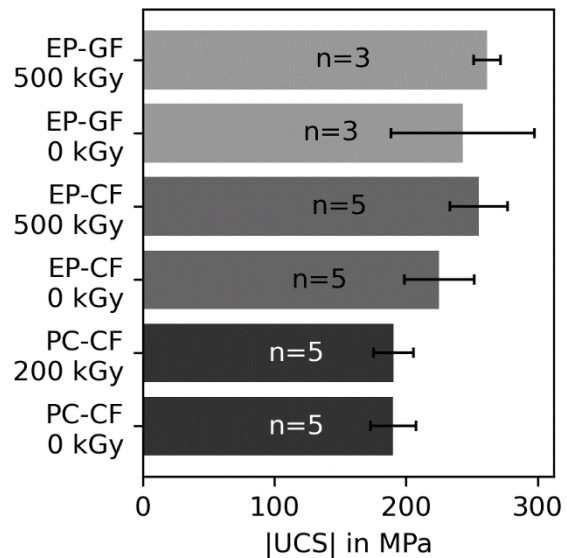


Figure 5-35 Mean failure stress per material and configuration; Error bars indicate the 95% confidence interval.

5.3.2 Load increase testing results

Figure 5-36 summarizes the results of all materials and configurations in terms of failure load level. For comparison, the quasi-static failure stress is also included. This reveals an unusual feature for both CFRP laminates, namely a failure stress above the quasi-static strength. For PC-CF, this effect is slightly more pronounced for the non-irradiated configuration, even though the UCS is nearly identical between the configurations. An even more drastic difference is evident for EP-CF. Here, non-irradiated and irradiated specimens fail 27% and 35% above the quasi-static failure level, respectively. In contrast to this, EP-GF fails consistently below the monotonic strength. It must be noted that fatigue loading appears to be more detrimental to the irradiated configuration, even to the extent that all improvements observed in monotonic loading of irradiated EP-GF are lost. Across all materials and configurations, failure is always catastrophic without any indication in terms of increasing displacements in the machine data (hydraulic piston displacement).

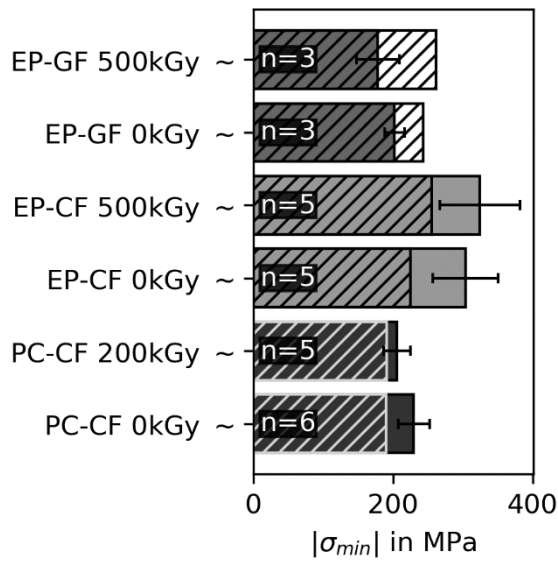


Figure 5-36 Mean failure stress per configuration in comparison to the monotonic failure stress (hatched area); Error bars indicate the 95% confidence interval.

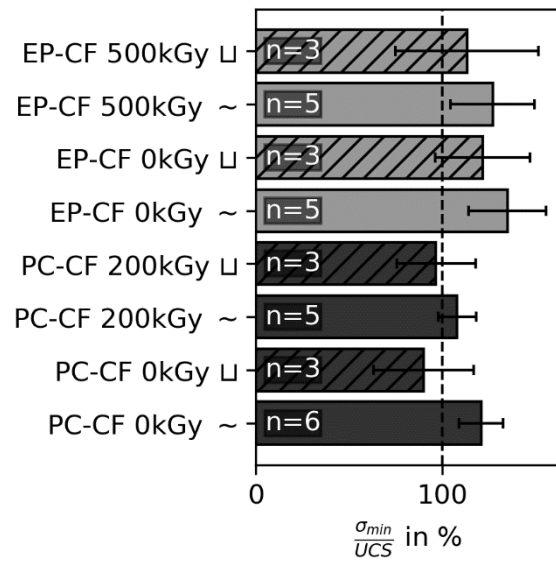


Figure 5-37 Effect of load signal (~ sinusoidal, □ trapezoidal) on the normalized load increase test failure stress per configuration; Error bars indicate the 95% confidence interval.

5.3.3 Influence of time under load

A major difference between monotonic loading and fatigue loading is time under peak load (i.e. at σ_{min}). Figure 5-37 gives the failure load normalized by the UCS for two types of loading signals. It can be seen that a trapezoidal loading signal lowers failure stresses across all investigated configurations and materials. For PC-CF specimens, a trapezoidal loading signal leads to stresses, below the monotonic strength. For EP-CF specimens, however, failure loads remain consistently above the monotonic value.

5.3.4 Damage formation

Due to the transparency of GFRP, damage formation can be evaluated in-situ by backlight illumination of the specimens during testing. As shown in Figure 5-38 for the non-irradiated configuration of EP-GF two signs of damage can be observed. First, at relatively low loads of approximately 45% of UCS, a longitudinal crack appears and grows along the specimen axis. This is indicated by a dashed line in Figure 5-38 for easier reference. During later stages of fatigue loading, an opaque area forms approximately at the notch root and grows outwards along the specimen axis in a diffuse manner. The dark appearance during backlight illumination indicates cracking and debonding. The elliptical shape of the expanding damage zone suggests that propagation along the fibers is favored. In contrast to these features in the non-

irradiated configuration, no longitudinal cracking is visible for irradiated specimens. In addition, the diffusive damage zone near the root of the notch is much more localized. Still, failure levels are lower for this material.

For CFRP, only microsections allow for a more comprehensive study of the type of final failure. In the analysis of the fracture zones it is necessary to acknowledge that the kink band will propagate further because of the elastic energy stored in the machine's load frame [150]. Furthermore, the machine stops³ were set as a compromise between early failure detection and a reliable testing procedure. Both factors could cause additional damage. Still, kink bands are visible for many specimens macroscopically and clearly within the microsections. Figure 5-39 shows with planes (a) and (b) two examples for a cyclically loaded PC-CF and an EP-CF specimen. Especially for EP-CF, failure often leads to crushing and significant scraping of the two fracture surfaces near the initiation point, making it appear featureless. However, the microsection prepared from the opposite edge (i.e., plane (b) in Figure 5-39) shows numerous kink bands many of which are oriented in- and out of plane. This is likely caused because this part of the specimen is constrained by the anti-buckling guide. A more in-depth study of longitudinal cracking in EP-CF was done by preparing microsections in plane (c) approximately 4 mm distant from the notch centerline. For a batch of four specimens prepared in this way, all showed a longitudinal crack independent of the irradiation configuration. However, no microsections are prepared focusing on longitudinal splitting for PC-CF specimens. This is because cracks and dry spots in the pristine condition would necessitate a considerable number of specimens to yield meaningful results. The presence of longitudinal splits might explain partly that the failure load is above UCS. It is hypothesized that as soon as a split exists, shear stresses will be lower and the detrimental effect on kink band initiation stresses will cease.

³ Machine stops are software limits for the allowable displacement of the piston.

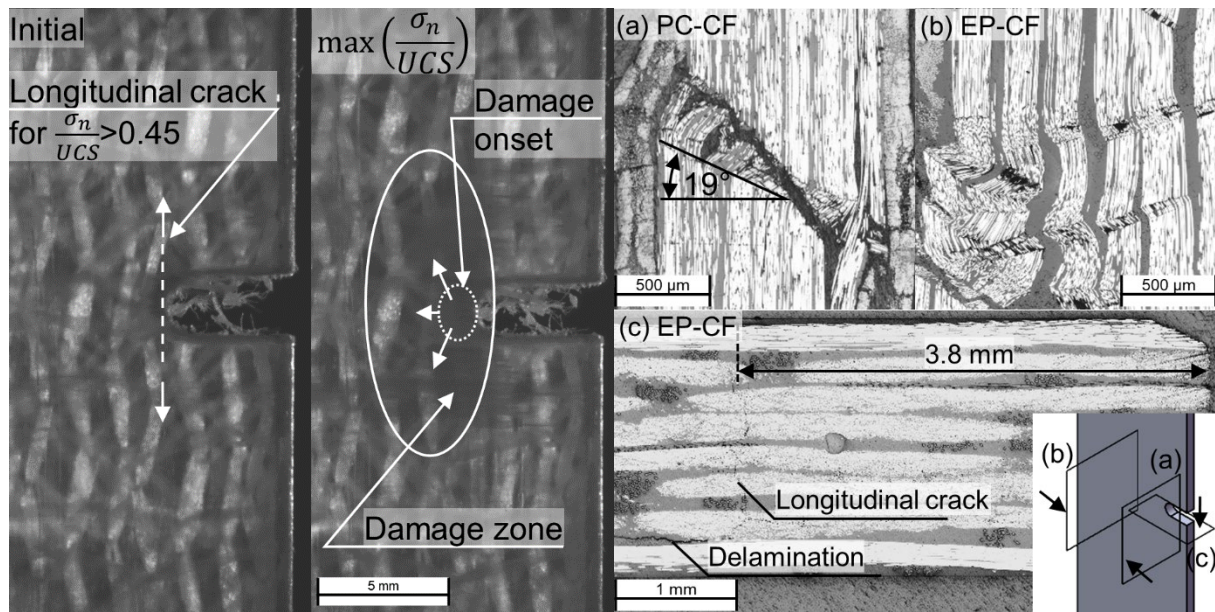


Figure 5-38 Damage formation in a non-irradiated EP-GF specimen at the beginning of loading and near final failure at the highest load level

Figure 5-39 Microsections of kink bands (a,b) and longitudinal cracks (c); Planes are marked in an isometric view of the notched specimen

Strains evaluated during monotonic loading can also give an indication of highly strained areas. Figure 5-40 shows a strain map of both ϵ_y and ϵ_{xy} . The strain distribution is comparable across all specimens. From the high-speed images, the failure location can be identified in the region where ϵ_y and ϵ_{xy} are present simultaneously. For the most part, this damage initiation point is not the strain peak for both strain components. Interestingly, shear strains are universally around 0.3% across all analyzed specimens despite differences in on-axis failure strains. For both EP laminates on-axis (ϵ_y) failure strain is approximately -0.7 to -0.8%. For PC laminates, scattering is relatively high, but failure strains are in the same strain range. However, on closer examination of transversal strains ϵ_x inconsistencies are present beyond effects caused by scattering. This raises the question if a single camera set-up might lead to errors because buckling and other out of plane movement is possible. To verify that this is not the case, it is possible to use facets near the anti-buckling guide as reference for true strain because out of plane movement is prevented by the set-up. From these points, both extensional strains should follow the same pattern if the specimen buckles. Furthermore, equation Eq. 4-2 suggests that a working distance of $WD_0=450$ mm allows only for minor errors if ΔWD is limited to the scales of sub-millimeter displacement. Therefore, the strain concentration is likely a true material response. The observed damage in the form of longitudinal cracking and localized debonding remains as explanation for these

anomalies. The latter is present across all quasi-statically loaded batches and points towards cracking and debonding as additional factor influencing kink band failure.

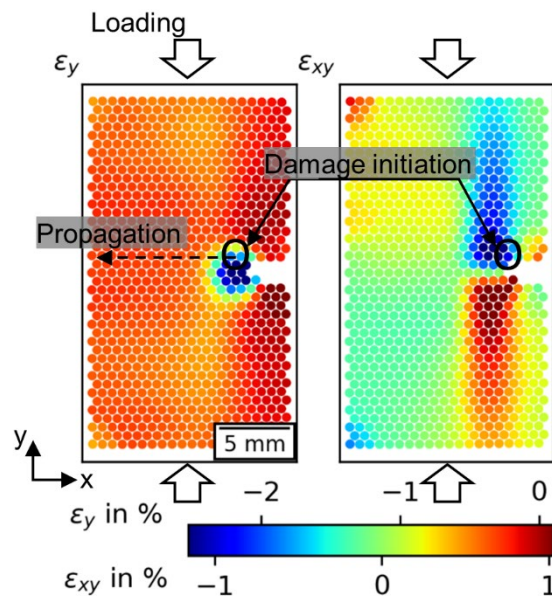


Figure 5-40 Facet strains evaluated from high speed images of a EP-CF specimen shortly before final failure with the unloaded state as reference frame

5.4 Fiber-Matrix adhesion

From the results and the literature, interface properties and failure are an important factor in damage initiation. A qualitative evaluation of the influence of irradiation treatment on the fiber-matrix adhesion is done by SEM images. Tensile specimens of all six materials and configurations are fractured manually by bending at room temperature after partial removal of one of the on-axis plies. In this way, excessive splitting of the on-axis plies could be avoided and still tensile stresses are mainly driving the crack through the transverse plies.

Figure 5-41 shows both configurations of PC-CF in direct comparison. Especially for the non-irradiated laminates, it can be seen that nearly no polycarbonate adheres to the fibers. In many cases, fibers appear to be in a tunnel formed by fully debonded polymer. In contrast to this finding, the crack propagated not only along the interface but also through the polymer for the irradiated configuration. This could point towards better adhesion or a weaker polymer matrix with reduced crack resistance, which draws the crack away from the interface. The latter explanation is supported by a reduced yield stress and lower fracture strain found in irradiated neat polymer specimens. In addition, the overall crack density of the laminate increases by

irradiation treatment, which suggests a weakening of one of the constituents. Considering this, any improvement in fiber-matrix adhesion contradicts the higher crack density. As a result, the polymer deterioration would need to overcompensate for this. An additional feature only found within the irradiated configuration is the presence of crazed polymer and drawn polymer fibrils. Figure 5-42 shows some examples of the observed features within the laminate together with a reference image of a craze within neat polymer. This also suggests a weakened matrix polymer and agrees with the observation that crazing starts earlier and at lower strains for the irradiated configuration. In some areas lamellae features can also be found similar to those found in the final fracture surface of fatigued neat polycarbonate viewed from the top. It can be concluded that crazing and shear banding are in principle possible within the laminate, despite limited space between the fibers. However, additional efforts to visualize crazing by x-ray microscopy were not successful, due to limited density differences and the sub-micro scale.

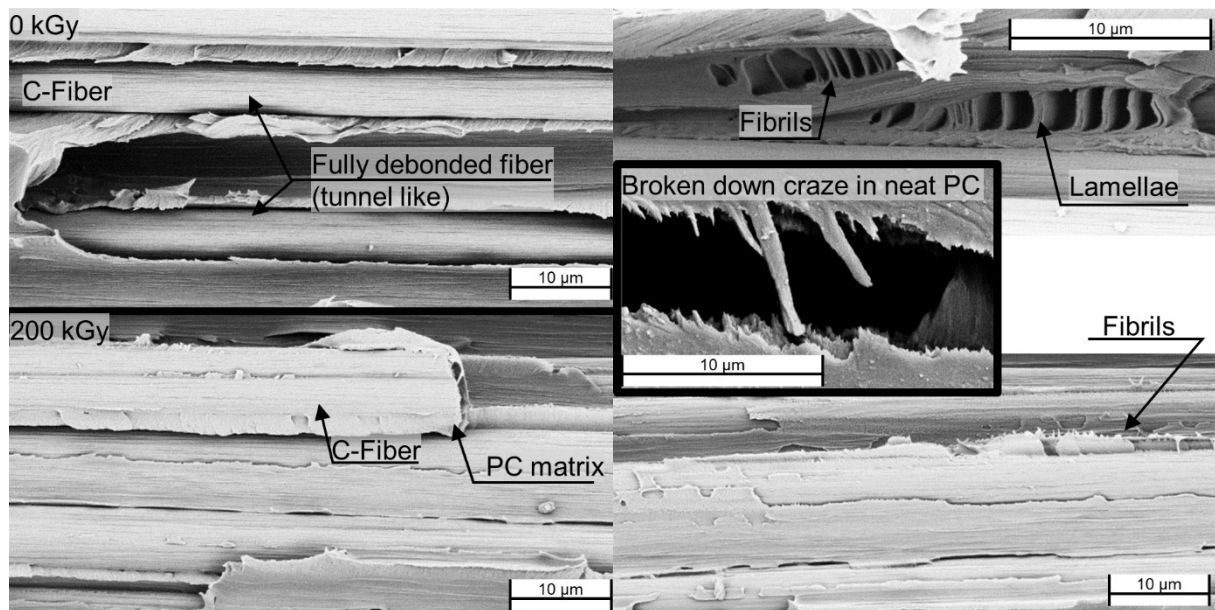


Figure 5-41 Fiber-matrix adhesion in PC-CF

Figure 5-42 Fibrils and lamellar shear yield zones in irradiated polycarbonate laminate

No significant changes in fiber matrix adhesion could be found in EP-CF laminates. This applies to the three different interfaces present in the laminates. Namely, the adhesion of the epoxy resin to carbon fibers, polyester fibers and glass fibers. The last two fiber types are used as stitching. Polyester fiber to epoxy resin appears to be a critical interface because many cracks and debonds form in the vicinity of these fiber bundles very early in the fatigue life. From the SEM images in Figure 5-43, it can be

seen that epoxy resin does not significantly adhere to the polyester fibers. This aligns with the in-situ strain measurements, marking these zones as failure location.

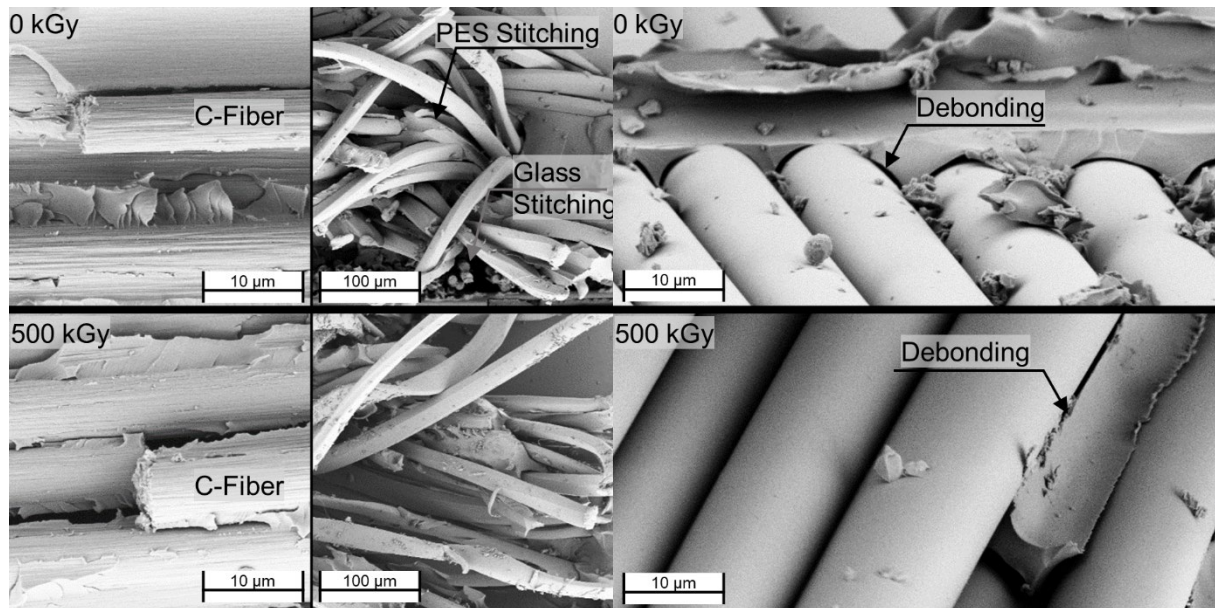


Figure 5-43 Fiber-matrix adhesion in EP-CF and EP-polyester (PES) stitching

Figure 5-44 Fiber-matrix adhesion in EP-GF

In EP-GF laminates, fiber matrix adhesion is generally much lower compared to the polymer's strength because cracks form nearly universally along the fiber-matrix interface. A direct comparison to the carbon fiber-reinforced laminates shows that no polymer residue remains on the glass fibers (see Figure 5-44). This observation, along with in-situ microscopic images, suggests that fiber-matrix debonding is the main source of damage initiation. This also explains why cracks are able to close nearly fully after unloading because the majority of the cracked surface is free of any plastically deformed areas preventing crack closure.

6 Multiscale modelling

6.1 Approach and aims

Based on the overall conceptual framework a synergistic approach is chosen to study the local stress state during fatigue loading for different polymer properties in combination with the processing specific geometry as shown schematically in Figure 6-1. It is the aim of the FE models to supplement the experimental findings of CFRP and get insights into locations of crack initiation. For EP-GF, in-situ strain maps already answered some of the questions addressed by the FE-models and were therefore not included in this section. Furthermore, the numerical models can also be used to study polymer properties like elasticity, visco-elasticity and plasticity separately. The analysis focuses on homogeneous polymer deformation. Experimentally observed damage sites are identified over several specimens and one FE-model per material is then generated based on a representative specimen and its load level. This mesoscopic model incorporates differences in local fiber volume content as well as features like dry spots. Loading is based on the actual macroscopically measured strain for the specific specimen chosen under the hypothesis of mainly strain controlled loading of the transverse ply. Because irradiation treatment does not change the geometric arrangement, the same model can be used across both irradiation configurations per material. The FE model focuses on TT loading because CC inherently spans two scales and kink banding is a stability problem with accompanying requirements for the modelling strategy. In addition, the mesoscopic structure could very well be important, but far fewer details on the damage progression could be gained experimentally for CC loaded specimens.

The mesoscopic stress distribution is used as input parameter for a RVE model. RVE generation follows the findings of the onset-theory and relies on a regular instead of a random fiber distribution. A regular hexagonal or cubic fiber arrangement has been identified as critical and representative as shown by several studies for UD composites [63], [109], [205]. The regular fiber arrangement has the benefit of fast and efficient RVE generation and meshing in the ABAQUS micromechanical plug-in (vers. 1.15). For simplicity, the analysis is limited to a hexagonal fiber arrangement. RVE as a sensor can then be used to investigate the resulting local stress states within the matrix at experimentally observed cracking sites. At the outset the role of neighboring cracks visible after the fatigue test needs additional consideration, because of their effect on

the stress state within the in-situ observation area used as object of study. Fitting a 3D-fracture criterion is not attempted in this work as determining the necessary material parameters (ply level) is beyond the scope of this work. This would require significant experimental effort, given in total four material-dose combinations and the need to account for varying fiber-volume contents.

Despite numerous experimental results in terms of in-situ images, the number of specimens that could be processed to a well-defined FE-model was deemed insufficient to compare numerically determined stresses directly between different specimens. The latter approach would be in line with the concept of an in-situ S-N curve discussed for EP-GF in section 5.2.1.3 and [199]. Still, a comparison between both irradiation conditions of EP-CF and PC-CF is possible under the assumption that cracking sites are independent of the polymer's properties. From the experimental results, no indication contradicting this assumption could be found. Analysis of the stress state at crack initiation sites necessitates an identification of the latter. For EP-CF, the identification of crack initiation sites is based on the in-situ observation. In the case of PC-CF laminates, the occurrence of cracking appears to be less random in nature, exhibiting a clear correlation with the presence of stress concentrations at dry spots. Therefore, these stress concentrations are compared as potential crack initiation site.

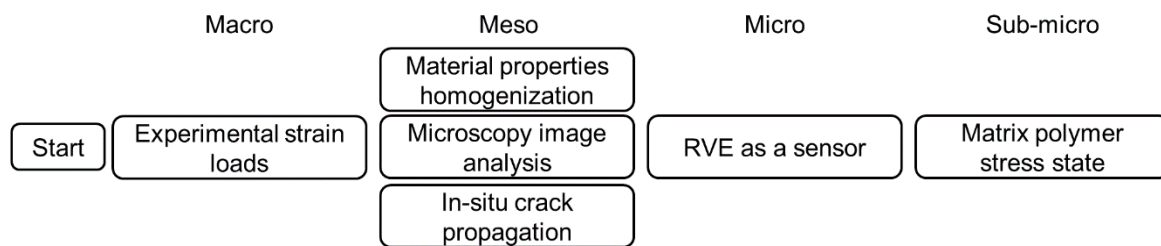


Figure 6-1 Macro to sub-micro FE based analysis

6.2 Homogenizing the material properties

The homogenized properties of a unidirectional ply for the mesoscopic model are calculated by the methods of cells as a function of fiber volume content. This model was introduced by Aboudi [163] and can be extended to visco-elastic constituent properties by Alfrey's correspondence principle. Due to the latter principle, it is possible to use essentially the elastic formulations with Laplace transformed material laws. The constitutive model for the matrix polymer is chosen as Wichert model as shown in equation Eq. 6-1. This model is essentially a generalized Maxwell model (second term

on the right in Eq. 6-1) with an additional spring in parallel E_∞ [206]. The time-dependent modulus can be expressed in the Laplace domain by Eq. 6-2. The additional factor in the Laplace transform can be explained by the transformation of the convolution integral Eq. 6-3, which leads to a stress-strain expression in the Laplace domain Eq. 6-4 similar to the elastic case Eq. 6-5 [206, p. 276].

$$E(t) = E_\infty + \sum_{i=1}^n E_i e^{-\frac{t}{\tau_i}} \quad \text{Eq. 6-1}$$

$$E^* = sE(s) = s \left(\frac{E_\infty}{s} + \sum_{i=1}^n \frac{E_i}{s + \frac{1}{\tau_i}} \right) \quad \text{Eq. 6-2}$$

$$\sigma(t) = \int_0^t E(t-\tau) \frac{d\varepsilon(\tau)}{d\tau} d\tau \quad \text{Eq. 6-3}$$

$$\sigma(s) = E^*(s)\varepsilon(s) \quad \text{Eq. 6-4}$$

$$\sigma(t) = E(t)\varepsilon(t) \quad \text{Eq. 6-5}$$

With this transformation, it is possible to construct the compliance tensor in Voigt notation for both matrix and fiber material. It is important to use also a Laplace transformed version of fiber compliance tensor of the fiber material, even though glass or carbon fibers can usually be taken to be purely elastic. Eq. 6-6 shows the abbreviated version for the matrix material, which is assumed to be isotropic. Furthermore, it is assumed that the compliance of the shear/elastic modulus and bulk modulus is synchronous. This assumption leads to a Poisson's ratio ν_m independent of time [206, p. 305].

$$C_{ij}^{-1} = \begin{pmatrix} \frac{1}{E_m^*} & \dots & 0 \\ \vdots & \ddots & \vdots \\ 0 & \dots & \frac{2(1-\nu_m)}{E_m^*} \end{pmatrix} \quad \text{Eq. 6-6}$$

The two compliance tensors for matrix and fiber together with the fiber volume fraction are used as input parameters for the model derived by Aboudi [163]. The inverse Laplace transform can then be used to calculate the components of the laminate compliance matrix as a function of time or the commonly used elastic constants e.g. E_{11} . In order to reduce the input parameters in the FE model the homogenization step

is separated into a pre-processing step and the homogenized compliance tensor is mapped up to 10^5 s.

6.3 Constituent properties

The underlying material properties of the matrix polymer are taken from the TTS relaxation experiments and the quasi-static tensile tests. The TTS relaxation experiments are used as reference for the time-dependent elastic modulus, whereas the tensile tests provide Poisson's ratio and act as reference for the elastic-plastic approximation. This choice allows a direct comparison of the fully relaxed state (elastic solution) and the visco-elastic overstresses. Both cases can be taken as the extremes and are necessary because relaxation speeds are limited for both cases and due to the numerical expense of differential implementation of the UMAT. The latter limits the incrementation (size of time steps) and requires numerous state variables. Fiber properties of the HT carbon fibers are taken from [207]. The interface is not explicitly modelled, due to the complexity and additional parameters necessary. In addition, polyester stitching fibers are also considered in the later discussion with an approximate elastic modulus of 15 GPa [208].

6.4 Transverse isotropic visco-elastic material

After mapping the elastic constants as a function of time, an appropriate transverse isotropic material model is necessary to account for the transient material behavior of the unidirectional plies. With the right set of elastic constants it is possible to remain in the rheological framework as shown by the implementation of Zobeiry et al. [164]. This approach is used within this work. The five elastic constants used within the model rely on the framework derived by Hashin [209], within which different elastic constants can be treated separately and can be recombined as linear combination. Eq. 6-7 gives the algebraic equations, which can be transformed back into the time domain by the inverse Laplace transformation.

$$\begin{aligned}
\eta(t) &= \mathcal{L}^{-1}C_{11}^* \\
l(t) &= \mathcal{L}^{-1}C_{12}^* \\
k(t) &= \mathcal{L}^{-1}\left(\frac{1}{2}(C_{22}^* + C_{23}^*)\right) \\
G_{13}(t) = G_{12}(t) &= \mathcal{L}^{-1}C_{44}^* \\
G_{23}(t) &= \mathcal{L}^{-1}\left(\frac{1}{2}(C_{22}^* - C_{23}^*)\right)
\end{aligned}
\tag{Eq. 6-7}$$

After mapping the components back into the time domain, η , l , k , G_{12} and G_{23} (Hashin constants) are available as time series. For the model employed by Zobeiry et al. it is necessary to provide the time-dependent Hashin constants as parameters for a Wichert model. Here again, fitting is employed with the same time constants τ_i already used for fitting the coefficients to the matrix polymer. In principle, it would also be possible to create a unified UMAT combining both steps but this would add a lot more complexity to the implementation of the UMAT.

A downside of the rheological framework is the great number of material parameters necessary for the model. The Wichert model consisting of five Maxwell elements in parallel and one spring requires 35 coefficients for full parametrization. Five elastic constants, which are described by six coefficients. In addition to these coefficients five time constants τ_i need to be specified, which are chosen identical across all elastic constants.

6.5 Fiber volume content dependent material

The fiber volume content is considered on both the micro- and the mesoscopic scale. On the micro scale within the RVE, the fiber spacing is adjusted to account for locally varying fiber volume contents. However, the implementation at the mesoscopic scale needs further explanation. Here, the method of cells gives a convenient way of generating a map of Hashin's elastic constants as a function of the fiber volume content. This route is chosen for the elastic material. For the visco-elastic material model, however, supplying a map of elastic constants to the UMAT implementation is not feasible. As an alternative, the identity of isochronous relation between elastic constant and fiber volume fraction can be used. This reduces the problem by one dimension. To further simplify the programmatic implementation and limit the complexity of the UMAT polynomial fits are used to capture the fiber volume

dependency. A 3rd order polynomial $p_E(v_f)$ was found sufficient to represent the dependency across the Hashin constants. E and the corresponding index denote the individual relations for each of the Hashin constants. As a result, the 35 coefficients are supplemented by additional 20 polynomial coefficients to account for the fiber volume content. By normalizing, the polynomial coefficients $p(v_f)$ with the elastic constant at reference time t_{ref} and reference fiber volume content v_f^{ref} the elastic constants inputted to describe the time dependency can be adjusted to the correct fiber volume content. It was verified that errors are small by mapping the elastic constants in the time and fiber volume content domain against values directly evaluated from the method of cells.

$$E(v_f, t) = \frac{p_E(v_f)}{E(v_f^{ref}, t_{ref})} \times E(v_f^{ref}, t) \text{ with } E = [\eta, l, k, G_{13}, G_{23}] \quad \text{Eq. 6-8}$$

6.6 Meso model generation from images

6.6.1 Geometry and boundary conditions

A spatial fiber volume distribution can be found by x-ray microscopy and light microscopy. Light microscopic imaging is used as main source in generating the model. A major challenge in this regard are artifacts from specimen preparation like scratches and broken out fibers. Three imaging systems are combined to capture a comprehensive description of the material and individual specimens. These are a x-ray microscope Zeiss Xradia 520 Versa (3D volume imaging), a Leica DM6000M and a custom infinity corrected microscope (in-situ microscope of section 4.4.2). The first step in preparing the meso-model is the identification of the area observed with the in-situ microscope. After identification, a stitched image is taken including areas beside the in-situ image (see also Figure 6-2). In this way, pores and inhomogeneity just outside the in-situ image can be included in the FE-model. This is especially relevant for the PC-CF material because for some specimens extended dry spots and numerous cracks are present. The size of the FE-model is then extended to the next transverse crack visible. It is therefore possible to include stress perturbations induced by neighboring cracks by switching the boundary conditions or loads ($BC_{mid,1}$, $U_{mid,2}$) on and off. This allows studying the effect these perturbations have for the extreme cases of no crack or a fully propagated transverse crack. Figure 6-2 shows how the different

image sources are combined to form the mesoscopic model. The model consists of three different zones with decreasing detail. Zone I is the most detailed area, including both dry spots and the fiber volume content. Zone II includes still dry spots but assumes a homogeneous fiber volume content. This buffer zone of 0.2 mm thickness allows for phasing out these geometric features without sharp cuts. Zone III acts as load introduction without both details. These zones span up to the next crack and allow for a gradual reloading of the ply. Because the cracking sequence during the fatigue test and the loading ramp are unknown, four permutations can be considered. Assuming neighboring cracks did not form outside the observation zone, cracks are either present on the left or right, or cracks to the left and right have fully propagated. Partial cracks are excluded from consideration, with all neighboring cracks assumed to be fully developed. Load application is done by displacing the right side of the model as required for the investigated global strain in a smooth step of 10 s (SMOOTH STEP in [210]). Within the coordinate system of the transverse ply symmetry is assumed in 1-direction. Therefore, the meso-model represents a cross-section in the middle of the specimen rather than on the edge. The overall assumption is that transverse cracks will span the width of the specimen instantly. At the outset of this work, these details were still undecided and therefore the model is based on C3D8 continuum elements. This would allow to model the stress state at the edges, too.

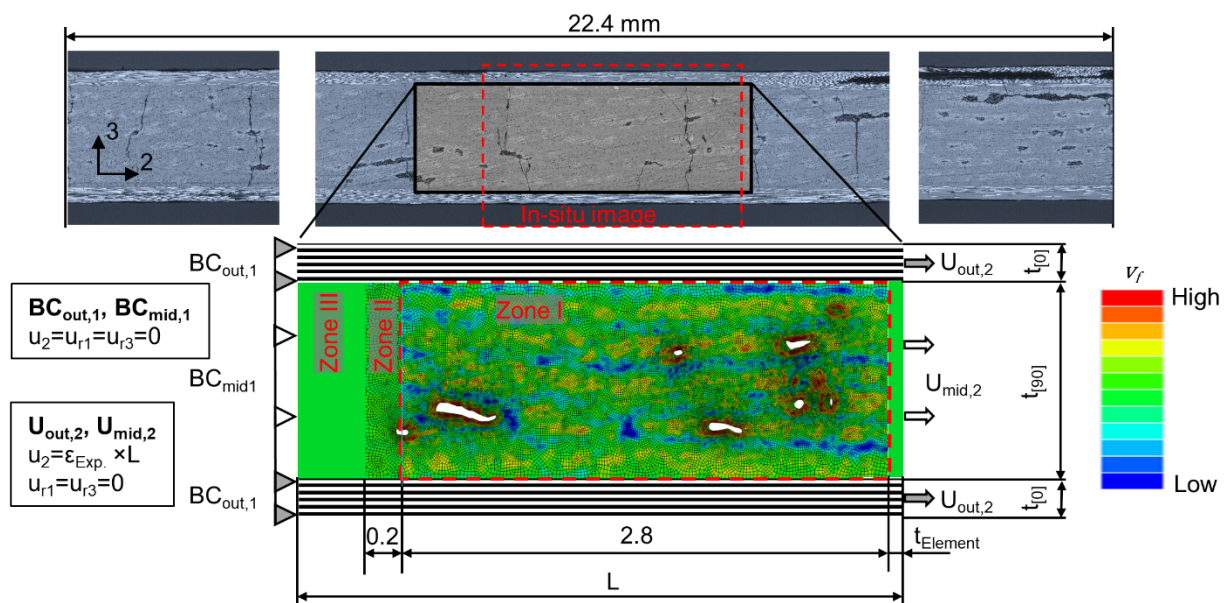


Figure 6-2 Mesoscopic model; Color map indicates the fiber volume content

6.6.2 Spatial fiber volume distribution

After defining the geometry and boundary conditions, the spatial fiber volume content can be incorporated into the model. The necessary image processing is done mainly by the use of functions available in the python modules OpenCV (vers. 4.6.0.66) and NumPy (vers. 1.21.5). The first processing step is a shading correction⁴ of the image brightness. This is done by a convolution with a Gaussian kernel. The kernel size and standard deviation is chosen large enough that only a global brightness difference remains. A standard deviation of three and a kernel size of $\frac{1}{50}$ of the image diagonal proved sufficient. By dividing the original image with the blurred image, the brightness is homogenized [211, p. 174]. Next, a threshold can be set for fiber rich areas, which yields a binary image. The next step in preparing the mesoscopic model is to smooth the image. This approach aims at bridging the resin between fibers to form a homogeneous group of pixels representing a roving or fiber rich area and is similar to the concept of text recognition, where missing pixels of a letter can be restored by smoothing [211, p. 282]. Smoothing can be done in the spatial or frequency domain by a convolution or a low pass frequency filter respectively [211, p. 163]. However, the frequency domain was chosen here for a higher processing speed and because it is easier to comprehend the effect of a cut-off frequency compared to kernel size and kernel design in the spatial domain. The filter process consists of a Fast Fourier Transformation (FFT) of the image. The resulting amplitude spectrum is then multiplied with a window function and transformed back into the spatial domain by an inverse FFT. The window function plays a crucial role for the resulting image. An ideal cut off induces ringing (rectangular window function) in the reconstructed image and is therefore only a theoretical option [211, p. 163]. Numerous alternative window functions can be used. The final choice within this work is a Hamming window, because it yielded good smoothing results and only one parameter is necessary, unlike Gauss windows, which are defined by radius and standard deviation. Another specific feature is the implied periodicity of the image during image reconstruction. This leads to artifacts on the edges of the image and can be overcome either by zero padding or mirroring [211, p. 268]. The ideal cut-off frequency is found by visual inspection of the

⁴ Many imaging systems produce slightly inhomogeneous illumination, which can be compensated by a shading correction.

reconstructed image. The criterion for selecting the right filter radius is that rovings are still visible, but no fibers can be singled out. Finally, it is necessary to calibrate the brightness distribution to represent the fiber volume distribution of the specimen appropriately. X-ray microscopic images are used as reference, as these images are free of any preparation artifacts from grinding or polishing. However not every fatigued specimen is scanned. Instead, one representative volume per laminate is analyzed and a single slice from this scan is used to fit the grey value distribution. By smoothing the image with the Hamming filter the local fiber volume distribution can be investigated for different cut-offs. With decreasing cut-off frequency, the image will be homogenized further until its histogram collapses into the global fiber volume content employed in macroscopic ply level properties (fiber pixels need to be normed to one).

Therefore, in an artifact free image segmented into fiber and matrix, smoothing can yield any desired degree of homogenization for a meso model. As already mentioned, it is the aim of the developed processing steps to resolve up to the level of rovings. The histogram of the x-ray microscopic image adjusted to the desired resolution is used as reference for the local fiber volume distribution, which should be in agreement with light microscopic images despite preparation artifacts. Even though histogram mapping is one solution to achieve this goal [211, p. 125] it was found that gamma transformation can also be used to adjust the histogram of the light microscopic image. Typically, fractional powers are needed for the adjustment. Exponents below one map a narrow band of dark pixel values to a broader range and vice versa for bright pixels [211, p. 125]. Therefore, the gamma below one used here implies that artifacts and broken out fibers lead to a fiber volume content information being compressed into a narrow band of darker pixels.

6.6.3 Pores and stitching fibers

Different approaches for the identification of pores and stitching fibers were tested but no satisfactory results could be obtained with the available images. An alternative approach was used based on the deep learning tool available in the software Dragonfly (vers. 2022.2). Here, training images are first manually segmented. These images are used to train a convolutional neural network. After training this model, pores or stitching fibers can be identified in the remaining images. EP-CF and PC-CF are trained in separate models. A manual verification is done for all images segmented in this way. Segmentation yields only binary information, which needs to be transformed into

geometry information. This step is accomplished within Potrace (vers. 1.16), which can identify edges and provide base points for a spline representation. The latter result is then used within an ABAQUS macro to generate automatically individual splines for each pore or fiber region with stitching fibers.

6.7 RVE

RVE generation is done within the ABAQUS micromechanical plug-in. For simplicity, only the hexagonal fiber arrangement is used. As discussed by Baar et al. [109] this is one of the critical fiber arrangements beside cubic. Rotating the RVE relative to the load application also affects the stresses encountered within the matrix material and for this reason the RVE is rotated from 0 to 30° [109]. For unloaded surfaces, periodic boundary conditions are employed. The driving field is stress-based and the mesoscopic stresses are transformed to account for the RVE's rotation. Figure 6-3 shows the definition of the rotation angle θ around the transverse ply fiber direction (1-direction). The constituent properties are identical to the ones used as basis for the mesoscopic model. A separate interface layer is not modelled, due to the numerous unknowns in this regard [65], [125], [212]. For the evaluation of the results, different evaluation points can be used [17], [109]. However, the point selection needs careful consideration and often includes assumptions about the relevant invariants.

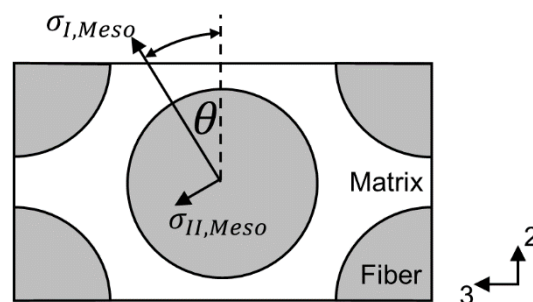


Figure 6-3 RVE definition and rotation angle of the principal stresses relative to the hexagonal fiber arrangement

6.8 Plasticity on the micro-scale

Incorporating plastic deformation is challenging for three reasons. As shown by Bergstrom [213] plastic material models need to be chosen carefully in order to capture repeated loading correctly, e.g., an isotropic hardening law can lead to unrealistic hysteresis opening. Krause [75] used an endochronic plasticity model, but later found the plasticity to be overestimated. A second challenge is the number of material parameters that need to be fitted for a transversely isotropic material. The latter

challenge would be further aggravated for the intended mesoscopic model with varying spatial fiber volume content. The third problem is that on a mesoscopic scale plasticity from cracks and debonds is indistinguishable from matrix plasticity. Because the models mainly focus on the latter, a top-down approach is not possible.

Neuber's approximation is an alternative approach, which does not require a definite choice of a material model. Under the assumption that only localized yielding will be present, this approximation allows for a correction of stress peaks predicted by an elastic solution to values of an elastic-plastic case. In this way, it is deemed possible to estimate if plastic deformation is a relevant feature of the polymer's behavior at cracking sites. Under Neuber's assumption, the stress correction is derived from the premise that the elastic strain energy $\varepsilon_e \sigma_e$ equals that of elastic-plastic deformation $\varepsilon_{e,p} \sigma_{e,p}$.

$$\varepsilon_e \sigma_e = \varepsilon_{e,p} \sigma_{e,p} \quad \text{Eq. 6-9}$$

As measures for stress and strain, the respective von Mises equivalents are used. Equivalent strain ε_{eqv} is defined as eq. Eq. 6-10 with the principal strains expressed as engineering strains $\varepsilon_I, \varepsilon_{II}, \varepsilon_{III}$ [109]. Other definitions can also be found [94].

$$\varepsilon_{eqv} = \sqrt{0.5[(\varepsilon_I - \varepsilon_{II})^2 + (\varepsilon_{II} - \varepsilon_{III})^2 + (\varepsilon_I - \varepsilon_{III})^2]} \quad \text{Eq. 6-10}$$

7 Numerical results

7.1 Influence of neighboring cracks

Neighboring cracks are especially relevant for the PC-CF laminates, due to the high number of cracks present before any mechanical loading. Besides, it is also the material with a high number of dry spots, which might hinder reloading of the transverse plies. To study the influence of neighboring cracks and evaluate the shear lag model's ability to account for differences in relative stiffness (fiber to matrix modulus), all four permutations of boundary condition and load application are analyzed by the FE-model. For most of the specimens, the crack spacing is greater than the in-situ observation area. As a result, the cracking sequence is not available. In the following, the crack initiation sequence will be discussed in the context of local cracking sites.

Figure 7-1 depicts the stress distribution, expressed relative to the stress values calculated for the uncracked case. To the left of the model the next crack is slightly outside zone I whereas at the right the neighboring crack is directly at the boundary. The FE model suggests much faster reloading compared to the shear-lag model prediction of two cracks separated 3.7 mm. Furthermore, dry spots seem to have no significant effect on the reloading distance as the relative stress distribution is only marginally affected. To verify that the analytical shear lag (SL) model indeed underpredicts reloading of the transverse ply, the in-situ strain measurements can also be used. Because the SL-model assumes a linear elastic material response, the stress and strain distributions are directly related.

Figure 7-2 shows a comparison of the strains evaluated on two different EP-CF specimens by DIC to the SL-model's stress distribution. The actual crack positions are marked by dotted lines and the DIC shows only the section observed by the in-situ microscope. Although attempted it was not possible to verify the FE-model of the PC-CF specimens against the strain distribution along a line, due to the low strains leading to cracking in this material. From Figure 7-2, it can be seen that the SL-model consistently underpredicts stresses in the interactive regime. This is in agreement with the literature and one of the reasons why adjustments have been suggested, which are typically calibrated against FE-models. However, all investigated cases lead to scaled stress states in the $(\sigma_{22}, \sigma_{33}, \tau_{23})$ space but no drastic shift between the stress components could be observed. In addition, any shift in this regard is also accounted

for by rotating the RVE in evaluations. Because the extreme cases are of foremost interest and for easier reference only the case without neighboring cracks will be studied further.

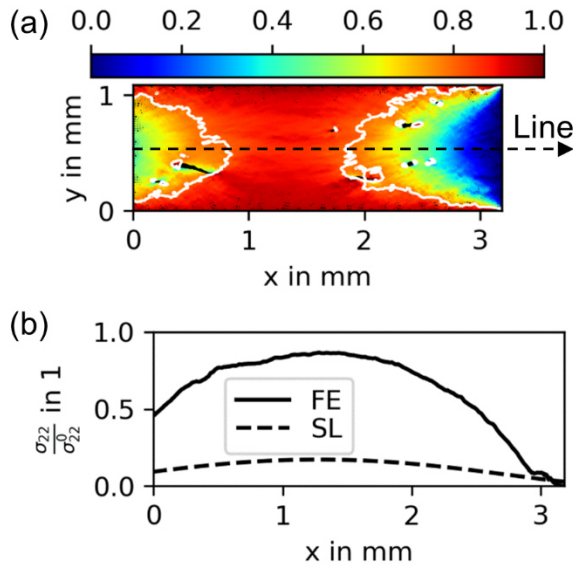


Figure 7-1 (a) Reloading of transverse ply between two cracks calculated by the FE-model; White line marks zones where the stress is above 80% of the uncracked case; (b) Reloading in the corresponding middle line from the FE results and the shear lag (SL) model

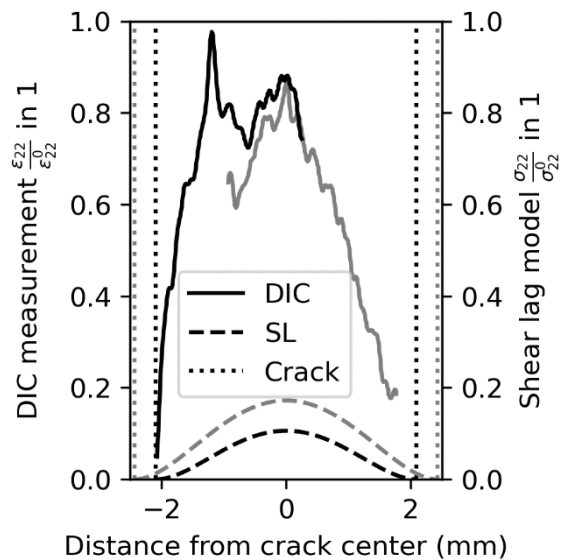


Figure 7-2 Comparison between measured DIC strain distribution and shear lag (SL) model predictions for both analyzed specimens (black and gray lines) with corresponding crack positions; DIC curves end at the fringes of the in-situ observation area relative to the middle between both cracks

7.2 Identification of damage initiation sites

7.2.1 PC-CF

During preparation of the mesoscopic model of PC-CF it became evident that dry spots are typically within a region of high fiber volume content. The latter could only be seen by comparing the microstructure of the microsections to that of the x-ray microscopic images because in x-ray images all fibers are still present whereas in microscopic images an empty void is left. Within the FE-model, a dry spot is captured as empty void with no stiffness. This feature inevitably leads to overstresses at dry spots. Comparing the stress peaks between the mapped fiber volume distribution and an artificial homogeneous distribution with nominal fiber volume content reveals however that stress peaks are further intensified by the surrounding high fiber volume content around dry spots. A measure to quantify the effect could be a stress concentration factor in the σ_{22} - σ_{33} -space. σ_{22}^* of the homogeneous transverse ply with no dry spots is used as reference stress. Since additional stress components in 3-direction can arise

at the dry spots, the first principal stress σ_I is used as effective stress in the notch root i.e. dry spot. Instead of a single value, the 98% percentile of all principal stresses within the observation area of the homogeneous fiber volume solution is used as selection criterion for highly stressed regions. This percentile has been found to capture over stresses satisfactory. The mean stress concentration of elements of this group reaches $\frac{\sigma_I^h}{\sigma_{22}^*} = 1.8$ in the homogeneous (^h) case and $\frac{\sigma_I^d}{\sigma_{22}^*} = 2.7$ with the actual fiber distribution (^d). Figure 7-3 shows the corresponding ratio in terms of the first principal stress $\frac{\sigma_I^d}{\sigma_I^h}$ between both cases. It can be seen that the non-uniform fiber distribution increases the already existing stress concentrations further. From this, it can be concluded that the observed inhomogeneity plays a crucial role for damage initiation. The effects on the microscopic stress state at these crack initiation zones will be discussed further as part of the matrix property effect. Unsurprisingly, all cracks originated from dry spots. With regard to the influence of neighboring cracks no significant change in the stress state at the crack initiation sites occurs. Instead, the stresses are merely proportionally lowered if cracks are present.

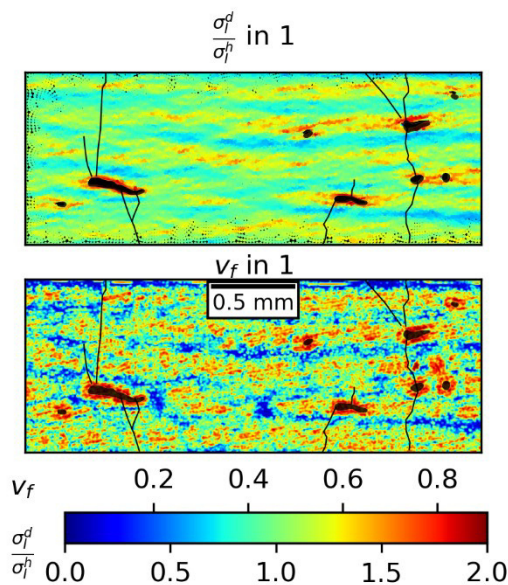


Figure 7-3 Relative overstress in terms of principal stress between the theoretical homogenous (σ_I^h) and actual principal stress (σ_I^d) (top) as a result of the actual fiber volume distribution v_f (bottom). Black patches marks dry spots. Lines mark the cracking paths after fatigue loading.

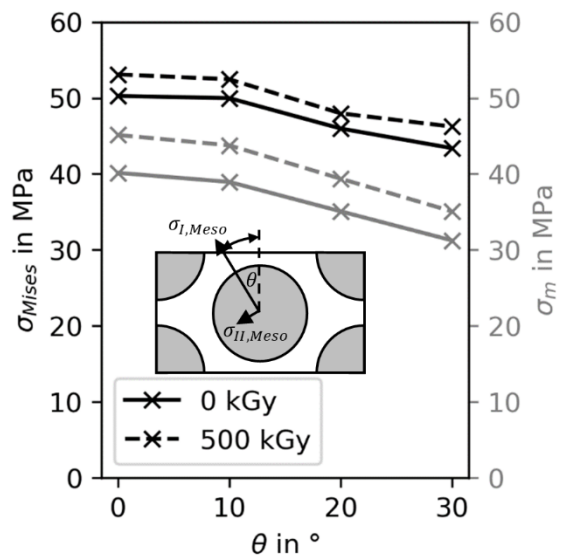


Figure 7-4 Effect of RVE rotation on the 95% percentile of von Mises stress and mean stress within the polymer matrix as a function of the orientation of the RVE relative to the first principal stress σ_I for both irradiation states (changed elastic modulus); See section 7.3

7.2.2 EP-CF

Carbon fiber-reinforced epoxy laminates showed stitching fibers to be the most prominent damage initiation sites. Experimentally some indications like strain jumps could be found pointing towards damage initiating within the stitching. Comparing the experimentally determined strain and the strains calculated by the mesoscopic model supports this conclusion because strain concentrations are visible within the experimentally determined strain map but not in the mesoscopic model. This observation is based on the assumption that the elastic properties within the stitched areas are comparable to those of resin rich areas of the laminate. Two drawbacks in this regard need to be considered. First, definite properties of the polyester stitching fibers can only be estimated to be comparable to those of transversely loaded carbon fibers. Furthermore, the mesoscopic model represents a slice of a laminate extending in the fiber direction of the transversely loaded ply indefinitely. However, the stitching fibers are an exception and violate this assumption especially at the failure prone interlacing points.

The local difference in fiber volume content, however, leads inevitably to significant overstresses within the rovings similar to the effects observed on PC-CF at stress concentrations. The local stresses at the crack initiation sites are 34% above those of a fictive EP-CF laminate in the non-irradiated configuration with a homogenous fiber distribution. This makes failure loads and crack initiation within the transverse layer hugely dependent on the mesoscopic structure and the manufacturing process.

7.3 Elasticity

On the microscale, only EP changed its elastic modulus significantly as result of irradiation treatment. For PC, on the other hand, no such change was observed considering the scatter in elastic moduli of this material. Therefore, the following analysis focuses on EP-CF. In the specimen taken as reference for the fiber distribution and geometry, two cracking sites were identified. For a detailed study of the stress state at these sites, averaged stresses within a search radius of 0.05 mm around the crack initiation point are analyzed and taken as input for the RVE. The search radius is small enough to be within a single ply (thickness 0.25 mm). The average fiber content at the crack initiation site is 56%. The increased elastic modulus of the irradiated epoxy increases the average first principal stress at the crack initiation site

by 7% compared to the non-irradiated configuration. The stress state is essentially uniaxial.

In the second step of the analysis, the mesoscopic stress is applied to the hexagonal fiber arrangement in the RVE. Different invariants can be considered for comparison, depending on which stresses are deemed critical. In the following, the hydrostatic pressure, i.e. the first invariant σ_m , is compared as a measure for principal stress driven polymer failure and the von Mises stress σ_{Mises} as measure for failure by deviatoric stress components. The latter would more likely lead to onset of plastic deformation, as will be discussed in the next section. An evaluation of the 95% percentile⁵ of both measures depicted in Figure 7-4 shows that stress peaks in terms of von Mises stresses are only moderately affected by changes in the elastic modulus of the polymer across all RVE orientations. In contrast to this, the hydrostatic stress component increases. This invariant has already been identified as a main controlling variable for damage initiation in transverse loading [17], [52]. Overall, RVE orientation alters the peak stress but not the relation between von Mises stress and the hydrostatic pressure. Hence, orientation will most likely not alter, which invariant will be critical.

The material's sensitivity to stress changes resulting from alterations in the elastic modulus of the matrix polymer can be assessed using the S-N curves of the neat polymer. This comparison appears prudent since neat epoxy has a low notch sensitivity and therefore the S-N curve is similar despite the presence of stress gradients. As a result, irradiated epoxy laminates should show a shorter lifetime, since both irradiation configurations lead to similar polymer S-N curves. However, this assertion is only possible if macroscopic loading is truly strain controlled and cracking starts within the matrix polymer. A strain controlled loading for the transverse ply was assumed for better convergence and easier definition of the boundary conditions within the mesoscopic model. To correct for this discrepancy the actual change in laminate stiffness can be used to correct the difference in over stresses. Irradiation treatment lead to an increase in laminate stiffness from 29.3 GPa 95% CI [28.3; 30.3] to 31.7 GPa 95% CI [30.7; 32.8]. Therefore, the laminate strain of the given specimen would correspondingly decrease to 0.62% or relatively to the applied strain in the FE model by 7.4%, which is approximately the over stress found in the mesoscopic model

⁵ Stress percentiles are evaluated in order capture an extended region of high stress. The 95 percentile is used as the standard. Only if stress peaks are not captured well does the choice deviate from this value.

at the crack initiation points. This said elastic properties of the polymer appear to be only relevant if strain controlled loading within the transverse layer is truly encountered. The latter depends mainly on the lay-up under investigation.

7.4 Triaxiality

From the elastic model, the influence of triaxiality can also be analyzed. Because no drastic differences in triaxiality are expected, the stress state of the EP-CF can be taken as reference across both CFRPs. Figure 7-5 and 7-6 show the two extreme cases of RVE orientation relative to the mesoscopic principal stress σ_I^{meso} . The black arrow in a quarter of the RVE indicates the loading direction relative to the RVE. Two lines plotted in the σ_m - σ_{Mises} space indicate the triaxiality $\frac{\sigma_m}{\sigma_{mises}}$ of a conventional tensile test with 0.33 and that achieved by the notched round bar in PC of 0.6.

If the mesoscopic load is oriented as shown in Figure 7-5, two distinct points with high stresses can be identified. The most prominent is point A, which is a point of high triaxiality and generally high stresses. From the notched round bar experiments on PC, this type of loading leads to increasing elastic modulus, later yielding and decreasing plastic strain. Furthermore, on a sub-micro level, this highly constraint zone might very well lead to micro cavitation and crazing given the necessary initiation time. Although high triaxiality experiments were not performed on EP the results of others [73], [77] indicate also a stiffening but in contrast to PC a decreasing strength and generally a brittle response because of earlier fracture. Point B in Figure 7-5 marks a zone with high von Mises stress and a moderate level of triaxiality. Despite the relative peak, yielding seems unlikely, due to the aforementioned effects of triaxiality on both matrix polymers. Rotating the RVE relative to the mesoscopic loads shifts the positions of high stresses along the circumference of the fibers. Figure 7-6 reveals lower values for σ_m throughout the model, whereas von Mises stress peaks are shifted in position but not significantly in magnitude. However, in this orientation yielding might take place since at point C the peak in von Mises stress is not a point of high triaxiality anymore. Because any rotation and fiber arrangement might be expected Figure 7-5 gives the most critical loading scenario with high stresses in a region of high triaxiality possibly leading to cavitation and fracture [17]. In addition, the hexagonal fiber arrangement is also one of the most critical, as identified by Baar et al. [109]. In contrast, a rotation

depicted in Figure 7-6 for $\theta=30^\circ$ is likely less critical because yielding is promoted and high cavitation stresses are reduced.

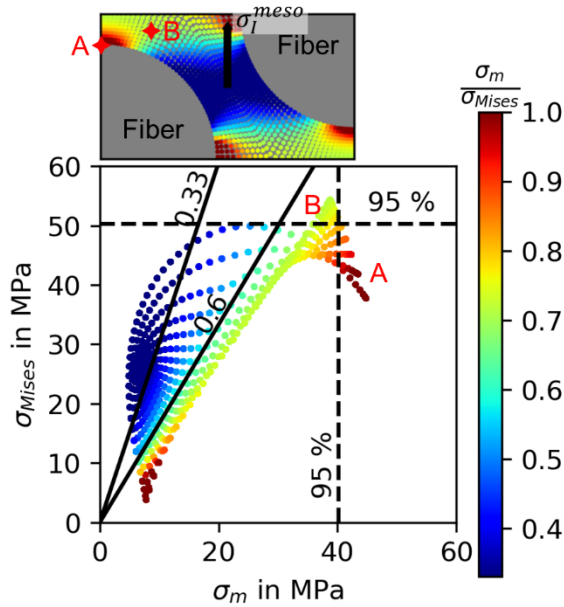


Figure 7-5 Element stresses in the σ_m - σ_{Mises} space and $\frac{1}{4}$ of the RVE with corresponding triaxiality for $\theta=0^\circ$ rotation between the RVE axis and the first principal stress (arrow) of the mesoscopic model at crack initiation sites in EP-CF

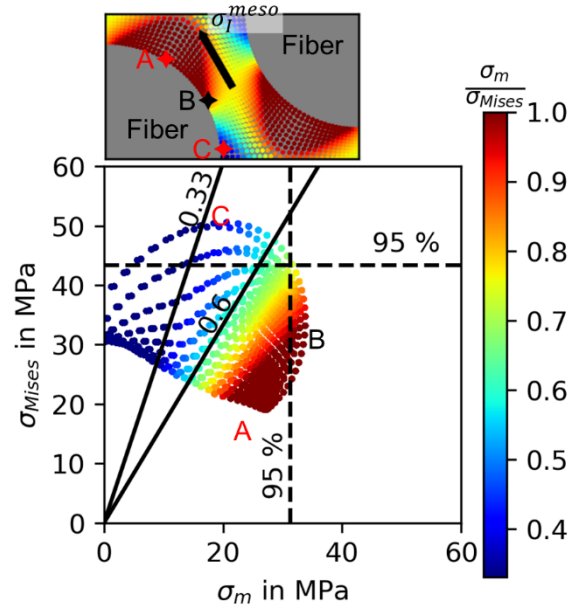


Figure 7-6 Element stresses in the σ_m - σ_{Mises} space and $\frac{1}{4}$ of the RVE with corresponding triaxiality for $\theta=30^\circ$ rotation between the RVE axis and the first principal stress (arrow) of the mesoscopic model at crack initiation sites in EP-CF

7.5 Plasticity

7.5.1 PC-CF

In order to apply Neuber's approximation for reduced stresses by plastic yielding the microscopic scale is studied. Only $\theta=0^\circ$ needs to be analyzed as this is the orientation of the RVE with the maximum von Mises stress as shown in Figure 7-5 for EP. The driving principal stresses σ_I^{meso} for the RVE is again the 98% percentile used before on PC-CF. Figure 7-7 shows the stress overprediction by the elastic solution relative to the stresses approximated by Neuber's approximation. It is anticipated that yielding will occur at point A in Figure 7-5, as it corresponds to the location of previously identified peak stresses. The overprediction is comparable for both irradiation configurations and differences between both states are within 1 MPa. Therefore, earlier yielding appears not to be accountable for the different crack densities of both PC-CF configurations. The Neuber predictions are also based on the stress-strain curve determined on smooth specimens and therefore under a triaxiality ratio of 0.33. From section 5.1.2, however, yielding might be delayed by higher triaxiality ratios and

therefore the influence of plasticity on stress concentrations might be overestimated. Since the notched PC specimens tested as reference for the influence of triaxiality are not able to provide a homogenous stress distribution, a Neuber approximation based on these stress-strain results is not attempted. Figure 7-8 depicts the point at which the 95% percentile of stress within the RVE has been located relative to the stress-strain response of both polycarbonate configurations. This stress state corresponds to the macroscopic strain of 0.4% and a global laminate stress of 60 MPa. The stresses assigned to by the approximation are still in the region of near linear elastic deformation.

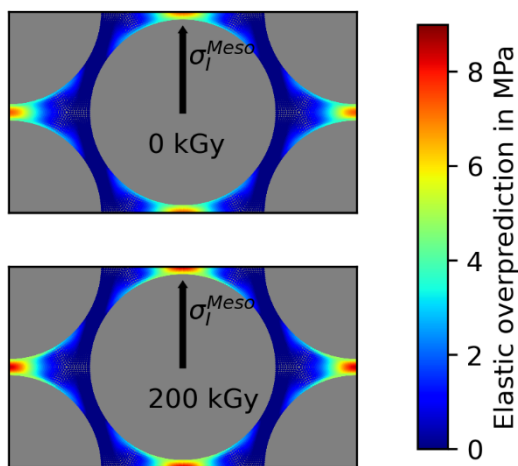


Figure 7-7 Stress overprediction calculated from the Neuber's approximation of reduced stress by plastic yielding for PC-CF in both irradiation configurations

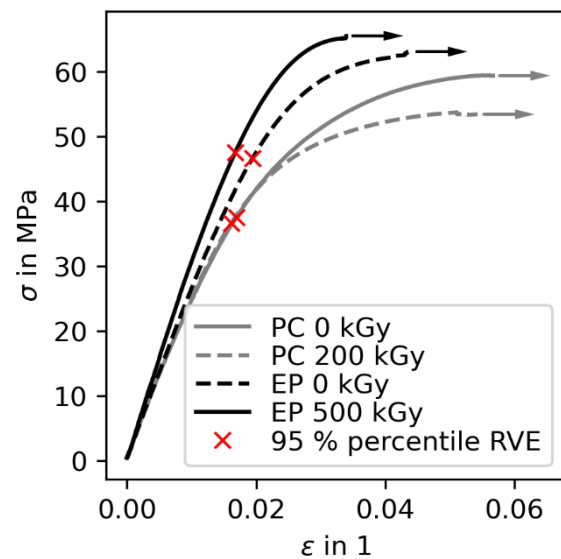


Figure 7-8 Neuber approximation of stress peaks in the RVE plotted in the stress-strain curve of EP and PC in both configurations

7.5.2 EP-CF

An analysis of EP-CF specimens yielded similar results to that of PC-CF, both in terms of elastic overprediction of stress concentrations as well as their relation between both irradiation configurations. The difference in stress overprediction between irradiated and non-irradiated epoxy is within 2 MPa and therefore only minor. On closer examination, Figure 7-8 shows also that the stresses assigned to by the plastic approximation are also in the near linear elastic part of the stress-strain curve.

7.6 Visco-elasticity

7.6.1 PC-CF

As already indicated by the neat polymer characterization, PC tends to relax relatively little in the time scales under consideration. The same is true for the visco-elastic mesoscopic model, where only minor changes between the fully relaxed state and the overstresses after load application within 10 s can be identified (ABAQUS keyword SMOOTH STEP).

7.6.2 EP-CF

A different picture reveals itself for EP-CF. Figure 7-9 compares the resulting stress state within the observation area right after application of a global laminate strain of 0.67% within 10 s to the fully relaxed state. As before, the first principal stress within the σ_{22} - σ_{33} -space of the transverse ply is shown. It can be seen that the material relaxes significantly across the complete cross-section. The stress map of Figure 7-10 shows the corresponding decrease in principal stress. It can be seen that especially fiber rich regions relax more in terms of absolute stresses. In relative terms, the relaxation is in the range of 18 to 23% of the initial stress across the entire cross-section. With an identical geometric arrangement and the irradiated laminate configuration, the results are comparable, although in absolute terms the stresses are higher, similar to the elastic case and the general offset of EP's elastic modulus throughout all times.

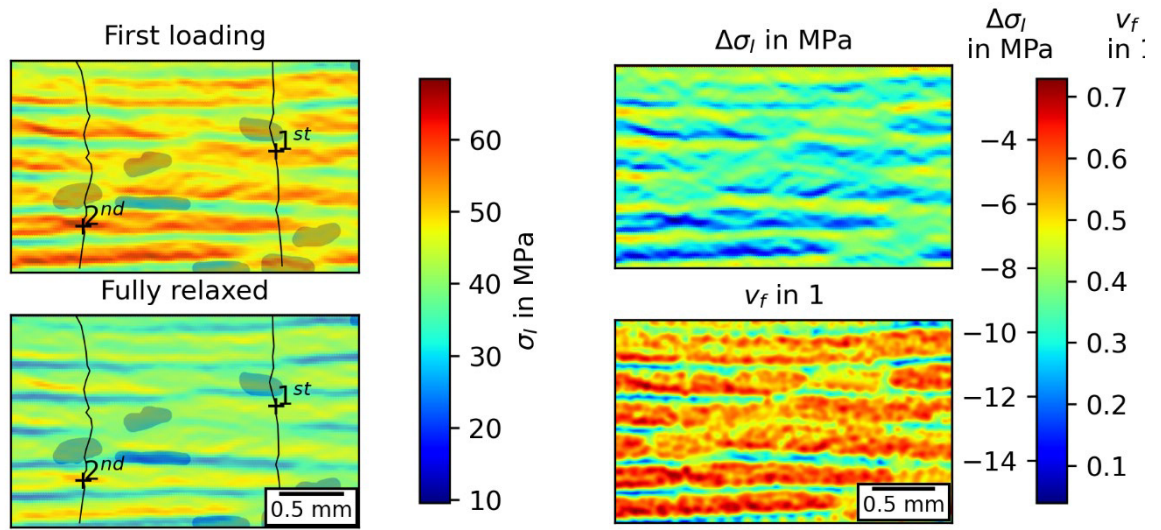


Figure 7-9 First in-plane principal stress within the mesoscopic model right after first loading (top) and in the fully relaxed state (bottom) for non-irradiated epoxy; Dark patches mark the positions of stitching fibers; 1st and 2nd crack initiation points are marked alongside the final cracking path

Figure 7-10 Stress relaxation in principal stress (top) for non-irradiated EP-CF and corresponding fiber volume content (bottom)

8 Discussion

8.1 Tension-tension loading

8.1.1 Macroscopic scale

On a macroscopic scale, a good correlation between crack density and stiffness degradation could be found across all investigated materials. Furthermore, the results also suggest loss energy to be an indicator of damage formation and load transfer between the on-axis and off-axis plies. A major drawback of the latter measure is a relatively low signal-to-noise ratio, which is defined by the amount of damage forming within one load cycle and the resolution of the measurement equipment. However, for the case of EP-GF this measure showed a good correlation to other damage indicators. Although stiffness during fatigue loading might be calculated between two points, this measure of damage appears to be much less error-prone if evaluated on fitted sinusoidal signals of stress and strain and thereby incorporating all available data points of one cycle. In this way, a frequently limited degradation could be measured. However, scattering within each configuration is often high but in combination with the in-situ crack observation and the post-fatigue crack density, the individual specimens could be identified as main source for scattering.

Crack formation within the first load cycle or pre-existing cracks have been found to be a challenging factor in regard to macroscopic damage parameters. This is because early or preliminary cracking will lead to an already reduced initial stiffness and therefore it is likely that parts of the damage formation will be missed. Especially since the stiffness during fatigue is typically evaluated across the complete stress-strain response instead of a very limited strain range used in monotonic loading. The latter would be able to capture early onset of damage during the first loading. In general, stiffness degradation and loss energy on the macroscopic scale should consider the possibility of a flawed material in order to avoid misinterpretations of additional degradation. A good example for this are the results of PC-CF. Here a higher initial crack density in the irradiated configuration leads to a subsequently lower stiffness degradation but not as a matter of improved fatigue resistance but merely because of decreasing damage rates in a later stage of fatigue life. The roles of irradiated and non-irradiated condition were reversed for EP-GF, but the same effect could be observed there.

8.1.2 Mesoscopic scale

On a mesoscopic scale, the in-situ images and FE results showed that the structure is highly relevant for damage initiation. A special role in this regard plays the spatial fiber distribution, which can lead to significant overstresses compared to a homogeneous structure. Under the assumption that similar fiber-matrix combinations lead to similar fatigue strength, the influence of processing and fiber architecture are neglected even though local stress concentrations can arise. As shown by Endruweit et al. [214] compaction affects the shape of the rovings and the resin pockets in between. As a result, the ratio of local fiber volume content to the global fiber volume content is a function of preform compaction. Similar effects can be expected for the tape material as the underlying semi-finished product of PC-CF. Zaami et al. [215] found different fiber arrangements across different tape suppliers and even within a given fiber-matrix combination from the same supplier but for different tape thicknesses. Therefore, it is likely that for identical combinations and fiber content fatigue performance might differ drastically as a result of localized stress concentrations. Further complications might arise moving from coupon specimens to real components as pre-forming can also affect compaction and the local fiber architecture. Multiple cracks within the observation area in EP-GF allow for the analysis of a kind of in-situ S-N curve or strain-life curve, which can effectively eliminate this effect by recognizing local variations in fiber distribution [199]. Although, variations in this regard are kept constant within each laminate type (e.g., EP-GF) the in-situ S-N curve nevertheless allows for an evaluation of both stress/ strain and number of cycles instead of just the number of cycles to failure. Across all three laminates, fiber-rich regions lead to onset of cracking, which could be an indication of both the criticality but also a leverage for optimization.

A second important mesoscopic factor observed especially for EP-CF and PC-CF is inhomogeneity in the form of stitching fibers and dry spots. Both factors are contributing to earlier crack onset. Especially NCF reinforcements are of special relevance because other than pores, stitching fibers are no obvious flaw but just an auxiliary component necessary for processing. If stitching fibers will dominate crack initiation is likely a matter of competing S-N curves. Namely, is the S-N curve of the stitching more critical or that of the neighboring transversely loaded roving. For EP-CF the observed strain concentrations within the stitching fibers points toward early onset of cracking within this zone. In contrast to this, EP-GF showed multiple cracks within the rovings

indicating these zones to be more critical than the stitched areas. Although both laminates have a similar fiber architecture, the relative constituent's properties are vastly different. The elastic moduli of transversely loaded carbon fibers and polyester stitching are comparable, whereas glass fibers show a five times higher elastic modulus. This might explain the dominant role of stitching within EP-CF compared to that of EP-GF. In the latter, stress concentrations are presumably drastically higher within the rovings compared to those in the stitched areas.

For PC-CF, a critical feature could be found regarding dry spots, since their severity in terms of stress concentrations is further increased by the fringe of densely spaced fibers surrounding the voids. This also explains the very low strain levels necessary to introduce transverse cracking in PC-CF.

8.1.3 Micro and sub-micro scale

Following the conceptual framework used to analyze and categorize the polymer properties first the influence of homogeneous deformation will be discussed followed by crack initiation and propagation. If the elastic modulus of the polymer will affect the stress state within the matrix is mainly a matter of the overall laminate lay-up. For the case that the transverse layer contributes only minor to the overall stiffness, this leads to strain controlled loading within the transverse plies with implications for the over stresses encountered within the rovings and subsequently the polymer as suggested by the FE modelling results of EP-CF laminates. However, despite an increase of 18% in the elastic modulus of the polymer the resulting laminates show only an increase by 8% in macroscopic stiffness. So even for the lay-ups under investigation, the feedback of the polymer's elastic properties on the strain load is limited even though transverse plies make up 75% of the total laminate. This said an increasing elastic modulus of the matrix polymers would also increase local stress concentrations, making the laminate more failure prone. Especially since the S-N curve of unreinforced EP did not change due to irradiation treatment.

A more detailed discussion can be done by comparing different lay-ups and the effect of the polymer's elastic modulus on the overall laminate stiffness. Figure 8-1 compares the influence of the matrix modulus for two cross-ply lay-ups. One laminate is fictive with a low transverse ply content and the other corresponds to the actual lay-up for the CFRP laminates within this work. It can be seen that the investigated lay-up is one with relatively high impact (slope of the curve) of the polymer's elastic modulus on the global

laminate stiffness whereas a reversed ratio would diminish this. For laminates of the first category only a minor influence of the matrix polymer stiffness can be expected but with decreasing contribution of the matrix stiffness to the overall stiffness the elastic modulus might become more dominant because loading in the transverse ply effectively shifts to strain controlled loading. EP-GF laminates are less sensitive to the elastic modulus because the transverse layer carries more of the overall load in the first place. This is because the on-axis layers of CFRP draw more of the total load, due to their higher stiffness. This finding is in agreement with the findings of Li et al. [48], who found only a marginal difference between strain and stress controlled loading for laminates where on-axis loaded plies dominate the overall response. In this case, the transverse ply will essentially experience strain controlled loading despite the global stress control.

However, because in the investigated laminates the transverse plies carry significant load the changes in elastic modulus cannot explain the difference in crack density and would suggest a higher crack density for irradiated EP-CF. If strain controlled loading of the transversely loaded plies would be present and stress concentrations would be higher in irradiated EP-CF, this would lead c.p. to a higher crack density in the irradiated configuration. Quite the opposite was found experimentally. The analysis of the EP-GF laminates support this argument because the evaluation of maximum stresses at cracking sites is not based on the FE model but on direct evaluation by in-situ DIC in the transverse ply. The results clearly show that despite higher stresses in irradiated EP-GF crack onset is delayed in terms of both stress and number of cycles. As suggested by Figure 8-1 the transverse plies of EP-GF are more in stress controlled loading compared to those in EP-CF and still the increase in global laminate stiffness cannot prevent higher stresses within the transverse plies. This has the effect that from an 18% increase in the polymer's elastic modulus, the macroscopic stiffness increase is diluted to only 8%, due to the contribution of unchanged stiffness in the remaining constituents.

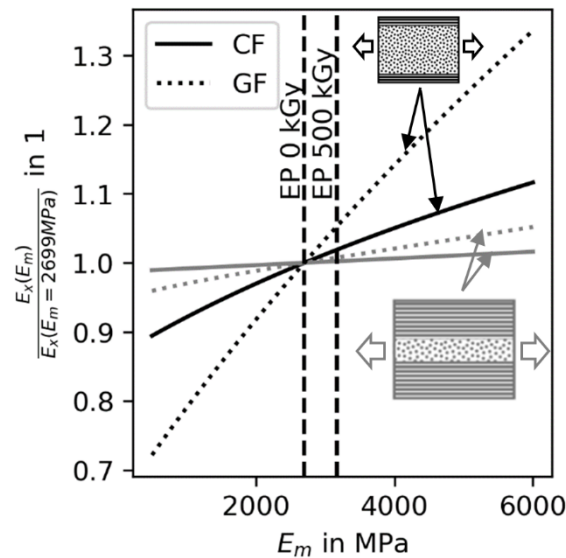


Figure 8-1 Effect of matrix modulus compared to the overall laminate for two cross-ply lay-ups of EP-CF and EP-GF laminates

In terms of plastic and visco-plastic deformation, it was found that plasticity might alter the stress state in highly loaded areas, preferably for $\theta=0$. However, these zones are also areas of high triaxiality and strain rates with implications for the polymer's stress-strain response, i.e. stiffening and delayed yielding for PC. In the case of EP stiffening was also observed by Asp et al. [77] for triaxial stress states but also a lower strength and ductility [73], [77]. In terms of strain rate Kody and Lesser [78] found an increasing yield strength for EP at higher strain rates, too. Even if yielding occurs, it is likely limited to zones of high fiber volume content with subsequently higher stress concentrations. This is because only limited plasticity is predicted by the Neuber's approximation, despite presumably overestimated plastic flow (time and triaxiality effect). In addition, the RVEs under investigation represented the most highly loaded areas within the transverse plies, where cracking was experimentally evident in PC-CF and EP-CF. Another indication of limited plasticity is found in a small global hysteresis in the absence of cracks. Furthermore, local strains did not show signs of non-linear behavior from the in-situ evaluation of strains in the time-strain signal. Finally, it needs to be considered that plastic yielding, if present cannot explain the different damage states between the material configurations, which agrees with only minor differences in plastic stress reduction observed across both CFRP materials in both configurations. An additional point not considered within this analysis is that plastic yielding could also affect the subsequent resistance to cracking and craze formation. For example does a reduced stress not always lead to prolonged fatigue life in pre-yielded PC [105].

Both numerical and experimental results show, that time-dependent polymer properties can significantly alter local stress states. However, given the fact the most transverse cracks formed very early in the fatigue life across all materials it would be necessary that viscous overstresses relax fast compared to the S-N curve of the transversely loaded ply. Since it was not within the scope of this work to determine the S-N curve of a transversely loaded ply, a comparison based on the polymers must suffice to show this point. Figure 8-2 and 8-3 directly compares the stress relaxation of an arbitrary constant strain applied to the polymer relative to its S-N curve. The S-N curve is adjusted to $R=0.1$ by Goodman's approximation from the experimentally determined S-N curves at $R=-1$. The relaxation behavior is calculated for a step loaded Wichert model parametrized in section 5.1.3.2. A major difference between the materials under investigation is the slope of the S-N curve relative to that of the relaxation curve. For EP, both slopes are comparable, which could suggest that under constant strain amplitude loading, the polymer may relax at a sufficient rate to remain consistently below the S-N curve. In contrast to this, PC relaxes slower, which leads to earlier crossing with the S-N curve and therefore earlier failure. A change in relaxation behavior during fatigue loading appears unlikely since both materials did not show any significant changes in their stress-strain response during fatigue loading of the neat polymer specimens. However, as already discussed in the course of the rheological characterization of the neat polymers, irradiation cannot significantly alter the relaxation but merely leads to an offset in the relaxation modulus comparable to that observed in tensile experiments. The latter offset remains constant across the investigated time scales. Subsequently, differences in relaxation behavior might explain earlier onset of cracking in PC compared to EP but not within one material and both irradiation states.

Although the discussion so far focused on the effect of relaxation in the context of the polymer's S-N curve, it is important to note that on a mesoscopic scale fiber rich regions shed more load compared to the rest of the laminate. Considering the fact that the stress concentration is also a function of fiber volume content the highest loaded zone within the inhomogeneous transverse ply relax more, which is c.p. positive considering unaffected S-N curves of the constituents. Relaxation was more pronounced for EP, which shows also slower crack propagation rates if the mean stress is lowered [113], [120].

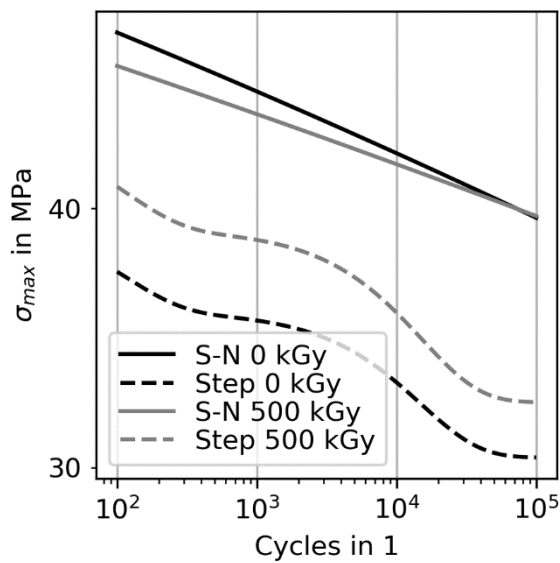


Figure 8-2 Relaxationspeed from step loading to mean strain relative to S-N curve estimated for 2 Hz loading frequency for EP

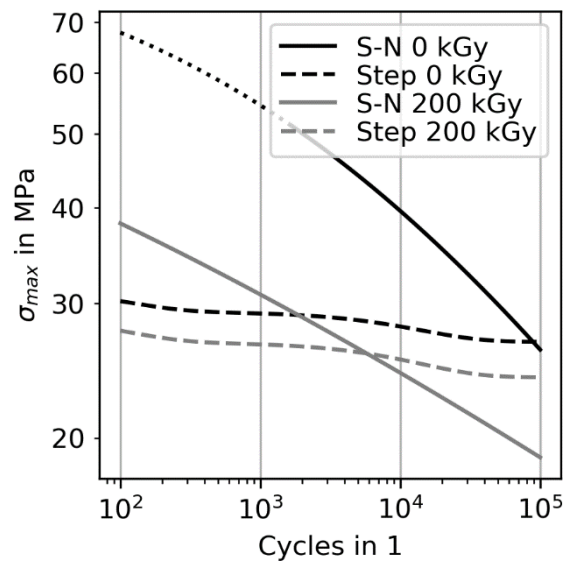


Figure 8-3 Relaxationspeed from step loading to mean strain relative to S-N curve estimated for 2 Hz loading frequency for PC

The effect of visco-plastic deformation appears to be even more relevant, since the visco-elastic model consistently underpredicts relaxation at higher strain levels. Therefore, unloading might be even more pronounced in failure prone fiber rich areas if visco-plastic effects are present. This is because the matrix in these areas is subjected to especially high strains.

Closely related to visco-plastic deformation is the concept of inhomogeneous deformation and the MSF-model of the polymer. As suggested by the literature review this behavior is more likely in PC for highly constrained loading conditions described within this work in terms of triaxiality. Time furthermore lowers craze initiation stresses and makes it effectively a visco-plastic mechanism. These aspects were also found for both PC configurations. However, craze stability was found to be drastically different and much lower for the irradiated PC. Hence, less stable crazes in the irradiated condition might explain the lowered fatigue performance. Especially since crazing has been identified in the literature as precursor of fatigue cracking in the DCG regime. Furthermore, stable crack growth and fracture toughness appeared to be mainly unaffected by irradiation treatment. Within the MSF-model this would point towards DCG as main difference between both PC configurations. Crazing and DCG could both explain differences in crack density within irradiated PC-CF, both after irradiation treatment (before mechanical loading) and fatigue loading. First, less stable crazing could lead to earlier cracking also in a constant load scenario like for example residual

stresses. This could be a possible explanation for an increased crack density found in irradiated PC-CF before any load application. Another indicator for this argument are craze morphologies present in the fractured specimen of the irradiated configuration (section 5.4 fiber-matrix adhesion). Since the specimens were fractured rapidly crazing was likely already present before fracture of the specimen because in any rapid loading scenario no crazes could be found in PC within this work. Second, a less stable craze could also shorten DCG or skip this phase altogether in highly loaded zones. Therefore, micro voids forming in the highly loaded zone between fibers likely forms an unstable craze. The same applies for existing debonds, which might also connect more rapidly if the DCG is shortened depending on the stress intensities active in such regions.

An important feature in this regard is the fiber-matrix adhesion, which appears to be higher relative to the PC's strength for the irradiated configuration. Still, it seems unlikely that fiber-matrix adhesion improved by irradiation treatment, since this would contradict the observed higher crack density in PC-CF. A similar contradiction arises concerning residual stresses, which were found also to decrease by irradiation treatment. This leaves deterioration of the irradiated PC's resistance during DCG as major driver of damage overcompensating lower residual stresses and possible but unlikely interface improvements. Residual stresses are assumed to be tensile stresses within the transverse ply, due to a higher shrinkage compared to the on-axis plies.

Within EP, no inhomogeneous deformation mechanisms could be observed in both configurations. In terms of the MSF-model, fracture toughness appears to be the most significant difference between both irradiation states, whereas crack initiation and propagation remains mostly unaffected. In addition, stress concentrations seem not very harmful to the fatigue performance of the material. Therefore, the resulting S-N curves for both configurations are nearly identical and are not significantly altered by stress concentrations around the fibers. Crack initiation within the polymer appears to be unlikely as cause for cracks in EP-GF and EP-CF, since crack growth and final fracture contributes little to the overall lifetime of the neat polymers (S-N curves).

From the literature and the microscopic images, it is clear that cracks adhere mostly to the fiber matrix interface. In terms of fiber-matrix adhesion, also no change could be detected for both EP based laminates across both configurations. If debonds are the primary mechanism of damage and irradiation treatment has minimal impact on the

crack growth phase, the primary distinction between the two irradiation states is the occurrence of unstable crack growth resulting from a series of debonds. It can be argued that the latter would henceforth become critical at an earlier stage for the irradiated EP, due to a reduction in fracture toughness in this configuration. In any case, this is again contradicting the experimental finding for fatigued laminate specimens. The only remaining explanation to the phenomenon are residual stresses, which are tensile in nature within the transverse ply. Irradiation treatment reduced these. Since a reduction in residual stresses will directly lower the stress intensity, which may result in an overcompensation for the reduced fracture toughness of the irradiated EP. In addition, slower fatigue crack propagation rates might also result from the lowered mean stress or stress intensity. The relatively large scattering in residual stress reduction may also reflect the fact that only some irradiated EP-CF specimens exhibited drastically lower crack densities. For EP-GF debonding and coalescence of debonds is the main driver for damage and reduced residual stresses could also explain delayed cracking. For both EP-GF configurations, the stress intensity at the crack tip was below even the lowered fracture toughness of irradiated EP because cracks were effectively stopped by resin pockets between the rovings. That cracks can be arrested by resin pockets or layers can be explained by faster crack propagation rates in plane strain conditions mainly experienced in fiber rich zones [97]. This aspect might explain in part also the rapid crack propagation for all materials once a crack formed, because for PC highly constrained crack tips are also reported to accelerate fatigue crack growth [122], [123], [124].

8.1.4 Damage state

A flawed material approach is necessary to capture and understand early damage formation in all six investigated laminates and configurations. The most prominent example within this work is PC-CF, with different initial crack densities obscuring to some degree the matrix influence on crack propagation. However, even for materials with evidently no obvious flaws after manufacturing, small debonds are often present as can be seen from the in-situ strain analysis. In the case of EP-CF, these flaws are mainly located in interlocking regions of stitching fibers. Similarly, cracks evolve during the first loading cycle of the non-irradiated EP-GF. This could also lead to a kind of pre-damage, as damage in such an early stage of loading is easily missed. In all but one case, it appears that fiber-matrix adhesion is very limited. Only for the case of

irradiated PC-CF, it appears that the matrix fails before the fiber-matrix interface. Under these conditions, a flawed material approach appears to be in order. Figure 8-4 shows how pre-damage can effectively define which material response will be addressed within the MSF-model for the example of debonds, e.g., homogenous deformation or small crack growth. After debonds initiate, the results show that from there on the matrix polymer can effectively only slow down or prevent further cracking. Crack initiation within the matrix polymer appears unlikely and might only be the case for irradiated PC-CF.

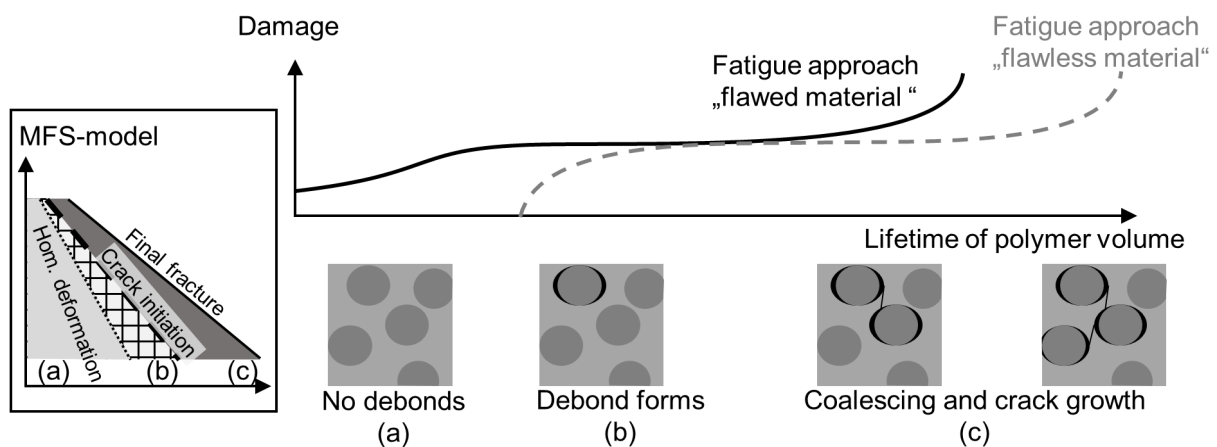


Figure 8-4 Distinction of relevant polymer properties (categorized in the MSF-model) depending on a flawed and flawless transversely loaded ply

8.2 On-axis compression-compression loading

Since it was not possible to observe damage formation under compression directly, the causes of damage on the microscale can only be derived based on the three different types of loading employed for on-axis compression.

Within the reign of homogeneous deformation, the influence of the elastic modulus but also the yield strength of the polymer on the kink-band initiation stress could clearly be observed. Figure 8-5 correlates the calculated shear modulus G_{12} at 10^4 s of the laminates to the compressive strength in monotonic loading. However, a similar correlation can also be found to the polymer's yield strength, depicted in Figure 8-6. Since both elastic modulus and the polymer's yield strength show also a correlation, identifying the main controlling variable becomes challenging. However, a self-reinforcing effect might be at play because a higher shear modulus of the composite effectively prevents excessive kinking and lowers shear stresses. This follows the common assumption that kink bands mainly initiate at misaligned fibers. Secondly, a higher yield strength of the polymer allows for even higher laminate stresses before

the tangential stiffness decreases. The correlation coefficients are 0.93 and 0.91 for the shear modulus G_{12} and the polymer's yield strength relative to the compressive strength, respectively. At the same time, G_{12} and the polymer's yield strength are also related with 0.9. Therefore, it is not possible to separate the effects of elasticity and plasticity. An important role of both is already documented in the literature by numerous analytical and numerical models.

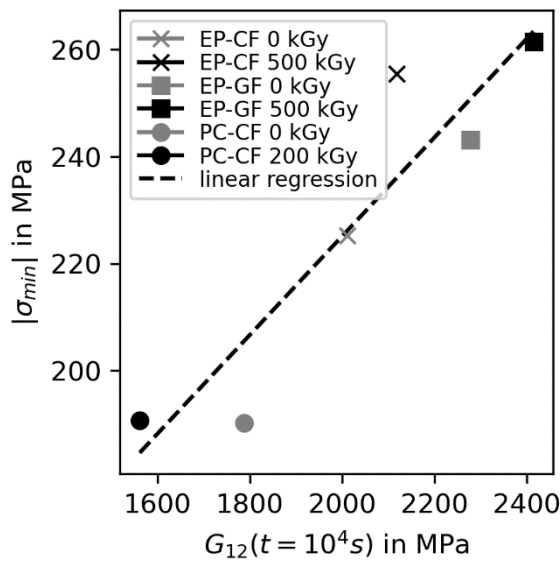


Figure 8-5 Influence of the laminates shear modulus G_{12} calculated from the constituent properties on the static compression strength determined in quasi-static compression tests

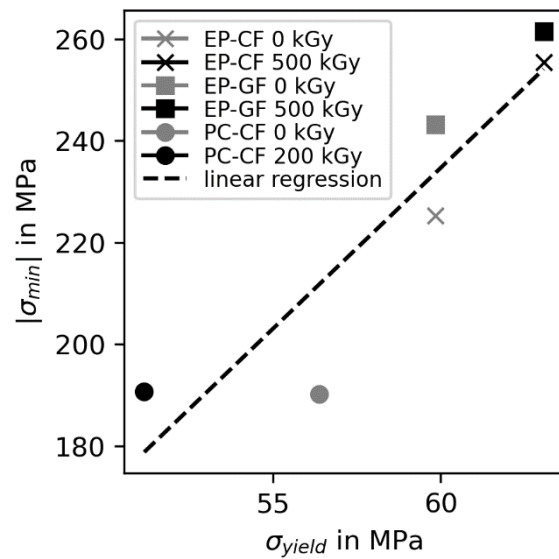


Figure 8-6 Influence of the polymer's yield strength on the static compression strength determined in quasi-static compression tests

Another relevant polymer property could be visco-elastic or visco-plastic deformation. This conclusion stems from higher failure loads under fatigue loading compared to the monotonic compression strength. To investigate this point further trapezoidal loading was employed and lead to lower failure loads compared to sinusoidal loading. The main difference between both signals is time under load, which accumulates much more rapidly for trapezoidal loading. If loading rate is the important factor, the difference between both signals is marginal in terms of time to reach peak load because the difference is only 0.025 s. The effect of loading rate on a time-dependent crack resistance would need sinusoidal and trapezoidal loading to be below the monotonic load, since for both materials fracture toughness is reported to decrease with increasing strain rates at least for mode I loading [87], [97]. Figure 8-7 shows the dependence of failure load for three different loading signals as a function of the laminates shear modulus. Arrows indicate the relative change for each configuration

with respect to the monotonic results. Both PC-CF and EP-CF show decreasing failure levels for trapezoidal loading compared to sinusoidal loading, which indicates an effect of time under load as relevant parameter. The effect is clearly visible, except for irradiated PC-CF, where a higher initial crack density might obscure the time dependence. If this time dependence is a matter of homogenous polymer deformation or crack propagation cannot be clarified from the results. The only indication that crack growth might be more relevant can be found in a relatively low correlation to all time dependencies, such as the slope of the TTS relaxation master curve. The assumption in this correlation attempt was that a steeper slope would encourage a more pronounced difference between the loading signals.

EP-GF laminates were not investigated under trapezoidal loading, due to the limited number of available specimens. It is this type of reinforcement, which differs from the rest in both configurations because sinusoidal loading decreases the failure load. A possible difference between EP-CF and EP-GF could be the presence of debonds visible by light transmission in EP-GF, whereas no debonds were visible in microsections of EP-CF. This might leave a relatively weak fiber-matrix interface under fatigue loading as explanation for EP-GF. It is possible that the same plot as in Figure 8-7 with the current shear modulus (including debonds etc.) of the specimens shortly before failure would again correlate all materials and configurations just like the monotonic correlation. Under this assumption, the shear modulus of EP-GF shortly before failure would be more in the range of PC-CF in the irradiated state and therefore degraded by approximately 35%.

These observations on the role of additional damage on the kink band initiation stress under fatigue loading highlights the importance of this factor. Again, the fiber-matrix interface might play an important role in this regard, whereas the role of crack initiation within the matrix polymer is most likely limited. This is because the correlation between failure load for sinusoidal and trapezoidal loading and the polymer's failure load for 10^4 cycles is low.

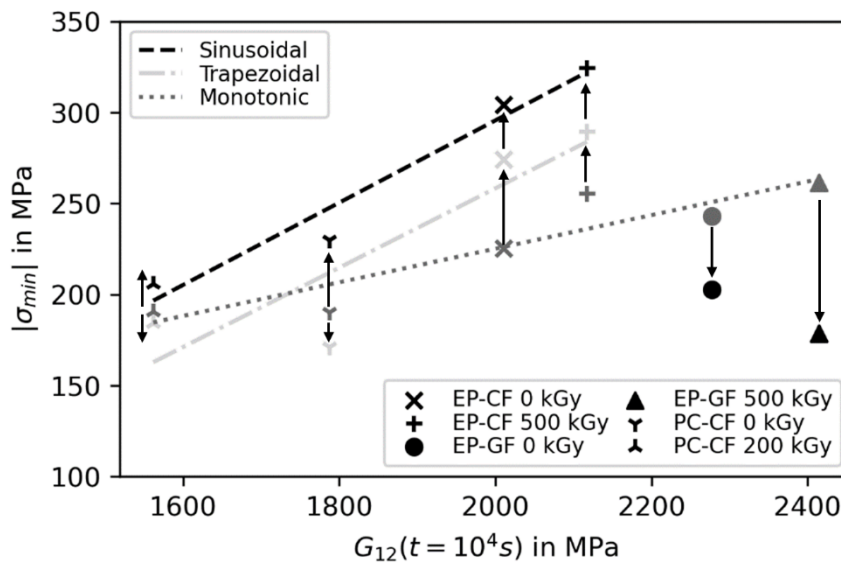


Figure 8-7 Laminates shear modulus G_{12} calculated from the constituent properties vs failure load under different loading conditions; Each laminate and configuration corresponds to a vertical line of constant G_{12}

8.3 Conflicting requirements

The aforementioned discussion for both off-axis tension-tension and on-axis compression loading shows that the requirements for the matrix polymer depend on the loading scenario, pre-damage (flawed fatigue approach) as well as on the lay-up. For transverse tension loading, it is required to shift load away from critical areas like pores or fiber rich zones in transverse tension. The exact opposite is necessary for on-axis compression. In terms of the developed framework, this requires a ductile low stiffness matrix polymer for transverse TT loading which keeps its ductility despite high triaxial stress states, i.e., red and green zones in Figure 8-8. On-axis CC loading, however, requires a high elastic modulus and high yield strength. For both loading scenarios, these properties need to be sustained during fatigue loading and therefore low degradation both in terms of strength and elastic modulus are preferred. Property maps provide a possible tool to locate suitable polymers in the relevant property spaces. Figure 8-8 shows the investigated polymers in the space of endurance limit under $R=-1$ and elastic modulus reported by Fleck et al. [216]. The values found within this experimental series are extrapolated with the S-N curve's regression to 10^7 . This extrapolation probably underestimates the endurance limit. Three distinct targets for the polymer properties can be distinguished based on the applied load and stacking sequence. For low transversely loaded plies, a compliant matrix polymer with high endurance limit might provide late onset of cracking, since loads will mainly be carried

by on-axis plies in cross-ply lay-ups. In contrast to this, a high content of transversely loaded plies will naturally carry more of the transverse load and the benefit of a lowered elastic modulus will depend on the trade-off between elastic modulus and endurance limit. The property maps by Fleck et al. [216] and Unwin et al. [217] show that many properties are related nearly linear in logarithmic scale. This agrees well with the correlation of yield strength and elastic modulus of both configurations of EP found within this work. The correlations might be extended also into the space of time-dependent properties as the map of Unwin et al. [217] suggests by the reciprocal relation between elastic modulus and the damping coefficient (ratio of loss modulus to storage modulus). For on-axis CC loading this aspect might play a more prominent role, due to the dependency on the loading signal. The latter would require mostly the blueish area marked in Figure 8-8 of high elastic modulus, high fatigue resistance and high yield strength. The elastic modulus could also be replaced by the relaxation modulus of the polymer, which should remain high during load application or inversely a constantly low creep compliance.

With respect to fracture mechanical properties, no significant differences except for the fracture toughness of irradiated EP were found within this work. Here the inverse correlation between elastic modulus suggested by Sohi et al. [138] could not be observed. However, given the property maps already discussed, a fixed relationship between the two across different polymers is likely.

With respect to the relative positions of both PC configurations in the property map, this might be one explanation for the generally very low fatigue performance of those laminates evident by the very low strains to onset cracking.

While property maps appear as a helpful tool for a rough selection, the results also suggest that a slightly altered macromolecular structure can significantly impact the fatigue performance of the laminate despite relatively small changes in the polymer properties (e.g., the case of PC). Thus, while beneficial, property maps should be used with an understanding of their limitations and the specific context of their application.

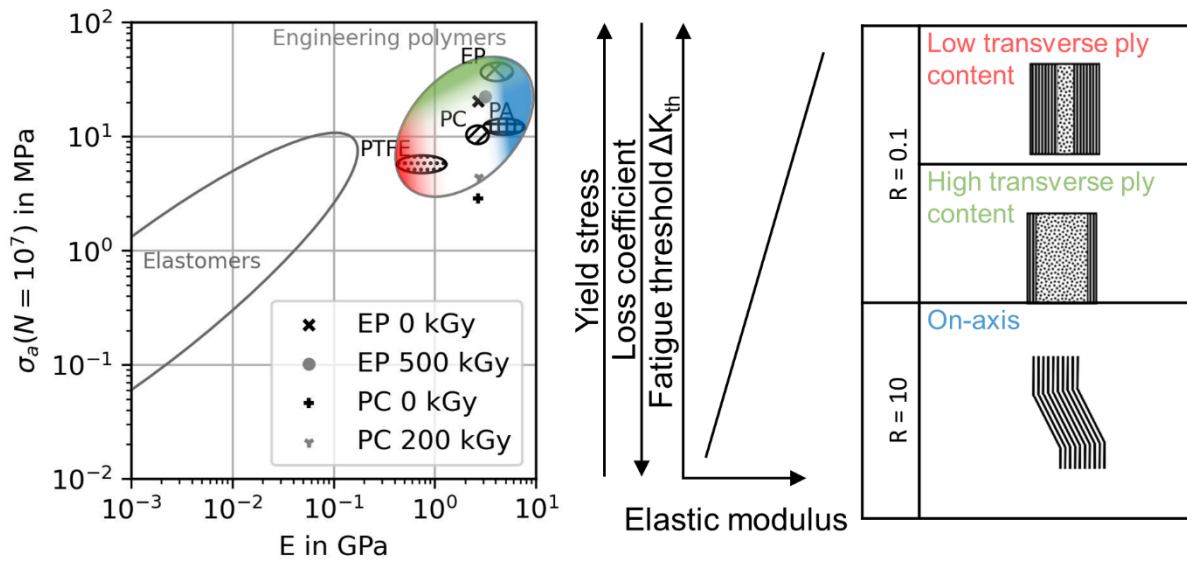


Figure 8-8 Target areas as a function of loading scenario; Correlation of the endurance limit and elastic modulus (data points found within this work are included to show the relative position); Property map adopted from [216]

9 Conclusion

It was the aim of this work to generate a deeper understanding of the matrix polymer's role in the fatigue damage of laminates for two loading scenarios with reportedly high relevance of the matrix for the overall performance. An answer to this question is one building block in addressing the question of a fatigue optimized laminate configuration. Closely related to the aspect of configuration is the arrangement of fibers, voids and matrix polymer across the different scales of any laminate. Although homogenized ply-by-ply analysis is a mighty tool for the design and evaluation of composite structures, it was also found to be non-conservative if local inhomogeneity exists beyond what is expected on the fiber-matrix level or was present in coupon specimen characterization underlying dimensioning. In-situ observation and an extension of a mesoscopic model capturing the fiber distribution was shown to be a viable tool in determining an in-situ S-N curve, which could be used to account for changes in compaction and fiber distribution.

In fact, the contribution of stitching fibers, voids and inhomogeneous fiber distribution in damage initiation might far exceed that of the matrix polymer. Especially since most properties are in a fixed relation and therefore can be adjusted only within a very limited range. A limiting factor across all investigated laminates and configuration is fiber-matrix adhesion, which often fails very early in the fatigue life. The matrix polymer therefore can only prevent early damage by unloading damage prone areas very early and contain already existing damage. The first part of this requirement is mainly found within the homogenous deformation phase, whereas the latter aspect is related to fatigue testing of notched specimens and generally fracture mechanical approaches. Therefore, the distinction between the flawed and flawless materials appears to be highly relevant with the flawed material being the one most likely experienced.

The assumption of a flawed material then agrees with the findings of many other works highlighting the importance of fracture toughness. Although within the findings of this work, the fatigue threshold leading to the first propagation of cracks appears to be of higher relevance. The introduction of a homogenization level between the fully homogenized ply and the resolved fiber-matrix arrangement in a mesoscopic model (meso and micro scale) was found to be a viable tool to investigate the load redistribution at unevenly distributed fibers and flaws. Furthermore, the concept of cells extended to visco-elastic properties is necessary to get a better understanding of the

time-dependent load transfer on this newly introduced intermediate scale. The experimental verification of cracking sites could be done via in-situ microscopic imaging for TT loading. In contrast to this, on-axis CC loading proved to be much less accessible to in-situ methods, not only because of the test set-up but also because kink band failure was found to be a sudden event. Although the monotonic compression strength aligned with literature suggestions on the role of the composite's shear modulus and matrix yielding during fatigue loading, additional damage mechanisms like debonding were found to be important for cyclic loading.

Different requirements for the polymers properties could be identified, despite the prominent role of flaws and voids in damage initiation. It was found that the requirements could differ depending on the macroscopic loading case and lay-up. Would transverse TT loading require a polymer with low yield strength, fast relaxation and generally low elastic modulus to limit overstresses are the requirements for on-axis CC loading exactly reversed. Based on property maps, it also became clear that some property combinations are unlikely to be found in currently available polymers. Furthermore, the results show that a thorough polymer characterization is necessary to capture all relevant properties and estimate the fatigue performance of a laminate. The characterization needs to be close to the loading conditions the polymer is subjected to, as part of the composite. Including effects like stress state and type of applied loading. In addition, PC also shows that even within a relatively narrow band of standardized properties (e.g. results of tensile test) major differences might arise from specifics like unstable crazing or triaxiality.

The unintended modification of residual stresses by irradiation treatment suggested that changes in residual stresses could easily obscure changes in polymer properties. Despite this, high-energy irradiation has been found to be a viable tool for modifying polymers and laminates without affecting the highly important fiber-matrix arrangement across the laminate. A major downside of this modification method is relatively high scattering within the polymer properties after irradiation treatment and more or less unpredictable changes. The latter necessitates a trial run before selecting the polymers to study in detail. Inadvertent changes in the residual stress state of the two polymers under investigation might also be a useful side effect of irradiation treatment if deterioration can be avoided.

10 Outlook

On-axis compression loading is a loading scenario, which experienced some attention especially for monotonic loading and numerous analytical and numerical models have been proposed. However, a full understanding of the driving mechanisms is still not reached. Within this work, debonding and additional damage like longitudinal cracking are believed to interact with the formation of a kink bands. Two extensions to this work could close some of the gaps between the models for monotonic loading and fatigue loading. First, the already implemented procedure to generate a sub-meso FE model could be used again to gain some more insights into the driving mechanisms and construct the possibility to drive an RVE sub-model. X-ray microscopic images could be used as a source for capturing misalignment and fiber distribution, as long as the trade-off between resolution and scanned volume can be overcome. Such a model could provide a more detailed understanding of increasing failure loads as a function of the loading signal. In addition, shear properties and fiber-matrix adhesion are highly important aspects and should be investigated in more detail for better kink band predictions under fatigue. Second, a notched specimen appears to be a suboptimal method for the investigation of kink band initiation in fatigue since the combined loading will likely change as a result of longitudinal cracking. Therefore, an improvement to the experimental method would be the use of pipe-like specimens in a compression-torsion set-up allowing for a defined combined loading. Furthermore, it would be possible to determine intermittently the shear modulus as a function of compressive cycles.

In TT loading transverse to the fiber direction inhomogeneous fiber distribution could easily affect the performance of a laminate drastically and might even vary across a component, due to differences in compaction. The latter parameter might be an interesting option to study the influence of fiber distribution on the fatigue performance of a laminate. A far-flung goal would be the establishment of manufacturing knockdown factors, which could be used to modify the coupon level specimen's fatigue performance accordingly.

A future goal across both loading scenarios would be to incorporate time-dependent properties more thoroughly. Ideally, this would require an extension of the model of cells or a comparable homogenization approach to plastic and visco-plastic polymer responses. The benefits of such an extension would be to close the observed gap between the visco-elastic polymers responses characterized at low strains to a more

realistic relaxation at typical strain levels. A major challenge in this regard will likely be the path dependence in combination with numerous applied cycles, which might lead to an accumulation of errors. Still, crazing and other morphological changes call for such an approach and might be captured by for example a multi-state material model [218] for the polymer. This point appears especially relevant for the important class of semi-crystalline polymers, which should be included in any extension of this work, too.

11 Appendix

A. Triaxiality in different testing methods

A major concern during the characterization of the neat polymer under enhanced triaxiality was the seemingly inconsistent evidence towards the role of hydrostatic pressure. A possible explanation could be that different testing methods yield different stress states expressed in terms of principal stresses but with identical triaxiality and pressure. A reduction of potentially 3D stress state to two variables will incorporate some information loss. To show this point, three different stress states are compared. First, in Figure 11-1 the pipe under inside pressure and with additional axial loading is shown. In this scenario, the natural combined loading with axial and tangential stresses, will lead to a triaxiality of 0.6 and can be reduced by additional axial loading either in tension or in compression, as shown in Figure 11-2. A third stress component is introduced by the inside pressure, although this stress will typically be low compared to the axial and tangential stress. Therefore, a pipe under inside pressure is essential in a biaxial stress state and triaxiality is somewhat misleading.

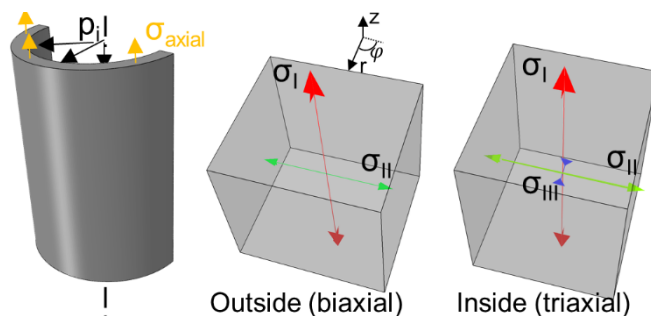


Figure 11-1 Biaxial stress state at different positions in a pipe specimen under inner pressure and additional axial loading

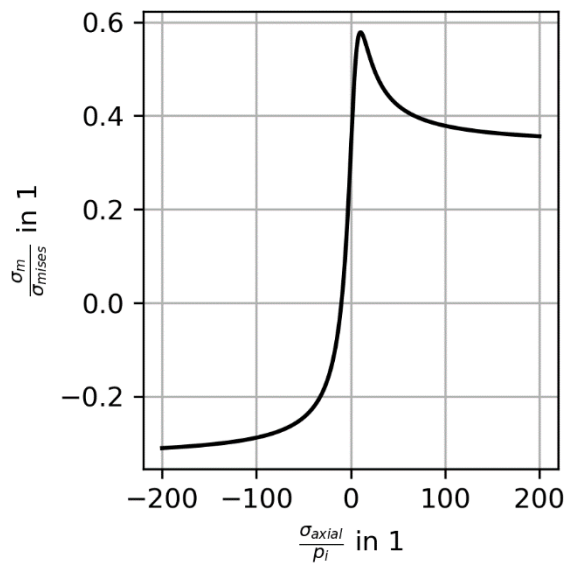


Figure 11-2 Effect of axial stress normed by inside pressure on the triaxiality ratio

Next Figure 11-3 shows the case of a notched round bar under axial tension. Due to a constrained lateral contraction, all three principal stresses are present and greater than zero. The second and third principal stress are similar in magnitude and the first principal stress is significantly larger and aligned with the loading direction. Investigations using a tensile specimen inside a pressure chamber will expose the specimen to a similar stress state but inverted signs for the second and third principal stress.

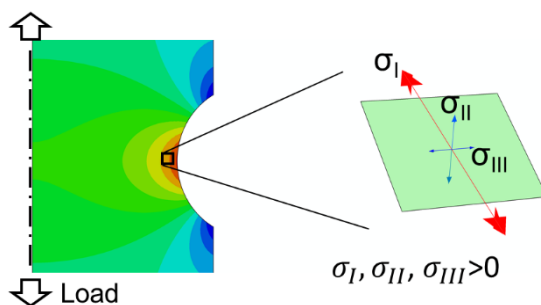


Figure 11-3 Triaxiality of a slice of the notched round bar under inside pressure

Finally, Figure 11-4 shows the stress state experienced by the matrix polymer near the fiber matrix interface under transverse tension. This comparison shows that the notched round bar is closer to the actual stress state of the matrix polymer in a transversely loaded ply.

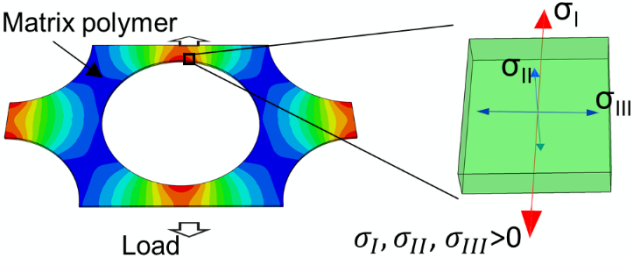


Figure 11-4 Triaxiality calculated for the RVE under transverse tension loading

B. Constituent properties visco-elastic model

Table 11-1 Wichert model parameters of neat polymers

Element	τ in s	EP 0kGy	EP 500 kGy	PC 0kGy	PC 200kGy
		E_i in MPa			
Spring	∞	2333	2481	2137	1920
Maxwell 1	2.4×10^{-5}	502	482	102	103
Maxwell 2	3.1×10^{-3}	218	255	125	123
Maxwell 3	4.1×10^{-1}	254	309	139	132
Maxwell 4	5.4×10^1	318	376	190	192
Maxwell 5	7.1×10^4	412	526	205	215

Table 11-2 Literature values of fiber properties

Reference	HT Carbon fibers	E-Glass fibers
	[207]	[162]
E_L in MPa	233000	73000
ν_{LT}	0.2	0.22
E_T in MPa	23100	-
G_{LT} in MPa	8963	-
ν_{TT}	0.4	-

12 Literature

- [1] M. Gilani and D. S. Körpe, "Airline weight reduction to minimize direct operating cost," in *4th International Aviation Management Conference*, 2019.
- [2] T. Ashuri, M. B. Zaaier, J. R. R. A. Martins, and J. Zhang, "Multidisciplinary design optimization of large wind turbines—Technical, economic, and design challenges," *Energy Conversion and Management*, vol. 123, pp. 56–70, Sep. 2016, doi: 10.1016/j.enconman.2016.06.004.
- [3] Society of Automotive Engineers and National Institute for Aviation Research (U.S.), Eds., *Composite Materials Handbook Volume 1 - Revision G*. Warrendale, Pa.: SAE International on behalf of CMH-17, a division of Wichita State University, 2012.
- [4] A.J. Davies, Q. Qineti, and P. T. Curtis, "Fatigue in aerospace applications," in *Fatigue in composites: science and technology of the fatigue response of fibre-reinforced plastics*, B. Harris, Ed., Boca Raton: CRC Press, 2003.
- [5] R. W. Hertzberg and J. A. Manson, *Fatigue of engineering plastics*. New York: Academic Press, 1980.
- [6] K. M. Jespersen, T. Lowe, P. J. Withers, J. Zangenberg, and L. P. Mikkelsen, Eds., *Micromechanical time-lapse X-ray CT study of fatigue damage in uni-directional fibre composites*. 2015. [Online]. Available: <https://www.iccm-central.org/Proceedings/ICCM20proceedings/>
- [7] S. Korkiakoski, E. Sarlin, R. Suihkonen, and O. Saarela, "Internal structure and fatigue performance of quasi-unidirectional non-crimp fabric reinforced laminates," *Journal of Composite Materials*, vol. 51, no. 24, pp. 3405–3423, Jan. 2017, doi: 10.1177/0021998316683783.
- [8] U. A. Mortensen, L. P. Mikkelsen, and T. L. Andersen, "Observation of the interaction between transverse cracking and fibre breaks in non-crimp fabric composites subjected to cyclic bending fatigue damage mechanism," *Journal of Composite Materials*, vol. 56, no. 23, pp. 3511–3527, Jan. 2022, doi: 10.1177/00219983221115795.
- [9] S. Ullah Nasir and A. Shahzad, "Effects of stabilization patterns on the static and fatigue behavior of glass fiber non-crimp fabric composites," *Journal of Composite Materials*, vol. 53, no. 25, pp. 3589–3598, Jan. 2019, doi: 10.1177/0021998319843994.
- [10] J. Zangenberg, P. Brøndsted, and J. W. Gillespie, "Fatigue damage propagation in unidirectional glass fibre reinforced composites made of a non-crimp fabric," *Journal of Composite Materials*, vol. 48, no. 22, pp. 2711–2727, Jan. 2014, doi: 10.1177/0021998313502062.
- [11] X. Wang and D. D. L. Chung, "Fiber breakage in polymer-matrix composites during static and fatigue loading, observed by electrical resistance measurement," vol. 503, 1998, pp. 81–86. [Online]. Available: <https://www.scopus.com/inward/record.uri?eid=2-s2.0-0031621790&partnerID=40&md5=34ba0da8a0f8e42ec9d9b937d4b60170>
- [12] E. K. Gamstedt, "Effects of debonding and fiber strength distribution on fatigue-damage propagation in carbon fiber-reinforced epoxy," *Journal of Applied Polymer Science*, vol. 76, no. 4, pp. 457–474, Jan. 2000, doi: 10.1002/(SICI)1097-4628(20000425)76:4<457::AID-APP3>3.0.CO;2-L.

- [13] H. C. Kim and L. J. Ebert, "Axial Fatigue Failure Sequence and Mechanisms in Unidirectional Fiberglass Composites," *Journal of Composite Materials*, vol. 12, no. 2, pp. 139–152, Jan. 1978, doi: 10.1177/002199837801200203.
- [14] J. Brunbauer and G. Pinter, Eds., *Fatigue-induced damage mechanisms in carbon/epoxy laminates influenced by mean stress and fibre volume content*. 2015. [Online]. Available: <https://www.iccm-central.org/Proceedings/ICCM20proceedings/>
- [15] O. Castro, P. A. Carraro, L. Maragoni, and M. Quaresimin, "Fatigue damage evolution in unidirectional glass/epoxy composites under a cyclic load," *Polymer Testing*, vol. 74, pp. 216–224, Jan. 2019, doi: 10.1016/j.polymertesting.2018.12.027.
- [16] S. Goutianos and T. Peijs, "Fatigue Damage Mechanisms in Carbon-Epoxy Multi-Fibre Model Composites," *Advanced Composites Letters*, vol. 10, no. 1, p. 096369350101000, Jan. 2001, doi: 10.1177/096369350101000103.
- [17] P. A. Carraro and M. Quaresimin, "A damage based model for crack initiation in unidirectional composites under multiaxial cyclic loading," *Composites Science and Technology*, vol. 99, pp. 154–163, Jul. 2014, doi: 10.1016/j.compscitech.2014.05.012.
- [18] R. Talreja, *Fatigue of composite materials*. Lancaster: Technomic Pub. Co, 1987.
- [19] A. Baumann and J. Hausmann, "Effect of high energy radiation on technical polymers," presented at the Proceedings 60th ISC, Ilmenau: ilmedia, 2023. doi: 10.22032/dbt.58861.
- [20] Y. Shao, K. Okubo, T. Fujii, O. Shibata, and Y. Fujita, "Effect of matrix properties on the fatigue damage initiation and its growth in plain woven carbon fabric vinylester composites," *Composites Science and Technology*, vol. 104, pp. 125–135, Jan. 2014, doi: 10.1016/j.compscitech.2014.09.010.
- [21] R. W. Hertzberg, H. Nordberg, and J. A. Manson, "Fatigue crack propagation in polymeric materials," *J Mater Sci*, vol. 5, no. 6, pp. 521–526, Jun. 1970, doi: 10.1007/BF00556040.
- [22] O. Erartsin, M. van Drongelen, and L. E. Govaert, "Identification of plasticity-controlled creep and fatigue failure mechanisms in transversely loaded unidirectional thermoplastic composites," *Journal of Composite Materials*, vol. 55, no. 14, pp. 1947–1965, Jan. 2021, doi: 10.1177/0021998320964252.
- [23] E. K. Gamstedt and R. Talreja, "Fatigue damage mechanisms in unidirectional carbon-fibre-reinforced plastics," *Journal of Materials Science*, vol. 34, no. 11, pp. 2535–2546, Jan. 1999, doi: 10.1023/A:1004684228765.
- [24] Z. Zhang and G. Hartwig, "Relation of damping and fatigue damage of unidirectional fibre composites," *International Journal of Fatigue*, vol. 24, no. 7, pp. 713–718, Jan. 2002, doi: 10.1016/S0142-1123(01)00206-7.
- [25] J. Brunbauer and G. Pinter, "Effects of mean stress and fibre volume content on the fatigue-induced damage mechanisms in CFRP," *International Journal of Fatigue*, vol. 75, pp. 28–38, Jan. 2015, doi: 10.1016/j.ijfatigue.2015.01.014.
- [26] A. Sudhir and R. Talreja, "Simulation of manufacturing induced fiber clustering and matrix voids and their effect on transverse crack formation in unidirectional composites," *Composites Part A: Applied Science and Manufacturing*, vol. 127, p. 105620, Dec. 2019, doi: 10.1016/j.compositesa.2019.105620.
- [27] G. Just, I. Koch, M. Brod, E. Jansen, M. Gude, and R. Rolfes, "Influence of Reversed Fatigue Loading on Damage Evolution of Cross-Ply Carbon Fibre Composites," *Materials (Basel)*, vol. 12, no. 7, Jan. 2019, doi: 10.3390/ma12071153.

- [28] L. Maragoni, P. A. Carraro, M. Peron, and M. Quaresimin, "Fatigue behaviour of glass/epoxy laminates in the presence of voids," *International Journal of Fatigue*, vol. 95, pp. 18–28, Feb. 2017, doi: 10.1016/j.ijfatigue.2016.10.004.
- [29] B. A. Sjögren and L. A. Berglund, "The effects of matrix and interface on damage in GRP cross-ply laminates," *Composites Science and Technology*, vol. 60, no. 1, pp. 9–21, Jan. 2000, doi: 10.1016/S0266-3538(99)00096-2.
- [30] W. Sun, A. P. Vassilopoulos, and T. Keller, "Experimental investigation of kink initiation and kink band formation in unidirectional glass fiber-reinforced polymer specimens," *Composite Structures*, vol. 130, pp. 9–17, Oct. 2015, doi: 10.1016/j.compstruct.2015.04.028.
- [31] B. Vieille, W. Albouy, D. Bouscarrat, and L. Taleb, "High-temperature fatigue behaviour of notched quasi-isotropic thermoplastic and thermoset laminates: Influence of matrix ductility on damage mechanisms and stress distribution," *Composite Structures*, vol. 153, pp. 311–320, Jan. 2016, doi: 10.1016/j.compstruct.2016.06.015.
- [32] B. S. Majumdar and G. M. Newaz, "Constituent damage mechanisms in metal matrix composites under fatigue loading, and their effects on fatigue life," *Materials Science and Engineering A*, vol. 200, no. 1–2, pp. 114–129, Jan. 1995, doi: 10.1016/0921-5093(95)07010-9.
- [33] T. H. Hsieh, A. J. Kinloch, K. Masania, J. Sohn Lee, A. C. Taylor, and S. Sprenger, "The toughness of epoxy polymers and fibre composites modified with rubber microparticles and silica nanoparticles," *J Mater Sci*, vol. 45, no. 5, pp. 1193–1210, Jan. 2010, doi: 10.1007/s10853-009-4064-9.
- [34] F. Hübner, A. Brückner, T. Dickhut, V. Altstädt, A. Rios de Anda, and H. Ruckdäschel, "Low temperature fatigue crack propagation in toughened epoxy resins aimed for filament winding of type V composite pressure vessels," *Polymer Testing*, vol. 102, p. 107323, Jan. 2021, doi: 10.1016/j.polymertesting.2021.107323.
- [35] N. Yousefi, S. J. Fisher, C. Burgstaller, M. S. P. Shaffer, and A. Bismarck, "Hierarchical carbon fibre composites incorporating high loadings of carbon nanotubes," *Composites Science and Technology*, vol. 222, p. 109369, Jan. 2022, doi: 10.1016/j.compscitech.2022.109369.
- [36] Z. Brocka-Krzeminska, "Werkstoff- und Einsatzpotential strahlenvernetzter Thermoplaste," Dissertation, Lehrstuhl für Kunststofftechnik, Erlangen, 2008.
- [37] U. Gohs *et al.*, "Crosslinked Continuous Glass Fiber-Reinforced Toughened Polypropylene Composites," *Adv. Eng. Mater.*, vol. 18, no. 3, pp. 409–416, 2016, doi: 10.1002/adem.201500479.
- [38] U. Gohs, M. T. Mueller, C. Zschech, and S. Zhandarov, "Enhanced Interfacial Shear Strength and Critical Energy Release Rate in Single Glass Fiber-Crosslinked Polypropylene Model Microcomposites," *Materials*, vol. 11, no. 12, 2018, doi: 10.3390/ma11122552.
- [39] J. M. Hughes, M. Lugo, J. L. Bouvard, T. McIntyre, and M. F. Horstemeyer, "Cyclic behavior and modeling of small fatigue cracks of a polycarbonate polymer," *International Journal of Fatigue*, vol. 99, pp. 78–86, Jun. 2017, doi: 10.1016/j.ijfatigue.2016.12.012.
- [40] A. J. Kinloch and R. J. Young, *Fracture Behaviour of Polymers*. Dordrecht: Springer Netherlands, 1995. doi: 10.1007/978-94-017-1594-2.
- [41] J. A. Sauer and G. C. Richardson, "Fatigue of polymers," *Int J Fract*, vol. 16, no. 6, pp. 499–532, Dec. 1980, doi: 10.1007/BF02265215.

- [42] P. Haupt, *Continuum mechanics and theory of materials*, 2. ed. in Physics and astronomy online library. Berlin; Heidelberg: Springer, 2002.
- [43] Z. Bin Ahmad and M. F. Ashby, "Failure-mechanism maps for engineering polymers," *J Mater Sci*, vol. 23, no. 6, pp. 2037–2050, Jun. 1988, doi: 10.1007/BF01115766.
- [44] L. Zhuang, R. Talreja, and L. Maragoni, "Crack Deflection Near a Ply Interface in a Composite Laminate," in *Volume 4: Advances in Aerospace Technology*, Virtual, Online: American Society of Mechanical Engineers, Nov. 2020, p. V004T04A023. doi: 10.1115/IMECE2020-23795.
- [45] R. Talreja, "Multi-scale modeling in damage mechanics of composite materials," *J Mater Sci*, vol. 41, no. 20, pp. 6800–6812, Nov. 2006, doi: 10.1007/s10853-006-0210-9.
- [46] M. Kawai and M. Koizumi, "Nonlinear constant fatigue life diagrams for carbon/epoxy laminates at room temperature," *Composites Part A: Applied Science and Manufacturing*, vol. 38, no. 11, pp. 2342–2353, Jan. 2007, doi: 10.1016/j.compositesa.2007.01.016.
- [47] M. Kawai and H. Suda, "Influences of Stress Ratio on the Off-Axis Fatigue Strength of Unidirectional CFRP," *Nihon Kikai Gakkai Ronbunshu, A Hen/Transactions of the Japan Society of Mechanical Engineers, Part A*, vol. 69, no. 7, pp. 1135–1142, Jan. 2003, doi: 10.1299/kikaia.69.1135.
- [48] C. Li, F. Ellyin, and A. Wharmby, "On matrix crack saturation in composite laminates," *Composites Part B: Engineering*, vol. 34, no. 5, pp. 473–480, Jul. 2003, doi: 10.1016/S1359-8368(03)00020-9.
- [49] A. Baumann, S. Backe, and J. Hausmann, "Investigation of the fatigue behavior of thermoplastic composites by load increase tests," *Journal of Composite Materials*, vol. 55, no. 4, pp. 541–550, Jan. 2021, doi: 10.1177/0021998320954524.
- [50] C. Peyrac, T. Jollivet, N. Leray, F. Lefebvre, O. Westphal, and L. Gornet, "Self-heating Method for Fatigue Limit Determination on Thermoplastic Composites," *Procedia Engineering*, vol. 133, pp. 129–135, 2015, doi: 10.1016/j.proeng.2015.12.639.
- [51] H. Shen, W. Yao, W. Qi, and J. Zong, "Experimental investigation on damage evolution in cross-ply laminates subjected to quasi-static and fatigue loading," *Composites Part B: Engineering*, vol. 120, pp. 10–26, Jul. 2017, doi: 10.1016/j.compositesb.2017.02.033.
- [52] M. Drvoderic, M. Gferrer, J. Wiener, G. Pinter, M. Pletz, and C. Schuecker, "Comparing crack density and dissipated energy as measures for off-axis damage in composite laminates," *International Journal of Fatigue*, vol. 169, p. 107486, Apr. 2023, doi: 10.1016/j.ijfatigue.2022.107486.
- [53] X. Li, J. Kupski, S. Teixeira De Freitas, R. Benedictus, and D. Zarouchas, "Unfolding the early fatigue damage process for CFRP cross-ply laminates," *International Journal of Fatigue*, vol. 140, p. 105820, Nov. 2020, doi: 10.1016/j.ijfatigue.2020.105820.
- [54] V. R. Pakkam Gabriel, M. S. Loukil, and J. Varna, "Analysis of intralaminar cracking in 90-ply of GF/EP laminates with distributed ply strength," *Journal of Composite Materials*, vol. 55, no. 26, pp. 3925–3942, Nov. 2021, doi: 10.1177/00219983211027346.
- [55] A. Wharmby, "Observations on damage development in fibre reinforced polymer laminates under cyclic loading," *International Journal of Fatigue*, vol. 25, no. 5, pp. 437–446, May 2003, doi: 10.1016/S0142-1123(02)00118-4.

- [56] S. Aratama *et al.*, “Microscopic observation of voids and transverse crack initiation in CFRP laminates,” *Advanced Composite Materials*, vol. 25, no. sup1, pp. 115–130, Dec. 2016, doi: 10.1080/09243046.2016.1206720.
- [57] K. Reifsnider and R. Jamison, “Fracture of fatigue-loaded composite laminates,” *International Journal of Fatigue*, vol. 4, no. 4, pp. 187–197, Oct. 1982, doi: 10.1016/0142-1123(82)90001-9.
- [58] W. Van Paepegem, I. De Baere, E. Lamkanfi, and J. Degrieck, “Poisson’s ratio as a sensitive indicator of (fatigue) damage in fibre-reinforced plastics,” *Fatigue Fract Eng Mat Struct*, vol. 30, no. 4, pp. 269–276, Apr. 2007, doi: 10.1111/j.1460-2695.2007.01095.x.
- [59] P. A. Carraro, L. Maragoni, and M. Quaresimin, “Characterisation and analysis of transverse crack-induced delamination in cross-ply composite laminates under fatigue loadings,” *International Journal of Fatigue*, vol. 129, p. 105217, Dec. 2019, doi: 10.1016/j.ijfatigue.2019.105217.
- [60] F. E. Oz, N. Ersoy, M. Mehdikhani, and S. V. Lomov, “Multi-instrument in-situ damage monitoring in quasi-isotropic CFRP laminates under tension,” *Composite Structures*, vol. 196, pp. 163–180, Jul. 2018, doi: 10.1016/j.compstruct.2018.05.006.
- [61] M. C. Lafarie-Frenot and C. Hénaff-Gardin, “Formation and growth of 90° ply fatigue cracks in carbon/epoxy laminates,” *Composites Science and Technology*, vol. 40, no. 3, pp. 307–324, Jan. 1991, doi: 10.1016/0266-3538(91)90087-6.
- [62] X. Li, R. Benedictus, and D. Zarouchas, “Analysis of Stochastic Matrix Crack Evolution in CFRP Cross-Ply Laminates under Fatigue Loading,” *Engineering Failure Analysis*, vol. 150, p. 107277, Aug. 2023, doi: 10.1016/j.engfailanal.2023.107277.
- [63] P. A. Carraro, L. Maragoni, and M. Quaresimin, “Prediction of the crack density evolution in multidirectional laminates under fatigue loadings,” *Composites Science and Technology*, vol. 145, pp. 24–39, Jun. 2017, doi: 10.1016/j.compscitech.2017.03.013.
- [64] M. Mehdikhani, E. Steensels, A. Standaert, K. A. M. Vallons, L. Gorbatikh, and S. V. Lomov, “Multi-scale digital image correlation for detection and quantification of matrix cracks in carbon fiber composite laminates in the absence and presence of voids controlled by the cure cycle,” *Composites Part B: Engineering*, vol. 154, pp. 138–147, Dec. 2018, doi: 10.1016/j.compositesb.2018.07.006.
- [65] M. Mehdikhani, N. A. Petrov, I. Straumit, A. R. Melro, S. V. Lomov, and L. Gorbatikh, “The effect of voids on matrix cracking in composite laminates as revealed by combined computations at the micro- and meso-scales,” *Composites Part A: Applied Science and Manufacturing*, vol. 117, pp. 180–192, Feb. 2019, doi: 10.1016/j.compositesa.2018.11.009.
- [66] Z. Hashin, “Analysis of cracked laminates: a variational approach,” *Mechanics of Materials*, vol. 4, no. 2, pp. 121–136, Jul. 1985, doi: 10.1016/0167-6636(85)90011-0.
- [67] T. Donhauser, A. Kenf, S. Schmeer, and J. Hausmann, “Calculation of highly stressed components made of carbonfiber-reinforced polyamide-6,” *Composite Structures*, vol. 280, p. 114830, Jan. 2022, doi: 10.1016/j.compstruct.2021.114830.
- [68] C. Andriß, A. Kenf, T. Donhauser, and S. Schmeer, “Characterization and modeling of continuous carbon fiber-reinforced polycarbonate under multiaxial loads,” *Composites Part B: Engineering*, vol. 235, p. 109740, Apr. 2022, doi: 10.1016/j.compositesb.2022.109740.

- [69] M. N. Bureau and J. Denault, "Fatigue resistance of continuous glass fiber/polypropylene composites: consolidation dependence," *Composites Science and Technology*, vol. 64, no. 12, pp. 1785–1794, Sep. 2004, doi: 10.1016/j.compscitech.2004.01.016.
- [70] S. Oshima, R. Higuchi, and S. Kobayashi, "Experimental characterization of cracking behavior initiating from microdefects in cross-ply CFRP laminates," *Engineering Fracture Mechanics*, vol. 281, p. 109116, Mar. 2023, doi: 10.1016/j.engfracmech.2023.109116.
- [71] F. Huang, X. Pang, F. Zhu, S. Zhang, Z. Fan, and X. Chen, "Transverse mechanical properties of unidirectional FRP including resin-rich areas," *Computational Materials Science*, vol. 198, p. 110701, Oct. 2021, doi: 10.1016/j.commatsci.2021.110701.
- [72] M. C. Boyce, D. M. Parks, and A. S. Argon, "Large inelastic deformation of glassy polymers. part I: rate dependent constitutive model," *Mechanics of Materials*, vol. 7, no. 1, pp. 15–33, Jan. 1988, doi: 10.1016/0167-6636(88)90003-8.
- [73] B. Fiedler, M. Hojo, S. Ochiai, K. Schulte, and M. Ando, "Failure behavior of an epoxy matrix under different kinds of static loading," *Composites Science and Technology*, vol. 61, no. 11, pp. 1615–1624, Aug. 2001, doi: 10.1016/S0266-3538(01)00057-4.
- [74] W. Tiejun, K. Kishimoto, and M. Notomi, "Effect of triaxial stress constraint on the deformation and fracture of polymers," *Acta Mech Sinica*, vol. 18, no. 5, pp. 480–493, Jan. 2002, doi: 10.1007/BF02486573.
- [75] D. Krause, "Mikromechanik des Ermüdungsverhaltens polymerer Verbundwerkstoffe," Dissertation, Köln, 2016.
- [76] L. E. Asp, L. A. Berglund, and R. Talreja, "Prediction of matrix-initiated transverse failure in polymer composites," *Composites Science and Technology*, vol. 56, no. 9, pp. 1089–1097, Jan. 1996, doi: 10.1016/0266-3538(96)00074-7.
- [77] L. E. Asp, L. A. Berglund, and P. Gudmundson, "Effects of a composite-like stress state on the fracture of epoxies," *Composites Science and Technology*, vol. 53, no. 1, pp. 27–37, Jan. 1995, doi: 10.1016/0266-3538(94)00075-1.
- [78] R. S. Kody and A. J. Lesser, "Deformation and yield of epoxy networks in constrained states of stress," *Journal of Materials Science*, vol. 32, no. 21, pp. 5637–5643, 1997, doi: 10.1023/A:1018693028394.
- [79] L. M. Carapellucci and A. F. Yee, "The biaxial deformation and yield behavior of bisphenol-a polycarbonate: Effect of anisotropy," *Polymer Engineering & Sci*, vol. 26, no. 13, pp. 920–930, Jul. 1986, doi: 10.1002/pen.760261303.
- [80] A. W. Christiansen, E. Baer, and S. V. Radcliffe, "The mechanical behaviour of polymers under high pressure," *The Philosophical Magazine: A Journal of Theoretical Experimental and Applied Physics*, vol. 24, no. 188, pp. 451–467, Aug. 1971, doi: 10.1080/14786437108227400.
- [81] R. Raghava, R. M. Caddell, and G. S. Y. Yeh, "The macroscopic yield behaviour of polymers," *J Mater Sci*, vol. 8, no. 2, pp. 225–232, Feb. 1973, doi: 10.1007/BF00550671.
- [82] H. Kishi, S. Matsuda, J. Imade, Y. Shimoda, T. Nakagawa, and Y. Furukawa, "The effects of the toughening mechanism and the molecular weights between cross-links on the fatigue resistance of epoxy polymer blends," *Polymer*, vol. 223, p. 123712, May 2021, doi: 10.1016/j.polymer.2021.123712.
- [83] M. N. James, Y. Lu, C. J. Christopher, and E. A. Patterson, "Crack path support for deformation mechanisms in fatigue of polycarbonate," *Engineering Fracture*

- Mechanics*, vol. 108, pp. 89–97, Aug. 2013, doi: 10.1016/j.engfracmech.2013.02.003.
- [84] J. Schijve, *Fatigue of Structures and Materials*. Dordrecht: Springer Netherlands Springer e-books, 2009.
- [85] C. G'Sell and A. J. Gopez, "Plastic banding in glassy polycarbonate under plane simple shear," *J Mater Sci*, vol. 20, no. 10, pp. 3462–3478, Oct. 1985, doi: 10.1007/BF01113753.
- [86] T. K. Mattioli and D. J. Quesnel, "Rate process analysis applied to the mechanical behavior of glassy bisphenol-A-polycarbonate," *Polymer Engineering & Sci*, vol. 27, no. 11, pp. 848–856, Jun. 1987, doi: 10.1002/pen.760271113.
- [87] M. Parvin and J. G. Williams, "Ductile-brittle fracture transitions in polycarbonate," *Int J Fract*, vol. 11, no. 6, pp. 963–972, Dec. 1975, doi: 10.1007/BF00033842.
- [88] R. W. Hertzberg, J. A. Manson, and M. Skibo, "Frequency sensitivity of fatigue processes in polymeric solids," *Polymer Engineering & Sci*, vol. 15, no. 4, pp. 252–260, Apr. 1975, doi: 10.1002/pen.760150404.
- [89] M. E. Mackay, T.-G. Teng, and J. M. Schultz, "Craze roles in the fatigue of polycarbonate," *J Mater Sci*, vol. 14, no. 1, pp. 221–227, Jan. 1979, doi: 10.1007/BF01028346.
- [90] S. Mortazavian and A. Fatemi, "Notch Effects on Fatigue Behavior of Thermoplastics," *AMR*, vol. 891–892, pp. 1403–1409, Jan. 2014, doi: 10.4028/www.scientific.net/AMR.891-892.1403.
- [91] Y. Murakami, *Metal Fatigue*. Elsevier, 2002. doi: 10.1016/B978-0-08-044064-4.X5000-2.
- [92] R. E. Peterson, *Stress concentration factors: charts and relations useful in making strength calculations for machine parts and structural elements*. in A Wiley-Interscience publication. New York: Wiley, 1974.
- [93] T. Misaki and J. Kishi, "Effect of notches and glass fiber reinforcement on fatigue behavior of polycarbonate," *J of Applied Polymer Sci*, vol. 22, no. 7, pp. 2063–2067, Jul. 1978, doi: 10.1002/app.1978.070220725.
- [94] L. Samuelsson, "Fatigue Analysis: The Super-Neuber Technique for Correction of Linear Elastic FE Results," in *26-th International Congress of the Aeronautical Sciences*, 2008, pp. 221–229.
- [95] M. T. Takemori, "Competition between crazing and shear flow during fatigue," in *Crazing in Polymers Vol. 2*, vol. 91/92, H.-H. Kausch, Ed., in *Advances in Polymer Science*, vol. 91/92. , Berlin, Heidelberg: Springer Berlin Heidelberg, 1990, pp. 263–300. doi: 10.1007/BFb0018023.
- [96] R. P. Kambour and R. W. Kopp, "Cyclic stress–strain behavior of the dry polycarbonate craze," *J. Polym. Sci. A-2 Polym. Phys.*, vol. 7, no. 1, pp. 183–200, Jan. 1969, doi: 10.1002/pol.1969.160070115.
- [97] K. Mishra, L. Brassart, and A. Singh, "Rate dependent fracture behavior of highly cross-linked epoxy resin," *Engineering Failure Analysis*, vol. 140, p. 106558, Oct. 2022, doi: 10.1016/j.engfailanal.2022.106558.
- [98] A. S. Argon, "Craze initiation in glassy polymers – Revisited," *Polymer*, vol. 52, no. 10, pp. 2319–2327, May 2011, doi: 10.1016/j.polymer.2011.03.019.
- [99] A. S. Argon and J. G. Hannoosh, "Initiation of crazes in polystyrene," *Philosophical Magazine*, vol. 36, no. 5, pp. 1195–1216, Nov. 1977, doi: 10.1080/14786437708239789.

- [100] R. J. Oxborough and P. B. Bowden, "A general critical-strain criterion for crazing in amorphous glassy polymers," *The Philosophical Magazine: A Journal of Theoretical Experimental and Applied Physics*, vol. 28, no. 3, pp. 547–559, Sep. 1973, doi: 10.1080/14786437308221002.
- [101] J. Lilley and D. G. Holloway, "Crazing in epoxy resins," *Philosophical Magazine*, vol. 28, no. 1, pp. 215–220, Jul. 1973, doi: 10.1080/14786437308217443.
- [102] H. A. Hristov, A. F. Yee, and D. W. Gidley, "Fatigue craze initiation in polycarbonate: study by transmission electron microscopy," *Polymer*, vol. 35, no. 17, pp. 3604–3611, Aug. 1994, doi: 10.1016/0032-3861(94)90535-5.
- [103] M. Kitagawa and M. Kawagoe, "Plastic deformation by crazing in polycarbonate," *J Mater Sci*, vol. 14, no. 4, pp. 953–960, Apr. 1979, doi: 10.1007/BF00550727.
- [104] Z. T. Wang, J. L. Chen, and R. C. Wang, "Microscopy Photoelasticity for Studying Crazes in Polycarbonate," *AMM*, vol. 37–38, pp. 648–651, Nov. 2010, doi: 10.4028/www.scientific.net/AMM.37-38.648.
- [105] A. M. Donald, E. J. Kramer, and R. P. Kambour, "Interaction of crazes with pre-existing shear bands in glassy polymers," *J Mater Sci*, vol. 17, no. 6, pp. 1739–1744, Jun. 1982, doi: 10.1007/BF00540802.
- [106] J. Lai and E. Van Der Giessen, "A numerical study of crack-tip plasticity in glassy polymers," *Mechanics of Materials*, vol. 25, no. 3, pp. 183–197, Apr. 1997, doi: 10.1016/S0167-6636(97)00006-9.
- [107] S. P. Petrie, A. T. Dibenedetto, and J. Miltz, "Effects of the state of stress on the toughness of polycarbonate," *Polymer Engineering & Sci*, vol. 18, no. 16, pp. 1200–1208, Dec. 1978, doi: 10.1002/pen.760181603.
- [108] G. L. Pitman, I. M. Ward, and R. A. Duckett, "The effects of thermal pre-treatment and molecular weight on the impact behaviour of polycarbonate," *J Mater Sci*, vol. 13, no. 10, pp. 2092–2104, Oct. 1978, doi: 10.1007/BF00541662.
- [109] S. Baar, L. Pavlov, and C. Kassapoglou, "Consistent approach to onset theory," *Journal of Composite Materials*, vol. 56, no. 22, pp. 3495–3507, Sep. 2022, doi: 10.1177/00219983221104865.
- [110] L. E. Asp, L. A. Berglund, and R. Talreja, "A criterion for crack initiation in glassy polymers subjected to a composite-like stress state," *Composites Science and Technology*, vol. 56, no. 11, pp. 1291–1301, Jan. 1996, doi: 10.1016/S0266-3538(96)00090-5.
- [111] E. J. Kramer, "The growth of shear bands in polystyrene," *J. Polym. Sci. Polym. Phys. Ed.*, vol. 13, no. 3, pp. 509–525, Mar. 1975, doi: 10.1002/pol.1975.180130305.
- [112] M. D. Skibo, R. W. Hertzberg, J. A. Manson, and S. L. Kim, "On the generality of discontinuous fatigue crack growth in glassy polymers," *J Mater Sci*, vol. 12, no. 3, pp. 531–542, Mar. 1977, doi: 10.1007/BF00540278.
- [113] C. Kanchanomai and A. Thammareuechuc, "Effects of stress ratio on fatigue crack growth of thermoset epoxy resin," *Polymer Degradation and Stability*, vol. 94, no. 10, pp. 1772–1778, Oct. 2009, doi: 10.1016/j.polymdegradstab.2009.06.012.
- [114] E. D. Crawford and A. J. Lesser, "Brittle to ductile: Fracture toughness mapping on controlled epoxy networks," *Polymer Engineering & Sci*, vol. 39, no. 2, pp. 385–392, Feb. 1999, doi: 10.1002/pen.11425.
- [115] A. J. Kinloch, D. G. Gilbert, and S. J. Shaw, "A mechanism for ductile crack growth in epoxy polymers," *J Mater Sci*, vol. 21, no. 3, pp. 1051–1056, Mar. 1986, doi: 10.1007/BF01117394.

- [116] M. George *et al.*, “In situ AFM investigation of slow crack propagation mechanisms in a glassy polymer,” *Journal of the Mechanics and Physics of Solids*, vol. 112, pp. 109–125, Mar. 2018, doi: 10.1016/j.jmps.2017.11.019.
- [117] M. J. W. Kanters, T. Kurokawa, and L. E. Govaert, “Competition between plasticity-controlled and crack-growth controlled failure in static and cyclic fatigue of thermoplastic polymer systems,” *Polymer Testing*, vol. 50, pp. 101–110, Apr. 2016, doi: 10.1016/j.polymertesting.2016.01.008.
- [118] J. A. Manson, R. W. Hertzberg, S. L. Kim, and W. C. Wu, “Fatigue Crack Propagation in Polycarbonate,” in *Toughness and Brittleness of Plastics*, vol. 154, R. D. Deanin and A. M. Crugnola, Eds., in *Advances in Chemistry*, vol. 154, WASHINGTON, D. C.: AMERICAN CHEMICAL SOCIETY, 1976. doi: 10.1021/ba-1976-0154.
- [119] A. Wolfenden, T. Clark, R. Hertzberg, and J. Manson, “Influence of Test Methodology on Fatigue Crack Propagation in Engineering Plastics,” *J. Test. Eval.*, vol. 18, no. 5, p. 319, 1990, doi: 10.1520/JTE12493J.
- [120] S. A. Sutton, “Fatigue crack propagation in an epoxy polymer,” *Engineering Fracture Mechanics*, vol. 6, no. 3, pp. 587–595, Oct. 1974, doi: 10.1016/0013-7944(74)90015-0.
- [121] P. Dumbleton and C. Bucknall, “Comparison of static and dynamic fatigue crack growth rates in high-density polyethylene,” *International Journal of Fatigue*, vol. 9, no. 3, pp. 151–155, Jul. 1987, doi: 10.1016/0142-1123(87)90070-3.
- [122] M. T. Hahn, R. W. Hertzberg, J. A. Manson, C. M. Rimnac, and I. M. Ward, “Comments on ‘The molecular weight dependence of fatigue crack propagation in polycarbonate,’” *J Mater Sci*, vol. 17, no. 5, pp. 1533–1537, May 1982, doi: 10.1007/BF00752271.
- [123] G. Pitman and I. M. Ward, “The molecular weight dependence of fatigue crack propagation in polycarbonate,” *J Mater Sci*, vol. 15, no. 3, pp. 635–645, Mar. 1980, doi: 10.1007/BF00551728.
- [124] M. T. Takemori, “Polymer fatigue fracture diagrams: BPA polycarbonate,” *Polymer Engineering & Sci*, vol. 28, no. 10, pp. 641–647, May 1988, doi: 10.1002/pen.760281002.
- [125] Y. Qiao, Q. Zhang, and M. Salviato, “Effects of In-situ Stress State on the Plastic Deformation, Fracture, and Size Scaling of Thermoset Polymers and Related Fiber-reinforced Composites,” in *American Society for Composites 2020*, DEStech Publications, Inc., Sep. 2020. doi: 10.12783/asc35/34951.
- [126] C. M. Rimnac, R. W. Hertzberg, and J. A. Manson, “On the nature of craze development and breakdown during fatigue,” *J Mater Sci Lett*, vol. 2, no. 7, pp. 325–328, Jul. 1983, doi: 10.1007/BF00726319.
- [127] R. J. Morgan, E. T. Mones, and W. J. Steele, “Tensile deformation and failure processes of amine-cured epoxies,” *Polymer*, vol. 23, no. 2, pp. 295–305, Feb. 1982, doi: 10.1016/0032-3861(82)90320-2.
- [128] H. Liu *et al.*, “Fatigue modeling for carbon/epoxy unidirectional composites under various stress ratios considering size effects,” *International Journal of Fatigue*, vol. 120, pp. 184–200, Mar. 2019, doi: 10.1016/j.ijfatigue.2018.11.009.
- [129] H. T. Hahn and J. G. Williams, “Compression failure mechanisms in unidirectional composites,” presented at the ASTM Symp. on Composite Mater., Philadelphia, PA, Jan. 1984. [Online]. Available: <https://ntrs.nasa.gov/citations/19840025452>

- [130] A. Baumann and J. Hausmann, "Compression Fatigue Testing Setups for Composites—A Review," *Adv Eng Mater*, vol. 23, no. 2, p. 2000646, Feb. 2021, doi: 10.1002/adem.202000646.
- [131] S. Kyriakides, R. Arseculeratne, E. J. Perry, and K. M. Liechti, "On the compressive failure of fiber reinforced composites," *International Journal of Solids and Structures*, vol. 32, no. 6–7, pp. 689–738, Mar. 1995, doi: 10.1016/0020-7683(94)00157-R.
- [132] S. W. Choi, H. T. Hahn, and P. Shyprykevich, "Damage development in notched composite laminates under compression-dominated fatigue," *Composites Science and Technology*, vol. 62, no. 6, pp. 851–860, 2002, doi: 10.1016/S0266-3538(02)00038-6.
- [133] N. Safdar, B. Daum, S. Scheffler, and R. Rolfes, "Experimental determination of a probabilistic failure envelope for carbon fiber reinforced polymers under combined compression–shear loads," *International Journal of Solids and Structures*, vol. 244–245, p. 111585, Jun. 2022, doi: 10.1016/j.ijsolstr.2022.111585.
- [134] H. T. Hahn and R. Y. Kim, "Proof Testing of Composite Materials," *Journal of Composite Materials*, vol. 9, no. 3, pp. 297–311, Jul. 1975, doi: 10.1177/002199837500900308.
- [135] J. P. Komorowski, D. Lefebvre, C. Randon, P. Larose, and C. Roy, "Edge effects on the compression dominated fatigue resistance of graphite-epoxy laminates," in *ICCM-10. Proceedings of the Tenth International Conference on Composite Materials. Whistler, British Columbia, Canada, Aug. 14 - 18, 1995. T. 1: Fatigue and fracture*, Cambridge: Woodhead, 1995.
- [136] C. V. Opelt, G. M. Cândido, and M. C. Rezende, "Compressive failure of fiber reinforced polymer composites – A fractographic study of the compression failure modes," *Materials Today Communications*, vol. 15, pp. 218–227, Jun. 2018, doi: 10.1016/j.mtcomm.2018.03.012.
- [137] B. Budiansky and N. A. Fleck, "Compressive failure of fibre composites," *Journal of the Mechanics and Physics of Solids*, vol. 41, no. 1, pp. 183–211, 1993, doi: 10.1016/0022-5096(93)90068-Q.
- [138] M. Sohi, H. Hahn, and J. Williams, "The Effect of Resin Toughness and Modulus on Compressive Failure Modes of Quasi-Isotropic Graphite/Epoxy Laminates," in *Toughened Composites*, N. Johnston, Ed., 100 Barr Harbor Drive, PO Box C700, West Conshohocken, PA 19428-2959: ASTM International, 1987, pp. 37–37–24. doi: 10.1520/STP24370S.
- [139] R. Gutkin, S. T. Pinho, P. Robinson, and P. T. Curtis, "A finite fracture mechanics formulation to predict fibre kinking and splitting in CFRP under combined longitudinal compression and in-plane shear," *Mechanics of Materials*, vol. 43, no. 11, pp. 730–739, Nov. 2011, doi: 10.1016/j.mechmat.2011.08.002.
- [140] N. L. Hancox, "The compression strength of unidirectional carbon fibre reinforced plastic," *J Mater Sci*, vol. 10, no. 2, pp. 234–242, Feb. 1975, doi: 10.1007/BF00540347.
- [141] J. Christoffersen and H. Myhre Jensen, "Kink band analysis accounting for the microstructure of fiber reinforced materials," *Mechanics of Materials*, vol. 24, no. 4, pp. 305–315, 1996, doi: 10.1016/S0167-6636(96)00052-X.
- [142] P. Diaz Montiel and S. Venkataraman, "Numerical Investigation of the Evolution of Fiber Kinking Damage in Composites Under Cyclic Loading," presented at the AIAA Scitech 2019 Forum, San Diego, California: American Institute of Aeronautics and Astronautics, 2019. doi: 10.2514/6.2019-1038.

- [143] S. P. H. Skovsgaard and H. M. Jensen, "Steady-State Kink Band Propagation in Layered Materials," *Journal of Applied Mechanics*, vol. 85, 061005 vols., no. 6, Jan. 2018, doi: 10.1115/1.4039573.
- [144] R. Gutkin, S. T. Pinho, P. Robinson, and P. T. Curtis, "Micro-mechanical modelling of shear-driven fibre compressive failure and of fibre kinking for failure envelope generation in CFRP laminates," *Composites Science and Technology*, vol. 70, no. 8, pp. 1214–1222, Aug. 2010, doi: 10.1016/j.compscitech.2010.03.009.
- [145] W. S. Slaughter and N. A. Fleck, "Viscoelastic Microbuckling of Fiber Composites," *Journal of Applied Mechanics*, vol. 60, no. 4, pp. 802–806, Dec. 1993, doi: 10.1115/1.2900986.
- [146] R. A. Schapery, "Compressive Strength and Failure Time Based on Local Buckling in Viscoelastic Composites," *Applied Mechanics Reviews*, vol. 46, no. 11S, pp. S221–S228, Nov. 1993, doi: 10.1115/1.3122640.
- [147] R. A. Schapery, "Analysis of Local Buckling in Viscoelastic Composites," in *Local Mechanics Concepts for Composite Material Systems*, J. N. Reddy and K. L. Reifsnider, Eds., Berlin, Heidelberg: Springer Berlin Heidelberg, 1992, pp. 229–250. doi: 10.1007/978-3-642-84792-9_13.
- [148] B. M. Leite, L. F. M. Leite, V. L. Reis, M. V. Donadon, and N. N. A. Da Silveira, "Strain rate effects on the intralaminar fracture toughness of composite laminates subjected to compressive load," *Composite Structures*, vol. 186, pp. 94–105, Feb. 2018, doi: 10.1016/j.compstruct.2017.11.091.
- [149] A. Vinet and D. Gamby, "Prediction of long-term mechanical behaviour of fibre composites from the observation of micro-buckling appearing during creep compression tests," *Composites Science and Technology*, vol. 68, no. 2, pp. 526–536, Feb. 2008, doi: 10.1016/j.compscitech.2007.06.032.
- [150] T. J. Vogler and S. Kyriakides, "On the axial propagation of kink bands in fiber composites : Part i experiments," *International Journal of Solids and Structures*, vol. 36, no. 4, pp. 557–574, Feb. 1999, doi: 10.1016/S0020-7683(98)00029-8.
- [151] J. Hapke, F. Gehrig, N. Huber, K. Schulte, and E. T. Lilleodden, "Compressive failure of UD-CFRP containing void defects: In situ SEM microanalysis," *Composites Science and Technology*, vol. 71, no. 9, pp. 1242–1249, Jun. 2011, doi: 10.1016/j.compscitech.2011.04.009.
- [152] W. S. Slaughter, N. A. Fleck, and B. Budiansky, "Compressive Failure of Fiber Composites: The Roles of Multiaxial Loading and Creep," *Journal of Engineering Materials and Technology*, vol. 115, no. 3, pp. 308–313, Jul. 1993, doi: 10.1115/1.2904223.
- [153] P. M. Jelf and N. A. Fleck, "The failure of composite tubes due to combined compression and torsion," *J Mater Sci*, vol. 29, no. 11, pp. 3080–3084, 1994, doi: 10.1007/BF01117623.
- [154] P. M. Jelf and N. A. Fleck, "Compression Failure Mechanisms in Unidirectional Composites," *Journal of Composite Materials*, vol. 26, no. 18, pp. 2706–2726, Dec. 1992, doi: 10.1177/002199839202601804.
- [155] S. T. Pinho, P. Robinson, and L. Iannucci, "Fracture toughness of the tensile and compressive fibre failure modes in laminated composites," *Composites Science and Technology*, vol. 66, no. 13, pp. 2069–2079, Oct. 2006, doi: 10.1016/j.compscitech.2005.12.023.
- [156] R. He, L. Cheng, Y. Gao, H. Cui, and Y. Li, "The fibre kinking fracture toughness of laminated composites under combined compression and shear," *Composites*

- Science and Technology*, vol. 244, p. 110307, Nov. 2023, doi: 10.1016/j.compscitech.2023.110307.
- [157] D. Wilhelmsson, L. P. Mikkelsen, S. Fæster, and L. E. Asp, "Influence of in-plane shear on kink-plane orientation in a unidirectional fibre composite," *Composites Part A: Applied Science and Manufacturing*, vol. 119, pp. 283–290, Apr. 2019, doi: 10.1016/j.compositesa.2019.01.018.
- [158] D. Wilhelmsson, F. Edgren, R. Gutkin, and L. E. Asp, "The transition from out-of-plane to in-plane kinking due to off-axis loading," presented at the ECCM18 - 18th European Conference on Composite Materials, Athens, Greece, Jun. 2018.
- [159] Z. P. Bažant, J.-J. H. Kim, I. M. Daniel, E. Becq-Giraudon, and G. Zi, "Size effect on compression strength of fiber composites failing by kink band propagation," *International Journal of Fracture*, vol. 95, no. 1/4, pp. 103–141, 1999, doi: 10.1023/A:1018640015465.
- [160] J. Lankford, "Compressive failure of fibre-reinforced composites: buckling, kinking, and the role of the interphase," *Journal of Materials Science*, vol. 30, no. 17, pp. 4343–4348, Sep. 1995, doi: 10.1007/BF00361515.
- [161] M. S. Madhukar and L. T. Drzal, "Fiber-Matrix Adhesion and Its Effect on Composite Mechanical Properties. III. Longitudinal (0°) Compressive Properties of Graphite/Epoxy Composites," *Journal of Composite Materials*, vol. 26, no. 3, pp. 310–333, Mar. 1992, doi: 10.1177/002199839202600301.
- [162] H. Schürmann, *Konstruieren mit Faser-Kunststoff-Verbunden*, 2nd ed. in VDI-Buch. Berlin, Heidelberg: Springer-Verlag Berlin Heidelberg, 2007. doi: 10.1007/978-3-540-72190-1.
- [163] J. Aboudi, *Mechanics of composite materials: A unified micromechanical approach*, vol. 29. in Studies in applied mechanics, vol. 29. Amsterdam; New York: Elsevier, 1991.
- [164] N. Zobeiry, S. Malek, R. Vaziri, and A. Poursartip, "A differential approach to finite element modelling of isotropic and transversely isotropic viscoelastic materials," *Mechanics of Materials*, vol. 97, pp. 76–91, Jun. 2016, doi: 10.1016/j.mechmat.2016.02.013.
- [165] R. A. W. Fraser and I. M. Ward, "Temperature dependence of craze shape and fracture in polycarbonate," *Polymer*, vol. 19, no. 2, pp. 220–224, Feb. 1978, doi: 10.1016/0032-3861(78)90043-5.
- [166] C. C. Chau and J. C. M. Li, "Fracture of shear bands in atactic polystyrene," *J Mater Sci*, vol. 16, no. 7, pp. 1858–1873, Jul. 1981, doi: 10.1007/BF00540634.
- [167] W. J. Cantwell, A. C. Roulin-Moloney, and T. Kaiser, "Fractography of unfilled and particulate-filled epoxy resins," *J Mater Sci*, vol. 23, no. 5, pp. 1615–1631, May 1988, doi: 10.1007/BF01115700.
- [168] L. Plangsangmas, J. J. Mecholsky, and A. B. Brennan, "Determination of fracture toughness of epoxy using fractography," *J. Appl. Polym. Sci.*, vol. 72, no. 2, pp. 257–268, Apr. 1999, doi: 10.1002/(SICI)1097-4628(19990411)72:2<257::AID-APP11>3.0.CO;2-M.
- [169] V. Trappe, S. Günzel, and M. Jaunich, "Correlation between crack propagation rate and cure process of epoxy resins," *Polymer Testing*, vol. 31, no. 5, pp. 654–659, Aug. 2012, doi: 10.1016/j.polymertesting.2012.03.007.
- [170] I. M. Barszczewska-Rybarek, A. Korytkowska-Wałach, M. Kurcok, G. Chladek, and J. Kasperski, "DMA analysis of the structure of crosslinked poly(methyl methacrylate)s," *Acta of Bioengineering and Biomechanics; 01/2017; ISSN 1509-409X*, 2017, doi: 10.5277/ABB-00590-2016-01.

- [171] A. Idesaki *et al.*, "Development of high radiation-resistant glass fiber reinforced plastics with cyanate-based resin for superconducting magnet systems," *Fusion Engineering and Design*, vol. 112, pp. 418–424, Jan. 2016, doi: 10.1016/j.fusengdes.2016.06.031.
- [172] A. Nishimura, Y. Izumi, M. Imaizumi, S. Nishijima, T. Hemmi, and T. Shikama, "Neutron and gamma ray irradiation effects on interlaminar shear strength of insulation materials with cyanate ester–epoxy blended resin," *Fusion Engineering and Design*, vol. 86, no. 6–8, pp. 1558–1561, Jan. 2011, doi: 10.1016/j.fusengdes.2011.01.093.
- [173] H. Ishii, N. Hirai, and Y. Ohki, "Aging behavior of soft and hard epoxy resins in simulated nuclear-power-plant environments," *Proceedings of the International Symposium on Electrical Insulating Materials*, vol. 2020-September, Jan. 2020, [Online]. Available: <https://ieeexplore.ieee.org/document/9275800>
- [174] F. Hacıoğlu, T. Özdemir, K. G. Kinalır, and A. Usanmaz, "Possible use of bisphenol-a polycarbonate in radioactive waste embedding," *Progress in Nuclear Energy*, vol. 90, pp. 98–104, Jul. 2016, doi: 10.1016/j.pnucene.2016.03.012.
- [175] T. Özdemir and A. Usanmaz, "Degradation of poly(bisphenol-a-epichlorohydrin) by gamma irradiation," *Radiation Physics and Chemistry*, vol. 77, no. 6, pp. 799–805, Jan. 2008, doi: 10.1016/j.radphyschem.2008.01.003.
- [176] D. Acierno, F. P. La Mantia, G. Titomanlio, E. Calderaro, and F. Castiglia, "γ-radiation effects on a polycarbonate," *Radiation Physics and Chemistry (1977)*, vol. 16, no. 2, pp. 95–99, Jan. 1980, doi: 10.1016/0146-5724(80)90213-7.
- [177] E. S. Araújo, H. J. Khoury, and S. V. Silveira, "Effects of gamma-irradiation on some properties of durolon polycarbonate," *Radiation Physics and Chemistry*, vol. 53, no. 1, pp. 79–84, Jan. 1998, doi: 10.1016/S0969-806X(97)00300-9.
- [178] J. Chen, M. Czayka, and R. M. Uribe, "Effects of electron beam irradiations on the structure and mechanical properties of polycarbonate," *Radiation Physics and Chemistry*, vol. 74, no. 1, pp. 31–35, Sep. 2005, doi: 10.1016/j.radphyschem.2004.12.004.
- [179] R. P. Weber, K. S. Vecchio, and J. C. M. Suarez, "Dynamic behavior of gamma-irradiated polycarbonate," *Matéria (Rio J.)*, vol. 15, no. 2, pp. 218–224, 2010, doi: 10.1590/S1517-70762010000200019.
- [180] K. Hareesh *et al.*, "Variation of lexan polycarbonate properties by electron beam," *J of Applied Polymer Sci*, vol. 127, no. 3, pp. 2010–2018, Feb. 2013, doi: 10.1002/app.37589.
- [181] R. P. Weber, S. N. Monteiro, J. C. M. Suarez, A. B.-H. S. Figueiredo, and C. J. V. De Oliveira, "Fracture toughness of gamma irradiated polycarbonate sheet using the essential work of fracture," *Polymer Testing*, vol. 57, pp. 115–118, Feb. 2017, doi: 10.1016/j.polymertesting.2016.11.021.
- [182] F. Hacıoglu, U. Tayfun, T. Ozdemir, and T. Tincer, "Characterization of carbon fiber and glass fiber reinforced polycarbonate composites and their behavior under gamma irradiation," *Progress in Nuclear Energy*, vol. 134, p. 103665, Apr. 2021, doi: 10.1016/j.pnucene.2021.103665.
- [183] F. S. Guarino, C. Hauviller, and J. M. Kenny, "Radiation effects on room temperature epoxy adhesive molecular structure: Mechanical tests and correlation with calorimetric and outgassing analyses," *Journal of Macromolecular Science - Physics*, vol. 38 (B), no. 5, pp. 623–633, Jan. 1999, doi: 10.1080/00222349908248126.
- [184] H. Schönbacher, A. Fontaine, and M. Tavlet, "Compilation of radiation damage test data, pt.2," CERN, Jan. 1998. doi: 10.5170/CERN-1998-001.

- [185] L.-F. Zheng, L.-N. Wang, Z.-Z. Wang, and L. Wang, "Effects of γ -Ray Irradiation on the Fatigue Strength, Thermal Conductivities and Thermal Stabilities of the Glass Fibres/Epoxy Resins Composites," *Acta Metall. Sin. (Engl. Lett.)*, vol. 31, no. 1, pp. 105–112, Jan. 2018, doi: 10.1007/s40195-017-0692-2.
- [186] S. Beura, A. P. Chakraverty, D. N. Thatoi, U. K. Mohanty, and M. Mohapatra, "Failure modes in GFRP composites assessed with the aid of SEM fractographs," *Materials Today: Proceedings*, vol. 41, Jan. 2019, doi: 10.1016/j.matpr.2020.08.518.
- [187] E. N. Hoffman and T. E. Skidmore, "Radiation effects on epoxy/carbon-fiber composite," *Journal of Nuclear Materials*, vol. 392, no. 2, pp. 371–378, Jan. 2009, doi: 10.1016/j.jnucmat.2009.03.027.
- [188] Z. X. Wu, J. W. Li, C. J. Huang, R. J. Huang, and L. F. Li, "Effect of gamma irradiation on the mechanical behavior, thermal properties and structure of epoxy/glass-fiber composite," *Journal of Nuclear Materials*, vol. 441, no. 1–3, pp. 67–72, Jan. 2013, doi: 10.1016/j.jnucmat.2013.05.041.
- [189] P. H. Kang, J. S. Park, and Y. C. Nho, "Effect of electron beam and γ -ray irradiation on the curing of epoxy resin," *Macromol. Res.*, vol. 10, no. 6, pp. 332–338, Jan. 2002, doi: 10.1007/BF03218327.
- [190] Y. C. Nho, P. H. Kang, and J. S. Park, "The characteristics of epoxy resin cured by γ -ray and E-beam," *Radiation Physics and Chemistry*, vol. 71, no. 1–2, pp. 243–246, Jan. 2004, doi: 10.1016/j.radphyschem.2004.03.047.
- [191] "Hexion Technical Data Sheet EPIKOTE™ Resin MGS™ RIMR 135 and EPIKURE™ Curing Agent MGS™ RIMH 134–RIMH 137." Hexion Inc., Aug. 2006. Accessed: Sep. 07, 2024. [Online]. Available: https://www.metyx.com/wp-content/uploads/PDF_Files/Hexion/TDS/TDS%20RIMH%20137.pdf
- [192] J. W. Hancock and A. C. Mackenzie, "On the mechanisms of ductile failure in high-strength steels subjected to multi-axial stress-states," *Journal of the Mechanics and Physics of Solids*, vol. 24, no. 2–3, pp. 147–160, Jan. 1976, doi: 10.1016/0022-5096(76)90024-7.
- [193] J. C. Earl and D. K. Brown, "Distributions of stress and plastic strain in circumferentially notched tension specimens," *Engineering Fracture Mechanics*, vol. 8, no. 4, pp. 599–611, Jan. 1976, doi: 10.1016/0013-7944(76)90034-5.
- [194] S. Timoshenko and J. M. Gere, *Theory of elastic stability*, 2nd ed., Dover ed. Mineola, N.Y: Dover Publications, 2009.
- [195] Fernández, Pelayo, Noriega González, Álvaro, Lamela Rey, María Jesús, and Fernández Canteli, Alfonso Carlos, "Comparison of viscoelastic moduli fitting using optimization methods," in *Fracture mechanics for durability, reliability and safety 19th European Conference on Fracture ; Kazan, Russia, 26 - 31 August 2012*, ESIS, 2012. Accessed: May 08, 2024. [Online]. Available: <http://hdl.handle.net/10651/36347>
- [196] M. Kästner, "Skalenübergreifende Modellierung und Simulation des mechanischen Verhaltens von textilverstärktem Polypropylen unter Nutzung der XFEM," Dissertation, Technische Universität Dresden, Dresden, 2010.
- [197] A. Baumann and J. Hausmann, "Effect of high-energy radiation on the relaxation of residual stresses in Polycarbonate and Epoxy resin by stress optics," *Radiation Physics and Chemistry*, Jan. 2025, doi: 10.1016/j.radphyschem.2024.112236.
- [198] Y. Zhang and H. Gross, "Systematic design of microscope objectives. Part I: System review and analysis," *Advanced Optical Technologies*, vol. 8, no. 5, pp. 313–347, Aug. 2019, doi: 10.1515/aot-2019-0002.

- [199] A. Baumann, M. Duhovic, and J. Hausmann, "In Situ Microscopy of Fatigue-Loaded Embedded Transverse Layers of Cross-Ply Laminates: The Role of an Inhomogeneous Fiber Distribution," *J. Compos. Sci.*, vol. 8, no. 9, p. 366, Sep. 2024, doi: 10.3390/jcs8090366.
- [200] M. A. Sutton, J. H. Yan, V. Tiwari, H. W. Schreier, and J. J. Ortu, "The effect of out-of-plane motion on 2D and 3D digital image correlation measurements," *Optics and Lasers in Engineering*, vol. 46, no. 10, pp. 746–757, Oct. 2008, doi: 10.1016/j.optlaseng.2008.05.005.
- [201] W. Langgemach, A. Baumann, M. Ehrhardt, T. Preußner, and E. Rädlein, "The strength of uncoated and coated ultra-thin flexible glass under cyclic load," *AIMSMATES*, vol. 11, no. 2, pp. 343–368, 2024, doi: 10.3934/mat.2024019.
- [202] *Publication manual of the American Psychological Association (7th ed.)*. Washington: American Psychological Association, 2020. doi: 10.1037/0000165-000.
- [203] D. C. Montgomery and G. C. Runger, *Applied statistics and probability for engineers*, 5th ed. Hoboken, NJ: Wiley, 2011.
- [204] W. Waldman, "Beta Factors for Collinear Asymmetrical Cracks Emanating from an Offset Circular Hole in a Rectangular Plate," Defence Science and Technology Group, Victoria 3207, Australia, Research report DST-Group-RR-0437, May 2016. Accessed: Jan. 08, 2024. [Online]. Available: <https://www.dst.defence.gov.au/publication/beta-factors-collinear-asymmetrical-cracks-emanating-offset-circular-hole-rectangular>
- [205] Yuanchen Huang, Kyo Kook Jin, and Sung Kyu Ha, "Effects of Fiber Arrangement on Mechanical Behavior of Unidirectional Composites," *Journal of Composite Materials*, vol. 42, no. 18, pp. 1851–1871, Sep. 2008, doi: 10.1177/0021998308093910.
- [206] H. F. Brinson and L. C. Brinson, *Polymer Engineering Science and Viscoelasticity: An Introduction*. in SpringerLink Bücher. Boston, MA: Springer US, 2008. doi: 10.1007/978-0-387-73861-1.
- [207] K. Kwok and S. Pellegrino, "Micromechanics Models for Viscoelastic Plain-Weave Composite Tape Springs," *AIAA Journal*, vol. 55, no. 1, pp. 309–321, Jan. 2017, doi: 10.2514/1.J055041.
- [208] A. R. Bunsell, Ed., *Handbook of tensile properties of textile and technical fibres*. in Woodhead publishing in textiles, no. 91. Boca Raton, Fla.: CRC Press [u.a.], 2009.
- [209] Z. Hashin, "Theory of fiber reinforced materials," Universtiy of Pennsylvania, Philadelphia, Contractor report NASA CR-1974, Mar. 1972. Accessed: Mar. 13, 2024. [Online]. Available: <https://ntrs.nasa.gov/citations/19720014282>
- [210] SIMULIA, Ed., "ABAQUS 6.6 Documentation." Accessed: Jun. 06, 2024. [Online]. Available: <https://classes.engineering.wustl.edu/2009/spring/mase5513/abaqus/docs/v6.6/books/gsa/default.htm?startat=ch13s02.html>
- [211] R. C. Gonzalez and R. E. Woods, *Digital image processing*, Fourth edition, Global edition. New York, NY: Pearson, 2018.
- [212] C. V. Singh and R. Talreja, "Analysis of multiple off-axis ply cracks in composite laminates," *International Journal of Solids and Structures*, vol. 45, no. 16, pp. 4574–4589, Aug. 2008, doi: 10.1016/j.ijsolstr.2008.04.004.
- [213] J. Bergstrom, *Mechanics of solid polymers: Theory and computational modeling*, First edition. Amsterdam: William Andrew Publishing, 2015.

- [214] A. Endruweit, F. Gommer, and A. C. Long, “Stochastic analysis of fibre volume fraction and permeability in fibre bundles with random filament arrangement,” *Composites Part A: Applied Science and Manufacturing*, vol. 49, pp. 109–118, Jun. 2013, doi: 10.1016/j.compositesa.2013.02.012.
- [215] A. Zaami, I. Baran, Ton. C. Bor, and R. Akkerman, “Optical characterization of fiber-reinforced thermoplastic tapes for laser-based composite manufacturing,” *Composites Part A: Applied Science and Manufacturing*, vol. 146, p. 106402, Jul. 2021, doi: 10.1016/j.compositesa.2021.106402.
- [216] N. A. Fleck, K. J. Kang, and M. F. Ashby, “Overview no. 112: The cyclic properties of engineering materials,” *Acta Metallurgica et Materialia*, vol. 42, no. 2, pp. 365–381, Feb. 1994, doi: 10.1016/0956-7151(94)90493-6.
- [217] A. P. Unwin, P. J. Hine, I. M. Ward, M. Fujita, E. Tanaka, and A. A. Gusev, “Escaping the Ashby limit for mechanical damping/stiffness trade-off using a constrained high internal friction interfacial layer,” *Sci Rep*, vol. 8, no. 1, p. 2454, Feb. 2018, doi: 10.1038/s41598-018-20670-0.
- [218] R. Song, A. Muliana, and K. Rajagopal, “A thermodynamically consistent model for viscoelastic polymers undergoing microstructural changes,” *International Journal of Engineering Science*, vol. 142, pp. 106–124, Jan. 2019, doi: 10.1016/j.ijengsci.2019.05.009.

13 Publications and symposia

Publications used within this work are highlighted.

- [A1] A. Baumann, A. Backes, and J. Hausmann, "Insights into a better understanding of organo sheets under fatigue loading," presented at the EUROMAT, Stockholm, Sweden, Jan. 09, 2019.
- [A2] A. Baumann and J. Hausmann, "A modified testing method for cyclic compression testing – Experimental evaluation of pros and cons of the usage of an anti-buckling device," presented at the Online session ECCM (Covid-19 Pandemic), 2020.
- [A3] A. Baumann, S. Backe, and J. Hausmann, "Investigation of the fatigue behavior of thermoplastic composites by load increase tests," *Journal of Composite Materials*, vol. 55, no. 4, pp. 541–550, Jan. 2021, doi: 10.1177/0021998320954524.
- [A4] A. Baumann and J. Hausmann, "Compression Fatigue Testing Setups for Composites—A Review," *Adv Eng Mater*, vol. 23, no. 2, p. 2000646, Feb. 2021, doi: 10.1002/adem.202000646.
- [A6] A. Baumann and J. Hausmann, "ERMÜDUNGSEIGENSCHAFTEN VON BAUTEILEN AUS GEWEBEVERSTÄRKTEN THERMOPLASTEN - WERKSTOFFBESCHREIBUNG UND BAUTEILVERHALTEN," in *Betriebsfestigkeit im Spannungsfeld neuer Mobilitätskonzepte und Fertigungstechnologien*, Kaiserslautern, 30.09 2021. doi: 10.48447/BF-2021-003.
- [A7] A. Baumann and J. Hausmann, "Experimental Investigation of Instabilities on Different Scales in Compressive Fatigue Testing of Composites," *J. Compos. Sci.*, vol. 5, no. 4, p. 114, Jan. 2021, doi: 10.3390/jcs5040114.
- [A8] A. Baumann and J. Hausmann, "Leak proof design of in-mold manufactured metallic feedthroughs in composite components," presented at the Euromat 2021 online (Covid-19 Pandemic), 2021.
- [A9] A. Baumann and J. Hausmann, "Understanding potential pitfalls in compression fatigue test data of composite materials in Review of Aeronautical Fatigue Investigations in Germany during the Period of April 2019 to May 2021," ICAF, Apr. 2021. [Online]. Available: https://www.icafe.aero/national_reviews.php?year=2021
- [A10] K. Schricker, A. Baumann, and J. P. Bergmann, "Local Shielding Gas Supply in Remote Laser Beam Welding," *JMMP*, vol. 5, no. 4, p. 139, Jan. 2021, doi: 10.3390/jmmp5040139.
- [A11] A. Baumann and J. Hausmann, "Irradiation induced crosslinking in thermoplastic polyurethanes for structural applications," presented at the 23. Symposium Verbundwerkstoffe und Werkstoffverbunde, Leoben, Austria, Jun. 2022.
- [A12] A. Baumann, D. May, and J. Hausmann, "Characterization of metallic bushings in RTM-made composites by in-situ leak detection under mechanical loading," *Composites Part C: Open Access*, vol. 7, p. 100226, Jan. 2022, doi: 10.1016/j.jcomc.2021.100226.
- [A13] A. Baumann and J. Hausmann, "Correlating composite fatigue to its matrix properties," presented at the Fatigue 2022+1, Hiroshima, Japan, 10.11 2023.

- [A14] A. Baumann and J. Hausmann, "Effect of high energy radiation on technical polymers," presented at the Proceedings 60th ISC, Ilmenau: ilmedia, 2023. doi: 10.22032/dbt.58861.
- [A15] W. Langgemach, A. Baumann, M. Ehrhardt, T. Preußner, and E. Rädlein, "The strength of uncoated and coated ultra-thin flexible glass under cyclic load," *AIMSMATES*, vol. 11, no. 2, pp. 343–368, 2024, doi: 10.3934/matetsci.2024019.
- [A16] A. Baumann, M. Duhovic, and J. Hausmann, "In Situ Microscopy of Fatigue-Loaded Embedded Transverse Layers of Cross-Ply Laminates: The Role of an Inhomogeneous Fiber Distribution," *J. Compos. Sci.*, vol. 8, no. 9, p. 366, Sep. 2024, doi: 10.3390/jcs8090366.
- [A17] A. Baumann and J. Hausmann, "Effect of high-energy radiation on the relaxation of residual stresses in Polycarbonate and Epoxy resin by stress optics," *Radiation Physics and Chemistry*, Jan. 2025, doi: 10.1016/j.radphyschem.2024.112236.

14 Student theses

Within the scope of this work, the following student works, among others, have been supervised.

Kneip, L.: Weiterentwicklung einer Prüfmethode zur Charakterisierung von Faserverbundwerkstoffen unter Druck, Studienarbeit, Kaiserslautern, IVW-Bericht, 2021, 21-005

Heimann, E.: Auslegung einer Versuchsmethode zur Druckprüfung von Faserverbundproben aus UD-Laminaten mit dem Ziel der Erzeugung eines definierten Versagensmechanismus, Studienarbeit HS Kaiserslautern, 2021

Blatz, Rudolf.: Auslegung einer Vorrichtung zur synchronisierten Bewegung eines Mikroskops zur Probenverformung. Studienarbeit, Kaiserslautern, IVW-Bericht, 2022, 22-028

Curriculum Vitae

Personal information

Andreas Stefan Baumann

Secondary education

Aug. 2000 – Jun. 2008 Werner-Heisenberg-Gymnasium in Bad Dürkheim

Academic education

Oct. 2016 – Sep. 2018 Master of Science Industrial Engineering Technical University Ilmenau

Apr. 2012 – Nov. 2015 Extra occupational study of Industrial Engineering at the university of applied science Kaiserslautern with the Degree Bachelor of Engineering

Work experience

Oct. 2018 - current Research assistant fatigue and lifetime prediction at the Leibniz-Institut für Verbundwerkstoffe GmbH (IVW)

Jul. 2011 - Jun. 2016 Materials tester (lab assistant) at BASF SE
Characterization of materials and component testing in static and fatigue loading

Sep. 2008 – Jun. 2011 Apprenticeship as a materials tester specializing in metals technology at BASF SE in Ludwigshafen

Kaiserslautern, June 2024